Atomic-Scale Investigations of Multiwall Carbon Nanotube Growth

A DISSERTATION
SUBMITTED TO THE FACULTY OF THE GRADUATE SCHOOL OF
THE UNIVERSITY OF MINNESOTA
BY

Michael John Behr

IN PARTIAL FULFILLMENT OF THE REQUIREMENTS
FOR THE DEGREE OF
DOCTOR OF PHILOSOPHY

Eray S. Aydil, Advisor

JUNE 2010

Acknowledgements

I have been so fortunate to have been surrounded by incredible people both in academia and at home. The help I have received from many has enabled me to achieve more than I could have imagined over the past five years while here at the University of Minnesota.

My thesis advisor, Professor Eray S. Aydil, has truly been an inspiration to me. Through the highs and lows of my research, he has offered me his time, energy, guidance, and provided me every opportunity to learn and grow as a scientist.

Professor K. Andre Mkhoyan became a second advisor for me over the past two years. He provided me a much-needed expertise in electron microscopy. I've learned an incredible amount from him; my thesis would not have been the same without his guidance.

I would like to thank Dr. Ozan Ugurlu for working tirelessly to keep the electron microscopes in excellent condition, for his willingness to teach me new microscopy techniques, and for always taking time to answer my questions. He has been an invaluable resource for me.

I also had the opportunity to work closely with E. Ashley Gaulding, an undergraduate researcher, for almost two years. She began working with me at a point when the direction of my research was in question. Her hard work, inquisitive questions, and strong desire to seek answers helped steer my research in a fruitful direction.

This journey through graduate school has been made easier and much more enjoyable because of the support I have received from my family. My wife, Anastasia, has given me her constant loving support, her companionship, and has even helped me with those tough mathematical derivations. My parents, John and Patricia, and my brother and sister, David and Jackie, have always been there for me. Their love, support, and encouragement has helped me every step of the way.

To my family

Abstract

The combination of unique mechanical, thermal, optical, and electronic properties of carbon nanotubes (CNTs) make them a desirable material for use in a wide range of applications. Many of these unique properties are highly sensitive to how carbon atoms are arranged within the graphene nanotube wall. Precise structural control of this arrangement remains the key challenge of CNT growth to realizing their technological potential. Plasma-enhanced chemical vapor deposition (PECVD) from methane-hydrogen gas mixtures using catalytic nanoparticles enables large-scale growth of CNT films and controlled spatial placement of CNTs on a substrate, however, much is still unknown about what happens to the catalyst particle during growth, the atomistic mechanisms involved, and how these dictate the final nanotube structure. To investigate the fundamental processes of CNT growth by PECVD, a suite of characterization techniques were implemented, including attenuated total-reflection Fourier transform infrared spectroscopy (ATR-FTIR), optical emission spectroscopy (OES), Raman spectroscopy, convergent-beam electron diffraction (CBED), high-resolution transmission and scanning-transmission electron microscopy (TEM, STEM), energy dispersive x-ray spectroscopy, and electron energy-loss spectroscopy (EELS).

It is found that hydrogen plays a critical role in determining the final CNT structure through controlling catalyst crystal phase and morphology. At low hydrogen concentrations in the plasma iron catalysts are converted to Fe_3C, from which high-quality CNTs grow; however, catalyst particles remain as pure iron when hydrogen is in abundance, and produce highly defective CNTs with large diameters. The initially faceted and equiaxed catalyst nanocrystals become deformed and are elongated into a teardrop morphology once a tubular CNT structure is formed around the catalyst particles. Although catalyst particles are single crystalline, they exhibit combinations of small-angle ($\sim 1^o$-3^o) rotations, twists, and bends along their axial length between adjacent locations. Distortions are most severe away from the base up into the nanotube where the number of walls is large. This suggests that the stresses generated by the surrounding nanotube distort the catalyst particle during growth. Fe_3C catalyst nanoparticles that are located inside the base of well-graphitized CNTs of similar structure and diameter do

not exhibit a preferred orientation relative to the nanotube axis. Thus, it does not appear that the graphene nanotube walls of a CNT are necessarily produced in an epitaxial process directly from Fe_3C faces. Chemical processes occurring at the catalyst-CNT interface during growth were inferred by measuring, *ex situ*, changes in atomic bonding at an atomic scale with a 0.15 nanometer electron probe. The observed variation in carbon concentration through the base of catalyst crystals reveals that carbon from the gas phase decomposes on Fe_3C, near where the CNT walls terminate at the catalyst base. An amorphous carbon-rich layer at the catalyst base provides the source for CNT growth. EELS measurements and Z-contrast STEM imaging provide evidence that carbon diffuses on the Fe_3C catalyst surface, along its interface with both the iron oxide shell and CNT walls. Atomic-scale EELS measurements at the catalyst surface in locations of CNT wall formation revealed no change in the iron L_{23} edge compared to the bulk of the catalyst, indicating that Fe_3C did not decompose to BCC iron and graphite during CNT wall formation.

Hydrogen atoms also interact with the graphene walls of CNTs. When the flux of H atoms is high, the continuous cylindrical nanotube walls can be etched and amorphized. Etching is not uniform across the length of the CNT, but rather, small etch pits form at defective sites on the CNT walls along the entire nanotube length. Once an etch pit is formed, etching proceeds rapidly, and the remainder of the CNT is quickly etched away. By examining the H-etching behavior of planar sheets of graphite, it is determined that H etching occurs preferentially at the graphite edges, or equivalently, at the exposed graphene edges present at nanotube etch pits.

Table of Contents

Acknowledgements i

Abstract iii

Table of Contents v

List of Tables ix

List of Figures x

1 INTRODUCTION 1

1.1 Carbon Nanotube Structure 1
1.2 Physical Properties of Carbon Nanotubes 6
1.2.a Mechanical and Thermal Properties 6
1.2.b Electronic Properties 6
1.3 Potential Applications of Carbon Nanotubes 9
1.4 Carbon Nanotube Synthesis Methods 11
1.5 Thesis Overview 12
1.6 References 16

2 CARBON NANOTUBE GROWTH USING PLASMAS AND PLASMA-SURFACE DIAGNOSTIC TOOLS 20

2.1 Introduction 20
2.2 Plasmas 20
2.3 Plasma Reactor 24
2.4 Plasma Diagnostics 25
2.4.a Optical Emission Spectroscopy using Actinometry 26
2.4.b Fourier Transform Infrared Spectroscopy 28
2.5 Spectroscopic Ellipsometry 31
2.6 References 33

3 MATERIALS CHARACTERIZATION TECHNIQUES 34

3.1 Introduction 34
3.2 The Transmission Electron Microscope 34
3.2.a Fast Electron Interactions with Matter 35
3.2.b Electron Optics 37

3.3 Electron Diffraction 41
3.4 Imaging Modes 43
3.5 Scanning Transmission Electron Microscopy 44
3.6 X-ray Energy-Dispersive Spectroscopy 47
3.7 Electron Energy-Loss Spectroscopy 48
3.7.a Instrumentation 49
3.7.b The Electron Energy-Loss Spectrum 50
3.7.c Energy Loss by Plasmon Excitation 51
3.7.d Energy Loss by Inner-Shell Ionization 52
3.8 Other Techniques 55
3.9 References 56

4 CATALYST ROTATION, TWISTING, AND BENDING DURING MULTIWALL CARBON NANOTUBE GROWTH 58

4.1 Introduction 58
4.2 Experimental 59
4.3 Results and Discussion 59
4.4 Conclusions 67
4.5 References 69

5 ORIENTATION AND MORPHOLOGICAL EVOLUTION OF CATALYST NANOPARTICLES DURING CARBON NANOTUBE GROWTH 71

5.1 Introduction 71
5.2 Experimental 73
5.2.a Catalyst Nanoparticle Deposition 73
5.2.b CNT Growth by PECVD 73
5.2.c Electron Microscopy 73
5.3 Results and Discussion 74
5.3.a Evolution of Structure and Morphology During CNT Growth 74
5.3.b Initial stages of CNT growth 79
5.3.c Catalyst Orientation With Respect to the CNT Axis 81
5.4 Conclusions 84
5.5 References 86

6 A HIGH-RESOLUTION ELECTRON ENERGY-LOSS SPECTROSCOPY STUDY OF THE CATALYST PARTICLE DURING PLASMA ENHANCED CHEMICAL VAPOR DEPOSITION OF CARBON NANOTUBES 89

6.1 Introduction 89
6.2 Experimental 91
6.3 Results and Discussion 93
6.4 Conclusions 103
6.5 References 105

7 EFFECT OF HYDROGEN ON CATALYST NANOPARTICLES IN CARBON NANOTUBE GROWTH 109

7.1 Introduction 109
7.2 Materials and Methods 110
7.3 Results and Discussion 112
7.3.a Gas Phase Analysis 112
7.3.b CNT Structure 117
7.3.c Catalyst Morphology and Crystalline Phase 121
7.3.d Discussion 124
7.4 Conclusions 125
7.5 References 127

8 HYDROGEN ETCHING AND CUTTING OF MULTIWALL CARBON NANOTUBES 130

8.1 Introduction 130
8.2 Materials and Methods 132
8.3 Results and Discussion 134
8.3.a Observations with TEM 134
8.3.b Raman spectroscopy 139
8.3.c Electron Energy-Loss Spectroscopy 141
8.3.d Discussion 143
8.4 Conclusions 144
8.5 References 146

9 ON THE TRANSFORMATION OF CARBON NANOTUBES TO DIAMOND 150

9.1 Introduction 150
9.2 Experimental Methods 152
9.3 Observations and Discussion 153
9.4 Conclusions 163
9.5 References 165

BIBLIOGRAPHY **168**

A APPENDIX: PLASMA DIAGNOSTICS **183**

A.1 Gas Temperature Measurements 183

A.2 CH_4 Dissociation Measurements 184

A.3 References 185

B APPENDIX: MEASUREMENT OF H-ATOM FLUX **186**

B.1 References 190

List of Tables

Table 4-1. α and β tilt angles and the calculated angular differences in crystal misorientation at each position shown in Figure 4-5 relative to position 5a. 65

Table 9-1. Comparison of observed d_{hkl} spacings through SAED with theoretical d_{hkl} spacings for cubic diamond, n-diamond, lonsdaleite, and the FCC phase. 158

Table 9-2. Comparsion of theoretical d_{hkl} spacings for cubic diamond, n-diamond, lonsdaleite, and the FCC phase with three cobalt phases: hexagonal cobalt, cubic cobalt, and cubic cobalt oxide. 163

List of Figures

Figure 1-1. (a) A planar sheet of graphene is the fundamental building block of (b) buckyballs, (c) nanotubes, and (d) graphite. Image from [9]. 2

Figure 1-2. (a) Graphene honeycomb hexagonal lattice. The unit basis vectors $\vec{a}_1$ and $\vec{a}_2$ define the primitive unit cell, indicated with a dotted line. (b) The corresponding reciprocal lattice of graphene is defined by the reciprocal lattice vectors, $\vec{b}_1$ and $\vec{b}_2$. The first Brillouin zone is shaded, and the high symmetry points K, M, and Γ are labeled. Image from [7]. 3

Figure 1-3. A carbon nanotube can be formed by rolling up a rectangular section of graphene. The structure of the carbon nanotube depends on the orientation of this rectangular section relative to the hexagonal graphene lattice. Two highly symmetric achiral nanotube structures exist, zigzag and armchair, as well as a variety of chiral nanotube structures. Image from [10]. 4

Figure 1-4. A CNT can be formed by rolling a graphene sheet along the chiral vector, $\vec{C}_h$ to form a cylinder such that points A and B, and C and D coincide. The resulting nanotube one-dimensional unit cell is defined by the axial vector $\vec{T}$ and chiral vector $\vec{C}_h$. The chiral angle, θ, is the angle between the armchair direction and $\vec{C}_h$, and can vary from 0° to 30°. All vectors are expressed in multiples of $\vec{a}_1$ and $\vec{a}_2$. Image from [12]. 6

Figure 1-5. (a) An illustration of the carbon valence orbitals, which consist of three in-plane σ (s, p_x, p_y) orbitals and one π (p_z) orbital perpendicular to the surface of the graphene sheet. (b) A molecular orbital energy diagram which shows the energy levels (bands) at the Γ-point of the σ and π bonding and σ^* and π^* anti-bonding orbitals near the Fermi level (E_F). Images from [20]. 7

Figure 1-6. The electronic band structure of graphene, calculated along high symmetry M-Γ-K directions, which are shown in Figure 1-2(b). The π bonding (valence) and π^* antibonding

(conduction) bands touch at the K point, resulting in semi-metallic characteristics. Image from [20]. 8

Figure 1-7. The allowed *k*-vectors of (5, 5), (7, 1), and (8, 0) CNTs are drawn as solid lines mapped onto the Brillouin zone of graphene. A CNT is metallic if one of these lines intersects the K point, as is the case for both the (5, 5) and (7, 1) nanotubes. Allowed *k*-vectors for the (8, 0) nanotube do not intersect the K point, thus it is semiconducting. Image from [19]. 9

Figure 2-1. The inductively-coupled plasma reactor equipped with an in situ infrared spectrometer and spectroscopic ellipsometer. 24

Figure 2-2. Optical emission spectrum obtained from an H_2/CH_4/Ar plasma used for carbon nanotube growth. Emission lines used in this work are labeled with the appropriate gas-phase species. 28

Figure 2-3. Full FTIR spectrum obtained from a H_2/CH_4/Ar gas mixture with no plasma (black curve) and with plasma activation (red curve). Rotation-vibration absorption bands of CH_4 and C_2H_2 are indicated. 30

Figure 3-1. (a) Vector diagrams for elastic scattering: $\boldsymbol{k}_0$ and $\boldsymbol{k}_1$ are the wavevectors of the fast electron before and after scattering, respectively. The scattering vector, $\boldsymbol{q}$, points in the direction of momentum transfer to the specimen; its magnitude is given by $q = 2k_0 \sin(\theta/2)$. (b) Vector diagram for inelastic scattering. For a given value of $\boldsymbol{k}_1$, or energy loss, there are a locus of possible values of $\boldsymbol{q}$ and θ, which are mapped by the dashed circle. Images from [4]. 36

Figure 3-2. Schematic diagram of a Schottky field-emission electron gun. Electrons extracted from the ZrO-coated tungsten tip are accelerated to 300 keV and brought to a crossover, which is then demagnified by the condenser lenses to illuminate the specimen. Image from [3]. 38

Figure 3-3. The illumination system of the TEM. (a) Condenser lenses C1 and C2 image the gun crossover at the front focal plane of the upper objective lens to provide parallel sample illumination. (b) A focused C2 lens illuminates a small area of the specimen. (c) The upper

objective lens and a weakened C2 lens combine to form a highly converged electron probe ~0.15 nm in diameter used for STEM imaging. Images from [3]. 40

Figure 3-4. The two primary modes of operation of the TEM imaging system. The intermediate lens is used to select either the back focal plane of the image plane of the objective lens as its object to project the (a) diffraction pattern or (b) image, respectively, on the viewing screen. Images from [3]. 41

Figure 3-5. (a) Selected-area electron diffraction pattern obtained from a BCC Fe single crystal with the incident electron beam oriented along the [001] zone axis. (b) Convergent-beam electron diffraction pattern obtained from an Fe_3C single crystal with the incident beam oriented along the [010] zone axis. 43

Figure 3-6. (a) Bright-field and (b) dark-field TEM images of an Fe metal catalyst crystal located inside of a multiwall carbon nanotube. 44

Figure 3-7. Schematic diagram of the three detectors used to form images in STEM mode. A disk-shaped detector centered on the optic axis is used to form bright-field images. Annular detectors collect electrons scattered through higher angles to form dark-field and high-angle Z-contrast images. 46

Figure 3-8. Schematic diagram of an EEL detection system that consists of pre-spectrometer focusing and alignment coils, a magnetic-prism spectrometer, quadrupole lenses, and a YAG scintillator that is fiber-optically coupled to a liner photodiode array. Image from [4]. 49

Figure 3-9. Electron energy-loss spectrum of a graphite flake with the measured electron intensity on a logarithmic scale, showing the zero-loss peak, plasmon peak, and carbon K ionization edge. 50

Figure 3-10. (a) Carbon K-edge EEL spectrum of graphite exhibits ELNES that consists of π^* and σ^* peaks. (b) Iron L_{23} core-loss edge exhibits ELNES that consists of two "white-lines", the L_3 and L_2 peaks. 53

Figure 4-1. (a) SEM image of the base region of the carbon nanotube bundles that have peeled off from the substrate. (b) Same bundle in higher magnification showing elongated catalyst nanocrystals located at the base of each nanotube. 60

Figure 4-2. (a) BF and (b) DF TEM images of an oriented cementite catalyst crystal inside the base of a multiwall carbon nanotube. The crystal [100] zone axis is parallel to the electron beam. The DF image was formed from the 020 spot. 61

Figure 4-3. BF TEM image (top) of a cementite crystal approximately 60 nm in length oriented along the [001] zone axis at position 3a and the CBED patterns (bottom) obtained from positions 3a-3c. The CBED intensity distribution changes as the probe is moved from position 3a to positions 3b and 3c, which indicates that the crystal orientation changes along its length. 62

Figure 4-4. BF TEM image (top) of a 225 nm long cementite crystal oriented along the [101] zone axis at position 4a and the CBED patterns (bottom) obtained from positions 4a-4f. The CBED intensity distribution changes significantly as the probe is moved along the crystal, which indicates a severe change in crystal orientation along its length. 63

Figure 4-5. HRTEM images comparing the number of graphene walls at the (a) top and (b) bottom region of a catalyst crystal inside the base of a carbon nanotube. Arrows indicate that the number of walls decreases significantly as one moves downwards towards the base of the catalyst crystal. (c) BF TEM image of a 400 nm long cementite crystal. Initially, the crystal was aligned along the [111] zone axis at position 5a. Tilt angles (α and β) required to return the crystal back to the same zone axis were recorded at each position 5a-e (see Table 4-1). 64

Figure 4-6. TEM images of (a) a catalyst nanoparticle before growth and (b) after nucleation of graphene layers. Before growth the catalyst nanoparticle is faceted. After growth of graphene layers the catalyst faces encapsulated by graphene layers lose their faceted shape and the catalyst exhibits strain contrast in the TEM. The regions not covered by graphene walls retain their facets. 67

Figure 5-1. (a) An SEM image of the iron catalyst film that was broken up into small nanometer-sized islands during the hydrogen plasma pretreatment. (b) A magnified view of the faceted iron catalyst islands. (c) Cross-section TEM image of the iron catalyst after pretreatment reveals the faceted nature of the catalyst crystals. (d) Cross-section TEM image of the catalyst film after 5 minutes of methane plasma exposure (growth conditions) shows deformed catalysts surrounded by ~5 nm thick layer of graphene walls. (e) Cross-section TEM image of an elongated crystal found inside a growing nanotube. (f) Cross-section SEM image of the ~4 micron thick CNT film after 30 minutes of growth. (g) A magnified view showing the CNT attachment to the substrate as well as catalysts that did not produce CNTs. (h) BF TEM image (left) of a similar crystal next to a schematic showing pictorially how catalyst crystals remain at the base of the CNT, attached to the substrate. (i) HAADF image of a representative Fe3C catalyst found inside the base of a MWCNT. 75

Figure 5-2. High-resolution (a) BF-TEM and (b) HAADF images of the base region of two similar catalyst crystals. Both Fe_3C catalysts exhibit clear faceting and are capped by a thin layer of iron oxide. CNT walls do not extend all the way to the base, but instead terminate at the iron oxide. (c) EEL and (d) EDX spectra obtained from the catalyst shown in the HAADF image of b confirm that the cap at the catalyst base contains iron, oxygen, and carbon..... 78

Figure 5-3. BF-TEM images of catalysts at early stages of CNT growth. (a) A catalyst at the base of a CNT beginning to elongate during the early stages of CNT growth. Adjacent sections of the catalyst are different sizes and are at different orientations. (b) A catalyst observed slightly further along in growth as evident by the more elongated shape. The arrow indicates a point of neck formation, where further growth would cause the catalyst to break in two. (c) A small portion of catalyst that had separated from the base catalyst through this necking process. CBED revealed that the orientation of the two pieces relative to the incident electron beam were identical. (d) An entire nanotube labeled with arrows that show small pieces of catalyst at various points along its length. The majority of catalyst that separates from the base occurs during early stages of growth, and therefore appears at the CNT tip. 81

Figure 5-4. An example illustrating the method used for determining the catalyst orientation relative to CNT axis. First, SAED patterns were obtained from an individual Fe_3C catalyst crystal at two different zone axes, in this example (a) [001] and (b) [102]. BF-TEM images of the same crystal at each orientation are also shown. Two diffraction spots from the surrounding CNT walls are also present in each pattern; one of these spots in each pattern is circled and denoted by its reciprocal lattice vector, g_{002}. This vector, by definition, is perpendicular to the nanotube axis. The Fe_3C crystallographic direction corresponding to the diffraction spot that is in line with this g_{002} vector is circled and labeled in each pattern, and is thus also perpendicular to the nanotube axis ([002] and $[40\bar{2}]$). The cross product between these two directions yields the orientation of the catalyst along the nanotube axis, [010]. 84

Figure 6-1. (a) HAADF image of an Fe_3C catalyst crystal located inside the base of a MWCNT. (b) Magnified HAADF image of the catalyst base reveals that Fe_3C is capped by a shell of iron oxide. (c) EELS spectrum of the iron oxide shell shows both oxygen and iron core-loss edges. (d) EDX spectrum of the iron oxide shell shows iron, oxygen, and carbon. (e) Schematic of the catalyst base region with arrows indicating the location where carbon from the gas phase enters into the catalyst. 94

Figure 6-2. (a) High-resolution ADF image of the bottom of the Fe_3C catalyst and iron oxide shell. EELS spectra were obtained every 0.6 nm along each colored line, in the direction indicated. Relative carbon concentration, as calculated from the carbon K-edges are plotted below. Plot colors correspond to the colored lines in the ADF image. 96

Figure 6-3. (a) High-resolution HAADF image exhibits decreased intensity in a carbon-rich region of the iron oxide near the triple interface of Fe_3C, iron oxide, and CNT walls. The carbon K-edge was measured at each position A, B, and C. (b) Comparison of the carbon K-edges from the three positions reveal that the carbon in the carbon-rich region is in an amorphous state. 98

Figure 6-4. (a) BF-TEM image of an Fe_3C catalyst located inside the base of a MWCNT attached to a substrate. Rectangles indicate regions of CNT wall growth, where the Fe L_{23} core-loss edge was measured. (b) High-resolution ADF image of the CNT-Fe_3C interface. The Fe

L_{23} core-loss edge was measured every 0.3 nm along each line. Measurements along the red line A probed the surface 1 of 2 atomic layers, while measurements along the blue line B probed mostly the bulk properties of the catalyst. (c) Averaged Fe L_{23} core-loss edge from each line scan. The red spectrum was multiplied by an appropriate factor to normalize intensity. The two spectra are identical, indicating that the surface is also Fe_3C, and does not contain a layer of metallic Fe 102

Figure 7-1. Optical emission intensities of H_α (656 nm, ○), CH (431 nm, □), and C_2 (516 nm, △) normalized with the Ar 750.4 nm emission intensity, and plotted as a function of H_2-to-CH_4 flow rate ratio. 113

Figure 7-2. (a) Typical rotation-vibration IR absorption spectra of methane gas at 10 Torr with plasma on (red) and plasma off (black). The first few rotational peaks of the R branch are labeled with the appropriate angular momentum quantum number. (b) The intensities of rotational absorption peaks from the R branch are displayed on a Boltzmann plot. A linear fit yielded a slope inversely proportional to the gas temperature. 115

Figure 7-3. (a) Fractional dissociation of CH_4 in the plasma (△), concentration of CH_4 that is not dissociated (○), and concentration of CH_4 that was dissociated in the plasma (□) as a function of H_2-to-CH_4 flow rate ratio. (b) Integrated intensity of acetylene absorption peak at 730 cm^{-1} as a function of H_2-to-CH_4 flow rate ratio. 116

Figure 7-4. (a)-(d) in the first column show cross-section SEM images of MWCNT films grown by catalytic PECVD using a 10 nm iron catalyst layer. H_2-to-CH_4 flow rate ratio increases from top to bottom, and is indicated on each image. (e)-(h) in the second column show representative BF-TEM images of the most commonly-observed CNT structures for each experiment in the first column. (i)-(l) in the third column show representative BF-TEM images of the most abundant catalyst crystal morphology observed inside the bases of the MWCNTs shown in the corresponding (same row) first and second columns. The MWCNTS were deposited with feed gas that contained (a,e,i) 0 sccm H_2 and 50 sccm CH_4, (b,f,j) 5 sccm H_2 and 5 sccm CH_4, (c,g,k) 25 sccm H_2 and 5 sccm CH_4, (d,h,l) 50 sccm H_2 and 5 sccm CH_4. 118

Figure 7-5. Average CNT diameter (□), and CNT length (○) as a function of H_2-to-CH_4 flow rate ratio. Error bars are the standard deviation for each sample and is a measure of the diameter distribution. 120

Figure 7-6. Raman spectra (inset) from a MWCNT film. The ratio of the D and G peak intensities, I(D)/I(G), as a function of H_2-to-CH_4 flow rate ratio. 121

Figure 7-7. BF-TEM images of (top two rows), and SAED patterns (bottom row) from, the most abundant catalyst crystals observed inside the base of MWCNTs grown using H_2-to-CH_4 flow rate ratios of (sccm H_2 : sccm CH_4) (a)-(c) 0:5, (d)-(f) 5:5, (g)-(i) 25:5 sccm, and (j)-(l) 50:5 sccm..... 123

Figure 8-1. (a)-(c) in the first column show BF-TEM images of segments of a MWCNT before H-atom exposure. (d)-(f) show the same segments after 15 minutes of H-atom exposure at room temperature. Nanotube walls show increased roughness due to formation of etch pits as indicated in (f). (g)-(i) show the same segments after a total H-atom exposure of 30 minutes. Numerous deep etch pits are observed along the nanotube lengths. Some regions are also now amorphous. The CNT shown in each panel is the same CNT across any row. 136

Figure 8-2. (a) and (b) High-resolution BF-TEM images of different locations along the edge of a HOPG flake after 60 minutes of H-atom exposure at room temperature. The initially highly-crystalline layered HOPG structure is now very disordered, as evident by the random and squiggly lattice fringes, and contains holes. (c) BF-TEM of a HOPG flake before H-atom exposure is highly crystalline, and does not contain holes. 138

Figure 8-3. (a) BF-TEM image of a high-quality, well-graphitized MWCNT that has received 10 minutes of H-atom exposure at 725 ^{o}C. Numerous etch pits are present along the nanotube length; one etch pit is indicated with the white rectangle. (b) Magnified imaged of the etch pit enclosed by the white rectangle in (a). (c) A MWNCT from the same sample that received an additional 2 minutes of H-atom exposure. During this short additional exposure, H atoms reacted rapidly at the exposed graphene edges of etch pits to completely cut through the

nanotube. (d) A magnified image of a location where the nanotube was cut shows that some of the carbon in this vicinity is amorphous. 139

Figure 8-4. First-order Raman spectra of a HOPG flake face (a) and edge (b) before H-atom exposure. The intensity ratio I(D)/I(G) is was calculated and is displayed on each plot. Raman spectra obtained from the face (c) and edge (d) of the HOPG flake after 60 minutes of H-atom exposure at room temperature. The greater increase in the intensity ratio I(D)/I(G) at the HOPG edge indicates that H preferentially reacts here. 141

Figure 8-5. (a) A representative EELS spectrum of the carbon K-edge obtained from a MWCNT. The π* and σ* peaks are labeled. The incident electron beam was defocused such that the entire diameter of the nanotube was probed. (b) A plot of the π*-to-(π*+σ*) intensity ratio as measured by integrating over a 1.5 eV-wide window centered around each peak, as a function of H-plasma exposure time. This ratio remains constant over the 30 minutes of H-plasma exposure, which indicates that the amorphous carbon formed remains sp^2-hybridized. 143

Figure 9-1. (a) BF-TEM image of strings of crystals present in locations were MWCNFs once laid. The nanofibers were exposed to an H-plasma at room temperature for 15 hours. The large cone-shaped crystals are the iron-based catalysts used to grow the nanofibers. (b) Magnified view of two nanocrystals strings. 154

Figure 9-2. An amorphous nanorod observed after H-plasma exposure of a MWCNT at room temperature for 10 hours. Nanocrystals are observed embedded in the amorphous rod. The inset shows a high-resolution image of one representative nanocrystal with a lattice fringe spacing of 0.21 nm. 155

Figure 9-3. BF-TEM image of large agglomerates of crystallites, ~5-40 nm in diameter. This sample was initially covered with MWCNTs, and then exposed to an H plasma for 10 hours at 450 ^{o}C. Similar agglomerates of crystallites were observed in all samples exposed to H-plamas over the temperature range from room temperature to 1073 K. 155

Figure 9-4. (a) SAED intensity versus interplanar spacing, d_{hkl}, for nanocrystals present after MWCNTs were exposed to an H plasma for 10 hours at 300 K, 727 K, and 1073 K and 3.5 hours of H exposure at 1073 K. Theoretical peak positions for cubic diamond and lonsdaleite are indicated by their 3- and 4-index Miller notation, respectively. Also indicated are the diffraction peaks at spacings of 0.178 nm and 0.246 nm that correspond to n-diamond and FCC carbon, respectively. (b)-(d) HRTEMs, inverse Fourier transforms (lower right insets), and power spectra (upper left insets) of nanocrystals present after exposure of MWCNTs to H for 10 hours at 300 K. (b) A nanocrystal showing lattice spacings consistent with diamond or n-diamond oriented along its [011] zone axis. (c) A nanocrystal showing lattice spacings consistent with lonsdaleite oriented along its [0001] zone axis. (d) An FCC nanocrystal with lattice parameter a = 0.426 nm oriented along its [011] zone axis. (E) CBED patterns obtained from a nanocrystal showing lattice fringe spacings of 0.246 nm and 0.213 nm. The patterns are superimposed on a simulated FCC Kikuchi map, which displays the symmetry and angular relationships (in boxes between CBED patterns) between pairs of zones. Individual CBED patterns show FCC symmetry with a = 0.426 nm. 156

Figure 9-5. (a) BF-TEM image of a MWCNF that was exposed to an H-plasma for 15 hours at room temperature. This is the same sample as shown in Figure 9-1 (b) The string of nanocrystals were examined with EDX, and found to be composed of iron. No carbon is present. The silicon and nitrogen peaks are due to the amorphous Si_3N_4 TEM support film. . 159

Figure 9-6. (a) Strings of nanocrystals present in locations where nanotubes once laid after H-plasma exposure under the same conditions used by Sun et al. (p = 1.1 Torr, 200 W, 1000 K). (b) Nanometer-scale EDX analysis of the nanocrystals reveals that they are in fact composed of cobalt, and cobalt and oxygen. No carbon is present. These crystals are hexagonal Co and FCC Co. 160

Figure 9-7. (a) A string of nanocrystals from an H-exposed MWCNT sample that was further annealed at high temperature. These crystals exhibited symmetries and d_{hkl} spacings consistent with FCC carbon a = 0.426 nm. Representative (b) EDX and (c) EELS spectra obtained from

these crystals reveal that they are composed of cobalt and oxygen. Especially evident in the EELS spectrum is the absence of a carbon peak at ~284 eV. These crystals are CoO. 162

Figure B-1. (a) Infrared absorption spectra, obtained in attenuated-total-reflection mode, of a 110 nm thick polycrystalline ZnO film after 20-second H-atom exposures at room temperature. The broad-band free-electron absorption increases as H atoms from the plasma are incorporated into the film. (b) A plot of the increase in carrier density as calculated from the absorption spectra as a function of the H-atom exposure time. The slope of this plot multiplied by the ZnO film thickness yields the H flux to the film surface, 2.2×10^{17} $cm^{-2}s^{-1}$……189

1 Introduction

Hybidization between *s* and *p* orbitals in carbon allows it to form a variety of allotropes such as diamond, lonsdaleite [1, 2], graphite, fullerenes [3], and carbon nanotubes [4]. The structural differences amongst these allotropes endow them with a wide range of physical properties. Carbon nanotubes (CNTs) are a cylindrical molecule and member of the fullerene structural family which have received tremendous attention due to their unique combination of novel structural, chemical, mechanical, thermal, optical, optoelectronic, and electronic properties. A CNT is the strongest and stiffest material known. The bonds between carbon atoms in a CNT are stronger than those in diamond, resulting in an overall tensile strength that is ~100 times that of steel [5]. The wall of a CNT is unrivaled in its ability to conduct electricity and is capable of carrying current densities ~1,000 larger than that of copper [6]. By changing its atomic structure, however, CNTs can also perform as semiconductors, whose conductivity can be precisely controlled [7]. Thus, CNTs find numerous applications that span many diverse fields; however, the majority of these applications have not yet been realized due to the inability to precisely control their atomic structure.

1.1 Carbon Nanotube Structure

The structure of a CNT is akin to a miniature drinking straw—whose wall is constructed of carbon atoms with an overall diameter ~10,000 times thinner than a human hair. Specifically, its structure can be conceptualized as a single sheet of graphite (graphene) which is rolled into a seamless cylinder. This sheet of graphene is also the basic building block of other carbon structures such as graphite and fullerenes, as depicted in Figure 1-1. When rolled to form a cylinder, the resulting diameters are typically less than 10 nm, while the length-to-diameter ratio can exceed 10,000,000:1 [8]. A nanotube constructed of a single sheet is referred to as a single-wall carbon nanotube (SWCNT); when multiple nanotubes are nested inside one another, similar to a set of Russian dolls, the resulting structure is referred to as a multiwall carbon nanotube (MWCNT).

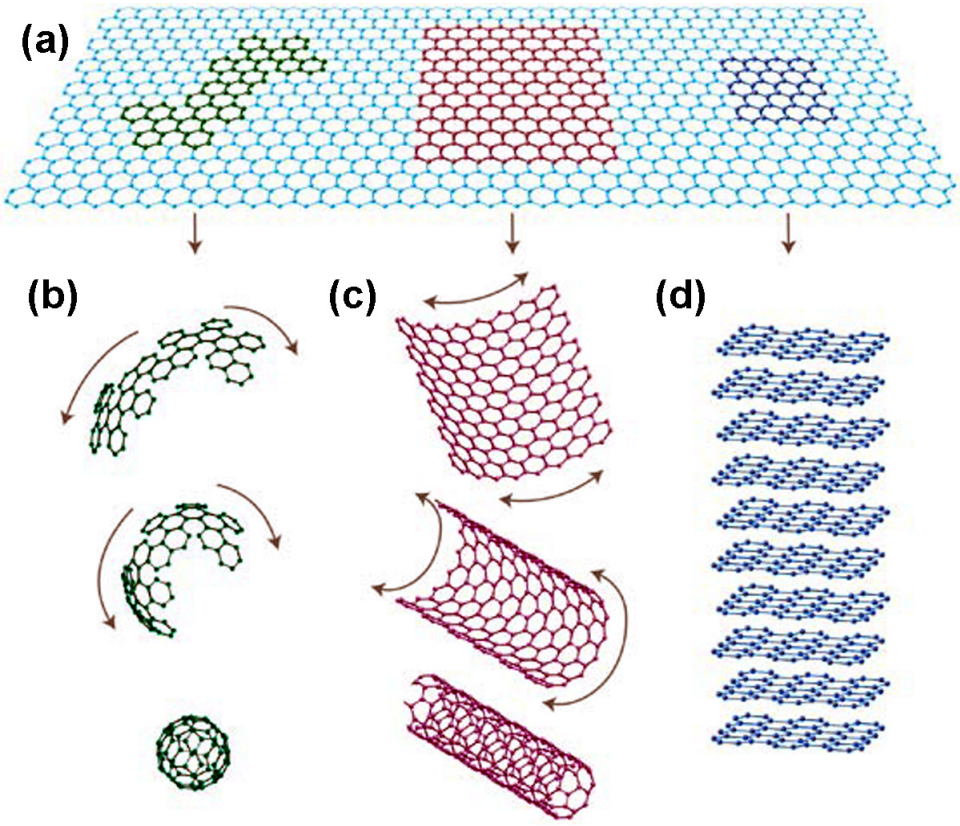

Figure 1-1. (a) A planar sheet of graphene is the fundamental building block of (b) buckyballs, (c) nanotubes, and (d) graphite. Image from [9].

Carbon atoms that make up each graphene wall are bonded through sp^2-hybridized bonds to form a hexagonal honeycomb lattice of six-membered rings. The unit cell and corresponding reciprocal lattice and Brillouin zone of the graphene lattice are shown in Figure 1-2. Vectors $\vec{a}_1$, $\vec{a}_2$, and $\vec{b}_1$, $\vec{b}_2$ are the unit basis vectors and reciprocal lattice vectors, respectively. When this planar sheet is rolled up to form a nanotube, the orientation of the in-plane six-membered rings of the graphene sheet wall defines the specific structure of the nanotube. The specific orientation of the in-plane hexagonal lattice is known as chirality. Nanotubes of many different chiralities are possible. Three of these different nanotube chiralities are shown in Figure 1-3; these nanotubes were formed by rolling up rectangular sections of the graphene sheet oriented at different angles relative the hexagonal lattice. In general, the structural symmetry of a nanotube can be classified as either achiral or chiral. An achiral nanotube is highly symmetric; its

structure is the same as its mirror image. Due to the six-fold symmetry of the graphene sheet, there are only two types of achiral nanotubes; armchair and zigzag nanotubes, which are formed from rectangular sections oriented along high-symmetry directions of the graphene sheet, as shown in Figure 1-3. Alternatively, a nanotube can be formed from a rectangular section that is not aligned along a high-symmetry direction to form a chiral nanotube (middle tube in Figure 1-3). Chiral nanotubes exhibit spiral symmetry, but do not posses the same mirror symmetry as achiral nanotubes [7].

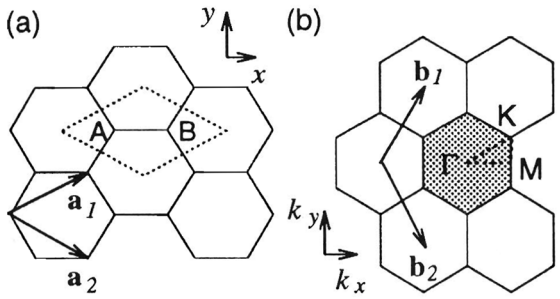

Figure 1-2. (a) Graphene honeycomb hexagonal lattice. The unit basis vectors $\vec{a}_1$ and $\vec{a}_2$ define the primitive unit cell, indicated with a dotted line. (b) The corresponding reciprocal lattice of graphene is defined by the reciprocal lattice vectors, $\vec{b}_1$ and $\vec{b}_2$. The first Brillouin zone is shaded, and the high symmetry points K, M, and Γ are labeled. Image from [7].

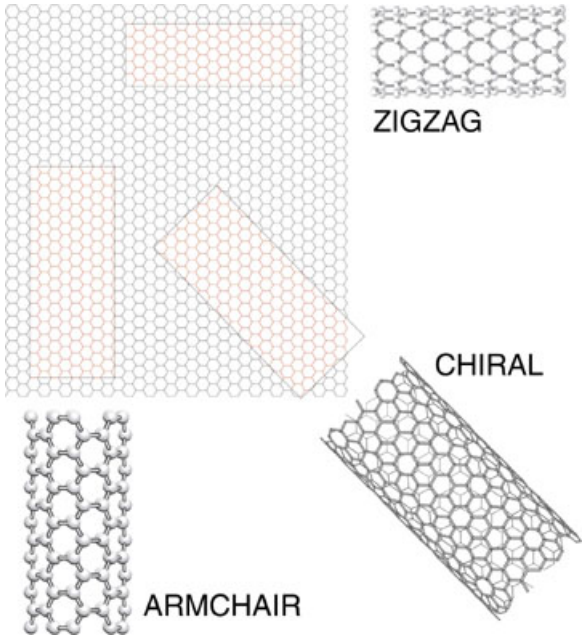

Figure 1-3. A carbon nanotube can be formed by rolling up a rectangular section of graphene. The structure of the carbon nanotube depends on the orientation of this rectangular section relative to the hexagonal graphene lattice. Two highly symmetric achiral nanotube structures exist, zigzag and armchair, as well as a variety of chiral nanotube structures. Image from [10].

The chirality of a nanotube, as well as its diameter can be specified exactly by a chiral index (n, m). The chiral indices (n, m) are integer multiples of the real-space unit basis vectors $\vec{a}_1$ and $\vec{a}_2$ of the hexagonal graphene lattice that define the chiral angle, θ, and nanotube diameter, which specifies each nanotube uniquely. As shown in Figure 1-4, a CNT can be formed by rolling the hexagonal graphene lattice along the chiral vector, $\vec{C}_h$, such that points A and B and C and D coincide. The resulting nanotube axis is parallel to the vector $\vec{T}$. A new unit cell is thus formed, the CNT unit cell, and is defined by the unit vectors $\vec{T}$ and $\vec{C}_h$; the nanotube axis is parallel to $\vec{T}$ and the circumference of the nanotube is $\left|\vec{C}_h\right|$. The chiral vector can be expressed in terms of the real-space unit vectors $\vec{a}_1$ and $\vec{a}_2$ of the hexagonal lattice through:

$$\vec{C}_h = n\vec{a}_1 + m\vec{a}_2$$

where n and m are integers and $0 \le |m| \le n$. The chiral index (n, m) thus uniquely defines the chiral angle and nanotube diameter. The nanotube diameter, d_t, is directly related to the length of the chiral vector, through

$$d_t = \frac{|\vec{C}_h|}{\pi} = \frac{a}{\pi}\sqrt{n^2 + m^2 + nm}\,.$$

And the chiral angle, θ, measured as the angle between $\vec{C}_h$ and the zigzag direction of the honeycomb lattice (n, 0) is related to the chiral index (n, m) through

$$\cos\theta = \frac{2n + m}{2\sqrt{n^2 + m^2 + nm}}\,.$$

Due to the six-fold symmetry of the hexagonal lattice the chiral angle θ can vary between 0 and 30°. Under this chiral index notation, the two highly-symmetric achiral CNTs, the armchair and zigzag, are described by (n, n) and (n, 0), respectively. In theory, there are an infinite number of possible chiral (n, m) nanotube structures, however due to diameter constraints, only a finite number are observed [11].

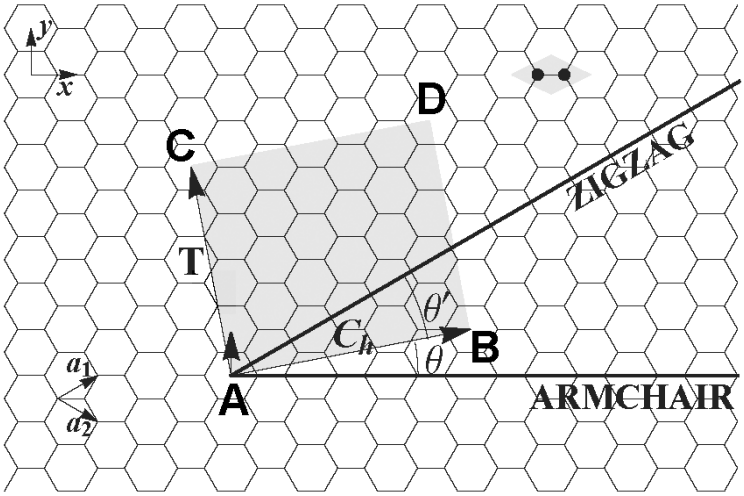

Figure 1-4. A CNT can be formed by rolling a graphene sheet along the chiral vector, $\vec{C}_h$ to form a cylinder such that points A and B, and C and D coincide. The resulting nanotube one-dimensional unit cell is defined by the axial vector $\vec{T}$ and chiral vector $\vec{C}_h$. The chiral angle, θ, is the angle between the armchair direction and $\vec{C}_h$, and can vary from 0° to 30°. All vectors are expressed in multiples of $\vec{a}_1$ and $\vec{a}_2$. Image from [12].

1.2 Physical Properties of Carbon Nanotubes

1.2.a Mechanical and Thermal Properties

The physical properties of CNTs are a direct result of their unique constituent strong carbon-carbon bonding. The primary sp^2-hybridized covalent atomic bonding in CNTs is the same as in graphite and graphene, which includes in-plane σ and π bonds that provide the strongest bonding in nature, and thus endows CNTs with extreme mechanical strength [13]. For example, CNTs are the stiffest and strongest known material, exhibiting Young's moduli in the terapascal (TPa) range [14, 15] and tensile strengths of a few 100 gigapascal (GPa) [5]. These values incredibly are an order of magnitude larger than those of well-known structural materials such as steel, carbon fibers, and Kevlar [16]. The strength of the C-C bonds additionally contributes to the superior heat transport properties of CNTs. Thermal conductivities of CNTs surpass that of diamond, ~2000 W/m-K [17].

1.2.b Electronic Properties

The above mentioned mechanical and thermal properties of CNTs are relatively insensitive to changes in nanotube chirality and diameter; however, this is not true when considering their electronic properties. Unlike the electronic properties of graphite and graphene, which are semimetals [18], a CNT can act as either a metal or a semiconductor, depending on its chirality and diameter. This phenomenon can be understood by first considering the structure of atomic bonding and the resulting electronic band structure of a two-dimensional sheet of planar graphene. Figure 1-5(a) shows schematically the electron valence orbitals of a constituent carbon atom in graphene. Each carbon atom contributes four valence orbitals, the 2s, $2p_x$, $2p_y$,

and $2p_z$ for its four valence electrons. The 2s, $2p_x$, and $2p_y$ orbitals combine, or hybridize, to form three equivalent in-plane σ bonding and σ^* anti-bonding orbitals, while the remaining $2p_z$ orbital is oriented perpendicular to the sheet, and interacts with neighboring p_z orbitals to form delocalized π bonding and π^* anti-bonding orbitals [19]. The energy levels associated with these different orbitals are shown in Figure 1-5(b). In-plane σ bonding σ^* anti-bonding orbitals are separated by a large gap (~12 eV) and do not produce energy levels close to the Fermi energy; thus, they do not contribute significantly to the electronic properties. The remaining π bonding and π^* anti-bonding orbitals do, however, contain energy states near the Fermi energy, and thus these delocalized orbitals control the electronic properties. Figure 1-6(a) shows the electronic band structure of the graphene hexagonal lattice as a function of electron momentum, $\vec{k}$, calculated along certain high-symmetry M-Γ-K directions in reciprocal (momentum) space in the Brillouin zone [19]; these high-symmetry directions are labeled in Figure 1-2(b). The bonding π (valence band) and antibonding π^* (conduction band) bands touch at the K point of the Brillouin zone. Thus, metallic properties are observed at these points, while semiconducting properties are observed elsewhere.

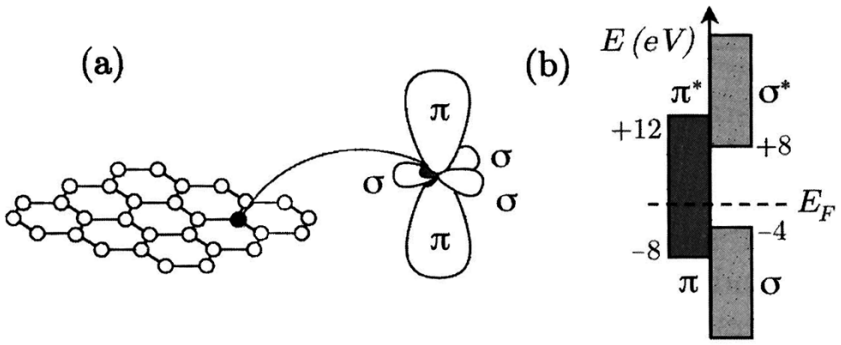

Figure 1-5. (a) An illustration of the carbon valence orbitals, which consist of three in-plane σ (s, p_x, p_y) orbitals and one π (p_z) orbital perpendicular to the surface of the graphene sheet. (b) A molecular orbital energy diagram which shows the energy levels (bands) at the Γ-point of the σ and π bonding and σ^* and π^* anti-bonding orbitals near the Fermi level (E_F). Images from [20].

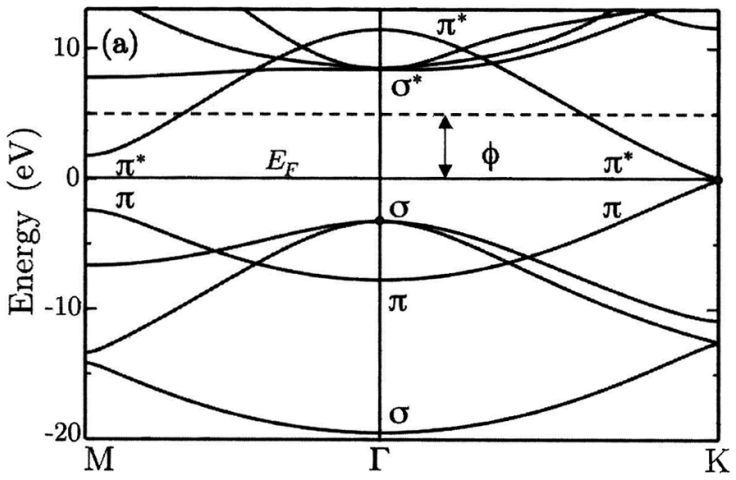

Figure 1-6. The electronic band structure of graphene, calculated along high symmetry M-Γ-K directions, which are shown in Figure 1-2(b). The π bonding (valence) and π* antibonding (conduction) bands touch at the K point, resulting in semi-metallic characteristics. Image from [20].

When a graphene sheet is rolled up to form a nanotube, periodic boundary conditions arise along the tube circumference that results in quantization of the allowed wave vectors $\vec{k}$, or electron momentum [19] along the $\vec{C}_h$ direction. The allowed values of $\vec{k}$ along the axis of the tube, however, remain continuous. Thus, reciprocal space of a carbon nanotube is a series of parallel lines that cut through the Brillouin zone of graphene to produce one-dimensional energy dispersion relations that are cross-sections of those of graphene [7], as shown in Figure 1-7. The length, orientation, and number of these parallel lines depend on the chiral indices (n, m) of the nanotube [19]. A particular (n, m) nanotube is metallic if one of its cutting lines passes through the K point of the graphene Brillouin zone, where the π bonding and π* anti-bonding orbitals overlap. This condition is met only when $(n-m)=3l$, where l is an integer. Metallic nanotubes include armchair (n, n) nanotubes, one third of all zigzag (n, 0) nanotubes when n is a multiple of 3, and approximately one third of chiral (n, m) nanotubes [7]. All other nanotubes, where a cutting line does not pass through the K (K') point, are semiconducting, with band gaps that vary from 0 to a few tenths of an eV [19]. The condition for a semiconducting nanotube is given by $(n-m)=3l\pm1$. The band gap of a semiconducting nanotube is further sensitive to

the nanotube diameter. Specifically, the band gap decreases as the inverse of nanotube diameter [21]. Thus, CNTs with a wide range of unique electronic properties can be obtained by simply changing their size or chirality.

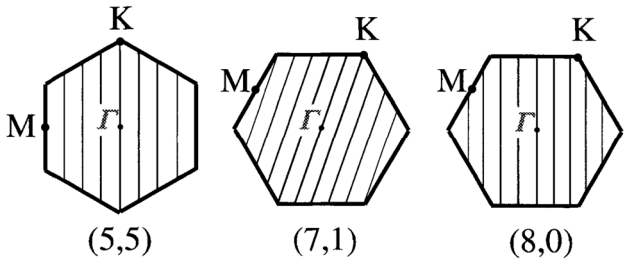

Figure 1-7. The allowed *k*-vectors of (5, 5), (7, 1), and (8, 0) CNTs are drawn as solid lines mapped onto the Brillouin zone of graphene. A CNT is metallic if one of these lines intersects the K point, as is the case for both the (5, 5) and (7, 1) nanotubes. Allowed *k*-vectors for the (8, 0) nanotube do not intersect the K point, thus it is semiconducting. Image from [19].

1.3 Potential Applications of Carbon Nanotubes

The extremely unique, superior, and diverse physical properties of CNTs naturally lend these structures to a number of tremendous applications in numerous fields. However, only a small fraction of their proposed uses have been commercialized due to enormous challenges related to the precise control of their structure during synthesis [22]. In this section, applications of carbon nanotubes that utilize their incredible mechanical strength and unique electronic and optical properties are discussed.

The relative insensitivity of the mechanical and thermal properties of CNTs to their diameter and chirality has resulted in a number of immediately accessible applications. Aligned arrays of CNTs can be utilized to conduct heat away from microprocessor chips to provide efficient cooling [23]. Though a more commonly investigated bulk application for CNTs is as an additive in polymers, to form a composite material with improved modulus and strength [24], thermal conductivity [25], vibration damping [26, 27], or other mechanical properties [28]. Addition of only a small (~1-2 %) weight fraction of CNTs can dramatically improve these properties. Challenges remain, however, to increase dispersive properties of nanotubes within

the host material, and to improve load transfer between the host material and the atomically-smooth walls of the dispersed CNTs [29]. Despite these challenges, CNTs in composites are an exciting application because they can impart a variety of desirable properties simultaneously.

The most exciting and potentially technologically-disruptive applications of CNTs utilize their unique electronic and optical properties. Most of these applications, however, remain as long-term (beyond ten years) because of the current lack of precise structural control during their synthesis. Over a decade ago, it was demonstrated that a semiconducting SWCNT can be switched from a conducting to an insulating state to operate as a field-effect transistor (FET) at room temperature [30, 31]. Their extremely small size, high on-off ratios (~10^5), higher (200 times more) current-carrying capability than conventional MOSFETs, and enormous carrier mobilities (~10^5 cm^2/Vs) [32] make CNT-FETs highly desirable, and represent a major step towards nanometer-scale electronics and molecular electronics [33, 34]. These devices, however, can also function as sensors. The resistance of individual semiconducting CNTs used in FETs has been shown to be highly sensitive to adsorbed molecules [35]; thus, CNT-FETs can be used as highly sensitive and selective gas sensors and biosensors [36]. Nanotubes that exhibit metallic characteristics can be integrated into electronic circuits as interconnects, or deposited as a thin conducting layer. In fact, CNTs exhibit ballistic electron transport of electrons, and can carry current densities ~1000 greater than copper [6]. All of the components of a transparent and flexible thin-film transistor, including semiconducting and conducting layers, can be constructed from networks of semiconducting and metallic SWCNTs to form a display device that is optically transparent and highly flexible [37, 38]. Thin films of SWCNTs also exhibit superior transmittance in the infrared and thus can be used in applications where a transparent conducting film is required, such as in LEDs or photovoltaic devices [39]. SWCNTs can also be utilized in photovoltaic devices to ballistically transport photo-excited charge carriers, or to aid in exciton generation and charge separation [40, 41]. Individual semiconducting CNTs can be used to absorb extended regions of the solar spectrum, as they generate additional excitons by absorbing light in the infrared region [42, 43]. The chirality and diameter of the CNT determines the range of absorption and exciton binding energies [19, 43].

The CNT applications discussed herein represent only a small fraction of the potential applications of CNTs. However, the challenges preventing realization of most potential applications are similar. Namely, the specific structure of a CNT, i.e. its chirality and diameter, can not yet be precisely controlled during its synthesis. In the following section, the various methods used to synthesize CNTs are presented in terms of their potential to enable such structural control.

1.4 Carbon Nanotube Synthesis Methods

There are four principal methods for synthesizing carbon nanotubes: (i) arc discharge evaporation [44], (ii) laser ablation [45], (iii) catalytic thermal chemical vapor deposition (C-TCVD) [46], and (iv) catalytic plasma enhanced chemical vapor deposition (C-PECVD) [47]. While arc discharge evaporation and laser ablation are very efficient methods for synthesizing large quantities of carbon nanotubes, they require extremely high temperatures (~3000 °C), complex purification processes, and offer no control over the spatial arrangement or structures of the produced carbon nanotubes [48]. Only C-TCVD and C-PECVD provide large-scale growth of CNT films, and controlled spatial placement of CNTs on a substrate [48].

In catalytic TCVD and PECVD, CNT growth occurs through a surface metal catalyst particle (e.g. cobalt, nickel, iron, etc.) from dissociated hydrocarbon gas molecules. Typical precursor gas mixtures include methane/hydrogen or acetylene/hydrogen. Dissociation of these hydocarbons can occur at the metal catalyst or in the plasma if PECVD is used, as described in chapter 2. An important, yet unexpected, benefit of PECVD growth is the vertical alignment (perpendicular to local surface) of the CNTs, presumably due to their interaction with the sheath electric field that exists directed perpendicular to the substrate [49]. PECVD is an attractive technique because of the control it offers over spatial placement of CNTs on a substrate, as well as the potential to grow CNTs at much lower temperatures than possible by TCVD [50]. However, C-PECVD also produces a wide variety of CNT structures and chiralities. It is has not yet been possible to grow CNT films consisting of nanotubes of a single chiral type and diameter.

Little is understood about the fundamental factors controlling the CNT growth process [22]. Hydrogen is a key parameter that dramatically affects the final CNT structure; however, its specific role during synthesis has remained speculative. Furthermore, much is still unknown about what happens to the catalyst particle during growth and how this in turn affects the resulting CNT structure as well as the chemical processes and diffusion mechanisms occurring during growth at the catalyst-CNT interface. The lack of fundamental understanding of how and when CNT chirality is determined has prevented structural control and thus the widespread application of this highly unique nanomaterial.

1.5 Thesis Overview

A fundamental understanding of the factors controlling the CNT growth process is key to progress towards precise structural control of CNTs. This thesis presents the results of a detailed systematic study using both *in situ* gas-phase and *ex situ* atomic-scale materials characterization techniques to examine the growth of CNTs from methane-hydrogen gas mixtures through catalytic PECVD.

Chapter two gives a brief review of the fundamentals of gas-phase plasmas, as well as a detailed description of the plasma deposition reactor used in this work for CNT growth and hydrogen-atom exposure experiments. Additionally, the fundamentals of three gas-phase plasma diagnostic tools used are presented, which were used to characterize the types and concentrations of various species formed in the plasma and the flux of hydrogen atoms from the plasma to the substrate.

Chapter three introduces the primary materials characterization tool used in this work, transmission electron microscopy. Specific microscopy techniques are discussed in detail, including selected-area and convergent-beam electron diffraction, bright- and dark-field imaging, scanning-transmission electron microscopy, Z-contrast imaging, X-ray energy dispersive spectrometry, and electron energy-loss spectroscopy. These microscopy tools were used to examine the atomic-scale properties of CNTs and the catalyst nanoparticles from which they grew.

The remaining chapters are presented in scientific journal article form.

Chapter four has been submitted for review as Michael J. Behr, K. Andre Mkhoyan, and Eray S. Aydil, "Catalyst Rotation, Twisting, and Bending During Multiwall Carbon Nanotube Growth," submitted to *Carbon* **2010**. In this work, the internal crystalline structure of cementite catalyst particles located inside the base of multiwall carbon nanotubes was studied using nanoprobe convergent-beam electron diffraction. The catalyst particles are single crystalline but exhibit combinations of small-angle (~1^{o}-3^{o}) rotations, twists, and bends along their axial length between adjacent locations. Distortions are most severe away from the base up into the nanotube where the number of walls is large. Near the attachment point to the substrate, however, where few, if any graphene walls exist, particles remain undistorted. This suggests that the stresses generated by the surrounding nanotube distort the catalyst particle during growth.

Chapter five has been submitted for review as Michael J. Behr, K. Andre Mkhoyan, and Eray S. Aydil, "Orientation and Morphological Evolution of Catalyst Nanoparticles During Carbon Nanotube Growth," submitted to *ACS Nano* **2010**. In this work, we examined the structure, morphology and orientation of catalyst nanoparticles used for seeding and growing multiwall carbon nanotubes (MWCNTs) by plasma enhanced chemical vapor deposition in CH_4/H_2 gas mixtures. Iron catalyst nanocrystals are converted to Fe_3C in CH_4/H_2 plasmas and the MWCNTs grow from Fe_3C nanocrystals. Initially faceted and equiaxed catalyst nanocrystals are distorted and elongated significantly once a tubular CNT structure is formed around the catalyst particles. Eventually, catalysts deform into elongated tear-drop shapes. Once this morphology forms, CNT structures produced are straight and have uniform diameters. Surprisingly, the Fe_3C nanocrystals located inside the base of well-graphitized nanotubes do not exhibit a preferred orientation relative to the nanotube axis. Catalyst nanocrystals in a variety of orientations relative to the nanotube axis still produce well-graphitized nanotubes with similar diameters and structures.

Chapter six has been prepared for submission as Michael J. Behr, K. Andre Mkhoyan, and Eray S. Aydil, "A High-Resolution Electron Energy-Loss Spectroscopy Study of the Catalyst Particle

During Plasma-Enhanced Chemical Vapor Deposition of Carbon Nanotubes." In this chapter, the chemical and carbon diffusion processes occurring at the catalyst-CNT interface were examined with electron energy-loss spectroscopy (EELS) in a scanning transmission electron microscope (STEM). A 0.15 nm electron probe was used to measure, *ex situ*, changes in atomic bonding and carbon concentration through Fe_3C catalyst crystals capped with a layer of iron oxide, located inside the bases of multiwall carbon nanotubes (MWCNTs). The observed variation in carbon concentration through the base of catalyst crystals reveals that carbon from the gas phase decomposes on Fe_3C, near where the CNT walls terminate at the catalyst base. An amorphous carbon-rich layer at the catalyst base provides the source for CNT growth. EELS measurements and Z-contrast STEM imaging provide evidence that carbon diffuses on the Fe3C catalyst surface, along its interface with both the iron oxide shell and CNT walls. Atomic-scale EELS measurements at the catalyst surface in locations of CNT wall formation revealed no change in the iron L_{23} edge compared to the bulk of the catalyst, indicating that Fe_3C did not decompose to BCC iron and graphite during CNT wall formation.

Chapter seven has been submitted for review as Michael J. Behr, E. Ashley Gaulding, K. Andre Mkhoyan, and Eray S. Aydil, "Effect of Hydrogen on Catalyst Nanoparticles in Carbon Nanotube Growth," submitted to *Journal of Applied Physics* **2010**. In this chapter, we use a suite of characterization techniques, including optical emission, infrared, and Raman spectroscopies combined with convergent-beam and selected-area electron diffraction, and high-resolution (Scanning)TEM imaging to systematically investigate the interrelation amongst plasma gas phase composition, catalysts morphology, catalyst structure, and carbon nanotube structure. It is found that the structures of carbon nanotubes grown from catalytic nanoparticles via plasma-enhanced chemical vapor deposition in CH_4/H_2 mixtures show a strong dependence on the H_2-to-CH_4 ratio in the feed gas. Hydrogen plays a critical role in determining the final carbon nanotube structure through its effect on the catalyst crystal structure and morphology. At low H_2-to-CH_4 ratios (~1), iron catalyst nanoparticles are converted to Fe_3C and well-graphitized nanotubes grow from elongated Fe_3C crystals. High (>5) H_2-to-CH_4 ratios in the feed gas result in high hydrogen concentrations in the plasma and strongly reducing conditions, which prevents conversion of Fe to Fe_3C. In the latter case, poorly-graphitized nanofibers grow

from ductile BCC iron nanocrystals that are easily deformed into tapered nanocrystals that yield nanotubes with thick walls.

Chapter eight has been submitted for review as Michael J. Behr, E. Ashley Gaulding, K. Andre Mkhoyan, and Eray S. Aydil, "Hydrogen Etching and Cutting of Multiwall Carbon Nanotubes," submitted to *Journal of Vacuum Science and Technology B* **2010**. In this chapter, the interaction of H atoms with the curved concentric graphene walls of a multiwall carbon nanotube (MWCNT) and the stacked planar graphene sheets of graphite was investigated using a combination of high resolution transmission electron microscopy (HRTEM) in conjunction with electron energy-loss and Raman spectroscopies. Continuous cylindrical graphene walls of a nanotube are etched and amorphized by the H atoms. Etching is not uniform across the length of the CNT, but rather, small etch pits form at defective sites on the CNT walls along the entire nanotube length. Once an etch pit is formed, etching proceeds rapidly, and the remainder of the CNT is quickly etched away. The carbon K core-loss edge spectra collected from etch pits do not differ from spectra collected from pristine CNT walls, indicating that reactions occur exclusively at the exposed graphene edges. Similar observations were made when sheets of planar graphite were exposed to H atoms. Confocal Raman spectroscopic measurements revealed that H etching occurs preferentially at the graphite edges. Eventually, large holes appear in the graphite, as observed under HRTEM. Etched holes in planar graphite are similar to the etch pits that form when a graphene layer is rolled up to form the cylindrical walls of a CNT. Once a hole or etch pit is formed, the edges of the planar graphene sheets or cylindrical CNT walls become exposed, and H etching proceeds quickly from these edges.

Chapter nine has been prepared for submission as Michael J. Behr and Eray S. Aydil, "On the Transformation of Carbon Nanotubes to Diamond." In this chapter, we used nanometer-scale x-ray and energy-loss spectroscopies combined with high-resolution electron imaging and diffraction techniques to examine the possibility of H-induced structural transformations of multiwall carbon nanotubes to form other crystalline carbon phases, such as cubic diamond, lonsdaleite, i-carbon, and n-diamond.

1.6 References

[1] Frondel, C.; Marvin, U. B., Lonsdaleite, a hexagonal polymorph of diamond. *Nature* **1967,** *214* (5088), 587-589.

[2] Hanneman, R. E.; Strong, H. M.; Bundy, F. P., Hexagonal diamonds in meteorites: implications. *Science* **1967,** *155* (3765), 995-997.

[3] Kroto, H. W.; Heath, J. R.; O'Brien, S. C.; Curl, R. F.; Smalley, R. E., C60: Buckminsterfullerene. *Nature* **1985,** *318* (6042), 162-163.

[4] Iijima, S., Helical microtubules of graphitic carbon. *Nature* **1991,** *354* (6348), 56-58.

[5] Yu, M. F.; Lourie, O.; Dyer, M. J.; Moloni, K.; Kelly, T. F.; Ruoff, R. S., Strength and breaking mechanism of multiwalled carbon nanotubes under tensile load. *Science* **2000,** *287* (5453), 637-640.

[6] White, C. T.; Todorov, T. N., Quantum electronics - Nanotubes go ballistic. *Nature* **2001,** *411* (6838), 649-651.

[7] Saito, R., *Physical properties of carbon nanotubes*. London : Imperial College Press: London, 1998.

[8] Wang, X. S.; Li, Q. Q.; Xie, J.; Jin, Z.; Wang, J. Y.; Li, Y.; Jiang, K. L.; Fan, S. S., Fabrication of ultralong and electrically uniform single-walled carbon nanotubes on clean substrates. *Nano Letters* **2009,** *9* (9), 3137-3141.

[9] Geim, A. K.; Novoselov, K. S., The rise of graphene. *Nat Mater* **2007,** *6* (3), 183-191.

[10] What is a Carbon Nanotube? www.seas.upenn.edu/mse/research/nanotubes.html.

[11] Ghosh, S.; Bachilo, S. M.; Weisman, R. B., Advanced sorting of single-walled carbon nanotubes by nonlinear density-gradient ultracentrifugation. *Nat Nano* **2010,** *advance online publication*.

[12] Alfonsi, J. Small Crystal Models for the Electronic Properties of Carbon Nanotubes. University of Padova, Padova, 2008.

[13] *Carbon nanotubes advanced topics in the synthesis, structure, properties, and applications*. Berlin ; New York : Springer: Berlin ; New York, 2008.

[14] Treacy, M. M. J.; Ebbesen, T. W.; Gibson, J. M., Exceptionally high Young's modulus observed for individual carbon nanotubes. *Nature* **1996,** *381* (6584), 678-680.

[15] Krishnan, A.; Dujardin, E.; Ebbesen, T. W.; Yianilos, P. N.; Treacy, M. M. J., Young's modulus of single-walled nanotubes. *Physical Review B* **1998,** *58* (20), 14013-14019.

[16] Endo, M.; Strano, M. S.; Ajayan, P. M., Potential applications of carbon nanotubes. In *Carbon Nanotubes*, Springer-Verlag Berlin: Berlin, 2008; Vol. 111, pp 13-61.

[17] Berber, S.; Kwon, Y. K.; Tomanek, D., Unusually high thermal conductivity of carbon nanotubes. *Physical Review Letters* **2000,** *84* (20), 4613-4616.

[18] Novoselov, K. S.; Geim, A. K.; Morozov, S. V.; Jiang, D.; Katsnelson, M. I.; Grigorieva, I. V.; Dubonos, S. V.; Firsov, A. A., Two-dimensional gas of massless Dirac fermions in graphene. *Nature* **2005,** *438* (7065), 197-200.

[19] Charlier, J. C.; Blase, X.; Roche, S., Electronic and transport properties of nanotubes. *Reviews of Modern Physics* **2007,** *79* (2), 677-732.

[20] Charlier, J. C.; Eklund, P. C.; Zhu, J.; Ferrari, A. C., Electron and phonon properties of graphene: Their relationship with carbon nanotubes. In *Carbon Nanotubes*, Springer-Verlag Berlin: Berlin, 2008; Vol. 111, pp 673-709.

[21] White, C. T.; Mintmire, J. W., Density of states reflects diameter in nanotubes. *Nature* **1998,** *394* (6688), 29-30.

[22] Meyyappan, M., A review of plasma enhanced chemical vapour deposition of carbon nanotubes. *Journal of Physics D-Applied Physics* **2009,** *42*, 213001.

[23] Kordas, K.; Toth, G.; Moilanen, P.; Kumpumaki, M.; Vahakangas, J.; Uusimaki, A.; Vajtai, R.; Ajayan, P. M., Chip cooling with integrated carbon nanotube microfin architectures. *Applied Physics Letters* **2007,** *90*, 123105.

[24] Coleman, J. N.; Khan, U.; Blau, W. J.; Gun'ko, Y. K., Small but strong: A review of the mechanical properties of carbon nanotube-polymer composites. *Carbon* **2006,** *44* (9), 1624-1652.

[25] Biercuk, M. J.; Llaguno, M. C.; Radosavljevic, M.; Hyun, J. K.; Johnson, A. T.; Fischer, J. E., Carbon nanotube composites for thermal management. *Applied Physics Letters* **2002,** *80* (15), 2767-2769.

[26] Gibson, R. F.; Ayorinde, E. O.; Wen, Y. F., Vibrations of carbon nanotubes and their composites: A review. *Composites Science and Technology* **2007,** *67* (1), 1-28.

[27] Koratkar, N. A.; Suhr, J.; Joshi, A.; Kane, R. S.; Schadler, L. S.; Ajayan, P. M.; Bartolucci, S., Characterizing energy dissipation in single-walled carbon nanotube polycarbonate composites. *Applied Physics Letters* **2005,** *87*, 063102.

[28] Moniruzzaman, M.; Winey, K. I., Polymer nanocomposites containing carbon nanotubes. *Macromolecules* **2006,** *39* (16), 5194-5205.

[29] Ajayan, P. M.; Schadler, L. S.; Giannaris, C.; Rubio, A., Single-walled carbon nanotube-polymer composites: Strength and weakness. *Advanced Materials* **2000,** *12* (10), 750-753.

[30] Tans, S. J.; Verschueren, A. R. M.; Dekker, C., Room-temperature transistor based on a single carbon nanotube. *Nature* **1998,** *393* (6680), 49-52.

[31] Martel, R.; Schmidt, T.; Shea, H. R.; Hertel, T.; Avouris, P., Single- and multi-wall carbon nanotube field-effect transistors. *Applied Physics Letters* **1998,** *73* (17), 2447-2449.

[32] Collins, P. C.; Arnold, M. S.; Avouris, P., Engineering carbon nanotubes and nanotube circuits using electrical breakdown. *Science* **2001,** *292* (5517), 706-709.

[33] Bachtold, A.; Hadley, P.; Nakanishi, T.; Dekker, C., Logic circuits with carbon nanotube transistors. *Science* **2001,** *294* (5545), 1317-1320.

[34] Javey, A.; Guo, J.; Wang, Q.; Lundstrom, M.; Dai, H. J., Ballistic carbon nanotube field-effect transistors. *Nature* **2003,** *424* (6949), 654-657.

[35] Kong, J.; Franklin, N. R.; Zhou, C. W.; Chapline, M. G.; Peng, S.; Cho, K. J.; Dai, H. J., Nanotube molecular wires as chemical sensors. *Science* **2000,** *287* (5453), 622-625.

[36] Besteman, K.; Lee, J. O.; Wiertz, F. G. M.; Heering, H. A.; Dekker, C., Enzyme-coated carbon nanotubes as single-molecule biosensors. *Nano Letters* **2003,** *3* (6), 727-730.

[37] Cao, Q.; Hur, S. H.; Zhu, Z. T.; Sun, Y. G.; Wang, C. J.; Meitl, M. A.; Shim, M.; Rogers, J. A., Highly bendable, transparent thin-film transistors that use carbon-nanotube-based conductors and semiconductors with elastomeric dielectrics. *Advanced Materials* **2006,** *18* (3), 304-309.

[38] Cao, Q.; Zhu, Z. T.; Lemaitre, M. G.; Xia, M. G.; Shim, M.; Rogers, J. A., Transparent flexible organic thin-film transistors that use printed single-walled carbon nanotube electrodes. *Applied Physics Letters* **2006,** *88* (11), 3.

[39] Wu, Z. C.; Chen, Z. H.; Du, X.; Logan, J. M.; Sippel, J.; Nikolou, M.; Kamaras, K.; Reynolds, J. R.; Tanner, D. B.; Hebard, A. F.; Rinzler, A. G., Transparent, conductive carbon nanotube films. *Science* **2004,** *305* (5688), 1273-1276.

[40] Guldi, D. M.; Rahman, G. M. A.; Prato, M.; Jux, N.; Qin, S. H.; Ford, W., Single-wall carbon nanotubes as integrative building blocks for solar-energy conversion. *Angewandte Chemie-International Edition* **2005,** *44* (13), 2015-2018.

[41] Landi, B. J.; Raffaelle, R. P.; Castro, S. L.; Bailey, S. G., Single-wall carbon nanotube-polymer solar cells. *Progress in Photovoltaics* **2005,** *13* (2), 165-172.

[42] Ichida, M.; Mizuno, S.; Tani, K.; Saito, Y.; Nakamura, A., Exciton effects of optical transitions in single-wall carbon nanotubes. *Journal of the Physical Society of Japan* **1999,** *68* (10), 3131-3133.

[43] Spataru, C. D.; Ismail-Beigi, S.; Benedict, L. X.; Louie, S. G., Quasiparticle energies, excitonic effects and optical absorption spectra of small-diameter single-walled carbon nanotubes. *Applied Physics a-Materials Science & Processing* **2004,** *78* (8), 1129-1136.

[44] Journet, C.; Maser, W. K.; Bernier, P.; Loiseau, A.; delaChapelle, M. L.; Lefrant, S.; Deniard, P.; Lee, R.; Fischer, J. E., Large-scale production of single-walled carbon nanotubes by the electric-arc technique. *Nature* **1997,** *388* (6644), 756-758.

[45] Thess, A.; Lee, R.; Nikolaev, P.; Dai, H. J.; Petit, P.; Robert, J.; Xu, C. H.; Lee, Y. H.; Kim, S. G.; Rinzler, A. G.; Colbert, D. T.; Scuseria, G. E.; Tomanek, D.; Fischer, J. E.; Smalley, R. E., Crystalline ropes of metallic carbon nanotubes. *Science* **1996,** *273* (5274), 483-487.

[46] Joseyacaman, M.; Mikiyoshida, M.; Rendon, L.; Santiesteban, J. G., Catalytic Growth of Carbon Microtubules with Fullerene Structure. *Applied Physics Letters* **1993,** *62* (2), 202-204.

[47] Ren, Z. F.; Huang, Z. P.; Xu, J. W.; Wang, J. H.; Bush, P.; Siegal, M. P.; Provencio, P. N., Synthesis of large arrays of well-aligned carbon nanotubes on glass. *Science* **1998,** *282* (5391), 1105-1107.

[48] Melechko, A. V.; Merkulov, V. I.; McKnight, T. E.; Guillorn, M. A.; Klein, K. L.; Lowndes, D. H.; Simpson, M. L., Vertically aligned carbon nanofibers and related structures: Controlled synthesis and directed assembly. *Journal of Applied Physics* **2005,** *97*, 041301.

[49] Bower, C.; Zhu, W.; Jin, S. H.; Zhou, O., Plasma-induced alignment of carbon nanotubes. *Applied Physics Letters* **2000,** *77* (6), 830-832.

[50] Meyyappan, M.; Delzeit, L.; Cassell, A.; Hash, D., Carbon nanotube growth by PECVD: a review. *Plasma Sources Science & Technology* **2003,** *12* (2), 205-216.

2 Carbon Nanotube Growth Using Plasmas and Plasma-Surface Diagnostic Tools

2.1 Introduction

Growth of multiwall carbon nanotube films and investigations of the effect of hydrogen atoms on the carbon nanotube structure were conducted using gas-phase plasmas. In this chapter, I review the fundamentals of plasmas and describe in detail the plasma deposition reactor that I built at the start of my graduate research. Finally, three in situ plasma characterization techniques, including optical emission spectroscopy, infrared spectroscopy, and spectroscopic ellipsometry are presented which were used to (i) monitor the dissociation of precursor gases and the relative concentrations of reactive species in the plasma, (ii) measure the flux of hydrogen atoms to the substrate, and (iii) calibrate the temperature of the substrate.

2.2 Plasmas

Plasmas are used to create reactive gas-phase species that facilitate growth of nanostructured materials and etching at low temperatures. The work in this dissertation made use of low pressure chemically reactive hydrogen and hydrocarbon plasmas to grow films of multiwall carbon nanotubes (MWCNTs) and to expose these materials to atomic hydrogen. Accordingly, in this section I review plasma characteristics, formation of reactive species, and plasma-surface interactions as they relate to the PECVD process.

A plasma is a partially ionized gas consisting of electrons, ions, and neutral species such as reactive radicals, molecular fragments, and stable molecules. It is formed by applying sufficient energy (via UV light, energetic particles, heat, or strong electric fields, for example) to a volume of gas to cause ionization [1]. Typically in PECVD or etching processes this applied energy source is a radio frequency (RF) or microwave electric field. The plasma source used in this work is an RF source operated at 13.56 MHz. Many types of plasmas exist, differing

mainly in their electron concentration, n_e, and average electron energy or temperature, T_e. For example, high-pressure arc plasmas are characterized by $n_e \sim 10^{16}$ cm^{-3} and $kT_e \sim 0.5$ eV, while the plasma filling interplanetary space is characterized by $n_e \sim 10$ cm^{-3} and $kT_e \sim 25$ eV [2].

In the deposition of nanostructured materials such as CNTs, the plasma performs two basic functions. First, through gas-phase electron-impact collisions, reactive species are generated at much lower temperatures than required via thermally-activated processes. In the case of the CH_4/H_2 precursor gas mixtures used in this work, plasma activation resulted in the formation of a variety of gas-phase species, such as CH_3, CH_2, CH, C_2, and C_2H_2, and atomic H. Second, the plasma bombards surfaces immersed within its confines with energetic radiation and species (e.g., ions, radicals, metastables, electrons, and photons) that affect surface and subsurface chemistry [2].

Low-pressure plasmas used in deposition of nanostructured materials are glow discharges excited by radio frequency or microwave sources. They are characterized by electron concentrations in the range 10^8-10^{13} cm^{-3} and average electron temperatures of 10^4-10^5 K (these temperatures correspond to average electron energies of 1-10 eV) [2]. These plasmas are considered non-equilibrium because the average electron temperature is greater than their average ion temperature (T_i). The ion temperature is close to the gas temperature (T_g) that characterizes the neutral molecules in the gas. Typically T_e is greater than ten times T_i, with $T_i \sim T_g \sim$ 300-600 K. On average, the bulk of the plasma is neutral, with the number of positive charge carriers equal to the number of negative charge carriers, both of which are much lower than the number of neutral (unionized) species present. In fact, the ratio of free electron density to neutral species density is of the order 10^{-6}-10^{-4} [2]. This means that atoms, radicals, and molecules are present in significantly higher concentrations than ions and electrons.

At the heart of plasmas are electrons, which are responsible for ionizing and dissociating gas molecules [2]. One common pathway through which reactive species are generated in the plasma is referred to as electron-impact. Free electrons that participate in electron-impact reactions are generated constantly as the applied RF field accelerates electrons to energies exceeding the ionization energies of gas molecules [1].

Electrons that undergo inelastic collisions are of main interest as they result in the generation of reactive radicals, metastable species, and ions. Depending upon the initial electron energy, an impact collision can result in a number of different reactions. Three basic electron-impact reactions are discussed below in order of increasing electron energy. An impacting electron can transfer energy to a gas-phase species that results in an excitation (rotational, vibrational, or electronic) given by the reaction

$$e^- + H_2 \rightarrow H_2^* + e^- .$$

Relaxation from this excited state is in most cases accompanied by emission of a UV or visible photon. This process creates a distinct glow in the plasma that is characteristic of specific gas-phase species present, and is utilized in optical emission spectroscopy to determine new species that form in the plasma. Slightly higher impact energies can result in dissociation reactions, producing reactive free radicals and ions [1]

$$e^- + H_2 \rightarrow 2H + e^- \text{ (dissociation)}$$
$$e^- + CH_4 \rightarrow CH_3^- + H^+ + e^- \text{ (dissociative attachment)}$$
$$e^- + H_2 \rightarrow H^- + H$$
$$e^- + H_2 \rightarrow H^+ + H + 2e^- \text{ (dissociative ionization)}$$

Finally, electrons with sufficient energy can eject an electron upon impact, ionizing the neutral species. Ionization reactions sustain the plasma by producing positive ions and new free electrons:

$$e^- + CH_4 \rightarrow CH_4^+ + 2e^- .$$

To maintain steady-state electron and ion concentrations, an external energy source is needed to drive these ionization reactions so that the rate of ionization equals the rate of recombination [3].

During the first moments of plasma formation, electrons are accelerated out of the bulk plasma region at a much higher rate than ions due to their higher mobility, and impinge on chamber walls, electrodes, and any other surface present [2]. As a result of this initial high flux of electrons arriving at the surface, a space charge layer forms in the gas phase near all surfaces exposed to the plasma. This layer produces an electric field which repels electrons away from the surface and accelerates positive ions toward the surface. This space charge region is called the sheath, and appears dark due to a lack of electron impact excitations within it. As a result of this layer, the plasma is left at a higher potential relative to all surfaces it touches; this in turn creates a barrier for further electron escape and thus acts to confine the plasma [1].

When a solid surface is exposed to a glow discharge plasma, ions, electrons, and radicals impinging on the surface can cause a variety of heterogeneous processes to occur. For example, ions accelerated by the sheath electric field can cause secondary electron emission, sputter atoms from the surface, or participate in ion-induced chemical reactions. Radicals can participate in material etching, or react on the substrate surface to deposit a thin film or other nanostructure, such as a CNT. The relative fluxes of the different species reaching the substrate can be changed by varying the applied plasma power, gas pressure, or the gas composition.

Material properties of the deposited carbon nanotube films are highly dependent on the relative fluxes of different species reaching the substrate. For example, the relative flux of hydrogen atoms to carbon-containing species is found to have a dramatic effect on carbon nanotube structure as well as on the iron catalyst from which the nanotubes grow. In fact, there is an optimum ratio of H-to-C flux to the substrate that produces the straightest, highest quality CNTs; these experimental findings are presented in detail in chapter seven.

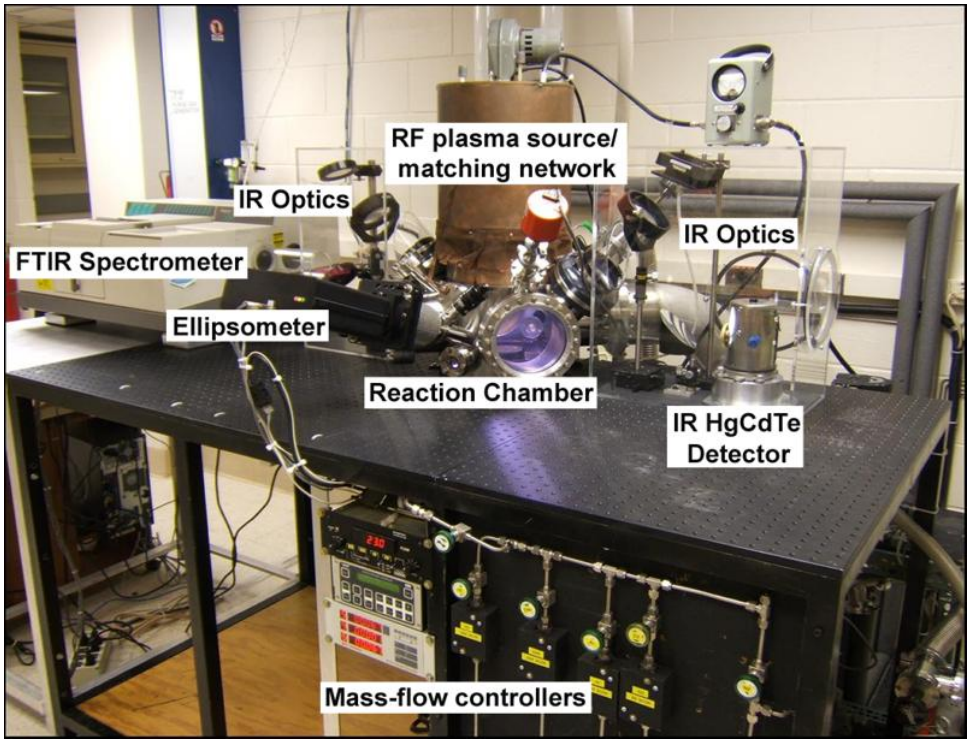

Figure 2-1. The inductively-coupled plasma reactor equipped with an in situ infrared spectrometer and spectroscopic ellipsometer.

2.3 Plasma Reactor

Carbon nanotube growth and hydrogen plasma exposure experiments were carried out in the inductively coupled plasma (ICP) deposition reactor shown in Figure 2-1. A turbo-molecular pump with a pumping speed of 1000 liters/second evacuates the stainless steel reaction chamber to a base pressure of 4×10^{-6} Torr. A mechanical pump backs the turbo pump, and is also used to pump the chamber down from atmospheric pressure. Samples are placed on a heated substrate platen with a K-type thermocouple at the bottom of the reactor that enables control of the substrate temperature from 25-850 °C. Gases are introduced into the bottom of the reaction chamber through a gas injection ring that surrounds the substrate platen. Flow rates of gases (Ar, CH_4, H_2, and O_2) are metered by mass-flow controllers, and are variable up to 200 standard cubic centimeters per minute (sccm). Chamber pressure, measured by a capacitance manometer, can be regulated and sustained independent of the gas flow over a range of 0.001-

10 Torr by use of a gate valve immediately in front of the turbo pump. The inductively coupled plasma source consists of a 6-inch planar spiral coil that rests on top of a quartz window 25 cm above the substrate platen. Radio frequency (rf) electromagnetic radiation at 13.56 MHz up to 500 watts, applied through a matching network to the center and edge of the planar coil, is coupled to feedstock gases in the chamber creating reactive ions, radicals, and free electrons that sustain the plasma directly below the quartz window. Most of the electromagnetic radiation is absorbed by the plasma within a few centimeters from the quartz window surface, so the bulk of the plasma is confined to the top of the reaction chamber, resulting in minimal ion bombardment of the sample located at the bottom of the chamber. To further prevent ion bombardment during H-atom exposure experiments, a grounded stainless-steel mesh can be inserted immediately above the substrate to prevent electric fields from forming a plasma immediately above the substrate. As a result, the sample is not irradiated with ions or electrons during plasma exposure. The specific plasma conditions, i.e. gas flows, pressure, temperature, reaction time, etc., used for carbon nanotube growth and H-atom exposure experiments are provided in the appropriate chapters.

2.4 Plasma Diagnostics

The plasma reactor described in section 2.3 is equipped with a number of *in situ* plasma diagnostics that provided real-time monitoring of the plasma characteristics during CNT growth and H-exposure experiments. Specifically, optical emission (OE) and infrared (IR) spectroscopy were used to provide information about the magnitude of precursor gas dissociation in the plasma, gas temperature, identity of new reactive species formed in the plasma, how the relative concentrations of these species changed with changes to the plasma conditions, and the H-atom flux to the substrate. Measurement of the plasma characteristics was necessary to understand the changes in carbon nanotube structure, for example, as observed using *ex situ* characterization techniques. This section will discuss the fundamentals of both OES and IR spectroscopy.

2.4.a Optical Emission Spectroscopy using Actinometry

The characteristic glow, or optical emission, from a plasma contains information about the types of gas-phase species present and how they are formed. By measuring the emission, the types of reactive species that are formed from dissociation of precursor gases in the plasma can be determined. When combined with actinometry, an estimate of the ground-state concentrations of optically-active gas-phase species can be determined. The work in this dissertation used optical emission spectroscopy (OES) with actinometry to (i) identify new species formed in $CH_4/H_2/Ar$ plasmas, and (ii) to measure changes in concentration of these species when the amount of precursor hydrogen gas was varied during carbon nanotube growth.

Optical emission spectroscopy (OES) measures optical emission intensity from electronically-excited species in the plasma. In my system, emission averaged over the entire plasma volume was coupled via a fiber-optic cable to an Acton Research Corporation SpectraPro-275 0.275 Meter Triple Grating Monochromoter/Spectrograph equipped with a photomultiplier tube. Using a grating with 1200 grooves/mm combined with a 50 μm entrance slit width yielded 0.15 nm spectral resolution. A representative emission spectrum obtained from a $CH_4/H_2/Ar$ plasma is shown in Figure 2-2. Peaks in the spectrum correspond to emission from specific optically-active electronically-excited species in the plasma, including H, CH, C_2, and Ar. The intensity of a peak depends on the emitting excited species' density and the electron energy distribution function, both of which are influenced by changes in plasma parameters. Actinometry is an attempt to isolate the changes in emission due to changes in concentration from emission changes due to other factors. Thus, actinometry is used to extract the reactive species' ground-state concentration from measurements of excited species' emission as a function of plasma parameters, independent of the electron energy distribution function [4]. Typically, this is accomplished by introducing a small amount of Ar (the "actinometer") to the plasma and then monitoring the emission from both Ar and the species of interest simultaneously. Actinometry is valid if the following conditions are realistic, where Ar is the actinometer and H is the species of interest: (i) The addition of Ar does not affect the emissions of other emitting species; (ii) the excited species, Ar^* and H^*, are predominantly produced through direct electron-impact excitation of corresponding ground state atoms or molecules; (iii) the excitation cross sections

of Ar and H have similar threshold energies and similar shapes as a function of energy; and (iv) the loss of Ar^* and H^* must be dominated by radiative processes. Within these assumptions actinometry is a valid method to obtain the relative ground-state atomic hydrogen concentration [5]. Specifically, if these conditions are met, the measured intensity ratio H*/Ar* is proportional to the concentration ratio [H]/[Ar]. As an example, the excitations and relaxations occurring in an H_2/Ar plasma with corresponding emission intensity dependencies are as follows,

$$H + e^- \xrightarrow{k_1} H^* + e^-$$
$$Ar + e^- \xrightarrow{k_1'} Ar^* + e^-$$
$$H^* \xrightarrow{k_2} H + h\upsilon \qquad I_H = k_2[H^*]$$
$$Ar^* \xrightarrow{k_2'} Ar + h\upsilon' \qquad I_{Ar} = k_2[Ar^*]$$

where the rate constants (k_i and k'_i, i = 1, 2) depend exponentially on the threshold energy and electron energy distribution function. Under steady state conditions, the H^* and Ar^* atom concentrations are constant as a function of time, and the measured intensities can be expressed through the corresponding electronic ground-state species,

$$I_H = k_1 n_e [H]$$
$$I_{Ar} = k_1' n_e [Ar].$$

If the above conditions are met, then the relative H atom concentration can be determined from measured emission intensities,

$$\frac{[H]}{[Ar]} = k \frac{I_H}{I_{Ar}},$$

where k is a constant roughly independent of plasma parameters [4]. For the work in this dissertation, H_2/CH_4/Ar plasmas used for carbon nanotube growth were monitored with OES. Actinometry was used successfully to calculate changes in relative ground-state concentration of the species H, CH, and C_2 from optical emission intensities occurring at 656 nm, 431 nm, and 516 nm, respectively, all normalized relative to the Ar* line at 750.4 nm [6].

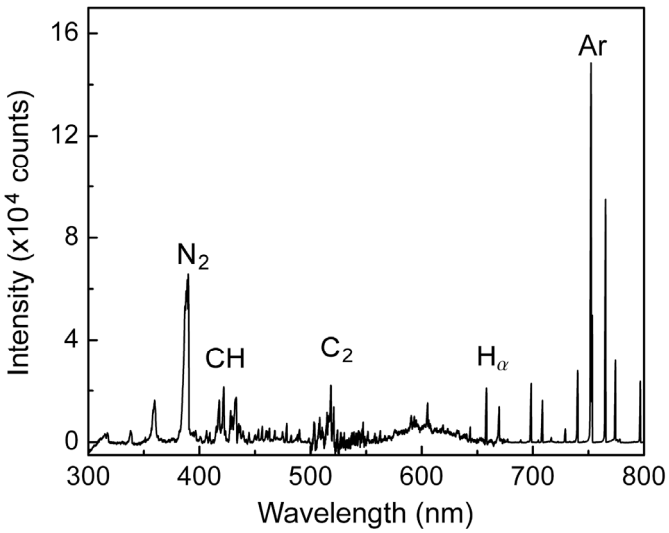

Figure 2-2. Optical emission spectrum obtained from an $H_2/CH_4/Ar$ plasma used for carbon nanotube growth. Emission lines used in this work are labeled with the appropriate gas-phase species.

2.4.b Fourier Transform Infrared Spectroscopy

Additional quantitative information about the $H_2/CH_4/Ar$ plasmas used in this work and their interaction with the substrate was obtained using Fourier transform infrared (FTIR) spectroscopy. Specifically, FTIR spectroscopy was used to measure in the plasma the fraction of dissociation of CH_4, the gas temperature, and was used to detect other species formed which were inaccessible to OES, such as C_2H_2. The flux of H atoms created in the plasma to the sample surface was also measured by using FTIR in attenuated total-reflection mode. In this section, the fundamentals of IR spectroscopy as they pertain to these specific applications are presented.

Infrared spectroscopy gives information on chemical structure through infrared absorption processes. IR absorption results when the electric field of an incident infrared radiation beam interacts with the oscillating dipole moment of a molecule, causing a quantum-mechanical transition between its vibrational or rotational energy levels. Depending on the energy, vibrations can be in the form of a stretch, bend, or wag and are easily understood in the harmonic-oscillator approximation, wherein different vibrations are called *normal modes* [7].

Energy level spacing between these vibrational levels falls within the infrared region (~0.1-1eV) of the electromagnetic spectrum. The identity or molecular structure can be determined by recording an IR spectrum. An IR spectrum is obtained when a sample absorbs radiation in the IR region; it is displayed as a plot of absorbance vs. wavenumber ($\tilde{\nu} = 1/\lambda$ cm^{-1}, range is typically 400-4000 cm^{-1}). Features in this spectrum are called absorption bands, or peaks; their positions and relative strengths give clues to the chemical structure [8] The magnitude of absorption is described by the absorbance, A, and is related logarithmically to the fraction, I, of incident light, I_o, that passes through the gas in the chamber by $A = -\log(I / I_0)$. The absorbance, A is also related to the concentration of absorbing species, N (cm^{-3}), their absorption cross-section, σ (cm^2), and the path length, l (cm), that the light travels through the absorbing medium by $A = \sigma\, n\, l$.

The FTIR apparatus used in this work is shown in image of Figure 2-1. The main parts of this apparatus include a Nicolet Magna-IR 550 FTIR spectrometer, a set of mirrors and lenses to direct the IR beam from the spectrometer into the plasma reaction chamber through KBr windows, and an external cooled HgCdTe detector. The beam path outside the chamber is purged to protect the KBr lenses and windows, and to minimize absorptions due to H_2O and CO_2. Absorption spectra were collected in two different geometries. For gas-phase measurements of the plasma, reflection geometry was used, whereby the incident IR beam was reflected a single time from a silicon substrate placed on the substrate platen. The path length of the IR beam through the gas atmosphere in the reaction chamber in this geometry was 54.5 cm. To measure the H-atom flux to the substrate, however, attenuated total-reflection (ATR) mode was used. In ATR mode, infrared radiation from a FTIR spectrometer is focused at normal incidence onto one of the beveled faces of a trapezoidal shaped ATR crystal/substrate (crystalline Si, Ge, or GaAs, for example) located on the substrate platen and undergoes multiple total internal reflections at both the top and bottom polished surfaces, typically ~35 total reflections. At each total reflection interface (ATR crystal/vacuum interface), an *evanescent* electromagnetic wave exists that extends into the lower refractive index material (vacuum in this case) a distance characterized by its penetration depth (d_p) [9]. Any thin film present on the ATR crystal will interact with this transmitted evanescent wave, absorbing and

thereby attenuating the transmitted infrared radiation at frequencies characteristic of the thin film. Because of the large number of total reflections from the top surface, typically ~15-20 but dependent on geometry, ATR-FTIR is two orders of magnitude more sensitive than transmission infrared spectroscopy, and is thus capable of detecting thin films on the substrate as thin as a monolayer [10].

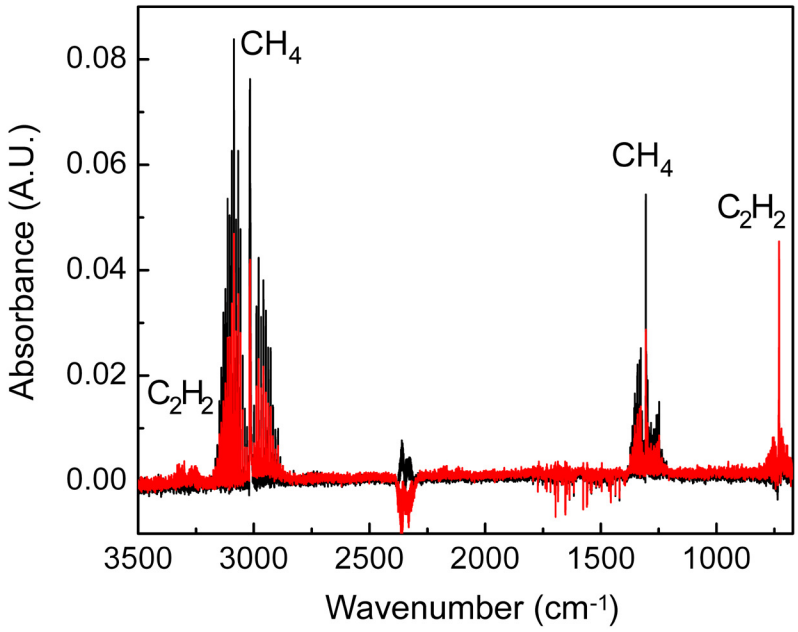

Figure 2-3. Full FTIR spectrum obtained from a $H_2/CH_4/Ar$ gas mixture with no plasma (black curve) and with plasma activation (red curve). Rotation-vibration absorption bands of CH_4 and C_2H_2 are indicated.

Figure 2-3 shows an FTIR spectrum obtained in reflection mode from a $H_2/CH_4/Ar$ plasma used for carbon nanotube growth. Absorption bands corresponding to CH_4 (3017 cm^{-1} and 1306 cm^{-1}) and C_2H_2 (3300 cm^{-1} and 730 cm^{-1}) are observed; each band is composed of a series of peaks that arise due to excitation of rotational levels of each molecule. In fact these absorption bands are referred to as rotation-vibration bands because the vibrational transition is accompanied by rotational transitions. The change, upon plasma excitation, in magnitude as well as the change in rotational-level population of the methane rotation-vibration absorption band was used to calculate the change in CH_4 density and gas rotational temperature, respectively, as described in

chapter seven. Additionally, FTIR was used to measure the flux of H atoms to the substrate. This method is based on IR measurements made in ATR mode of the change in free-electron absorption in a polycrystalline ZnO film when this film is exposed to H atoms. Details of this method are discussed in chapter eight.

2.5 Spectroscopic Ellipsometry

Growth of carbon nanotube films requires precise control of the substrate temperature. In addition, a method for measuring the rise in temperature due to plasma heating effects was important in investigations of H-atom etching of these films. Spectroscopic ellipsometry (SE) was used *in situ* to calibrate the substrate temperature during carbon nanotube film growth, and to measure the rise in temperature due to plasma heating. In this section, the fundamentals of spectroscopic ellipsometry are presented.

Ellipsometry is a sensitive diagnostic technique that uses polarized light to characterize thin films and surfaces. Through model-based analysis, physical properties of interest are extracted from measured ellipsometric parameters. In this technique, the substrate is illuminated with light of a known polarization and the resulting change in polarization upon reflection is measured. The amount of change to the polarization state provides information about the optical properties of films or adsorbates on the substrate [11]. Specifically, ellipsometry measures the complex reflectance ratio,

$$\tilde{\rho} = \frac{\tilde{r}_p}{\tilde{r}_s} = \tan\Psi e^{i\Delta},$$

which is expressed in terms of the ellipsometric angles Ψ and Δ, where $\tilde{r}_p$ and $\tilde{r}_s$ are the total reflection coefficients for radiation polarized parallel to and perpendicular to the plane of incidence, respectively. Total reflection coefficients are defined as the ratio of the amplitude of the reflected wave to the amplitude of the incident wave; information about the sample is contained in these coefficients. The ellipsometric angle, Ψ is the amplitude ratio of the total reflection coefficients, and Δ is their relative phase difference, or phase shift. In spectroscopic

ellipsometry, the ellipsometric angles (Ψ and Δ) are measured experimentally as a function of wavelength; they depend on the optical properties of the substrate and any films or adsorbed species present [11]. By fitting the measured data to an appropriate model, these optical properties can be extracted, which in turn are related to the structure of the overlayers. For example, ellipsometry was used in this work to measure the position of the direct band edge of silicon as a function of temperature to calibrate the substrate temperature. A model that consisted of a thin film of native SiO_2 on a silicon substrate was needed to model the variation of the ellipsometric angles Ψ and Δ with wavelength.

The *in situ* characterization techniques described in this chapter were used to probe the reactions occurring in the plasma and at the substrate in real time. Thus, when changes were made to the process parameters, such as changes to gas flows, pressure, power, or temperature, the direct result of these changes could be observed, and correlated with *ex situ* characterization techniques. In the next chapter, the *ex situ* materials characterization techniques used to examine the carbon nanotube and graphite films are introduced.

2.6 References

[1] Smith, D. L., *Thin-film deposition : principles and practice*. New York : McGraw-Hill: New York, 1995.

[2] *Introduction to microlithography*. Washington, DC : American Chemical Society: Washington, DC, 1994.

[3] Chapman, B. N., *Glow discharge processes : sputtering and plasma etching*. New York : Wiley: New York, 1980.

[4] Coburn, J. W.; Chen, M., Optical-Emission Spectroscopy of Reactive Plasmas - A Method for Correlating Emission Intensities to Reactive Particle Density. *Journal of Applied Physics* **1980,** *51* (6), 3134-3136.

[5] Dreyfus, R. W.; Jasinski, J. M.; Walkup, R. E.; Selwyn, G. S., Optical Diagnostics of Low-Pressure Plasmas. *Pure and Applied Chemistry* **1985,** *57* (9), 1265-1276.

[6] Payling, R., *Optical emission lines of the elements*. Chichester ; New York : Wiley: Chichester ; New York, 2000.

[7] McQuarrie, D. A.; Simon, J. D., *Physical Chemistry: A Molecular Approach*. University Science Books: Sausalito, 1997.

[8] Lambert, J. B.; Shurvell, H. F., *Introduction to Vibrational Spectroscopy: Introduction to Organic Spectroscopy*. Prentice Hall: New Jersey, 1987.

[9] Harrick, N. J., *Internal reflection spectroscopy*. New York, Interscience Publishers: New York, 1967.

[10] Aydil, E. S.; Gottscho, R. A., Probing plasma/surface interactions. *Solid State Technology* **1997,** *40* (10), 181-190.

[11] Tompkins, H. G., *Spectroscopic ellipsometry and reflectometry : a user's guide*. New York : Wiley: New York, 1999.

3 Materials Characterization Techniques

3.1 Introduction

A suite of materials characterization techniques and methods were used to examine the structure, morphology, chemical composition, and atomic bonding of carbon nanotubes and the catalyst crystals from which they grew. In this chapter, each characterization tool as well as the specific techniques and methods that were used throughout this work are described. The primary characterization tool used in this work, transmission electron microscopy, is introduced first. Specific microscopy techniques are then presented, including selected-area and convergent-beam electron diffraction, bright- and dark-field imaging, scanning-transmission electron microscopy, Z-contrast imaging, X-ray energy dispersive spectrometry, and electron energy-loss spectroscopy.

3.2 The Transmission Electron Microscope

Examination of nanostructured materials, such as carbon nanotubes (CNTs) as studied in this work, requires characterization tools that are able to probe the physical, chemical, and electronic properties of a material at the atomic-scale. The transmission electron microscope (TEM) was an essential tool in this work because of its unique capability to measure all of these properties with atomic spatial resolution. A wide variety of microscopy techniques and spectroscopic measurements were conducted within the TEM to give a complete atomic-scale structural and chemical picture of the materials investigated.

Electrons are at the heart of a TEM. The invention of the TEM by Knoll and Ruska [1] in the early 1930s came shortly after Louis de Broglie first theorized that the electron had wave-like properties, and that the electron wavelength was much shorter than the wavelength of visible light [2]. The initial development of the TEM sought to overcome the resolution limits imposed by the relatively long wavelength of visible light (400-700 nm) that optical microscopes used. By using electrons instead of light, the ultimate resolution could be drastically improved. The

wavelength of an electron (λ) is given by the de Broglie equation, corrected for relativistic effects:

$$\lambda = \frac{h}{p} = \frac{h}{\sqrt{2m_0 eV\left(1+\frac{eV}{2m_0c^2}\right)}}$$

where h is Planck's constant, p is the momentum of the electron, m_0 is the rest-mass of the electron, e is the electron charge, V is the accelerating voltage of the microscope, and c is the speed of light in vacuum. In the FEI-Tenai F30 TEM used in this work, a 300 keV accelerating voltage imparts significant energy to the electrons, which produces a wavelength of 0.00197 nm. Thus, a theoretical point resolution of ~0.001 nm is achievable, as estimated using the Rayleigh criterion for light microscopy [3]. As will be discussed in the following sections, the improved resolution is only one of many reasons for using electrons to probe nanostructured materials.

3.2.a. Fast Electron Interactions with Matter

Interaction of fast electrons with matter produces a wealth of information. Electrons that are transmitted or scattered through the sample are used to form images and diffraction patterns, while the amount of energy lost during this interaction contains information about the types of atoms present in the sample and how they are bonded. Additionally, a number of secondary signals are generated when an incident electron interacts with the sample, such as x-rays and auger electrons which contain information about the chemical identity of the atomic species present. The strength of interaction of an electron with matter is very strong due to the electron's inherent negative charge. Thus, an electron interacts, via the Coulomb interaction, with both the negative electron cloud and positive nucleus of an atom [4]. The Coulomb interaction is very strong, in fact, this interaction is ~1000 times stronger than the interaction of other types of incident radiation with matter, such as X-rays [5], thus providing a clear advantage to using electrons to examine materials that are small in size or are scarce.

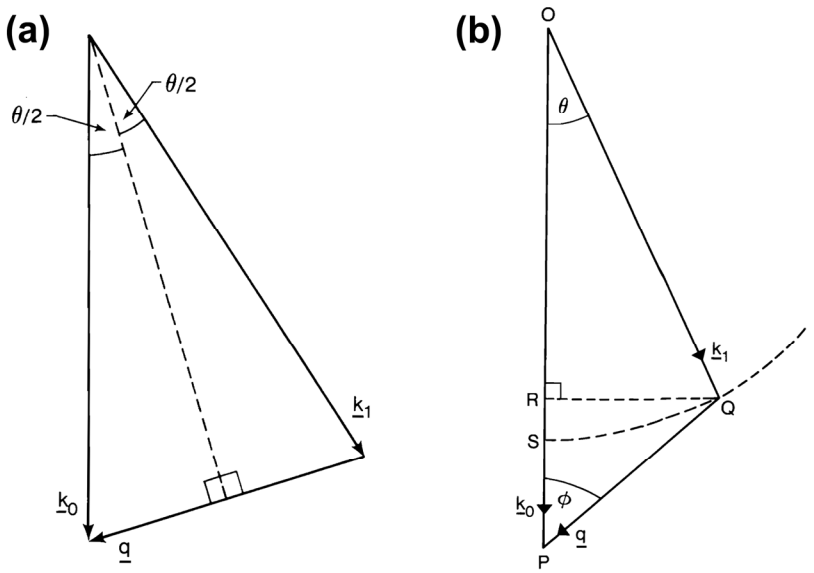

Figure 3-1. (a) Vector diagrams for elastic scattering: $\boldsymbol{k}_0$ and $\boldsymbol{k}_1$ are the wavevectors of the fast electron before and after scattering, respectively. The scattering vector, $\boldsymbol{q}$, points in the direction of momentum transfer to the specimen; its magnitude is given by $q = 2k_0 \sin(\theta/2)$. (b) Vector diagram for inelastic scattering. For a given value of $\boldsymbol{k}_1$, or energy loss, there are a locus of possible values of $\boldsymbol{q}$ and θ, which are mapped by the dashed circle. Images from [4].

An incident electron that enters a material experiences a collection of electrostatic forces from the constituent atoms. As a result of these forces, an electron may undergo a scattering process, whereby it changes direction, loses energy, or both. There are two types of electron scattering that may occur; each type is utilized differently in the TEM to obtain specific information about the specimen under investigation. Elastic scattering occurs when an incident electron interacts with the screened electrostatic field of an atomic nucleus, or with the electron cloud around the nucleus. In this type of scattering, the electron may change direction, but usually does not lose a measureable amount of energy (small fraction of an eV), thus both the total kinetic energy and momentum are conserved, as shown in the vector diagram of Figure 3-1(a) [4, 6]. Typical scattering angles for elastically-scattered electrons are ~1-10^o in the forward direction [3]. Elastically-scattered electrons are the foundation of electron diffraction and many imaging techniques, including selected-area and convergent-beam electron diffraction, and diffraction-contrast and phase-contrast imaging. Alternatively, an incident electron can be inelastically scattered through interaction with either the outer- or inner-shell atomic electrons that surround

the nucleus. The vector diagram showing this type of scattering is shown in Figure 3-1(b). This interaction involves the excitation of the atomic electrons, and results in the incident electron losing some measureable amount of energy, ranging from ~20 meV to over a few keVs. Energy is primarily transferred to create phonons, plasmons or interband electronic transitions, which are less localized than elastic scattering processes [6]. However, the incident electron can also give up some of its energy to an inner-shell electron in an ionization process, which is highly localized on a single atomic site [7]. Typical scattering angles for inelastically-scattered electrons are small, usually $<1^{o}$ in the forward direction [3]. Electrons that have lost energy through interaction with the specimen contain an enormous amount of information about the chemical identity of the atoms and how they are bonded together. This type of information can be obtained by measuring the amount of energy loss of the incident electrons after they pass through the sample with an electron energy-loss spectrometer attached to the bottom of the microscope as described in section 3.7 [4]. Finally, other secondary signals are generated when electrons transfer energy to the specimen, such as X-rays, secondary electrons, and Auger electrons. In the TEM, X-rays can be collected and used in analytical electron microscopy.

Throughout the remaining chapters of this dissertation, the sensitivity of the TEM to these electron-matter interactions will be become clear. All features in TEM images and diffraction patterns are a result of the electron interactions with the sample. For example, the spots observed in diffraction patterns are a result of coherent elastic scattering from a material with long-range atomic order, and can be used for structure determination. Lattice fringes observed in high-resolution phase-contrast images of crystals are formed by the interference of multiple diffracted electron beams. Other contrast in images can be used to identify strain, sample bending, or changes in sample orientation. And finally, changes in atomic composition can be easily imaged by collecting only those electrons that are scattered incoherently at high angles.

3.2.b. Electron Optics

In order for an instrument that uses electrons to operate as a microscope, a way of focusing the electron beam is required. Fortunately, electrons can be manipulated within an external magnetic field. In fact, electrons were first successfully focused with an electromagnet by

Busch in 1927 [8]. The most primitive form of an electromagnetic lens is simply a cylindrical coil of wire through which a current is passed [9]. When a current is passed through the coil, an axially-symmetric magnetic field is formed inside of the coil, which acts to focus electrons that pass through the coil in an analogous fashion to the way in which a convex optical lens focuses light [3]. In the TEM, there are many electromagnetic lenses that act to manipulate the incident electron beam as it moves down the microscope column to illuminate the sample, and also to collect the transmitted beam(s) to form images, diffraction patterns, and to direct electrons into the EEL spectrometer.

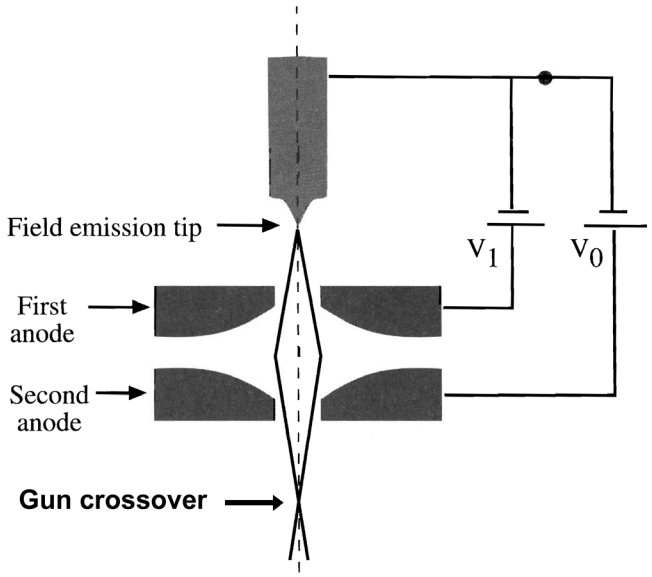

Figure 3-2. Schematic diagram of a Schottky field-emission electron gun. Electrons extracted from the ZrO-coated tungsten tip are accelerated to 300 keV and brought to a crossover, which is then demagnified by the condenser lenses to illuminate the specimen. Image from [3].

Electrons begin their journey at the top of the microscope at the electron gun. All work in this dissertation was conducted using microscopes with Schottky field-emission guns (FEGs). Field-emission sources have the advantage of very high brightness, current density, and a low energy spread [3]. A FEG consists of a pointed cathode and at least two anodes, as shown in Figure 3-2. The cathode is composed of an oriented tungsten wire that is etched to a fine tip with radius ~0.1-1 μm on which ZrO is formed at high temperature to lower the work function of the tungsten from 4.5 eV to 2.7 eV [6]. During operation the tungsten cathode is heated to a

temperature of 1800 K so that electrons can escape from the filament tip. Field-emission electron sources operate on the principle that an electric field strength is greatly enhanced at sharp points, specifically the strength is inversely proportional to the radius of curvature [10]. Thus, a positive voltage of ~4 keV applied at the first anode creates an enormous electric field strength at the cathode tip that acts to extract electrons preferentially from a narrow region located at the sharp filament tip. Electrons are then accelerated by the potential (accelerating voltage) applied between the cathode and the grounded second anode, to their final energy of 300 keV. The combination of two anodes also acts as an electrostatic lens to form a focused image of the cathode tip at the lens crossover, which is ~10 nm in diameter. It is this crossover point that is the virtual source of electrons for the rest of the microscope and is imaged by the condenser lenses to illuminate the sample. As shown in Figure 3-3, there are a set two condenser lenses, C1 and C2 that make up the illumination system of the TEM, and are used to demagnify the virtual source of electrons (at gun crossover) to illuminate the sample with either a parallel or converged beam of electrons. Demagnification is necessary in order to reduce lens aberrations and the non-homogeneous electron emission from the gun cathode, as well as to reduce effects of mechanical instability of the electron source [11]. A parallel beam of electrons is necessary for conventional TEM imaging, including bright- and dark-field and phase-contrast imaging as well as selected-area electron diffraction. A convergent beam of electrons however, is used to obtain diffraction patterns from nanometer-sized regions through the convergent-beam electron diffraction technique and in scanning-TEM mode where a fine electron probed is scanned across the sample to form images or to perform atomic-scale chemical analysis. In this mode, the upper objective lens acts as a third condenser lens to form a small electron probe ~0.15 nm in diameter, as shown in Figure 3-3.

After electrons interact with the sample they must be manipulated to form images, diffraction patterns, or directed into an energy-loss spectrometer. The set of three lenses, including an objective lens, intermediate lens(es), and a projector lens work together to accomplish this, and are collectively referred to as the imaging system. In conventional TEM, the objective lens located just below the sample collects all the electrons emerging from the exit surface of the sample and recombines them to form an image, which is located in the image plane. The focusing action of the objective lens is such that electrons traveling at similar trajectories exiting

the sample are brought back to focus in the back-focal plane to create a diffraction pattern. An intermediate lens is used to select either the back-focal plane or image plane of the objective lens to magnify with the projector lens, to display either the diffraction pattern or image on the viewing screen, respectively, as shown in Figure 3-4. The intensity, focus, and magnification are controlled by varying the strength of the lenses. Alternatively, the intermediate lenses can project either the diffraction pattern or image into an electron energy-loss spectrometer so the energy of the electrons can be measured. A number of apertures located both before and after the sample can be inserted to control the convergence and acceptance angles, or to form images from a selected set of electron beams.

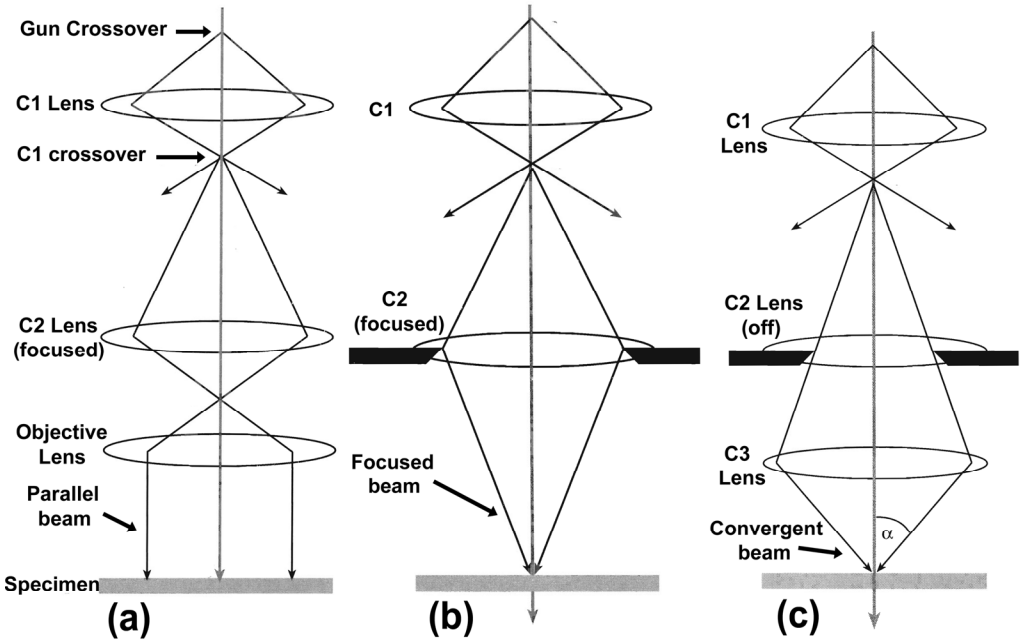

Figure 3-3. The illumination system of the TEM. (a) Condenser lenses C1 and C2 image the gun crossover at the front focal plane of the upper objective lens to provide parallel sample illumination. (b) A focused C2 lens illuminates a small area of the specimen. (c) The upper objective lens and a weakened C2 lens combine to form a highly converged electron probe ~0.15 nm in diameter used for STEM imaging. Images from [3].

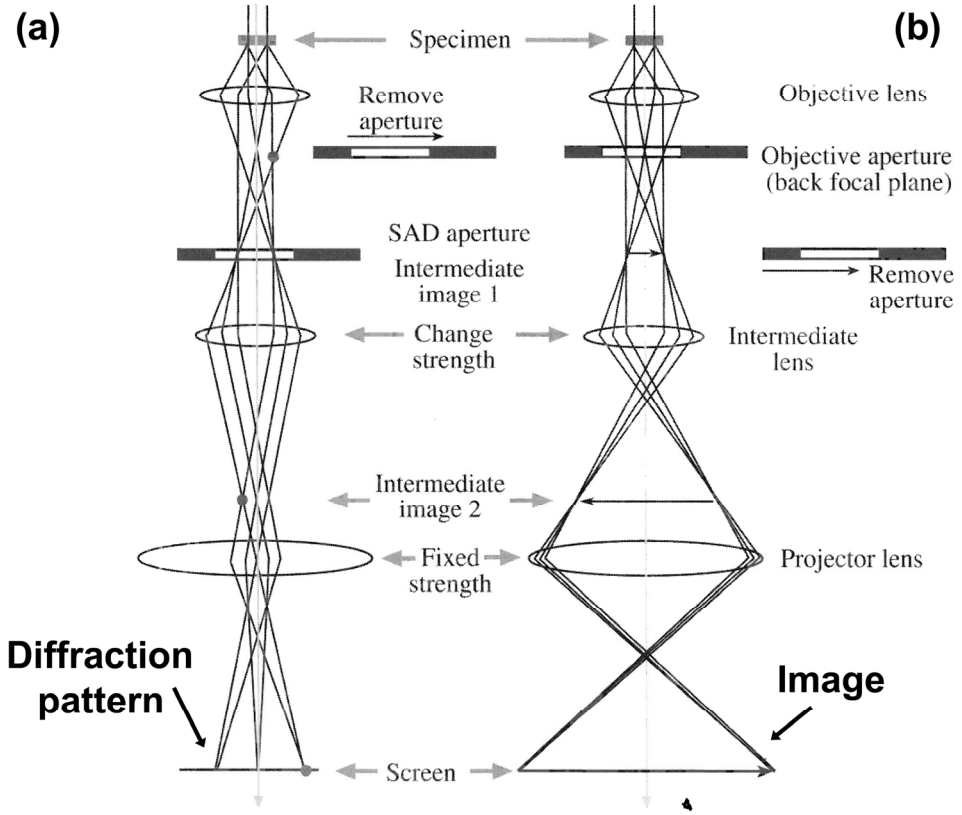

Figure 3-4. The two primary modes of operation of the TEM imaging system. The intermediate lens is used to select either the back focal plane of the image plane of the objective lens as its object to project the (a) diffraction pattern or (b) image, respectively, on the viewing screen. Images from [3].

3.3 Electron Diffraction

Electron diffraction is the most important scattering phenomenon that occurs in the TEM. When discussing diffraction, the wave-like nature of the electron becomes especially evident. Diffraction enables the structure and orientation of a crystalline material to be determined. In the TEM, a variety of techniques are used to obtain this structural information from specific regions of the specimen, either over a relatively a large region, or on a nanometer scale.

The phenomenon of electron diffraction occurs because of the order that exists in a crystalline material. A crystal is composed of an ordered array of regularly-spaced atoms. The average spacing of atoms is typically on the order of ~0.2 nm. Since the wavelength of an electron used

in a TEM is much shorter (~0.002 nm) than this atomic spacing, the electron wave can be diffracted by the periodically-spaced atoms, analogous to the diffraction of visible light by a grating, or a set of slits [12]. In a crystal, each atom acts as a scattering center. Following from the Huygens-Fresnel approach for the diffraction of visible light, when an incident electron wave interacts with a scattering center, it acts as a source of a new wave. Because there are many scattering centers present, multiple new waves are created that interfere with each other and with the incident electron wave. This interference changes the distribution of scattered intensity, or diffracts the electron wave, such that the intensity is sharply peaked at specific angles, which are characteristic of the atomic order. The application of this phenomenon to study the atomic structure of crystals was first developed by von Laue and Bragg [13]. Bragg showed that in order for waves scattered by adjacent scattering centers to interfere constructively, their path-length difference must be an integral number of wavelengths. When waves are diffracted from the atomic planes of a crystal, Bragg's law provides a simple criterion for constructive interference that relates the wavelength of the incident electron wave to the spacing between atomic planes in the crystal:

$$n\lambda = 2d\sin\theta$$

where n is an integer, d is the spacing between adjacent atomic planes, and θ is the angle of scatter, which is called the Bragg angle when waves constructively interfere to produce a diffracted beam [5]. In the TEM, interplanar spacings in a crystal and crystal orientation are determined by measuring the angle of electron scatter.

The TEM is unique in that diffraction can be obtained from extremely small areas of the specimen, so that structure can be probed at the nanometer scale. One method is to insert a selected-area (SA) aperture below the objective lens, as shown in Figure 3-4, to obtain diffraction from a region ~a few 100 nm or less in size. This method uses a parallel beam of incident electrons, so the resulting selected-area electron diffraction (SAED) pattern is composed of a set of diffraction spots, as shown in Figure 3-5(a). Alternatively, the incident electron beam can be converged to form a small probe that enables diffraction patterns to be obtained from nanometer-sized domains of the sample. The convergent-beam electron

diffraction (CBED) patterns obtained in this way are composed of a set of diffraction disks instead of spots, as shown in Figure 3-5(b). In this dissertation, SAED and CBED techniques were both utilized to examine the phase and quality of iron-based catalyst crystals located inside the bases of carbon nanotubes, and to determine the crystallographic orientational relationship between the catalysts and their surrounding nanotubes.

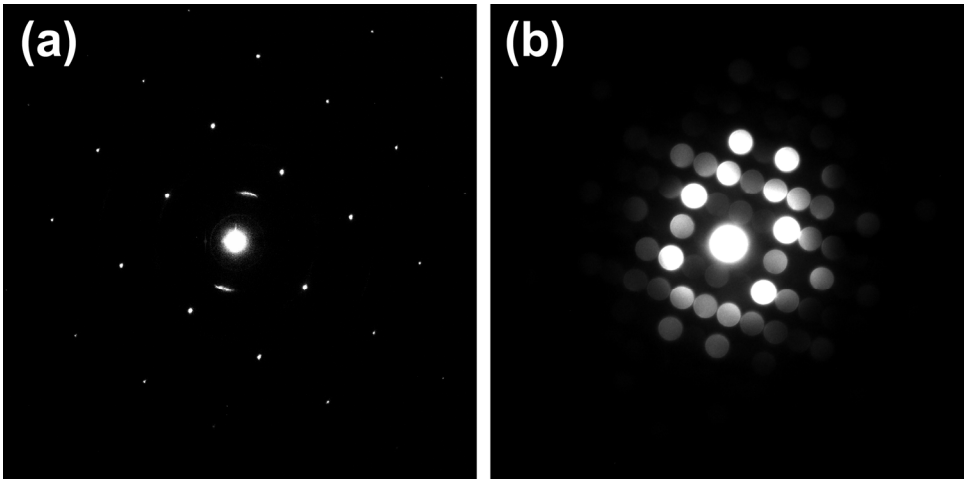

Figure 3-5. (a) Selected-area electron diffraction pattern obtained from a BCC Fe single crystal with the incident electron beam oriented along the [001] zone axis. (b) Convergent-beam electron diffraction pattern obtained from an Fe_3C single crystal with the incident beam oriented along the [010] zone axis.

3.4 Imaging Modes

Combining a diffraction pattern with an image in the TEM is a very powerful method for characterizing a crystalline material. In the TEM there are a number of ways to form an image; each way provides useful complementary information. The most common type of image formed with a TEM is a bright-field (BF) image. A BF-TEM image is formed by blocking out those electrons which are diffracted or scattered at high angles by the sample [see Figure 3-6(a)]. Specifically, an objective aperture is first centered on the direct beam (central spot) of a SAED pattern. The SAED aperture is then removed, and the intermediate lens changed such that its object plane is the image plane of the objective lens. Alternatively, the objective aperture can be used to select an individual diffracted beam to create a dark-field (DF) image

[see Figure 3-6(b)]. This mode of imaging is particularly useful for identifying the specific regions of a sample that are oriented properly to satisfy the Bragg condition for diffraction. Finally, if instead of excluding certain beams, the direct beam plus one or more of the diffracted beams are allowed to contribute to the image, a high-resolution phase-contrast image is formed. This is accomplished by using a very large objective aperture. The relative phases of the multiple beams interfere to form the image contrast, which often appears as a set of periodically-spaced fringes which correspond to the atomic planes of the crystal that are oriented perpendicular to the incident electron beam. As long as the particular atomic spacing is larger than the point resolution of the microscope, ~0.14 nm for the microscope used in this work, it is possible to form this type of high-resolution image [3].

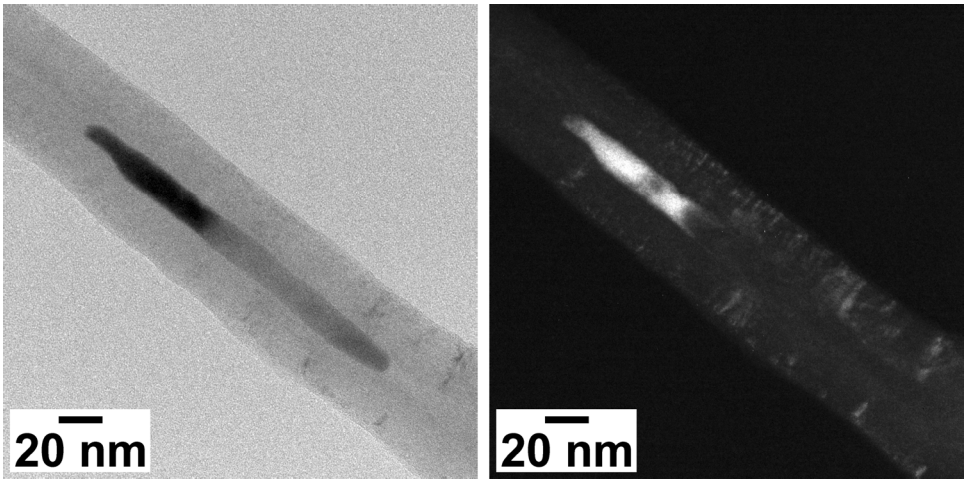

Figure 3-6. (a) Bright-field and (b) dark-field TEM images of an Fe metal catalyst crystal located inside of a multiwall carbon nanotube.

3.5 Scanning Transmission Electron Microscopy

Many TEMs can also be operated in scanning mode, where the incident electron beam is converged to a small probe that is scanned in a raster across the sample [14-16]. For the microscopes used in this work, an electron beam of ~0.15 nm in diameter was used for scanning TEM (STEM). To create such a small probe, the upper objective lens acts as a third condenser lens, while the second condenser lens is weakened or turned off completely; this results in maximum demagnification of the gun crossover, and thus the smallest electron probe [see

Figure 3-3(c)] [3]. Dark-field STEM imaging is an incoherent imaging mode, which unlike phase-contrast imaging, does not rely on the coherent interference of multiple beams to form an image [17, 18]. The dark-field incoherent images obtained with STEM are directly interpretable, unlike in TEM [19]. In fact, no lenses are required below the objective lens, thus many of the things that limit the point resolution of conventional TEM, such as lens defocus and chromatic aberration are not are not present in STEM [3, 6]. Further, the extremely small electron probe in STEM is ideal for atomic-scale x-ray microanalysis and electron energy-loss spectroscopy, which is discussed in section 3.7.

Image-formation in STEM mode is fundamentally different than in conventional TEM. In STEM, an image is formed by scanning a CCD with the electron beam that is being scanned across the sample. Image intensity at each pixel is proportional to the number of electrons collected by one of three semiconductor electron detectors placed at the back focal plane of the objective lens, where the stationary diffraction pattern is located [see Figure 3-7]. Strictly speaking, for a microscope that functions as both a conventional and scanning TEM, these detectors can not be placed at the back focal plane of the objective lens because the objective aperture is already there. So instead, detectors are usually placed lower in the column, into a conjugate plane to the diffraction pattern near the viewing screen, and the projector lens is used to transfer the diffraction pattern at the back focal plane of the objective lens to this conjugate plane. Detectors in STEM play a similar role as apertures in conventional TEM; they control which electrons contribute to form the image. Bright-field STEM images are formed by placing a disk-shaped electron detector aligned with the optic axis to collect unscattered electrons or those scattered through small angles. Dark-field STEM images can be formed by shifting this BF detector off axis to collect diffracted beams, however they are more commonly formed using an annular detector. A low-angle annular dark-field (LAADF) detector collects Bragg-diffracted electrons that have been scattered through angles ~10-50 milliradians. A smaller fraction of electrons are scattered incoherently through much higher angles (~50 to >200 milliradians) because of their interaction with atomic nuclei, in a Rutherford-like scattering process. A high-angle (HA) annular detector can be used to collect these electrons to form a HAADF image whose contrast is sensitive to atomic number, Z [18, 19]. Image intensity in HAADF images is in fact proportional to $Z^{1.7}$ [6, 20]. Because no two detectors overlap, BF,

LAADF, and HAADF images can be obtained simultaneously. Additionally, the geometry of the doughnut-shaped ADF detectors enables DF images to be obtained in conjunction with atomic-scale EELS [7].

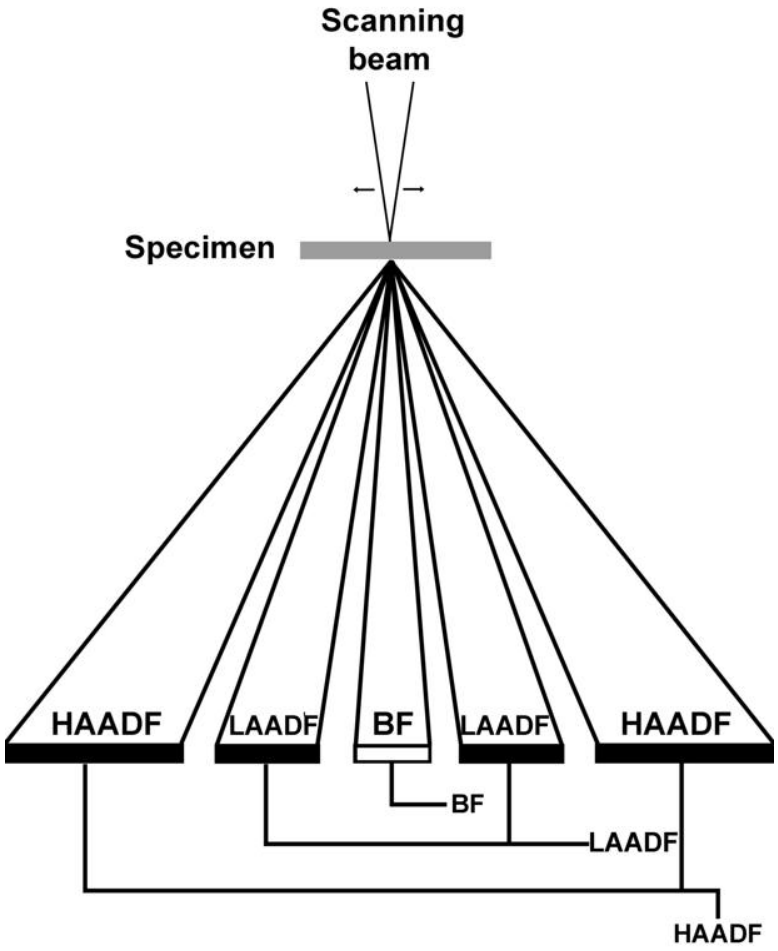

Figure 3-7. Schematic diagram of the three detectors used to form images in STEM mode. A disk-shaped detector centered on the optic axis is used to form bright-field images. Annular detectors collect electrons scattered through higher angles to form dark-field and high-angle Z-contrast images.

3.6 X-ray Energy-Dispersive Spectroscopy

The chemical composition of a sample can be investigated with relative ease by using an X-ray energy-dispersive spectrometer (XEDS) attached to the TEM to analyze the X-rays that are generated when the incident electron beam interacts with the sample [21]. Specifically, the atomic species present are determined by detecting the characteristic X-rays emitted by the sample. In the generation of a characteristic X-ray, an incident electron first ionizes an atom in the sample by losing a portion of its energy to eject an inner-shell electron from the atom, which leaves a vacancy at that inner-shell level and the atom in an electronically-excited state. The ionized atom can subsequently de-excite when a higher-energy electron from one of its outer shells falls into the inner-shell vacancy. As a result of this transition, a photon with energy equal to the energy difference between the two states is emitted; this energy difference is unique to or characteristic of the ionized atom [22]. For example, when a fast electron ejects an inner K-shell electron from a silicon atom, the vacancy in the K shell can be filled by an electron from the L shell, and a photon with $K_\alpha = 1.74$ keV is emitted [11].

X-rays generated when fast electrons interact with the sample are detected and identified with an XEDS equipped with a silicon-lithium semiconductor detector. Typically, the XEDS is inserted from the side of the TEM column, at a small angle above the horizontal plane of the specimen, and the sample tilted towards the detector. X-rays generated when the electron beam strikes the sample are detected and dispersed according to their energy to produce a plot of X-ray counts versus X-ray energy [3]. Peaks present in this spectrum correspond to the energies of the characteristic X-rays, and are used to immediately identify the types of atoms present in the sample. The X-ray spectrum also contains a continuum X-ray which contributes to the background on which the characteristic X-ray peaks are superimposed. This continuum is a result of the acceleration of incident electrons through interaction with the Coulomb field of the nucleus. The angular distribution of each type of X-ray is different; characteristic X-rays are emitted isotropically, while the angular distribution of the continuous X-rays is highly anisotropic in the forward direction [6].

Unfortunately, not every ionization of an inner shell results in the emission of an X-ray. Instead of X-ray emission, the energy can be transferred to another atomic electron which then leaves as an Auger electron. The probability that an X-ray will be emitted is described by its X-ray fluorescence yield, which is very low for light elements [22]. Thus XEDS is a poor technique for analyzing samples that contain elements with small atomic nuclei. Further, often more detailed information is needed about the sample, such as the atomic bonding. In such cases, electron energy-loss spectroscopy is a clear choice, as it can be used to probe samples that contain light elements ($Z<10$) very efficiently, and provides a plethora of information about the atomic structure [4, 23].

3.7 Electron Energy-Loss Spectroscopy

Fast electrons that are inelastically scattered contain an enormous amount of information about the chemistry, structure, and electronic properties of the sample. The amount of energy an electron loses to the sample is characteristic of the specific type of excitation it causes in the material. Instead of detecting secondary processes such as X-ray emission, as is done in XEDS, electron energy-loss spectroscopy (EELS) detects the primary processes of electron excitation by measuring directly how much energy the incident fast electron loses. This is accomplished by directing the scattered electrons into a magnetic-prism electron spectrometer attached to the bottom of the TEM column, which separates electrons according to their kinetic energy to produce an energy-loss spectrum that shows the scattered intensity as a function of energy loss of the fast electron.

EELS offers a number of advantages compared to XEDS. By detecting primary excitation processes in EELS, detection limits imposed by the low fluorescence yield of light elements are overcome. In fact, EELS provides much higher sensitivity to light elements than XEDS when $Z < 10$, where Z is the atomic number [23]. Further, inelastically-scattering is concentrated over relatively small angles (typically less than 1 degree), so most of the electrons can be collected by the EEL spectrometer, whereas characteristic X-ray emission is isotropic, so only a small fraction of the signal is collected by the small solid angle of the XEDS detector [4]. And

finally, the fine structure of peaks in an EELS spectrum contains information about the atomic bonding, band structure, and coordination number; no such information is available with XEDS.

3.7.a. Instrumentation

Figure 3-8 shows a schematic of a 90° magnetic-prism electron energy-loss spectrometer. Electrons that enter through the entrance aperture of the spectrometer are bent by the transverse magnetic field of the prism; the radius of their trajectory is proportional to their momentum [6]. Thus, an electron that has lost energy to the sample will be more strongly bent than electrons that pass through the sample without losing energy. In this way, the prism creates an energy dispersion of the electrons. The spectrometer also acts as a lens to focus the electrons such that electrons of the same energy, but traveling at different angles relative to the optic axis as they enter into the lens, are focused to the same spot on the dispersion plane. Thus the dispersion plane contains the energy-loss spectrum. Additional lenses (quadrupoles and sextupoles) after the prism magnify this spectrum, or dispersion, and project it on to a YAG scintillator, which is coupled via fiber-optics to a linear photodiode array detector [4].

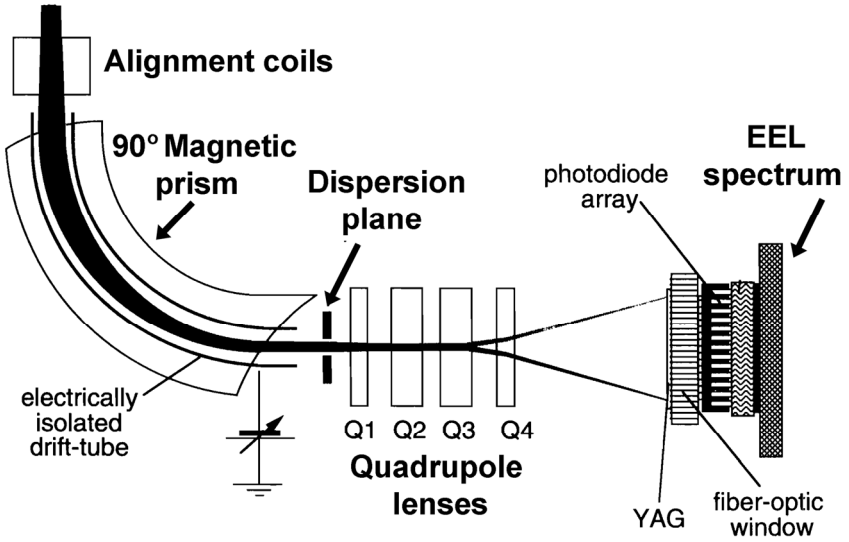

Figure 3-8. Schematic diagram of an EEL detection system that consists of pre-spectrometer focusing and alignment coils, a magnetic-prism spectrometer, quadrupole lenses, and a YAG scintillator that is fiber-optically coupled to a liner photodiode array. Image from [4].

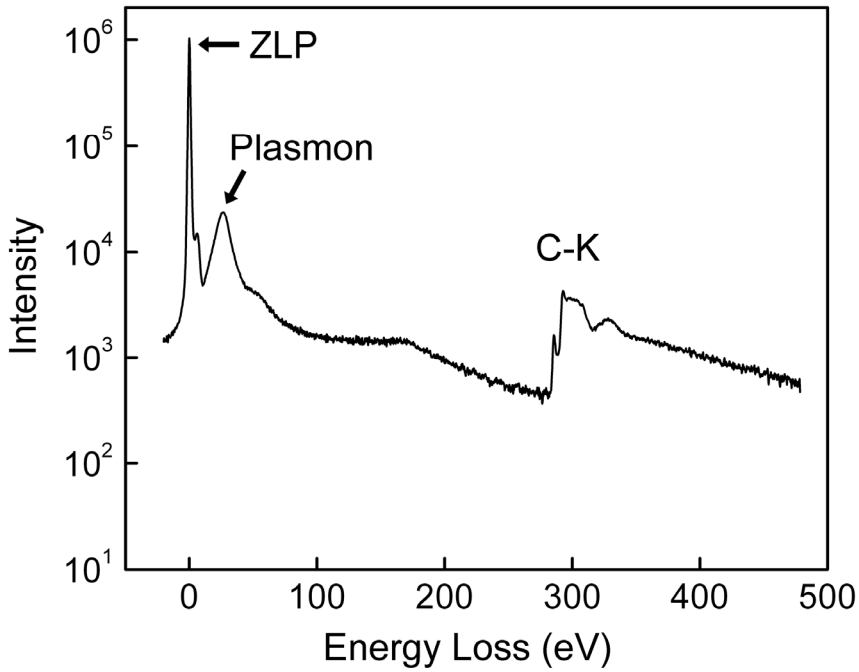

Figure 3-9. Electron energy-loss spectrum of a graphite flake with the measured electron intensity on a logarithmic scale, showing the zero-loss peak, plasmon peak, and carbon K ionization edge.

3.7.b. The Electron Energy-Loss Spectrum

Figure 3-9 shows an example electron energy-loss (EEL) spectrum, recorded from a thin flake of graphite. In an EEL spectrum, there are two primary regions which contain features that correspond to different types of excitations that occur within the material; these features provide different, yet complementary information about the chemical identity, atomic bonding, and atomic structure. The low-loss region, $\Delta E \leq 50$ eV, contains the most prominent peak in the EEL spectrum, namely, the zero-loss peak (ZLP) which corresponds to those electrons that that are transmitted though the sample without losing a measureable amount of energy. Contributing to this peak are electrons that transmit through the sample without being scattered, those which have excited phonon modes in the sample, and those which are elastically scattered in the forward direction. Inelastic scattering from outer-shell electrons results in plasmon excitations and interband transitions, which appear as peaks in the 0.5-50 eV region of the spectrum. In the EEL spectrum of Figure 3-9, a plasmon peak is present at an energy loss of

about 27 eV. Energy losses from interaction with outer-shell electrons are in fact related to the optical constants of the material [4]. At higher energy losses, additional peaks are present in the EEL spectrum that correspond to inner-shell ionization processes. Ionization edges can be used for elemental analysis since the position of an ionization edge is sensitive to the atomic number of the scattering atom [6].

3.7.c. Energy Loss by Plasmon Excitation

The low-loss region of the EEL spectrum is dominated by plasmon excitations. These plasmons correspond to the collective longitudinal excitations of electron density in valence bands to empty states in the conduction bands. The main application of plasmons is estimating electron density, however, optical constants can also be extracted by use of dielectric theory to describe the plasma excitation [6].

A fast electron can lose energy, E_p, to generate a plasmon excitation with characteristic angular frequency ω_p, given by

$$E_p = \hbar\omega_p = \hbar\sqrt{\frac{ne^2}{\varepsilon_0 m^*}}$$

where n is the electron density, e is the electron charge, ε_0 is the permittivity of vacuum, and m^* is the effective electron mass [24]. The double differential cross-section of this inelastic scattering, is proportional to the scattered intensity, or the EEL spectrum, and is given by

$$\frac{d^2\sigma}{dEd\Omega} \approx A \cdot \mathrm{Im}\left[-\frac{1}{\varepsilon(E)}\right] \cdot \frac{1}{\theta^2 + \theta_E^2}$$

where $d\Omega$ is the differential solid scattering angle, A is a constant, $\varepsilon(E)$ is the complex dielectric function, and θ_E is the characteristic angle of scattering [25]. The energy loss function is defined as

$$\mathrm{Im}\left[-\frac{1}{\varepsilon(E)}\right]=\frac{E\left(\Delta E_p\right)E_p^2}{\left(E^2-E_p^2\right)^2+\left(E\Delta E_p\right)^2}$$

where ΔE_p is the plasma peak full width at half-maximum. From an EEL measurement, the real and imaginary parts of the dielectric function can be extracted using the Kramers-Kronig relation, and thus direct comparisons with optical data of the optical constants can be made [4].

3.7.d. Energy Loss by Inner-Shell Ionization

Energy losses can occur when an electron in an inner-shell transitions to an unoccupied state. Losses associated with these types of transitions appear as peaks in the EEL spectrum over an energy range 50-2000 eV and are referred to as ionization or core-loss edges. Peak position and intensity indicate the identity of atoms present, and their concentration, respectively. The position of the resulting ionization peak, or equivalently, its ionization threshold energy, is the difference in energy between the core-level initial state and the lowest-energy unoccupied final state above the Fermi level of the excited electron [6]. Edges are thus labeled according to the ionized shell. For example, Figure 3-10(a) shows the carbon K-edge for graphite; this edge is a result of electrons being ionized from an initial 2s level (K shell). Shown in Figure 3-10(b) is the iron L-edge, which is a result of electrons being ionized from an initial 2p level (L shell).

The fine structure present in ionization edges obtained from solids contains a wealth of information about the type of atomic bonding and electronic band-structure, as well as the crystallographic structure of the material. Two types of fine structure are present in ionization edges. Energy-loss near-edge structure (ELNES) appears within the first ~30 eV beyond the edge onset; this structure contains information specifically about the bonding and band structure. Extended energy-loss fine structure (EXELFS) extends several hundred electron volts beyond the edge onset and contains information about the coordination of neighboring atoms [6]. The work conducted in this dissertation utilized extensively ELNES structure in core-loss edges to characterize atomic bonding in carbon nanotubes and metallic catalyst nanoparticles, as discussed in chapters six and eight.

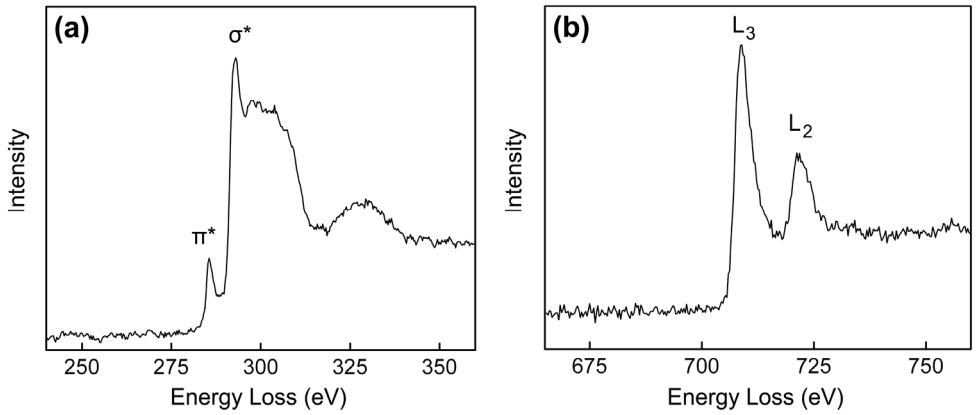

Figure 3-10. (a) Carbon K-edge EEL spectrum of graphite exhibits ELNES that consists of π^* and σ^* peaks. (b) Iron L_{23} core-loss edge exhibits ELNES that consists of two "white-lines", the L_3 and L_2 peaks.

Energy-Loss Near-Edge Structure (ELNES)

Core-loss edges obtained from solids exhibit fine structure in the form of peaks or intensity oscillations superimposed on the basic edge shape within ~30 eV of the edge onset. This near-edge fine structure is a direct result of the surrounding atoms; thus, it is only observed when atoms exist in a condensed phase. It is strongly dependent on the ionic charge, bonding, and atomic coordination, however, interpretation can be quite complex [26]. Two alternative models, or explanations for ELNES structure are commonly used and will be discussed here: the density of states interpretation, and the molecular orbital interpretation.

Variations in intensity, or fine structure, can be related to the band structure of the material. The intensity of the fine structure of the ionization edge is proportional to the differential scattering cross-section in energy loss E and solid angle Ω which is derived from Fermi's Golden Rule [27] and the independent electron model [28] to yield

$$\frac{d^2\sigma}{dEd\Omega} = \frac{A}{q^4}\left|\left\langle \psi_f \left| exp\left(i\bar{q}\cdot\bar{r}\right)\right|\psi_i \right\rangle\right|^2 N(E)$$

where A is a constant, q is the momentum transfer, ψ_i and ψ_f are the initial- and final- state atomic wave functions, respectively, and $N(E)$ is the density of final unoccupied states, which

depends on the chemical and crystallographic environment of the excited atom [4]. For an incident energy E_0 and corresponding wave vector $\bar{k}$, the momentum transfer $\bar{q}$ is related to the scattering angle by [see Figure 3-1] $q^2 = k^2\left(\theta^2 + \theta_E^2\right)$, where $\theta_E = E / 2E_0$. Transitions between ψ_i and ψ_f are governed by the dipole selection rule, $\Delta l = \pm 1$, thus any observed variations in fine-structure intensity are a direct result of variations in unoccupied density of states, *N(E)*. To be specific, the observed density of states is highly localized at the site of the excited atom, is symmetry-projected, and is overlapped, or joint between the final state density and that of the core level [4]. For example, the observed variations in the carbon K-edge intensity (initial 1s state) for graphite, as shown in Figure 3-10(a), reflects mainly the density of unoccupied 2p states in the conduction band. Similarly, the L_2 and L_3 peaks (2p initial state) in the iron L-edge, shown in Figure 3-10(b), are a result of peaks in the density of 3d states.

An alternative view of ELNES in terms of bonds between pairs of atoms, as in molecular orbital theory, is often more usable because of its direct physical interpretation. In this picture, the local band structure is approximated as a linear combination of atomic orbitals (LCAO) of the excited atom and its immediate neighbors [4]. To use graphite as an example, the four valence electrons of each carbon atom are sp^2-hybridized, which results in three strong σ bonds to nearest neighbors in-plane, and the fourth electron contributes to a delocalized π orbital. The unoccupied states to which core electrons can be excited are the corresponding antibonding orbitals, σ* and π*. These unoccupied antibonding orbitals give rise to distinct ELNES peaks in the carbon K-edge EEL spectrum as shown in Figure 3-10(a). Because of the spatial anisotropy of these orbitals, particularly the final state orbital, the measured EELS intensity of the σ* and π* peaks is dependent on the orientation of the crystal relative to the incident electron beam, as an EEL measurement probes the states in the direction of $\bar{q}$ [6]. In the case of diamond, however, the four valence electrons of each carbon atom are sp^3-hybridized and form four symmetric σ orbitals in tetrahedral coordination. Thus, the ELNES contains only the σ* peak. The relative intensity ratio of the σ* and π* peaks can therefore be used as a measure of the relative fraction of sp^2- versus sp^3-hybridized carbon bonding in an amorphous material, as described in chapter eight.

Another case where molecular orbital theory is particularly useful is in the description of L_{23} core-loss edges of transition metals for the determination of valency, or oxidation state. Figure 3-10(b) shows the iron L_{23} edge which exhibits two white-line peaks close to the ionization threshold that are due to excitation of 2p electrons to bound unoccupied 3d states. Spin-orbit splitting of the 2p subshell results in peak splitting to form separate L_3 and L_2 peaks, whose intensities are related to number of unoccupied 3d states [6]. During excitation of a 2p electron, the atomic state of the Fe atom changes from the $2p^6 3d^n$ ground state to a $2p^5 3d^{n+1}$ excited state, where n = 5 for Fe^{3+} and n = 6 for Fe^{2+} [29]. Specifically, the L_3 and L_2 edges are due to the excitation of $2p_{3/2}$ and $2p_{1/2}$ electrons to unoccupied bound $3d_{3/2}$ and $3d_{5/2}$ states, where j = 5/2, 3/2, and 1/2 indicates the total angular momentum quantum number for each electron [29]. It has been found that both the edge position [30] and the intensity $I(L_3)/I(L_2)$ ratio [31] of the two white lines change with Fe valency, which reflects the change in core-level energy and occupancy of the 3d level, respectively [4].

3.8 Other Techniques

Although most of the work in this dissertation was conducted with the electron microscopy techniques described herein, other techniques such as Raman spectroscopy provided invaluable information about the structure of the carbon nanotube films and graphite crystals over a micron length scale. Details of the Raman technique are discussed in the chapter in which it is relevant.

3.9 References

[1] Ruska, E.; Knoll, M., Das Elektronenmikroskop. *Z. Physik* **1932,** *36*.

[2] de Broglie, L., Recherches sur la théorie des quanta. *Annales de Physique* **1925,** *3*.

[3] Williams, D. B.; Carter, C. B., *Transmission electron microscopy : a textbook for materials science*. New York : Plenum Press: New York, 1996.

[4] Egerton, R. F., *Electron energy-loss spectroscopy in the electron microscope*. New York : Plenum Press: New York, 1996.

[5] Cullity, B. D., *Elements of x-ray diffraction*. Upper Saddle River, NJ : Prentice Hall: Upper Saddle River, NJ, 2001.

[6] Kohl, H., *Transmission Electron Microscopy Physics of Image Formation*. New York, NY : Springer-Verlag New York: New York, NY, 2008.

[7] Browning, N. D.; Wallis, D. J.; Nellist, P. D.; Pennycook, S. J., EELS in the STEM: Determination of materials properties on the atomic scale. *Micron* **1997,** *28* (5), 333-348.

[8] Busch, H., On the mode of action of the concentrating coil in the Braun tube. *Arch. Elektrotechnik* **1927,** *18*, 583-594.

[9] Hawkes, P. W., *Electron optics and electron microscopy*. London, Taylor and Francis: London, 1972.

[10] Griffiths, D. J., *Introduction to electrodynamics*. Upper Saddle River, N.J. : Prentice Hall: Upper Saddle River, N.J., 1999.

[11] Loretto, M. H., *Electron beam analysis of materials*. London ; New York : Chapman & Hall: London ; New York, 1994.

[12] Young, T., Experimental demonstration of the general law of the interference of light. *Philosophical Transactions of the Royal Society of London* **1804,** *94*.

[13] Bragg, W. L., The Diffraction of Short Electromagnetic Waves by a Crystal. *Proceedings of the Cambridge Philosophical Society* **1913,** *17*, 43-57.

[14] Crewe, A. V.; Wall, J.; Welter, L. M., A high-resolution scanning transmission electron microscope. *Journal of Applied Physics* **1968,** *39* (13), 5861-5868.

[15] Crewe, A. V.; Isaacson, M.; Johnson, D., A simple scanning electron microscope. *Rev. Sci. Instrum.* **1969,** *40* (2), 241-246.

[16] von Ardenne, M., Das Elektronen-Rastermikrosop. *Z. Physik A-Hadron Nucl.* **1938,** *109*, 553-572.

[17] Loane, R. F.; Xu, P.; Silcox, J., Incoherent imaging of zone axis crystals with ADF STEM. *Ultramicroscopy* **1992,** *40* (2), 121-138.

[18] Nellist, P. D.; Pennycook, S. J., Incoherent imaging using dynamically scattered coherent electrons. *Ultramicroscopy* **1999,** *78* (1-4), 111-124.

[19] Pennycook, S. J.; Jesson, D. E., High-resolution z-contrast imaging of crystals. *Ultramicroscopy* **1991,** *37* (1-4), 14-38.

[20] Nellist, P. D.; Pennycook, S. J., The principles and interpretation of annular dark-field Z-contrast imaging. *Advances in Imaging and Electron Physics, Vol 113* **2000,** *113*, 147-203.

[21] Fuchs, E., X-Ray Spectrometer Attachment for Elmiskop I electron microscope. *Review of Scientific Instruments* **1966,** *37* (5), 623-626.

[22] Goldstein, J.; Newbury, D.; Joy, D.; Lyman, C.; Echlin, P.; Lifshin, E.; Sawyer, L.; Michael, J., *Scanning Electron Microscopy and X-ray Microanalysis*. Kluwer Academic/Plenum Publishers: New York, 2003.

[23] Leapman, R. D.; Hunt, J. A., Comparison of Detection limits for EELS and EDXS. *Microscopy Microanalysis Microstructures* **1991,** *2* (2-3), 231-244.

[24] Kittel, C., *Introduction to solid state physics*. New York, Wiley: New York, 1966.

[25] Raether, H., *Excitation of plasmons and interband transitions by electrons*. Berlin ; New York : Springer-Verlag: Berlin ; New York, 1980.

[26] *Transmission electron energy loss spectrometry in materials science and the EELS atlas*. Weinheim [Germany] : Wiley-VCH: Weinheim [Germany], 2004.

[27] Inokuti, M., Inelastic collisions of fast charged particles with atoms and molecules; the Bethe theory revisited. *Reviews of Modern Physics* **1971,** *43* (3), 297-347.

[28] Bethe, H., The theory of the passage of rapid neutron radiation through matter. *Annalen der Physik* **1930,** *5* (3), 325-400.

[29] van Aken, P. A.; Liebscher, B., Quantification of ferrous/ferric ratios in minerals: new evaluation schemes of Fe L-23 electron energy-loss near-edge spectra. *Physics and Chemistry of Minerals* **2002,** *29* (3), 188-200.

[30] Tafto, J.; Krivanek, O. L., Site-specific valence determination by electron energy-loss spectroscopy. *Physical Review Letters* **1982,** *48* (8), 560-563.

[31] Sparrow, T. G.; Williams, B. G.; Rao, C. N. R.; Thomas, J. M., L_3/L_2 White-line intensity ratios in the electron energy-loss spectra of 3D transition-metal oxides. *Chemical Physics Letters* **1984,** *108* (6), 547-550.

4 Catalyst Rotation, Twisting, and Bending During Multiwall Carbon Nanotube Growth

Internal crystalline structure of cementite catalyst particles located inside the base of multiwall carbon nanotubes was studied using nanoprobe convergent-beam electron diffraction. The catalyst particles are single crystalline but exhibit combinations of small-angle (~1^{o}-3^{o}) rotations, twists, and bends along their axial length between adjacent locations. Distortions are most severe away from the base up into the nanotube where the number of walls is large. Near the attachment point to the substrate, however, where few, if any graphene walls exist, particles remain undistorted. This suggests that the stresses generated by the surrounding nanotube distort the catalyst particle during growth.

4.1 Introduction

Precise structural control of carbon nanotubes (CNTs) remains one of the key challenges to realizing their technological potential. Plasma-enhanced chemical vapor deposition (PECVD) using catalytic metal nanoparticles enables large-scale growth of CNT films, however, much is still unknown about what happens to the catalyst particle during growth [1-3]. Numerous studies with electron microscopy have captured the dynamics of in situ CNT growth from crystalline catalyst particles [4-9]. In these studies, and in others, conducted ex situ, close inspection of bright–field (BF) transmission electron microscope (TEM) images reveals significant contrast variations along the length of the catalyst particles [10,11]. Sources of contrast variation in BF-TEM images include changes in crystal orientation relative to incident electron beam, strain, or thickness, and can indicate a distorted crystalline structure [12]. We examined, in detail, the crystalline structure of iron carbide catalyst particles found inside the base of multiwall carbon nanotubes using a nano-scale electron probe in the TEM.

4.2 Experimental

Multiwall carbon nanotubes (MWCNTs) with diameters ranging from 20-70 nm were grown using an inductively-coupled plasma and iron catalyst through catalytic PECVD. The iron catalyst was deposited on a native-oxide coated silicon substrate as a 10 nm-thick film using electron-beam evaporation. Before nanotube growth, the iron catalyst film was exposed to a plasma maintained in a mixture of H_2 and Ar (50 sccm H_2 and 5 sccm Ar) at 200 W and 700 ^oC for 15 minutes. This hydrogen plasma pretreatment breaks apart the iron film to form nanometer-sized metal islands, and reduces iron oxides present in the catalyst film. Nanotubes were grown at 800 ^oC and 10 Torr using a 13.56 MHz radio-frequency plasma maintained with 200 W power in a CH_4 (5 sccm) H_2 (5 sccm) and Ar (68 sccm) gas mixture. A dense film of multiwall carbon nanotubes grew to an average length of 4 microns after 30 minutes of plasma deposition. Nanotubes were removed from the Si/SiO_2 substrate by sonication in ethanol for 30 seconds, and then transferred to a copper TEM grid coated with a lacey carbon support film. In some experiments the metal catalyst was deposited directly on SiO_2 TEM grids and carbon nanotubes were grown and examined on these grids without removing them by sonication. TEM analysis was conducted using an FEI Tecnai F-30 microscope with a Schottky field-emission electron gun operated at 300 keV. Nanoprobe electron diffraction techniques were used to collect convergent-beam electron diffraction (CBED) patterns from nanometer-size regions along the length of individual catalyst particles located inside the base of MWCNTs. Diffraction patterns were recorded using a Gatan charge-coupled device (CCD). This method was instrumental in identification of small angle rotations between various sections in 5-10 nm thick CdSe quantum rods reported by Yu et al. [13].

4.3 Results and Discussion

Carbon nanotubes grow up with respect to the substrate from catalyst particles which remain attached to the substrate. Figure 4-1 shows an SEM of a bundle of nanotubes, which has partially peeled off from the substrate. Elongated catalyst particles are clearly visible (brighter regions) at the bases of nanotubes where catalysts and nanotubes were attached to the substrate. The thick part of each catalyst is at the bottom of the nanotube, while the crystal becomes

thinner as one moves up from the nanotube base. The majority of nanotubes have outer diameters between 20 and 40 nm, and appear well-graphitized. The crystalline catalyst particle located inside the base of each nanotube exhibits an elongated tear-drop morphology, as is shown in the BF-TEM images in Figure 4-2 – Figure 4-5. Symmetries and planar spacings in electron diffraction patterns obtained from these catalyst crystals are consistent with the cementite (Fe_3C) phase (orthorhombic space group Pnma no. 62, a = 0.5008 nm, b = 0.4465 nm, c = 0.6725 nm).

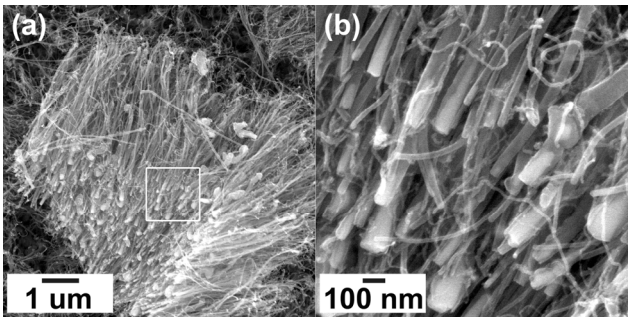

Figure 4-1. (a) SEM image of the base region of the carbon nanotube bundles that have peeled off from the substrate. (b) Same bundle in higher magnification showing elongated catalyst nanocrystals located at the base of each nanotube.

All catalyst crystals examined exhibit significant contrast variation along their lengths when imaged under bright- and dark-field conditions. For example, Figure 4-2 shows representative BF and dark-field (DF) TEM images of a cementite catalyst single crystal inside the base of a MWCNT oriented with its [100] zone axis aligned along the electron beam direction. Evident in both images, but more pronounced in the DF image, is the change in contrast along the length of the catalyst crystal even though the particle is a single crystal. Significant contrast variation present along the length of the crystal indicates possible changes in thickness, strain, or orientation of the crystal.

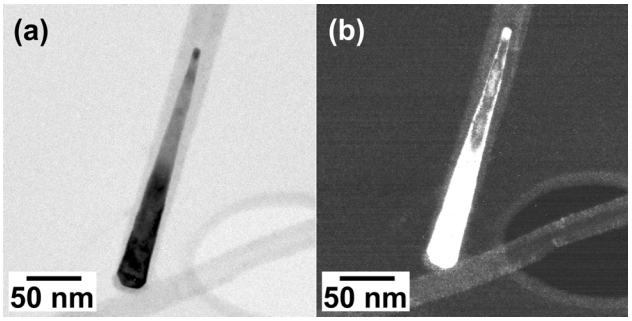

Figure 4-2. (a) BF and (b) DF TEM images of an oriented cementite catalyst crystal inside the base of a multiwall carbon nanotube. The crystal [100] zone axis is parallel to the electron beam. The DF image was formed from the 020 spot.

To determine the cause of this variation, a series of CBED patterns were recorded using an electron nanoprobe positioned at different points along the catalyst. Figure 4-3 shows CBED patterns obtained from three different positions along a cementite catalyst crystal that was approximately 60 nm in length. An electron probe was initially placed at position 3a, and the crystal was tilted such that the electron beam was aligned with the [001] zone axis. The probe was then moved along the length of the catalyst and CBED patterns recorded at positions 3b-3c.

Diffraction from position 3a, at the very base of the nanotube, shows full symmetry of the cementite [001] zone axis, as expected. However, at positions 3b and 3c, the intensity distribution in the diffraction disks changes, which indicates that the orientation of the cementite crystal relative to the incident electron beam has changed. This change in orientation is also evident in the TEM image; the well resolved lattice image at point 3a changes into less well-resolved lattice fringes at points 3b and 3c as the crystal orientation changes and the zone axis and the electron beam become slightly misaligned.

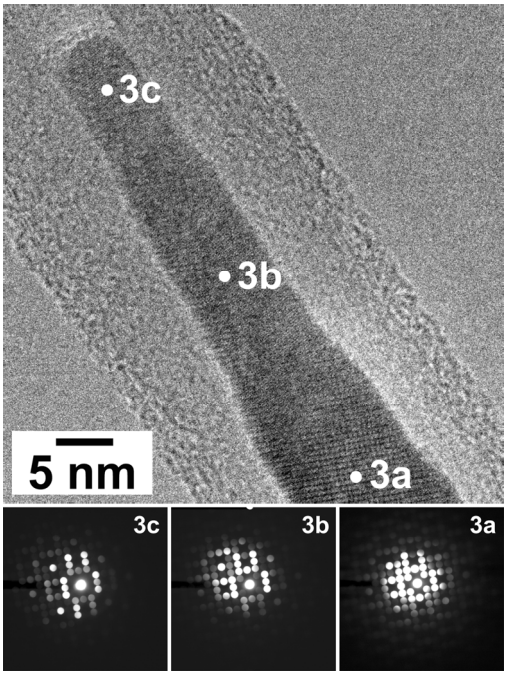

Figure 4-3. BF TEM image (top) of a cementite crystal approximately 60 nm in length oriented along the [001] zone axis at position 3a and the CBED patterns (bottom) obtained from positions 3a-3c. The CBED intensity distribution changes as the probe is moved from position 3a to positions 3b and 3c, which indicates that the crystal orientation changes along its length.

More severe variations in orientation are observed in longer single crystalline cementite catalyst particles. For example, Figure 4-4 shows a series of CBED patterns obtained from six different positions along a crystal that was approximately 225 nm in length. The base (position 4a) of this crystal is oriented along its [101] zone axis, but as the probe was moved to positions 4b-4f, the intensity distribution in the diffraction disks changed significantly, again indicating changes in crystal orientation. Careful examination of the intensity distributions in the CBED patterns in Figure 4-3 and Figure 4-4 indicates that these changes in orientation are not continuous in the same direction, but are random misorientations as one moves from the base to the tip of the catalyst particle. No visible grain boundaries were observed between sections of different orientation. Each catalyst crystal, therefore, is an imperfect single crystal and exhibits a combination of random rotation, twist, and bend components along its length.

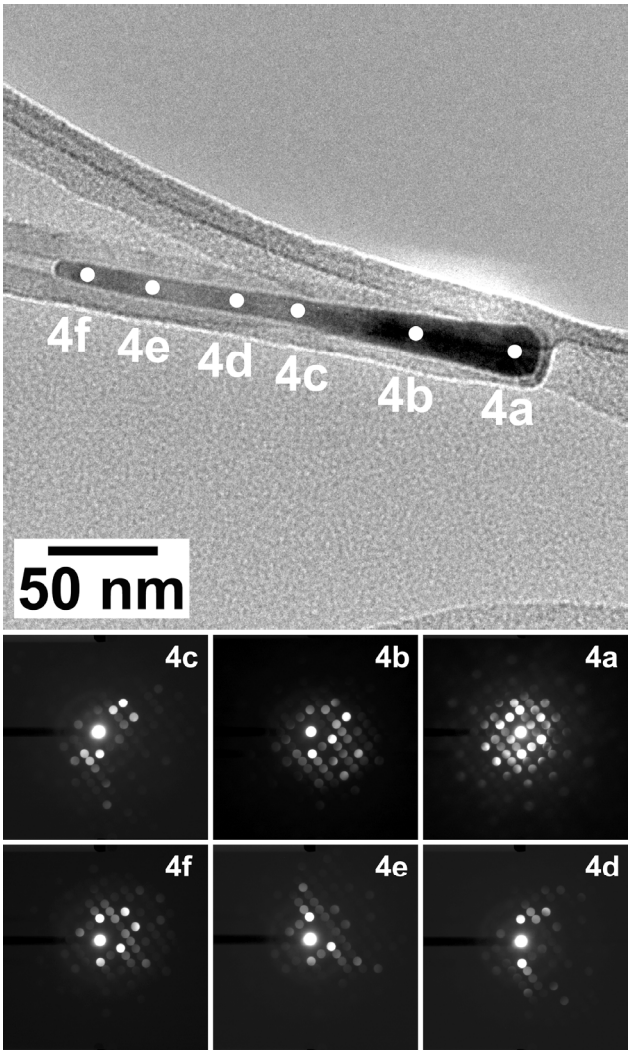

Figure 4-4. BF TEM image (top) of a 225 nm long cementite crystal oriented along the [101] zone axis at position 4a and the CBED patterns (bottom) obtained from positions 4a-4f. The CBED intensity distribution changes significantly as the probe is moved along the crystal, which indicates a severe change in crystal orientation along its length.

We used nanoprobe diffraction in combination with crystal tilting in the electron microscope to quantify the magnitude of the observed misorientations between different sections of each catalyst crystal. One such measurement is shown in Figure 4-5(c) and the results are summarized in Table 4-1. First, the electron nanoprobe was positioned at the base (position 5a) of a catalyst crystal that had been tilted using a double-tilt holder to a specific low-index zone axis, [111] in the case shown in Figure 4-5. Second, the nanoprobe was moved along the

catalyst to position 5b, where the crystal was now misorientated with respect to this zone axis. Third, the crystal was again tilted to bring the zone axis at position 5b parallel to the electron beam and the angular tilts required to accomplish this realignment were recorded. This process was continued at the remaining positions along the catalyst, and effective angular differences were calculated. Table 4-1 lists the two angle values of the double-tilt holder (α and β) for each of the five positions along the catalyst particle shown in the BF image of Figure 4-5, as well as the calculated angular difference in orientation of the crystal at each spot relative to position 5a. Orientation differences between adjacent sections of catalyst crystals range from 1^{o} to 3^{o}. The unsystematic changes in α and β values are typical and indicative of the random nature of the crystalline misorientations and show that the catalyst particle, although single crystalline, is significantly deformed. However, misorientations at different sections of the crystal are uncorrelated.

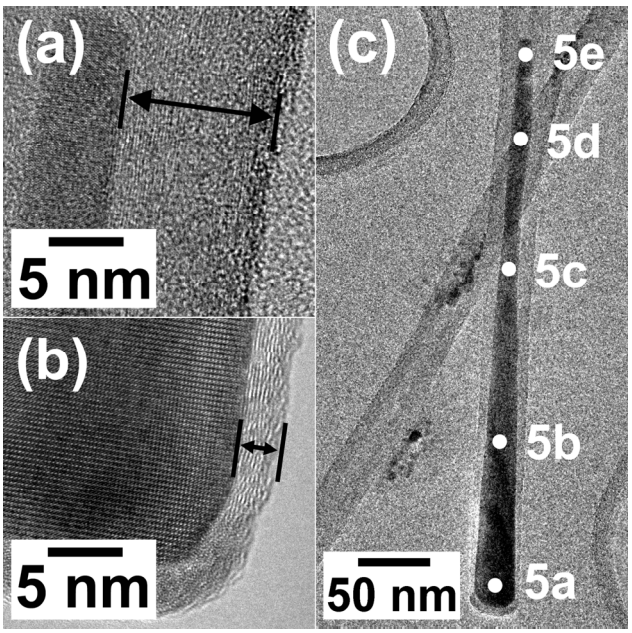

Figure 4-5. HRTEM images comparing the number of graphene walls at the (a) top and (b) bottom region of a catalyst crystal inside the base of a carbon nanotube. Arrows indicate that the number of walls decreases significantly as one moves downwards towards the base of the catalyst crystal. (c) BF TEM image of a 400 nm long cementite crystal. Initially, the crystal was aligned along the [111] zone axis at position 5a. Tilt angles (α and β) required to return the crystal back to the same zone axis were recorded at each position 5a-e (see Table 4-1).

Position	Alpha (±0.1°)	Beta (±0.1°)	Angular Difference (°)
5a	-3.8	-5.1	reference
5b	-4.1	-5.3	0.3
5c	-4.5	-4	1.3
5d	-7.6	-6.2	4
5e	-8.4	-8.3	5.6

Table 4-1. α and β tilt angles and the calculated angular differences in crystal misorientation at each position shown in Figure 4-5 relative to position 5a.

We have considered that the deformation of a catalyst crystal might be induced by the electron beam irradiation; however, control experiments eliminated the possibility that nanocrytsals are deforming while in the microscope. For example, diffraction patterns did not change with time over the time scales that crystals were examined. Moreover, diffraction spots in SAED patterns of entire crystals with the electron beam spread substantially showed either small arc segments, or multiple spots instead of single sharp diffraction spots, indicating that the crystal orientation was slightly different over the entire crystal. We estimated the temperature rise of a crystal due to electron irradiation from a converged electron beam using the Bethe expression for mean energy loss of an incident electron [14, 15]. Using the maximum current density of $\sim 2\times10^{6}$ A/cm^2, which represents the highest current density used during all TEM techniques described herein, we find that this temperature rise is less than 1 ^{o}C, and is insufficient to change or deform the catalyst particle. These experiments show that the deformation exists in the catalyst crystals before they were put in the microscope and that the electron beam did not alter the sample.

Careful examination of the misorientations along a single catalyst suggests that the surrounding graphene walls exert forces on the catalyst particle to deform it during growth. Catalyst particles exhibit a relatively large region near their attachment point to the substrate, which appears undistorted and does not change in orientation. This is evident from the large constant (dark) contrast region at the base of each catalyst particle in the BF-TEM images of Figure 4-2

– Figure 4-5, and by the large bright region in the associated DF-TEM image in Figure 4-2. Farther away from the base, where the crystal orientation has changed, the catalyst crystal appears lighter in the BF image and darker in the DF image. Examination of the carbon nanotube structure that encapsulates the crystal reveals that the number of graphene walls near the base region decreases dramatically, as is evident in the HRTEM images of Figure 4-5 (a) and (b). In many cases, the graphene walls do not extend completely to the end (base) of the catalyst crystal. Crystal faceting is observed where the tube walls terminate. In contrast, away from the base and farther up into the tube, the number of walls increases. Sun et al. estimated pressures exerted by multiwall carbon onions and nanotubes on encapsulated metal particles in heating and electron irradiation experiments to be 10-30 GPa [16]. In separate early-growth experiments, we found that catalyst crystals lose their pronounced faceting and exhibit strain contrast once they became encapsulated in graphene layers. Figure 4-6 shows such an example that has been observed during initial stages of carbon nanotube growth on SiO_2 TEM grids. Such an experiment simulates carbon nanotube growth on native oxide covered silicon but the catalyst can be observed in cross section without disturbing it by sonication. Figure 4-6(a) shows that before graphene layers form on the catalyst, the nanocrystals are faceted. Once graphene layers form, the portion of the catalyst that is encapsulated by graphene loses its faceted shape and become rounded. Moreover, the region adjacent to the graphene walls exhibits strain contrast in the TEM. In contrast, the regions not covered by graphene walls remain faceted. This shows that indeed it is the surrounding walls that deform the catalyst. Such deformations have also been seen in carbon-onion encapsulated metal crystals [17]. These observations suggest that the catalyst particles are subjected to significant stresses by graphene layers that surround them. It seems reasonable to conclude that the observed shape and misorientation of the cementite catalyst crystals along their length is due to the compressive stresses generated by the surrounding graphene layers.

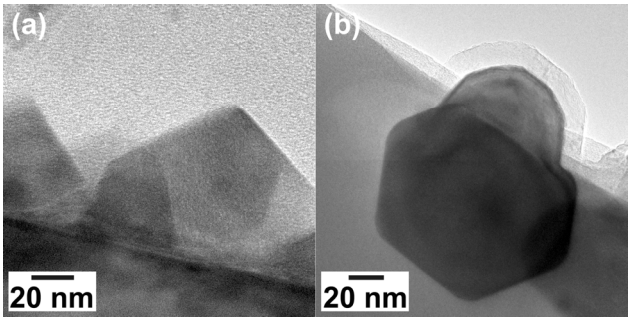

Figure 4-6. TEM images of (a) a catalyst nanoparticle before growth and (b) after nucleation of graphene layers. Before growth the catalyst nanoparticle is faceted. After growth of graphene layers the catalyst faces encapsulated by graphene layers lose their faceted shape and the catalyst exhibits strain contrast in the TEM. The regions not covered by graphene walls retain their facets.

Observations of random small-angle rotations, twists, and bends of the catalyst crystal may have significant implications on the structure of the nanotube that it produces. Recent in situ TEM studies have captured carbon nanotube walls growing from individual metal crystalline catalyst particles [4-9]. Close inspection of these catalyst crystals from BF images reveals non-uniform changes in diffraction contrast across the crystals, as well as the appearance and disappearance of lattice fringes covering partial sections of the crystals. These observations indicate that small sections of the catalyst are being rotated, twisted, or bent by the growing carbon nanotube. If the catalyst crystal acts as a template for carbon atoms to form graphene walls of the nanotube, then a significant number of defects and strain may be introduced whenever a portion of the catalyst is deformed and changes orientation. This may also cause tube growth to change direction, as observed here and by others [18].

4.4 Conclusions

In conclusion, a nanoprobe electron beam in the TEM was used to obtain CBED patterns from nanometer-size regions along the lengths of individual cementite catalyst crystals located inside the base of multiwall carbon nanotubes. Random small-angle (1^{o}-3^{o}) misorientations between adjacent sections along catalyst crystals indicate that the carbon nanotubes exert stresses that rotate, twist, and bend small sections of the catalyst during growth. These findings may have

significant implications on the ability to control carbon nanotube structure using catalytic PECVD.

4.5 References

[1] Ren, Z. F.; Huang, Z. P.; Xu, J. W.; Wang, J. H.; Bush, P.; Siegal, M. P.; Provencio, P. N., Synthesis of large arrays of well-aligned carbon nanotubes on glass. *Science* **1998,** *282* (5391), 1105-1107.

[2] Meyyappan, M.; Delzeit, L.; Cassell, A.; Hash, D., Carbon nanotube growth by PECVD: a review. *Plasma Sources Science & Technology* **2003,** *12* (2), 205-216.

[3] Melechko, A. V.; Merkulov, V. I.; McKnight, T. E.; Guillorn, M. A.; Klein, K. L.; Lowndes, D. H.; Simpson, M. L., Vertically aligned carbon nanofibers and related structures: Controlled synthesis and directed assembly. *Journal of Applied Physics* **2005,** *97*, 041301.

[4] Helveg, S.; Lopez-Cartes, C.; Sehested, J.; Hansen, P. L.; Clausen, B. S.; Rostrup-Nielsen, J. R.; Abild-Pedersen, F.; Norskov, J. K., Atomic-scale imaging of carbon nanofibre growth. *Nature* **2004,** *427* (6973), 426-429.

[5] Rodriguez-Manzo, J. A.; Terrones, M.; Terrones, H.; Kroto, H. W.; Sun, L. T.; Banhart, F., In situ nucleation of carbon nanotubes by the injection of carbon atoms into metal particles. *Nature Nanotechnology* **2007,** *2* (5), 307-311.

[6] Schaper, A. K.; Hou, H. Q.; Greiner, A.; Phillipp, F., The role of iron carbide in multiwalled carbon nanotube growth. *Journal of Catalysis* **2004,** *222* (1), 250-254.

[7] Yoshida, H.; Takeda, S.; Uchiyama, T.; Kohno, H.; Homma, Y., Atomic-scale in-situ observation of carbon nanotube growth from solid state iron carbide nanoparticles. *Nano Letters* **2008,** *8* (7), 2082-2086.

[8] Hofmann, S.; Sharma, R.; Ducati, C.; Du, G.; Mattevi, C.; Cepek, C.; Cantoro, M.; Pisana, S.; Parvez, A.; Cervantes-Sodi, F.; Ferrari, A. C.; Dunin-Borkowski, R.; Lizzit, S.; Petaccia, L.; Goldoni, A.; Robertson, J., In situ observations of catalyst dynamics during surface-bound carbon nanotube nucleation. *Nano Letters* **2007,** *7* (3), 602-608.

[9] Begtrup, G. E.; Gannett, W.; Meyer, J. C.; Yuzvinsky, T. D.; Ertekin, E.; Grossman, J. C.; Zettl, A., Facets of nanotube synthesis: High-resolution transmission electron microscopy study and density functional theory calculations. *Physical Review B* **2009,** *79* (20), 205409.

[10] Yao, Y.; Falk, L. K. L.; Morjan, R. E.; Nerushev, O. A.; Campbell, E. E. B., Synthesis of carbon nanotube films by thermal CVD in the presence of supported catalyst particles. Part I: The silicon substrate/nanotube film interface. *Journal of Materials Science-Materials in Electronics* **2004,** *15* (8), 533-543.

[11] Kim, H.; Sigmund, W., Iron particles in carbon nanotubes. *Carbon* **2005,** *43* (8), 1743-1748.

[12] Williams, D. B.; Carter, C. B., *Transmission electron microscopy : a textbook for materials science*. New York : Plenum Press: New York, 1996.

[13] Yu, Z. H.; Hahn, M. A.; Maccagnano-Zacher, S. E.; Calcines, J.; Krauss, T. D.; Alldredge, E. S.; Silcox, J., Small-angle rotation in individual colloidal CdSe quantum rods. *Acs Nano* **2008,** *2* (6), 1179-1188.

[14] Mkhoyan, K. A.; Silcox, J.; McGuire, M. A.; Disalvo, F. J., Radiolytic purification of CaO by electron beams. *Philosophical Magazine* **2006,** *86* (19), 2907-2917.

[15] Kohl, H.; Reimer, L., *Transmission Electron Microscopy Physics of Image Formation*. New York, NY : Springer-Verlag New York: New York, NY, 2008.

[16] Sun, L.; Banhart, F.; Krasheninnikov, A. V.; Rodriguez-Manzo, J. A.; Terrones, M.; Ajayan, P. M., Carbon nanotubes as high-pressure cylinders and nanoextruders. *Science* **2006,** *312* (5777), 1199-1202.

[17] Sun, L. T.; Krasheninnikov, A. V.; Ahlgren, T.; Nordlund, K.; Banhart, F., Plastic deformation of single nanometer-sized crystals. *Physical Review Letters* **2008,** *101*, 156101.

[18] Yoshida, H.; Uchiyamai, T.; Takeda, S., Environmental transmission electron microscopy observations of swinging and rotational growth of carbon nanotubes. *Japanese Journal of Applied Physics Part 2-Letters & Express Letters* **2007,** *46* (36-40), L917-L919.

5 Orientation and Morphological Evolution of Catalyst Nanoparticles During Carbon Nanotube Growth

We examined the structure, morphology and orientation of catalyst nanoparticles used for seeding and growing multiwall carbon nanotubes (MWCNTs) by plasma enhanced chemical vapor deposition in CH_4/H_2 gas mixtures. Iron catalyst nanocrystals are converted to Fe_3C in CH_4/H_2 plasmas and the MWCNTs grow from Fe_3C nanocrystals. Initially faceted and equiaxed catalyst nanocrystals are distorted and elongated significantly once a tubular CNT structure is formed around the catalyst particles. Eventually, catalysts deform into elongated tear-drop shapes. Once this morphology forms, CNT structures produced are straight and have uniform diameters. Surprisingly, the Fe_3C nanocrystals located inside the base of well-graphitized nanotubes do not exhibit a preferred orientation relative to the nanotube axis. Catalyst nanocrystals in a variety of orientations relative to the nanotube axis still produce well-graphitized nanotubes with similar diameters and structures.

5.1 Introduction

A wide-range of potential applications that utilize the unique electronic, mechanical, and optical properties of CNTs requires precise control of their structure, but such control has not yet been achieved [1-10]. Plasma-enhanced chemical vapor deposition (PECVD), and related CVD processes from CH_4/H_2 gas mixtures using metallic catalyst nanoparticles enable large-scale growth and controlled spatial placement of carbon nanotubes on substrates [3, 11], but these methods always produce a mixture of nanotube structures and sizes. Progress in our fundamental understanding of the atomic-level processes at the catalyst-CNT interface and growth mechanisms has come primarily through careful studies of the structure, phase, and shape of catalyst crystals, from which the nanotubes grow. Both ex situ and in situ transmission electron microscopy (TEM) techniques and x-ray photoelectron spectroscopy (XPS) have been used to characterize catalyst shape and structure. One surprising finding is that Fe, Co, and Ni

based catalysts dynamically change their shape yet remain fully crystalline during high temperature CNT growth by CVD [12-18]. Recently, we used a convergent beam electron diffraction (CBED) technique in the TEM to show that segments of single crystal Fe_3C catalysts located inside the base of multiwall carbon nanotubes (MWCNTs) grown by PECVD were twisted, rotated, and bent [19] by stresses exerted, during growth, by the graphene walls surrounding the catalyst. These observations suggest that the catalyst nanoparticle and the graphene walls undergo complex dynamic interactions that influence how CNTs grow.

Whether CNTs grow epitaxially on catalyst nanoparticles remains an open issue. If epitaxy is important in CNT growth, orientation of the catalyst nanoparticle and the CNT growth axis should be correlated; observation of an ensemble of CNT-catalyst nanoparticle pairs should show preferred catalyst orientations with respect to the CNT growth axis. It was suggested that decomposition of carbon-containing species and graphite formation may occur on specific crystallographic faces that have high catalytic activity [20], which may also result in a preferential catalyst orientation relative to the nanotube axis [21, 22]. In the case of an Fe_3C nanoparticle catalyst, epitaxial growth of graphene layers from catalyst faces oriented perpendicular to the CNT axis seems unlikely because the symmetry of the two structures, orthorhombic and hexagonal, are incommensurate. However, epitaxy could occur at step edges along the length of the catalyst. Indeed, there are a number of Fe_3C crystallographic planes whose spacing is either equal to, or an integer multiple of the 0.34 nm CNT wall spacing, and this could lead to epitaxial growth of graphene layers. Specifically, the (001), (110), (002), (030), (220), (004), and (023) planes could potentially support epitaxial growth. In support of this hypothesis, Wen et al. reported that Fe_3C catalyst crystals were preferentially oriented with either their [100] or [101] direction parallel to the nanotube axis. In contrast, other studies highlighted the importance of the initial graphitic seed that forms on the metal in facilitating nanotube growth [23, 24]. For example, Marchand et al. used field emission microscopy to observe the incremental axial rotation of SWCNTs during growth from nickel nanoparticles [25], and concluded that this rotation was evidence for growth via a screw-dislocation mechanism one carbon dimer at a time, as proposed by Ding et al. [26] In this latter case, metal nanoparticles only serve to produce the initial graphene seed layers and to catalytically decompose the hydrocarbon gas source rather than acting as a nanometer-sized substrate for

epitaxial growth. Herein, we use (S)TEM imaging and diffraction techniques to examine the structure, shape, and orientation of more than twenty Fe_3C catalyst crystals found inside the base of MWCNTs and show that CNTs of similar structure and size grow from catalyst crystals that are in no particular preferred orientation.

5.2 Experimental

5.2.a Catalyst Nanoparticle Deposition

The iron catalyst was deposited as a 10 nm thick film on native-oxide coated silicon substrates using electron-beam evaporation. Substrates were placed on a resistively-heated substrate platen located 25 cm below the planar transformer-coupled plasma coil [27]. Before nanotube growth, the iron catalyst film was heated to 700 ^{o}C and exposed to an H_2:Ar (50:5 sccm) plasma maintained with 200 W RF power at 150 mTorr for 15 minutes to form nanometer-sized metal islands, and to reduce iron oxides present in the catalyst film.

5.2.b CNT Growth by PECVD

Carbon nanotubes were grown by PECVD from CH_4 and H_2 diluted in Ar. To grow nanotubes, the temperature was increased to 800 ^{o}C after pretreatment and a mixture of CH_4 and H_2 diluted in Ar was introduced into the chamber. A gas mixture of H_2:CH_4:Ar (5:5:68 sccm) was used during this growth step, and was chosen based on a previous study [37] where we found that addition of a small amount of hydrogen to a methane plasma was necessary to grow well-graphitized straight CNTs with a narrow diameter distribution. These conditions are also typical of many growth protocols that have been reported in the literature [7].

5.2.c Electron Microscopy

Characterization of individual CNTs and catalysts, including high-resolution bright field (BF) and high-angle annular dark field (HAADF), (S)TEM imaging, electron diffraction (CBED and SAED), energy-dispersive x-ray spectroscopy (EDXS), and electron energy-loss spectroscopy

(EELS) was conducted using an FEI Tecnai F-30 (S)TEM with a Schottky field-emission electron gun operated at 300 keV and equipped with a Gatan Enfina spectrometer attached to the bottom of the TEM column. Cross-section TEM samples were made by a standard wedge-polishing technique. For the remainder of the microscopy work, nanotubes were removed from the Si/SiO_2 substrates by sonication in ethanol for 30 seconds, and then transferred to copper TEM grids coated with a lacey carbon support film.

5.3 Results and Discussion

5.3.a Evolution of Structure and Morphology During CNT Growth

Multiwall carbon nanotubes were grown using a radio-frequency (13.56 MHz) inductively-coupled plasma and iron catalyst through PECVD. Using SEM and TEM, we examined the structure and morphology of the catalysts at each point throughout the carbon nanotube growth process. Figure 5-1 (a) and (b) show low- and high- magnification SEM images of the iron catalyst particles on silicon after pretreatment of the iron film by exposing it to an H_2/Ar plasma. This pretreatment efficiently breaks apart the continuous 10 nm thick film to form nanometer-sized metal islands. A range of metal island sizes was observed, from approximately 10 nm to larger than 100 nm. Although not as evident in the SEM images, the cross-sectional TEM images of the pretreated film [see Figure 5-1(c)] clearly show that these metal islands are highly faceted BCC iron crystals. TEM and electron diffraction of these crystals show that they are body-centered cubic (BCC) [28].

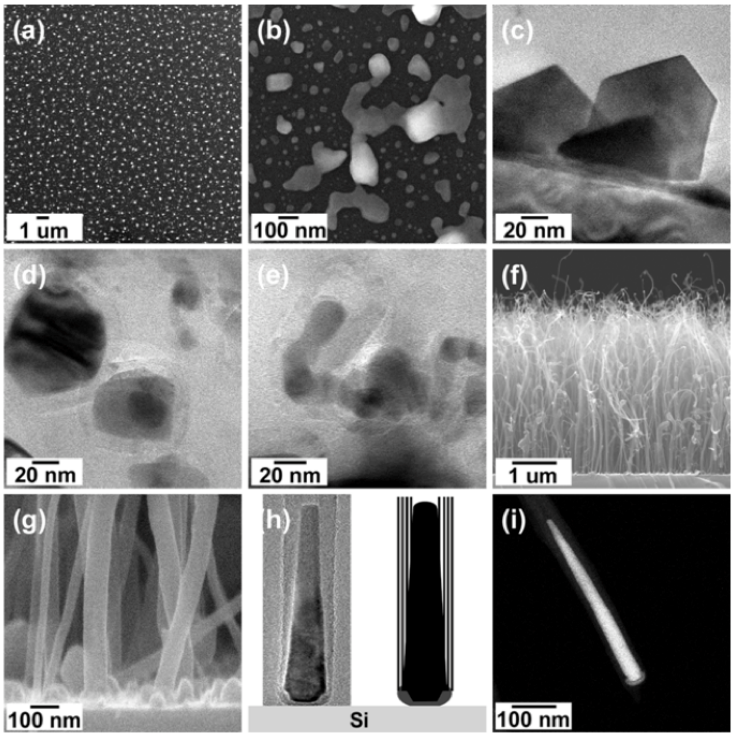

Figure 5-1. (a) An SEM image of the iron catalyst film that was broken up into small nanometer-sized islands during the hydrogen plasma pretreatment. (b) A magnified view of the faceted iron catalyst islands. (c) Cross-section TEM image of the iron catalyst after pretreatment reveals the faceted nature of the catalyst crystals. (d) Cross-section TEM image of the catalyst film after 5 minutes of methane plasma exposure (growth conditions) shows deformed catalysts surrounded by ~5 nm thick layer of graphene walls. (e) Cross-section TEM image of an elongated crystal found inside a growing nanotube. (f) Cross-section SEM image of the ~4 micron thick CNT film after 30 minutes of growth. (g) A magnified view showing the CNT attachment to the substrate as well as catalysts that did not produce CNTs. (h) BF TEM image (left) of a similar crystal next to a schematic showing pictorially how catalyst crystals remain at the base of the CNT, attached to the substrate. (i) HAADF image of a representative Fe3C catalyst found inside the base of a MWCNT.

After 5 minutes of H_2/CH_4 plasma exposure, cross-sectional TEM images revealed visible changes to the catalyst crystal shapes and structures [see Figure 5-1 (d) and (e)]. Through CBED analysis, we found that the initially BCC iron crystals had been transformed into an Fe_3C (cementite) crystal phase (orthorhombic space group Pnma no. 62, a = 0.5008 nm, b = 0.4465 nm, c = 0.6725 nm) [19]. All catalyst crystals by this point were covered with graphene walls approximately ~5 nm thick, as shown in Figure 5-1 (d) and (e). Catalyst crystals no longer

exhibited faceting, and either appeared slightly spherical or deformed from their well-faceted shapes when they were BCC iron. Sun et al. [29] showed that CNTs and carbon onions can exert internal pressures up to ~40 GPa, which can cause metal nanocrystals located inside these structures to deform. Such pressures are well above the yield strength of bulk Fe (~140 MPa) and the deformation can be a direct consequence of the enormous pressures that are exerted by the encapsulating graphene walls. The order of catalyst deformation, transformation to Fe_3C and graphene wall formation is unknown but the catalysts seemed to lose their facets always after graphene layers had formed around them. Regardless of the order, these events formed the initial seed for the subsequent CNT growth. In fact, some of the catalyst crystals appeared elongated and were found inside short nanotubes, in the very beginning stages of growth. At this initial stage of growth, the nanotubes were typically short (~100-150 nm) and highly deformed, exhibiting severe curves or kinks as shown in Figure 5-1(f).

CNTs grew from the Fe_3C catalyst crystals to a length of about 4 μm during plasma exposure for an additional 25 minutes [see Figure 5-1(f)]. The majority of CNTs have an average diameter of 29 ± 5 nm, as measured from BF TEM images, however, larger tubes ~80 nm in diameter that grew from catalyst nanoparticles of different morphologies were also present. As is evident from these SEM images, the straightness of each nanotube varies along its length. Typically, the tips of CNTs are curled and usually contain large chunks of the catalyst. This curled- and kinked-tip morphology resembles the morphology of the short nanotubes observed during the initial stages of growth [see Figure 5-1(f)]. This morphology would be expected as CNTs grew longer and this initially-deformed section was pushed upwards. Towards the base, nanotubes straighten out considerably, as evident in the cross-section SEM image of Figure 5-1(g). Thus, the CNT growth seems to settle into a steady growth process after the deformation and break-up of the initial catalyst particle. This process leaves the tip curled and kinked. Additionally, many catalyst particles did not produce tubes, as is evident by the numerous spherical-shaped graphene-covered catalyst particles in the SEM image shown in Figure 5-1(h). In these cases, we presume that the process that brings additional C atoms to add to the CNT had stopped. Catalyst particles that are completely enclosed in CNTs do not participate in CNT growth. Based on this observation we conclude that graphene walls form a

diffusion barrier around these catalyst particles and prevent the gas-phase precursor from interacting with the catalyst particle. In contrast, we always observe, on nanoparticles that lead to CNT growth, a section that is free of graphene walls to allow carbon precursor access to the nanoparticle.

Catalyst particles that produced well-graphitized CNTs remained attached to the substrate. In general, CNTs grew via a base-growth mode, whereby the catalyst remained attached to the substrate [7]. Our BF-TEM and ADF-STEM images (Figure 5-1 (h) and (i)) revealed that the Fe_3C catalysts located inside CNT bases exhibited an elongated tear-drop shape with a constant smooth taper and lengths typically greater than 150-200 nm. Despite a wide distribution of initial catalyst nanoparticle sizes, diameters were very consistent and produced CNTs with a narrow diameter distribution (29 ± 5 nm). These tear-drop shaped catalyst particles, although single crystalline, have combinations of small angle (~1-3 degree) misorientations along their axial lengths [19]. The catalyst edges oriented approximately parallel to the axis of the CNT appeared very smooth, while the bases exhibited clear faceting, which is consistent with observations by Begtrup et al. who found that Fe catalysts inside CNTs exhibited facets only on the end surfaces exposed to the carbon source [15]. The opposite end of the catalyst usually appeared rounded, and often was covered with a layer of graphene. Previous *in situ* microscopy studies have correlated spherical catalyst shape with formation of hemispherical graphene domes during CNT growth [16]. Interior graphene cups observed at various locations along the length of most nanotubes were formed on this rounded end of the catalyst [28].

Closer examination of the base region of the catalysts, where they were attached to the substrate, revealed that Fe_3C is capped by a ~5 nm thick layer of iron oxide (Fe_xO_y) as determined from EDX and EELS analysis [see Figure 5-2 (c) and (d)]. Figure 5-2 (a) and (b) show BF-HRTEM and HAADF-STEM images of this oxide cap, respectively. The oxide was observed on all catalysts, and existed in both crystalline and amorphous forms. The HAADF-STEM image of Figure 5-2(b), where the intensity is proportional to $Z^{1.7}$ (Z is the average atomic number) [29] clearly shows the different components of the base region. Thin layers of iron oxide were observed by Blank et al. on iron carbide catalyst crystals located at the tips of CNFs grown by disproportionation of CO [30]. However, a study by Heresanu et al. showed

that iron oxides can also form during the cooling step, after CNT growth [31]. In our case, we believe that the oxide is present during the entire growth as a result of oxides not being completely reduced during the pretreatment step, or by interaction of the catalyst with the native oxide. The amorphous nature of many of the oxides, as well as the carbon concentration found to exist in the oxide as measured with EELS support this conclusion.

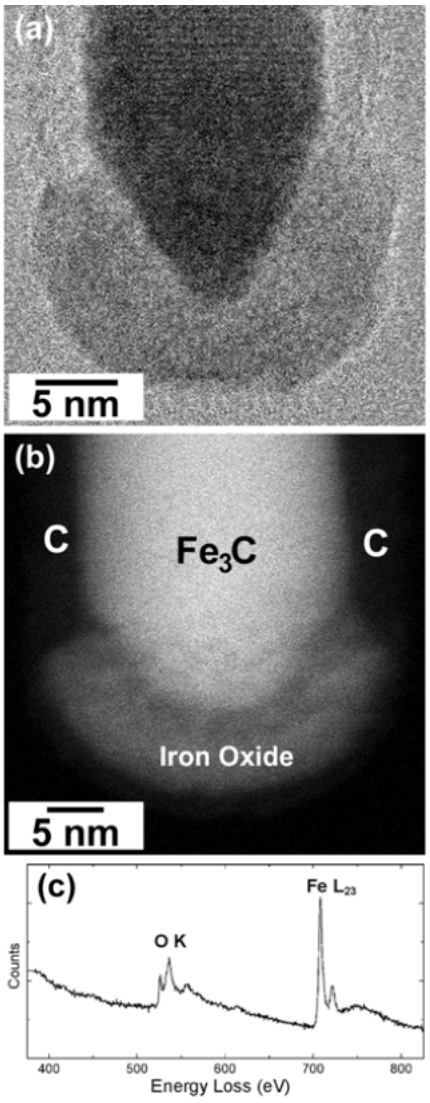

Figure 5-2. High-resolution (a) BF-TEM and (b) HAADF images of the base region of two similar catalyst crystals. Both Fe_3C catalysts exhibit clear faceting and are capped by a thin layer of iron oxide. CNT walls do not extend all the way to the base, but instead terminate at

the iron oxide. (c) EEL and (d) EDX spectra obtained from the catalyst shown in the HAADF image of b confirm that the cap at the catalyst base contains iron, oxygen, and carbon

5.3.b Initial stages of CNT growth

Next, we examined the early stages of CNT growth to understand how the catalyst morphology changes with the growing nanotube. Figure 5-3 shows BF-TEM images of Fe_3C catalysts at different stages of CNT growth. Previous *in situ* TEM studies have captured the dynamics of carbon cap formation on Fe_3C catalyst crystals and subsequent cap lift-off from the catalyst during the initial stages of CNT growth [14]. We found that, once a tubular carbon structure formed, the catalyst became severely elongated during growth. For example, Figure 5-3(a) shows a BF-TEM image of a catalyst shortly after the tubular structure of a CNT had formed. It has been elongated in the direction of tube growth and consists of adjacent sections that are of different sizes and orientations. The surrounding graphene walls follow the contours of the catalyst, and thus exhibit significant amounts of strain and many kinked sections. This structure reinforces the earlier observation that the curling and bending of the nanotubes, as observed in SEMs, like in Figure 5-1(f), is associated with catalyst deformation and break-up. Figure 5-3(b) shows a catalyst inside the base of a CNT that was slightly further along in its growth, as evident by the catalyst's increased elongation. The general shape of the catalyst near the base looks similar to the elongated tear-drop shape of catalysts observed in CNTs grown for 30 minutes. Large chunks of catalyst are visible inside and farther up the CNT; as more carbon is added from the gas phase, these sections move upwards with the growing nanotube. Stresses exerted by the growing nanotube deform the catalyst during growth. Some regions, as indicated by the arrow in Figure 5-3(b) experience necking, i.e., plastic deformation as a result of these stresses, which eventually causes the top section of the catalyst to break away from its base. Necking suggests that the catalyst particles experience tensile stresses exerted in the direction parallel to the CNT axis as a result of CNT growth. Figure 5-3(c) shows a small section of Fe_3C catalyst that was separated through this process. Continued addition of carbon at the very base of the nanotube after separation caused this small section to move upwards approximately 40 nm with the growing nanotube. CBED patterns recorded from this small section and the base revealed that the orientation of the small section was the same as the larger catalyst from which

it separated. This process may repeat itself many times as the nanotube grows; the resulting nanotube thus contains numerous Fe_3C catalyst crystals of various lengths from ~10 nm to >100 nm along its length. Figure 5-3(d) shows a BF-TEM image of an entire nanotube oriented such that the base of the nanotube is at the bottom of the image. Once detached from the parent catalyst, which remains attached to the substrate, the smaller catalysts inside the growing nanotube no longer participate in the CNT growth process, i.e., they no longer produce graphene layers. We conclude that these catalyst particles do not have access to the carbon source; CNT walls stop the carbon precursor diffusion. Typically, the largest chunks of catalyst are separated from the base catalyst during the initial stages of growth, and thus remain at the CNT tip [see Figure 5-3(d)]. Because the graphene layers follow the contour of these crystals, the CNT tip usually exhibits many kinks and curves which are not present throughout the rest of the relatively straight CNT, as seen in earlier SEM images [see Figure 5-1(f)].

We conclude that our catalysts remain solid and crystalline during growth, based on previous *in situ* observations of CNT growth from crystalline Fe_3C catalysts [12, 14] as well as on molecular dynamics simulations of the size-dependent melting behavior of Fe-C particles [32] that indicate catalysts are only completely molten at temperatures above 1200 ^{o}C. Yet, we observe that catalysts undergo severe deformations and break apart. As shown in Figure 5-3, Fe_3C catalyst crystals start to elongate once a tubular CNT structure has formed. At the growth temperature of 800 ^{o}C, the thermal expansion coefficient of Fe_3C (4.1×10^{-5} K^{-1}) [33] is approximately one order of magnitude larger than the thermal expansion coefficient of the surrounding CNT (3×10^{-6} K^{-1}) [34]. Additionally, the surrounding CNT walls exert significant internal pressures on the catalysts, ranging from ~20 GPa for single wall to more than 40 GPa for 6 or more walls [35]. These internal pressures are well above the estimated tensile and compression strengths of ~5 GPa for Fe_3C [36]. The combination of these two effects constrains the catalyst along the CNT axis, elongating the catalyst. The most severe distortions, including neck formation, occur at locations where the number of encapsulating CNT wall is large, i.e., locations experiencing the highest internal pressures.

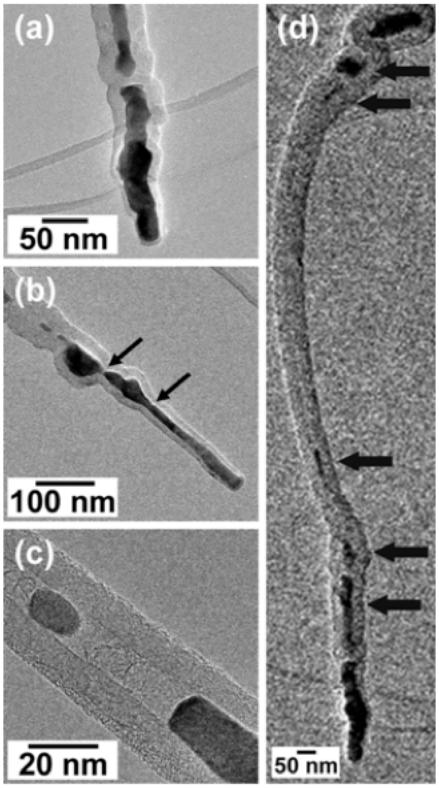

Figure 5-3. BF-TEM images of catalysts at early stages of CNT growth. (a) A catalyst at the base of a CNT beginning to elongate during the early stages of CNT growth. Adjacent sections of the catalyst are different sizes and are at different orientations. (b) A catalyst observed slightly further along in growth as evident by the more elongated shape. The arrow indicates a point of neck formation, where further growth would cause the catalyst to break in two. (c) A small portion of catalyst that had separated from the base catalyst through this necking process. CBED revealed that the orientation of the two pieces relative to the incident electron beam were identical. (d) An entire nanotube labeled with arrows that show small pieces of catalyst at various points along its length. The majority of catalyst that separates from the base occurs during early stages of growth, and therefore appears at the CNT tip.

5.3.c Catalyst Orientation With Respect to the CNT Axis

We determined the orientations of Fe_3C nanocrystals with respect to the CNT growth direction and examined whether there is a preferred orientation between the CNT and the catalyst crystallographic orientation. An unambiguous way to determine the orientation of an Fe_3C crystal located inside a CNT is by searching for and identifying two crystallographic directions of the crystal, each perpendicular to the CNT walls. A double-tilt holder within the TEM

enabled tilting of the crystal to multiple zone axes and facilitated this search. The cross product of these two directions yields the catalyst's crystallographic direction that lies along the axis of the CNT. Two SAED patterns used to determine the orientation of a catalyst inside the base of a CNT are shown as an example in Figure 5-4. In this particular case, the Fe_3C catalyst crystal was tilted to two different zone axes, [001] and [102]. The Fe_3C crystal at each orientation is shown in the BF-TEM images of Figure 5-4. A SAED pattern was recorded at each zone axis such that diffraction from both the catalyst crystal and CNT walls were simultaneously visible. The reciprocal lattice vector, g_{002}, associated with the 002 diffraction spot of the surrounding CNT walls, is perpendicular to the nanotube axis, and is indicated on each pattern. The diffraction spots from the Fe_3C crystal at each orientation that are in line with the diffraction spots from the CNT walls are thus also perpendicular to the nanotube walls. Both diffraction spots are also circled in each SAED pattern. In this example, at the [001] zone axis, the [002] crystallographic direction is perpendicular to the CNT walls, while at the [100] zone axis, the $[40\bar{2}]$ crystallographic direction is perpendicular to the CNT walls. The cross product of these two directions, $[002] \times [40\bar{2}]$, gives the Fe_3C crystallographic direction that is parallel to the CNT axis, [010] in this example. More than 20 Fe_3C crystals located inside the base of CNTs were examined using this method. To our surprise, we did not find a consistent preferred catalyst orientation relative to the nanotube axis. Observed directions relative to the nanotube axis included [001], [031], [114], [010], [100]. Often, however, the CNT g_{002} vector appeared at a small angle (less than ~5^o) relative to Fe_3C diffraction spots at the zone axes visited, and thus a definitive orientation relationship between the catalyst and CNT axis was not even possible. This is only possible if the catalyst was oriented with a much higher-order plane parallel to the CNT axis, or if there was no orientational relationship. Our observed lack of correlation between the catalyst and CNT axis is in contrast to a previous study by Wen et al. who found that Fe_3C catalyst crystals were preferentially oriented with either their [100] or [101] direction parallel to the nanotube axis [21]. Their findings appear to be based on a single diffraction pattern for each catalyst, which is correct only if the nanotube axis is oriented perpendicular to the incident electron beam. It is unclear if this criterion was satisfied during their analysis. Moreover, many tubes need to be examined to draw statistically significant conclusions and to establish that the same catalyst orientations are observed multiple times. Observation of a

variety of relative CNT and catalyst orientations even within a modest sample of 20 CNTs is surprising and support the conclusion that catalysts with many different orientations with respect to the CNT axis can lead to growth.

Our observation that CNTs of similar structure and size grow from catalyst crystals that are in no particular orientation suggests that the initial CNT seed that forms on the catalyst nanocrystals is key to understanding and controlling CNT growth. It appears that what is necessary for CNT growth is simply a spherical or hemispherical graphene seed on a catalyst, a source of decomposed carbon, and a location where the graphene walls are attached to the catalyst for the C atoms to add. Well-faceted catalyst nanoparticles deform into more rounded shapes as graphene layers form on their surfaces and act as the seeds from which the CNTs begin to grow. If the graphene walls form a nearly perfect and continuous layer on a nanoparticle, access to the carbon source is blocked and the catalyst does not lead to CNT growth. The lack of catalyst orientation suggests that either the initial cylindrical or hemispherical graphene seed can be formed on a variety of Fe_3C crystalline faces, or the catalyst changes its relative orientation after a graphene seed is formed from specific faces. It does not appear that the graphene nanotube walls are necessarily produced in an epitaxial process directly from Fe_3C faces.

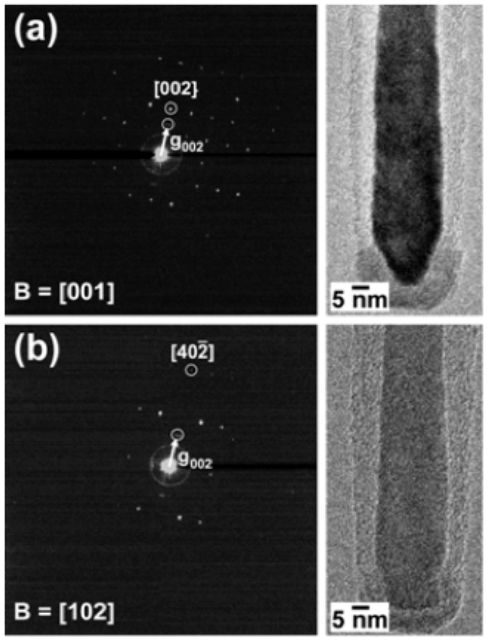

Figure 5-4. An example illustrating the method used for determining the catalyst orientation relative to CNT axis. First, SAED patterns were obtained from an individual Fe_3C catalyst crystal at two different zone axes, in this example (a) [001] and (b) [102]. BF-TEM images of the same crystal at each orientation are also shown. Two diffraction spots from the surrounding CNT walls are also present in each pattern; one of these spots in each pattern is circled and denoted by its reciprocal lattice vector, g_{002}. This vector, by definition, is perpendicular to the nanotube axis. The Fe_3C crystallographic direction corresponding to the diffraction spot that is in line with this g_{002} vector is circled and labeled in each pattern, and is thus also perpendicular to the nanotube axis ([002] and $[40\bar{2}]$). The cross product between these two directions yields the orientation of the catalyst along the nanotube axis, [010].

5.4 Conclusions

The growth of CNTs from iron-based catalyst crystals by PECVD was examined *ex situ* with (S)TEM and SEM imaging, EDX and EELS spectroscopy, and diffraction techniques. Although the catalyst film was deposited as BCC iron, CNTs grew during CH_4/H_2 plasma exposure from Fe_3C catalyst crystals. The Fe_3C crystals were located inside the CNT base, and remained attached to the substrate. By examining the orientations and structures of the catalysts with TEM at early stages of growth, we determined that the catalyst deforms and breaks apart to yield catalyst particles at the tip and along the length of a CNT. The elongated tear-drop shaped

Fe_3C catalyst crystals attached to the substrate, from which the CNTs grew, were found to exist in a variety of different orientations relative to the CNT axis. Despite this, the resulting CNT structures were very similar, and of high quality. This suggests that CNTs do not grow via epitaxy on the catalyst particles.

5.5 References

[1] Baughman, R. H.; Zakhidov, A. A.; de Heer, W. A., Carbon nanotubes – the route towards applications. *Science* **2002**, *297*, (5582), 787-792.

[2] Dresselhaus, M. S.; Dresselhaus, G.; Charlier, J. C.; Hernandez, E., Electronic, mechanical and thermal properties of carbon nanotubes. *Philos. T. Roy. Soc. A* **2004**, *362*, 2065-2098.

[3] Melechko, A. V.; Merkulov, V. I.; McKnight, T. E.; Guillorn, M. A.; Klein, K. L.; Lowndes, D. H.; Simpson, M. L., Vertically alligned carbon nanofibres and related structures: controlled synthesis and directed assembly. *J. Appl. Phys.* **2005**, *97*, 041301.

[4] Tans, S. J.; Verschueren, A. R. M.; Dekker, C., Room temperature transistor based on a single carbon nanotube. *Nature* **1998**, *393*, 49-52.

[5] Trojanowicz, M., Analytical applications of carbon nanotubes: a review. *Trac-Trend. Anal. Chem.* **2006**, *25*, 480-489.

[6] Merkoci, A.; Pumera, M.; Llopis, X.; Perez, B.; del Valle, M.; Alegret, S., New materials for electrochemical sensing VI: carbon nanotubes. *Trac-Trend. Anal. Chem.* **2005,** *24*, 826-838.

[7] Meyyappan, M., A review of plasma enhanced chemical vapour deposition of carbon nanotubes. *J. Phys. D Appl. Phys.* **2009**, *42*, 213001.

[8] Barone, P. W.; Baik, S.; Heller, D. A.; Strano, M. S., Near-infrared optical sensors based on single-walled carbon nanotubes. *Nat. Mater.* **2005**, *4*, 86-U16.

[9] Granqvist, C. G., Transparent conductors as solar energy materials: a panoramic review. *Sol. Energ. Mat. Sol. C.* **2007**, *91*, 1529-1598.

[10] Landi, B. J.; Raffaelle, R. P.; Castro, S. L.; Bailey, S. G., Single wall carbon nanotube polymer solar cells. *Prog. Photovoltaics* **2005**, *13*, 165-172.

[11] Ren, Z. F.; Huang, Z. P.; Xu, J. W.; Wang, J. H.; Bush, P.; Siegal, M. P.; Provencio, P. N., Synthesis of large arrays of well-alligned carbon nanotubes on glass. *Science* **1998**, *282*, 1105-1107.

[12] Sharma, R.; Moore, E.; Rez, P.; Treacy, M. M. J., Site specific fabrication of Fe particles for carbon nanotube growth. *Nano Lett.* **2009,** *9*, 689-694.

[13] Hofmann, S.; Sharma, R.; Ducati, C.; Du, G.; Mattevi, C.; Cepek, C.; Cantoro, M.; Pisana, S.; Parvez, A.; Cervantes-Sodi, F.; Ferrari, A. C.; Dunin-Borkowski, R.; Lizzit, S.; Petaccia, L.; Goldoni, A.; Robertson, J., In situ observation of catalyst dynamics during surface-bound carbon nanotube nucleation. *Nano Lett.* **2007**, *7*, 602-608.

[14] Yoshida, H.; Takeda, S.; Uchiyama, T.; Kohno, H.; Homma, Y., Atomic scale in situ observation of carbon nanotube growth from solid state iron carbide nanoparticles. *Nano Lett.* **2008**, *8*, 2082-2086.

[15] Begtrup, G. E.; Gannett, W.; Meyer, J. C.; Yuzvinsky, T. D.; Ertekin, E.; Grossman, J. C.; Zettl, A., Facets of nanotube synthesis: high resolution transmission electron microscopy study and density functional theory calculations. *Phys. Rev. B* **2009**, *79*, 205409.

[16] Rodriguez-Manzo, J. A.; Terrones, M.; Terrones, H.; Kroto, H. W.; Sun, L. T.; Banhart, F., In situ nucleation of carbon nanotubes by the injection of carbon atoms into metal particles. *Nat. Nanotech.* **2007**, *2*, 307-311.

[17] Helveg, S.; Lopez-Cartes, C.; Sehested, J.; Hansen, P. L.; Clausen, B. S.; Rostrup-Nielsen, J. R.; Abild-Pedersen, F.; Norskov, J. K., Atomic scale imaging of carbon nanofibre growth. *Nature* **2004**, *427*, 426-429.

[18] Schaper, A. K.; Hou, H. Q.; Greiner, A.; Phillipp, F., The role of iron carbide in multiwalled carbon nanotube growth. *J. Catal.* **2004**, *222*, 250-254.

[19] Behr, M. J.; Mkhoyan, K. A.; Aydil, E. S., Catalyst rotation, twisting, and bending during multiwall carbon nanotube growth. **2010,** in review.

[20] Jiang, D. E.; Carter, E. A., Carbon atom adsorption on and diffusion into Fe(110) and Fe(100) from first principles. *Phys. Rev. B* **2005,** *71*, 6.

[21] Wen, C. Y.; Huang, C. C.; Cheng, H. Z.; Lu, H. Y., Orientation relations between carbon nanotubes grown by chemical vapour deposition and residual iron-containing catalysts. *J. Mater. Sci.* **2008**, *43*, 123-131.

[22] Golberg, D.; Mitome, M.; Muller, C.; Tang, C.; Leonhardt, A.; Bando, Y., Atomic structures of iron-based single-crystalline nanowires crystallized inside multi-walled carbon nanotubes as revealed by analytical electron microscopy. *Acta Mater.* **2006**, *54*, 2567-2576.

[23] Yao, Y. G.; Feng, C. Q.; Zhang, J.; Liu, Z. F., "Cloning" of single-walled carbon nanotubes via open-end growth mechanism. *Nano Lett.* **2009,** *9*, 1673-1677.

[24] Smalley, R. E.; Li, Y. B.; Moore, V. C.; Price, B. K.; Colorado, R.; Schmidt, H. K.; Hauge, R. H.; Barron, A. R.; Tour, J. M., Single wall carbon nanotube amplification: en route to a type-specific growth mechanism. *J. Am. Chem. Soc.* **2006**, *128*, 15824-15829.

[25] Marchand, M.; Journet, C.; Guillot, D.; Benoit, J. M.; Yakobson, B. I.; Purcell, S. T., Growing a carbon nanotube atom by atom: "And Yet It Does Turn". *Nano Lett.* **2009**, *9*, 2961-2966.

[26] Ding, F.; Harutyunyan, A. R.; Yakobson, B. I., Dislocation theory of chirality-controlled nanotube growth. *P. Natl. Acad. Sci. USA* **2009**, *106*, 2506-2509.

[27] Behr, M. J.; Gaulding, E. A.; Mkhoyan, K. A.; Aydil, E. S., Effect of hydrogen on catalyst in carbon nanotube growth. **2010**, in review.

[28] Sun, L.; Rodriguez-Manzo, J. A.; Banhart, F., Elastic deformation of nanometer-sized metal crystals in graphitic shells. *Appl. Phys. Lett.* **2006,** *89*, 263104.

[29] Nellist, P. D.; Pennycook, S. J., The principles and interpretation of annular dark-field z-contrast imaging. *Adv. Imag. Electr. Phys.* **2000**, *113*, 147-203.

[30] Blank, V. D.; Kulnitskiy, B. A.; Batov, D. V.; Bangert, U.; Gutierrez-Sosa, A.; Harvey, A. J., Electron microscopy and electron energy loss spectroscopy studies of carbon fiber formation at Fe catalysts. *J. Appl. Phys.* **2002,** *91*, 1657-1660.

[31] Heresanu, V.; Castro, C.; Cambedouzou, J.; Pinault, M.; Stephan, O.; Reynaud, C.; Mayne-L'Hermite, M.; Launois, P., Nature of the catalyst particles in CCVD synthesis of multiwalled carbon nanotubes revealed by the cooling step study. *J. Phys. Chem. C* **2008,** *112*, 7371-7378.

[32] Ding, F.; Bolton, K.; Rosen, A., Iron-carbide cluster thermal dynamics for catalyzed carbon nanotube growth. *J. Vac. Sci. Technol. A* **2004**, 22, 1471-1476.

[33] Wood, I. G.; Vocadlo, L.; Knight, K. S.; Dobson, D. P.; Marshall, W. G.; Price, G. D.; Brodholt, J., Thermal expansion and crystal structure of cementite, Fe_3C, between 4 and 600 K determined by time-of-flight neutron powder diffraction. *J. Appl. Crystallogr.* **2004**, *37*, 82-90.

[34] Li, C. Y.; Chou, T. W., Axial and radial thermal expansions of single-walled carbon nanotubes. *Phys. Rev. B* **2005**, *71*, 235414.

[35] Sun, L.; Banhart, F.; Krasheninnikov, A. V.; Rodriguez-Manzo, J. A.; Terrones, M.; Ajayan, P. M., Carbon nanotubes as high-pressure cylinders and nanoextruders. *Science* **2006,** *312*, 1199-1202.

[36] Tomota, Y.; Lukás, P.; Neov, D.; Harjo, S.; Abe, Y. R., In situ neutron diffraction during tensile deformation of a ferrite-cementite steel. *Acta Mater.* **2003**, *51*, 805-817.

[37] Agarwal, S.; Takano, A.; van de Sanden, M. C. M.; Maroudas, D.; Aydil, E. S., Abstraction of atomic hydrogen by atomic deuterium from an amorphous hydrogenated silicon surface. *J. Chem. Phys.* **2002,** *117*, 10805-10816.

6 A High-Resolution Electron Energy-Loss Spectroscopy Study of the Catalyst Particle During Plasma-Enhanced Chemical Vapor Deposition of Carbon Nanotubes

Plasma enhanced chemical vapor deposition is widely used for growing carbon nanotubes from methane and a metal nanoparticle, which acts as a seed and a catalyst. To provide insight into the chemical and diffusion processes occurring in the vicinity of the catalyst, the catalyst nanoparticle and the catalyst-carbon nanotube interface were examined with high-resolution electron energy-loss spectroscopy (EELS) in a scanning transmission electron microscope (STEM) with a 1.5 Å diameter electron probe. We find that the CNT walls emanate from a chemically complex catalyst nanoparticle consisting of iron carbide capped with a thin amorphous carbon and iron oxide layer at its base. Atomic-scale EELS measurements at the catalyst surface in locations of CNT wall formation revealed no change in the iron L_{23} edge compared to the bulk of the catalyst, indicating that Fe_3C does not decompose to BCC iron and graphite during CNT wall formation in a process similar to "metal dusting," as has been suggested previously. Instead, we found a very thin layer of amorphous carbon at the interface between the iron oxide cap and the Fe_3C catalyst particle and this layer is thought to provide the carbon source for CNT growth. Carbon concentration and amount of amorphous carbon is highest at the triple junction formed by the Fe_3C, iron oxide and the CNT walls. The distribution of carbon throughout the base of catalyst crystals reveals that carbon from the gas phase decomposes on Fe_3C, near this triple junction and where the CNT walls terminate at the catalyst base.

6.1 Introduction

A wide-range of potential carbon nanotube (CNT) applications that utilize their unique electronic and optical properties, such as sensors, transistors and nanocircuits, and energy

conversion devices rely on precise control of the CNT structure. This high level of structural control has not yet been achieved [1-10]. Growth methods such as plasma-enhanced chemical vapor deposition (PECVD) that use hydrocarbon gas mixtures with iron, cobalt, or nickel nanoparticles enable large-scale growth and controlled spatial placement of carbon nanotubes on a substrate [3, 7, 11]. While empirical trial-and-error process development has led to practical progress in producing carbon nanotubes by PECVD, the fundamental chemical and diffusion processes occurring at the metal catalyst that lead to the formation of graphene nanotube walls has remained speculative.

Considering iron-based catalysts only, CNTs have been reported to grow from metallic iron in both BCC and FCC phases, as well as from the iron-carbide phase (Fe_3C) that forms in situ when Fe nanoparticles are exposed to carbon during growth [12-22]. That CNTs are frequently found to grow from Fe_3C crystals is in contrast to an earlier report which suggested that Fe_3C is catalytically inactive [23]. It has been speculated that Fe_3C plays only an intermediate role in the formation of graphene nanotube walls [22, 24]. A process similar to metal dusting [25], i.e., the disintegration of metal carbides to form a dust of metal particles and graphite which occur in carburizing environments at moderate to high temperatures, has been proposed as a possible mechanism for CNT growth [12, 13, 26]. In this mechanism, the surface of the Fe_3C catalyst crystals would decompose into Fe metal and graphite to produce the CNT graphene walls [12, 13, 26]. If this is the case, a thin layer of Fe metal is expected to exist at the interface between the Fe_3C catalyst and the CNT walls.

Hydrocarbon molecules and radicals from the gas phase decompose on the catalyst surface and provide the source of carbon atoms which diffuse and add to the base of the growing CNT walls. Isotopic substitution has been used to show that carbon incorporation occurs at the end that contains the catalyst [27]. However, the exact location where and how carbon incorporates into the growing nanotube remains unclear. Decomposition of carbon-containing species and subsequent graphene wall formation may occur on specific crystallographic faces [28]. however, we recently showed that Fe_3C catalyst crystals located inside the bases of CNTs did not exhibit a preferred orientation relative to the CNT axis, which suggests that these processes are not restricted to specific crystallographic faces [29]. A high energy barrier of 2.3 eV exists

for migration of carbon atoms through a graphene wall by site exchange, and an extremely high barrier of ~10 eV for carbon penetration through a hexagonal hole in the graphene wall [24, 30]. Thus, for a catalyst that remains attached to the substrate, as is the case during base growth, either carbon must diffuse through the substrate subsurface region to reach the base of the catalyst or the CNT walls must terminate above the substrate, leaving the sides of the catalyst exposed to the carbon-containing gas atmosphere. Once decomposed on the catalyst, carbon atoms must diffuse to the base of the growing CNT walls. Theoretical ab initio models and molecular dynamics simulations have predicted low energy barriers for carbon diffusion on the surface of Ni [31, 32] and Fe [32, 33] catalyst particles. Although some experimental observations of CNT growth supports that diffusion occurs on the catalyst surface [32, 34, 35], other observations indicate that diffusion might occur through the bulk of iron-based catalysts [15, 24, 36].

Electron energy-loss spectroscopy (EELS) with high spatial resolution is well suited for exploring the atomic-scale changes in bonding and carbon concentration at the catalyst-CNT interface. Here, we use EELS with atomic scale resolution to map the chemical variations near the catalyst-CNT interface and discuss the implications of our observations on the active state of the catalyst, the location of carbon decomposition, and carbon diffusion mechanisms. EELS is especially well-suited for these investigations because of its sensitivity to atomic bonding [37]. Specifically, changes in Fe valence, as well as differentiation between crystalline and amorphous carbons could be determined using EELS [37-40]. Moreover, the use of the STEM enabled formation of an extremely small electron probe, 1.5 Å in diameter, which allowed us to measure chemical composition and bonding in single atomic layers.

6.2 Experimental

Multiwall carbon nanotubes (MWCNTs) were grown using a radio-frequency (RF at 13.56 MHz) inductively-coupled plasma and iron catalyst through PECVD. The iron catalyst was deposited as a 10 nm thick film on native-oxide-coated silicon substrates using electron-beam evaporation. Substrates were placed on a resistively-heated substrate platen located 25 cm below the planar transformer-coupled plasma coil. Before nanotube growth, the iron catalyst

film was heated to 700 ^{o}C and exposed, for 15 minutes, to H_2:Ar (50:5 sccm) plasma maintained with 200 W RF power at 150 mTorr, This H_2-plasma exposure converts the iron film to nanometer-size metal islands, and is supposed to reduce iron oxides present in the catalyst film. MWCNTs were grown at 800 ^{o}C and 10 Torr for 30 minutes using a plasma maintained with 200 W RF power in a CH_4:H_2:Ar (5:5:68 sccm) gas mixture. Nanotubes were removed from the Si/SiO_2 substrates by sonication in ethanol for 30 seconds, and then transferred to copper TEM grids coated with a lacey carbon support film.

Characterization of individual CNTs and catalysts, including high-resolution BF and HAADF (Z-contrast) STEM imaging, and atomic-scale EELS, was conducted using an FEI Tecnai F-30 microscope with a Schottky field-emission electron gun operated at 300 keV. All samples were held under a heat lamp for approximately 1 hour before inserting them into the microscope. HAADF imaging was conducted using an annular detector, which did not interfere with the low-angle inelastic electron scattering used for EELS. EELS spectra were collected with a post-column Enfina spectrometer attached to the bottom of the microscope while operating the microscope in STEM mode. HAADF images were always captured before EELS acquisition to identify structural features of interest. Typically, EELS spectra were collected along line scans, in incremental steps, separated by approximately 0.6 nm. This ensured that fresh, undamaged material was probed with each measurement. HAADF images were automatically acquired every few (~2-5) steps to correct for sample drift. Acceptable levels of sample drift were only obtained after the sample had been in the microscope for ~4-5 hours. A 70 μm condenser aperture and 2 mm spectrometer entrance aperture yielded convergence and acceptance angles of 2.7 ° and 8.7 ° respectively, at a camera length of 80 mm. These values were kept constant throughout this entire study. For acquisition of the carbon K, oxygen K, and Fe L_{23} core-loss edges, 4-8 second acquisition times produced acceptable signal-to-noise ratios. Dispersions of 0.1-0.5 eV/channel were used, depending on whether a single core-loss edge or multiple core-loss edges were acquired in an energy-loss measurement. The energy resolution, measured as the full-width-at-half the maximum of the zero-loss peak was ~0.5 eV.

All EELS spectra were processed individually within Gatan Digital Micrograph and OriginLab software packages. The slowly-decreasing background present in all spectra, arising from

multiple inelastic scattering events, was subtracted from each core-loss edge by fitting the pre-edge background over a 60 eV wide window to an inverse power law function $I = AE^{-r}$, where r ranged from 2-5 [37]. Relative changes in carbon concentration through the Fe_3C catalysts were calculated by integrating carbon K-edges over a 30 eV window, aligned with the onset of the carbon K-edge, from background-subtracted spectra. Changes in sample thickness across the iron oxide and Fe_3C catalyst were corrected for by approximating their cross-section as circular, and thus a simple relationship between thickness and radius was obtained. This also enabled easy correction in cases where one material encapsulated another of interest. Changes in the iron oxidation state were monitored by comparing the intensity ratio of the Fe L_3 and L_2 white lines. Finally, to asses the levels of carbon contamination, HAADF images taken before and after EELS acquisitions were compared. No detectable amorphous carbon was found to build up as a result of the brief electron beam exposures used in this study.

6.3 Results and Discussion

The most abundant catalyst morphology observed inside the base of MWCNTs is shown in the HAADF images of Figure 6-1 (a) and (b). In a previous study, we determined that these catalysts are single crystal Fe_3C [19]. Fe_3C, or cementite, has an orthorhombic crystal structure, space group Pnma no. 62, a = 0.5008 nm, b = 0.4465 nm, c = 0.6725 nm. On average, the nanotubes that grew from these catalysts were vertically aligned, perpendicular to the substrate, and grew via a base-growth mode, whereby the catalyst remained attached to the silicon substrate, as shown schematically in Figure 6-1(e). Catalysts exhibited an elongated tear-drop shape with a constant smooth taper on faces oriented approximately parallel to the CNT axis. Catalyst diameters near the base were very consistent; these catalyst particles produced MWCNTs with an average outer diameter of 29 nm and a narrow diameter distribution (5 nm standard deviation). In a previous study, we found that although each catalyst was single crystalline, combinations of small angle (~1-3 degree) misorientations existed along their axial lengths [41]. Clear faceting was observed near the base of crystals.

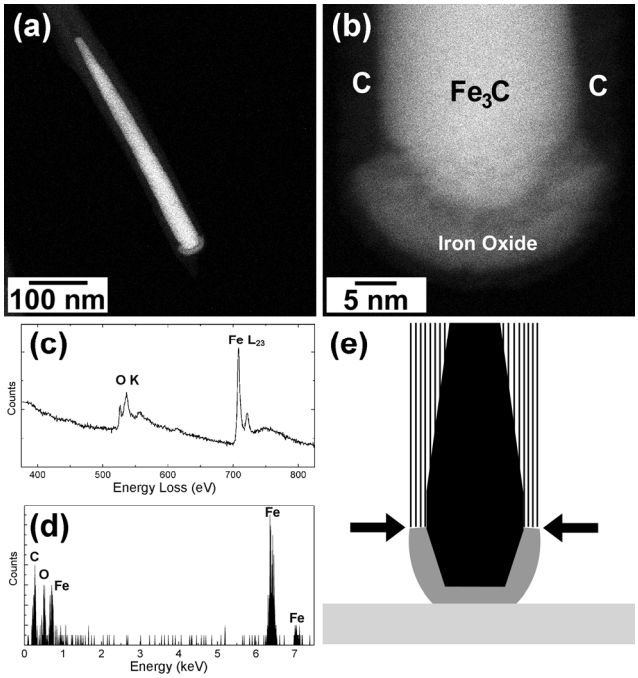

Figure 6-1. (a) HAADF image of an Fe_3C catalyst crystal located inside the base of a MWCNT. (b) Magnified HAADF image of the catalyst base reveals that Fe_3C is capped by a shell of iron oxide. (c) EELS spectrum of the iron oxide shell shows both oxygen and iron core-loss edges. (d) EDX spectrum of the iron oxide shell shows iron, oxygen, and carbon. (e) Schematic of the catalyst base region with arrows indicating the location where carbon from the gas phase enters into the catalyst.

EELS and EDX analysis, shown in Figure 6-1 (c) and (d), revealed that Fe_3C catalyst particles are capped by a layer of amorphous iron oxide, approximately 5 nm thick. The oxide either forms from iron interaction with the native oxide on the silicon substrate, or is already present in the initial iron film and is not completely reduced during the H_2-plasma pretreatment stage. Indeed, characterization of the iron catalyst film before growth, but after pretreatment does reveal substantial oxidation. This oxide cap can be seen clearly in the HAADF STEM images of in Figure 6-1 (a) and (b) as a darker region because the image intensity is proportional to $Z^{1.7}$, where Z is the atomic number, and iron oxide has a higher average Z than cementite [42]. CNT walls, barely visible in HAADF image, do not extend all the way to the base, but instead terminate at the iron oxide, ~12 nm above the base of the oxide. The opposite end of the catalyst, within the carbon nanotubes, usually appears rounded, and often is covered with a

layer of graphene. Interior graphene cups observed at various locations along the length of most nanotubes were formed on this rounded end of the catalyst [19].

The chemical composition, structure and morphology of the catalyst, especially around the base where the graphene walls are emanating from the particle contains clues on how and where C is incorporated into the growing nanotube. First, the Fe_3C catalyst particle is rounded at the top where it is covered by a thin layer of graphene but is faceted at the bottom where it makes an interface with the iron oxide cap. It is known that graphene walls can exert tremendous internal pressures that act to deform encapsulated metal nanoparticles [43]. Indeed, in a previous study we showed that during the initial stages of CNT nucleation the portions of the catalyst covered with graphene lose their facets while those surfaces not covered with graphene remain faceted [29]. Second, the carbon nanotube walls were found to terminate at the exact location where catalyst crystal faceting begins, at the edge of the iron oxide cap. The bottom portion of catalyst that was not surrounded by CNT walls did not experience the same high stresses during growth that the top portion did, and remain undeformed and faceted. Third, the observed faceting at the very bottom of the catalyst may indicate that this is the location where carbon-containing species from the gas phase were decomposed, consistent with Begtrup et al. who found that Fe catalysts inside CNTs exhibited facets only on the end which was exposed to a carbon supply [35]. Decomposed carbon at the catalyst facets would next have to diffuse on the surface or through the bulk of the catalyst to a location where it could add to the growing graphene CNT walls. While these structural observations suggest that the carbon is adding at the faceted interface between the iron oxide and the CNT walls, chemical composition of this region can give additional insights to form a more complete picture of this region. To examine this, we measured the variation in carbon concentration in this region of the catalyst using high resolution EELS collected with a 1.5 Å electron probe.

Figure 6-2 shows an ADF image of the base region of a catalyst crystal where carbon concentration was measured. Atomic-scale EELS measurements of the carbon K-edge were made at locations separated by 0.6 nm along each of the colored lines as indicated in the ADF image through both the Fe_3C catalyst and the iron oxide cap. CNT walls terminated at the iron oxide, above the location where the majority of our measurements were taken. Thus, the

measured carbon K-edge intensity was solely due to carbon contained on the surface or in the bulk of the Fe_3C catalyst or in the iron oxide cap, and not from the surrounding CNT walls. The first few measurements along the beginning of the black, red, and green lines did contain contributions from the surrounding CNT walls. However, in these cases, the additional carbon K-edge intensity due to the CNT walls was subtracted. Variation of the integrated carbon K-edge intensity as a function of position along each line is shown in three plots below the image in Figure 6-2. Carbon K-edge intensity was calculated by integrating over a 30 eV-wide window that was aligned with the carbon K-edge onset, after correcting for changes in catalyst thickness along each line, as described earlier. The shape of the carbon K-edge feature, shown in Figure 6-3, remained the same throughout the region examined, and thus the measured integrated intensity from different positions in the catalyst was a direct measure of the relative carbon concentration.

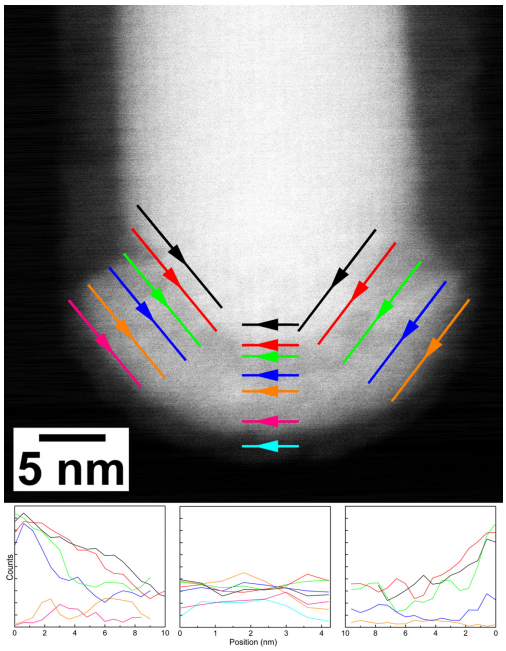

Figure 6-2. (a) High-resolution ADF image of the bottom of the Fe_3C catalyst and iron oxide shell. EELS spectra were obtained every 0.6 nm along each colored line, in the direction indicated. Relative carbon concentration, as calculated from the carbon K-edges are plotted below. Plot colors correspond to the colored lines in the ADF image.

Figure 6-2 shows significant variations in carbon concentration in both the iron oxide cap and the Fe_3C catalyst. The highest measured carbon concentrations were near the triple junction formed by Fe_3C, iron oxide, and the CNT walls. Carbon concentration was found to decrease significantly as the electron probe moved along any single line away from this triple interface, towards the bottom, in both the Fe_3C and the iron oxide. Careful comparison between adjacent line scans in all three panels reveals that the carbon concentration increases with radial position inward through the iron oxide cap, towards the Fe_3C catalyst. This increase is not gradual, but exhibits a jump in concentration at approximately 3 nm outside the faceted Fe_3C-oxide interface. Comparison between the blue and orange concentration profiles on the left side and between the green and blue profiles on the right side clearly shows this jump in carbon concentration. Additionally, careful examination of the HAADF image of Figure 6-3(a) reveals a ~2-3 nm thick region within the iron oxide adjacent to the interface with the Fe_3C that does not appear as bright as the rest of the iron oxide shell; this indicates that the average atomic number in this region is smaller compared to the rest of the bulk iron oxide shell, a sign of higher carbon concentration in this region. A decrease in HAADF image intensity in this region is consistent with the observed increase in carbon concentration detected with EELS measurements presented in Figure 6-2. Thus, it appears that this region, which begins at the triple junction formed by Fe_3C, iron oxide, and CNT walls and along the Fe_3C iron oxide faceted interface is carbon-rich. The Fe_3C-oxide interface is not sharp but diffuse and there is a 2-3 nm thick carbon rich transition region between the iron oxide and the Fe_3C.

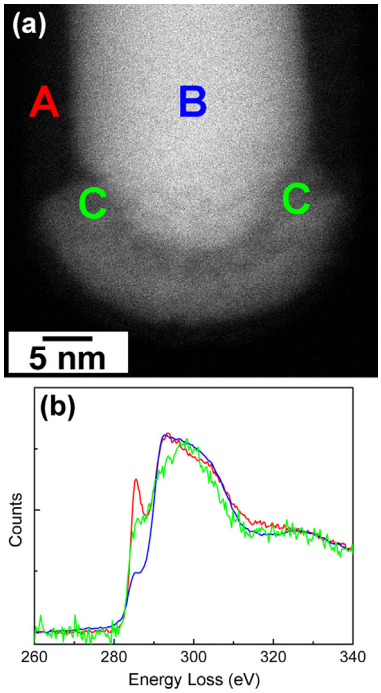

Figure 6-3. (a) High-resolution HAADF image exhibits decreased intensity in a carbon-rich region of the iron oxide near the triple interface of Fe_3C, iron oxide, and CNT walls. The carbon K-edge was measured at each position A, B, and C. (b) Comparison of the carbon K-edges from the three positions reveal that the carbon in the carbon-rich region is in an amorphous state.

From careful examination and comparison of carbon K-edge spectra measured at different locations in the catalyst, and the CNT walls, we determined that the carbon present in this carbon-rich region is in a disordered, amorphous state. A representative carbon K-edge EELS spectrum obtained from this carbon-rich region is shown in green in Figure 6-3(b). Carbon K-edge spectra measured from the crystalline CNT walls at two different locations are also shown for comparison. The intensities of all spectra were normalized. The red spectrum was obtained from position A, where CNT walls are oriented such the 0.34 nm wall spacing (edge plane) is parallel to the incident electron beam. The blue spectrum was obtained from position B, where CNT walls are oriented such that the 0.34 nm wall spacing of the basal planes is perpendicular to the incident electron beam. There are two primary peaks in the carbon K core-loss edge of graphite (CNT walls), the π^* peak at 285.5 eV, and the σ^* peak at 292.5 eV [44]. These fine structure features are clear and distinct in the two spectra obtained at positions A and B,

indicating that the CNT walls are indeed crystalline. The intensity ratio between the π* and σ* peaks is different because the CNT wall orientation relative to the incident electron beam is different at these two positions [44]. In contrast to these spectra, the green carbon K-edge spectrum, obtained from the carbon-rich region at the Fe_3C-oxide interface, lacks the distinct fine structure present in the spectra obtained from the crystalline CNT walls. Specifically, neither the π* or σ* peaks are evident, but rather the spectrum consists of a broad loss feature. This lack of fine structure and overall shape of the core-loss edge is indicative of carbon in an amorphous state [37, 40].

The variation in carbon concentration through the catalyst base and identification of an amorphous carbon-rich region at the Fe_3C-oxide interface provides clues to the chemical and diffusion processes occurring during CNT growth. It is clear that carbon must be added to the growing walls along the edges of the graphene rings. Surprisingly, the graphene walls terminate at three different materials, iron oxide, the amorphous carbon at the triple junction, and the Fe_3C catalyst walls. This indicates that the CNT growth mechanism is robust and not specific to a particular interface or part of the catalyst. Apparently, CNT walls can grow from a variety of interfaces. It seems that a graphene edge and a carbon source is all that is required to sustain the growth. This raises the question of what the carbon source is and how carbon from the gas phase eventually gets to the edges of the CNT walls. Carbon has to reach the walls emanating from the base of the catalyst as well as those emanating from the tapered side walls of the catalyst.

There are three obvious ways carbon can reach the edge of the growing CNT walls. One possibility is that carbon containing species or carbon diffuses through the CNT walls. This is highly unlikely. First, diffusion through graphene walls has very high activation energy barriers and second, there are many observations in the literature where catalyst particles completely covered in graphene shells never grow CNTs.

The second possibility is that carbon diffuses through the iron oxide cap and Fe_3C to reach the CNT wall edges. Carbon concentrations measured in the outer portion of the iron oxide shell are substantially lower [see magenta and orange scans on the left, and blue and orange scans on

the right of Figure 6-3] and imply that carbon does not reach the CNT walls by diffusing through the substrate and the iron oxide. Moreover, along the bottom facet of the Fe_3C catalyst particle, oriented perpendicular to the CNT axis, carbon concentration in the iron oxide is low. This facet is completely covered with iron oxide, and is far from the triple interface. It is unlikely that this region plays a role in the growth.

Since the Fe_3C is completely surrounded by CNT walls and iron oxide cap, the remaining third possibility is that carbon reaches the edges of the CNT walls by diffusion through the interface between the iron oxide and the CNT walls. The EELS data is consistent with this third possibility. Highest carbon concentrations were measured near the triple junction formed by the Fe_3C, the iron oxide, and the CNT walls. These observations suggest that the amorphous carbon in this region serves as the carbon source for growth. High carbon concentration at this triple junction also indicates that decomposition of carbon-containing species occurs here. Carbon or a carbon-containing species (e.g., CH_x) must diffuse between the iron oxide shell and the CNT walls. It is easy to imagine that the loose arrangement of atoms at this oxide-CNT wall interface allows easy transport of species along this boundary. The diffusing species must adsorb onto the iron oxide and diffuse to the triple junction where they dissociate to give carbon. These carbon atoms then diffuse to the edges of the CNT walls where they add to the existing graphene ring edges to sustain the growth. After decomposition, diffusion of carbon may occur along the iron oxide-CNT wall interface, the Fe_3C-CNT interface or the Fe_3C-oxide interface. Indeed, the carbon concentration decreases as one moves away from the triple junction along the oxide-CNT wall interface and the Fe_3C-oxide interface. While we do not see an amorphous carbon region between the CNT walls and the tapered side walls of the Fe_3C catalyst, C can also diffuse through this interface and add to the edges of the walls. It does not appear that there is a need for carbon to diffuse through the bulk of the Fe_3C catalyst for CNT growth to occur. Most CNT walls originate at the triple interface, where carbon concentration is already high. Once decomposed at Fe_3C, carbon can almost immediately add to the growing CNT. Diffusion of carbon along the surface of the tapered Fe_3C faces, oriented approximately parallel to the CNT axis, may occur, and fuel the growth of inner CNT walls attached to the Fe_3C.

It has been speculated that CNTs grow from Fe_3C by a process similar to metal dusting [25], whereby the surface of the Fe_3C catalyst decomposes into Fe metal and graphite to produce the CNT graphene walls [12, 13, 26]. Thus a thin layer of Fe metal is expected to exist at the interface between the Fe_3C catalyst and the CNT walls where these graphene walls are attached to the catalyst. Even though this mechanism can not explain how outer CNT walls that have no connection to Fe_3C can grow, we considered metal dusting as a possible growth mechanism. Specifically, to evaluate this possibility we measured the Fe L_{23} core-loss edge using the atomic-scale EELS method. Using a 1.5 Å electron probe in the STEM we examined the outermost single atomic layer on the catalyst surface where Fe_3C ends and CNT walls begin. Specifically, the Fe L_{23} core-loss edge was measured at this Fe_3C-CNT interface, and compared to the Fe L_{23} core-loss edge measured in the bulk of the catalyst. The Fe L_{23} core-loss edge is composed of two main features, called "white lines", which result from transitions of electrons in $2p_{1/2}$ and $2p_{3/2}$ initial states. Jin et al. reported a downward shift of ~0.7 eV in the Fe L_{23} edge onset as well as a decrease in the spacing between the two white lines for Fe metal as compared to Fe_3C [45]. While the uncertainty in the absolute position of the edge onset precludes one to distinguish Fe metal and Fe in Fe_3C, the energy separation between the white lines can be used to determine the Fe bonding. Thus, if a thin Fe metal layer exists between the Fe_3C and the CNT walls one should be detect this layer within 1.5 Å resolution.

The two catalyst locations that were examined in this study are indicated with rectangles drawn on the BF TEM image shown in Figure 6-4(a). CNT walls were observed to form at these two locations on the Fe_3C catalyst; the cylindrical CNT walls grew from the long tapered catalyst face that is oriented approximately parallel to the CNT axis, while interior graphene cup structures oriented perpendicular to the CNT axis formed at the rounded catalyst end, opposite from the catalyst base. A high-resolution ADF image of the lower region is also shown. In both locations, the Fe L_{23} core-loss edge was measured every 0.3 nm along the length of two lines, which are drawn on the ADF image of Figure 6-4(b). Measurements obtained along the red line A contain information from only the outer 1 or 2 atomic layers on the surface of the catalyst at the CNT interface, while measurements along the blue line B, located approximately 5 nm inside the catalyst-CNT interface, contain mostly information from the bulk of the catalyst

(less than ~5% contribution from the surface of the catalyst, calculated assuming a surface layer thickness of 0.5 nm).

The averaged Fe L_{23} core-loss edges measured along each line show a striking similarity and are shown in Figure 6-4(c). Edge intensity was normalized by multiplying the spectrum obtained from the catalyst surface (along red line A) by an appropriate factor for easier comparison. Both spectra have the same L_3/L_2 peak intensity ratio, as well as the same spacing between the two peaks. This indicates that the surface and bulk of the catalyst are the same Fe_3C phase. We do not observe evidence for the presence of a metallic Fe layer at the catalyst-CNT interface. Identical results were also obtained, although not shown, from other regions of the catalyst, for example, near the rounded tip opposite of the catalyst base as indicated in the BF TEM image shown in Figure 6-4(a).

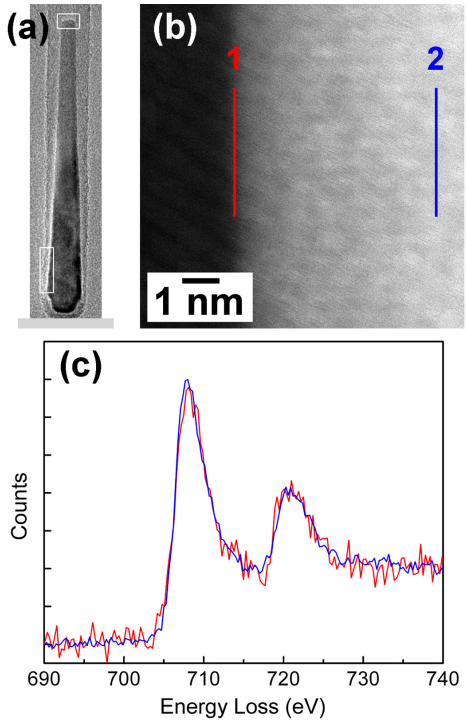

Figure 6-4. (a) BF-TEM image of an Fe_3C catalyst located inside the base of a MWCNT attached to a substrate. Rectangles indicate regions of CNT wall growth, where the Fe L_{23} core-

loss edge was measured. (b) High-resolution ADF image of the CNT-Fe_3C interface. The Fe L_{23} core-loss edge was measured every 0.3 nm along each line. Measurements along the red line A probed the surface 1 of 2 atomic layers, while measurements along the blue line B probed mostly the bulk properties of the catalyst. (c) Averaged Fe L_{23} core-loss edge from each line scan. The red spectrum was multiplied by an appropriate factor to normalize intensity. The two spectra are identical, indicating that the surface is also Fe_3C, and does not contain a layer of metallic Fe

The absence of a metallic Fe layer at the catalyst-CNT interface as determined from our atomic-scale EELS measurements, suggests that CNTs grow directly from the Fe_3C. CNT growth does not appear to proceed via a metal dusting process. Examination of smaller catalysts located at various points along the length of the CNT, that had broken away from a parent catalyst at the CNT base, were also found to be Fe_3C, which further supports that decomposition of Fe_3C did not occur during CNT growth [41]. These findings are consistent with Sharma et al. who observed *in situ* that CNTs grew directly from Fe_3C crystals [18]. They concluded that growth of CNTs were a result of the super-saturated state of the Fe_3C catalysts.

Our observations here are consistent with other studies that have highlighted the importance of the initial graphene seed in facilitating further nanotube growth [46, 47]. Once a cylindrical or hemispherical graphene seed is formed on the catalyst, further growth requires a source of decomposed carbon. We observe an amorphous carbon-rich region very close to the location where CNT walls grow; this indicates that this region acts as the carbon source for growth. Although many inner CNT walls are observed to grow directly from the tapered faces of the Fe_3C catalyst, the main, outer CNT walls terminate at the iron oxide shell, which suggests that they are not produced in an epitaxial process directly from the Fe_3C catalyst. Further, because all CNT walls are observed to grow at the same rate, this suggests that the growth process is reaction limited. The role of Fe_3C may solely be to provide a source of decomposed carbon for addition to an existing CNT seed.

6.4 Conclusions

High-resolution EELS method was used to probe the chemical and diffusion processes occurring at the catalyst-CNT interface during CNT growth by PECVD. Variation of relative

carbon concentration on an atomic-scale at different locations in the base of the catalyst and characterization of the type of carbon bonding reveal that gas-phase carbonaceous species are decomposed at the Fe_3C surface, near the triple interface of Fe_3C, iron oxide, and CNT walls. This source of decomposed carbon, now in an amorphous state, can directly incorporate into the CNT walls at this triple interface, or diffuse upwards, along the Fe_3C-CNT interface to produce inner CNT walls. Atomic-scale measurements of the Fe L_{23} core-loss edge show that the chemical state of the iron-carbide catalyst does not change at the catalyst-CNT interface, indicating that CNT walls grow directly from Fe_3C, and not by a metal dusting process. The atomic-scale EELS method is well suited for studying the chemical bonding state and composition of the catalyst nanoparticles and we hope that in the future the *ex situ* study described herein may be extended to *in situ* to measure the diffusion and chemical processes occurring during CNT growth in real time.

6.5 References

[1] Baughman, R. H.; Zakhidov, A. A.; de Heer, W. A., Carbon nanotubes - the route toward applications. *Science* **2002,** *297* (5582), 787-792.

[2] Dresselhaus, M. S.; Dresselhaus, G.; Charlier, J. C.; Hernandez, E., Electronic, thermal and mechanical properties of carbon nanotubes. *Philosophical Transactions of the Royal Society a-Mathematical Physical and Engineering Sciences* **2004,** *362* (1823), 2065-2098.

[3] Melechko, A. V.; Merkulov, V. I.; McKnight, T. E.; Guillorn, M. A.; Klein, K. L.; Lowndes, D. H.; Simpson, M. L., Vertically aligned carbon nanofibers and related structures: Controlled synthesis and directed assembly. *Journal of Applied Physics* **2005,** *97*, 041301.

[4] Tans, S. J.; Verschueren, A. R. M.; Dekker, C., Room-temperature transistor based on a single carbon nanotube. *Nature* **1998,** *393* (6680), 49-52.

[5] Trojanowicz, M., Analytical applications of carbon nanotubes: a review. *Trac-Trends in Analytical Chemistry* **2006,** *25* (5), 480-489.

[6] Merkoci, A.; Pumera, M.; Llopis, X.; Perez, B.; del Valle, M.; Alegret, S., New materials for electrochemical sensing VI: Carbon nanotubes. *Trac-Trends in Analytical Chemistry* **2005,** *24* (9), 826-838.

[7] Meyyappan, M., A review of plasma enhanced chemical vapour deposition of carbon nanotubes. *Journal of Physics D-Applied Physics* **2009,** *42*, 213001.

[8] Barone, P. W.; Baik, S.; Heller, D. A.; Strano, M. S., Near-infrared optical sensors based on single-walled carbon nanotubes. *Nature Materials* **2005,** *4* (1), 86-U16.

[9] Granqvist, C. G., Transparent conductors as solar energy materials: A panoramic review. *Solar Energy Materials and Solar Cells* **2007,** *91* (17), 1529-1598.

[10] Landi, B. J.; Raffaelle, R. P.; Castro, S. L.; Bailey, S. G., Single-wall carbon nanotube-polymer solar cells. *Progress in Photovoltaics* **2005,** *13* (2), 165-172.

[11] Ren, Z. F.; Huang, Z. P.; Xu, J. W.; Wang, J. H.; Bush, P.; Siegal, M. P.; Provencio, P. N., Synthesis of large arrays of well-aligned carbon nanotubes on glass. *Science* **1998,** *282* (5391), 1105-1107.

[12] Golberg, D.; Mitome, M.; Muller, C.; Tang, C.; Leonhardt, A.; Bando, Y., Atomic structures of iron-based single-crystalline nanowires crystallized inside multi-walled carbon nanotubes as revealed by analytical electron microscopy. *Acta Materialia* **2006,** *54* (9), 2567-2576.

[13] Kim, H.; Sigmund, W., Iron particles in carbon nanotubes. *Carbon* **2005,** *43* (8), 1743-1748.

[14] Yao, Y.; Falk, L. K. L.; Morjan, R. E.; Nerushev, O. A.; Campbell, E. E. B., Synthesis of carbon nanotube films by thermal CVD in the presence of supported catalyst

particles. Part II: the nanotube film. *Journal of Materials Science-Materials in Electronics* **2004,** *15* (9), 583-594.

[15] Yoshida, H.; Takeda, S.; Uchiyama, T.; Kohno, H.; Homma, Y., Atomic-scale in-situ observation of carbon nanotube growth from solid state iron carbide nanoparticles. *Nano Letters* **2008,** *8* (7), 2082-2086.

[16] Blank, V. D.; Kulnitskiy, B. A.; Batov, D. V.; Bangert, U.; Gutierrez-Sosa, A.; Harvey, A. J., Electron microscopy and electron energy loss spectroscopy studies of carbon fiber formation at Fe catalysts. *Journal of Applied Physics* **2002,** *91* (3), 1657-1660.

[17] Hofmann, S.; Blume, R.; Wirth, C. T.; Cantoro, M.; Sharma, R.; Ducati, C.; Havecker, M.; Zafeiratos, S.; Schnoerch, P.; Oestereich, A.; Teschner, D.; Albrecht, M.; Knop-Gericke, A.; Schlogl, R.; Robertson, J., State of transition metal catalysts during carbon nanotube growth. *Journal of Physical Chemistry C* **2009,** *113* (5), 1648-1656.

[18] Sharma, R.; Moore, E.; Rez, P.; Treacy, M. M. J., Site-specific fabrication of Fe particles for carbon nanotube growth. *Nano Letters* **2009,** *9* (2), 689-694.

[19] Behr, M. J.; Gaulding, E. A.; Mkhoyan, K. A.; Aydil, E. S., Effect of hydrogen on catalyst in carbon nanotube growth. **Submitted 2010**.

[20] Mattevi, C.; Hofmann, S.; Cantoro, M.; Ferrari, A. C.; Robertson, J.; Castellarin-Cudia, C.; Dolafi, S.; Goldoni, A.; Cepek, C., Surface-bound chemical vapour deposition of carbon nanotubes: In situ study of catalyst activation. *Physica E-Low-Dimensional Systems & Nanostructures* **2008,** *40* (7), 2238-2242.

[21] Emmenegger, C.; Bonard, J. M.; Mauron, P.; Sudan, P.; Lepora, A.; Grobety, B.; Zuttel, A.; Schlapbach, L., Synthesis of carbon nanotubes over Fe catalyst on aluminium and suggested growth mechanism. *Carbon* **2003,** *41* (3), 539-547.

[22] Schaper, A. K.; Hou, H. Q.; Greiner, A.; Phillipp, F., The role of iron carbide in multiwalled carbon nanotube growth. *Journal of Catalysis* **2004,** *222* (1), 250-254.

[23] Zhang, J. Q.; Ostrovski, O., Cementite formation in CH_4-H_2-Ar gas mixture and cementite stability. *Isij International* **2001,** *41* (4), 333-339.

[24] Rodriguez-Manzo, J. A.; Terrones, M.; Terrones, H.; Kroto, H. W.; Sun, L. T.; Banhart, F., In situ nucleation of carbon nanotubes by the injection of carbon atoms into metal particles. *Nature Nanotechnology* **2007,** *2* (5), 307-311.

[25] Grabke, H. J., Metal dusting. *Materials and Corrosion-Werkstoffe Und Korrosion* **2003,** *54* (10), 736-746.

[26] He, K.; Brown, A.; Brydson, R.; Edmonds, D. V., Analytical electron microscope study of the dissolution of the Fe_3C iron carbide phase (cementite) during a graphitisation anneal of carbon steel. *Journal of Materials Science* **2006,** *41* (16), 5235-5241.

[27] Fan, S. S.; Liu, L.; Liu, M., Monitoring the growth of carbon nanotubes by carbon isotope labelling. *Nanotechnology* **2003,** *14* (10), 1118-1123.

[28] Jiang, D. E.; Carter, E. A., Carbon atom adsorption on and diffusion into Fe(110) and Fe(100) from first principles. *Physical Review B* **2005,** *71*, 045402.

[29] Behr, M. J.; Mkhoyan, K. A.; Aydil, E. S., Orientation and morphological evolution of catalyst nanoparticles during carbon nanotube growth. **submitted 2010**.

[30] Xu, C. H.; Fu, C. L.; Pedraza, D. F., Simulations of point-defect properties in graphite by a tight-binding-force model. *Physical Review B* **1993,** *48* (18), 13273-13279.

[31] Abild-Pedersen, F.; Norskov, J. K.; Rostrup-Nielsen, J. R.; Sehested, J.; Helveg, S., Mechanisms for catalytic carbon nanofiber growth studied by ab initio density functional theory calculations. *Physical Review B* **2006,** *73*, 115419.

[32] Hofmann, S.; Csanyi, G.; Ferrari, A. C.; Payne, M. C.; Robertson, J., Surface diffusion: The low activation energy path for nanotube growth. *Physical Review Letters* **2005,** *95*, 036101.

[33] Raty, J. Y.; Gygi, F.; Galli, G., Growth of carbon nanotubes on metal nanoparticles: A microscopic mechanism from ab initio molecular dynamics simulations. *Physical Review Letters* **2005,** *95*, 096103.

[34] Helveg, S.; Lopez-Cartes, C.; Sehested, J.; Hansen, P. L.; Clausen, B. S.; Rostrup-Nielsen, J. R.; Abild-Pedersen, F.; Norskov, J. K., Atomic-scale imaging of carbon nanofibre growth. *Nature* **2004,** *427* (6973), 426-429.

[35] Begtrup, G. E.; Gannett, W.; Meyer, J. C.; Yuzvinsky, T. D.; Ertekin, E.; Grossman, J. C.; Zettl, A., Facets of nanotube synthesis: High-resolution transmission electron microscopy study and density functional theory calculations. *Physical Review B* **2009,** *79*, 205409.

[36] Wirth, C. T.; Zhang, C.; Zhong, G. F.; Hofmann, S.; Robertson, J., Diffusion- and reaction-limited growth of carbon nanotube forests. *Acs Nano* **2009,** *3* (11), 3560-3566.

[37] Egerton, R. F., *Electron energy-loss spectroscopy in the electron microscope*. New York : Plenum Press: New York, 1996.

[38] Colliex, C.; Manoubi, T.; Ortiz, C., Electron-Energy-Loss-Spectroscopy Near-Edge Fine-Structures in the Iron-Oxygen System. *Physical Review B* **1991,** *44* (20), 11402-11411.

[39] van Aken, P. A.; Liebscher, B.; Styrsa, V. J., Quantitative determination of iron oxidation states in minerals using Fe L-2,L-3-edge electron energy-loss near-edge structure spectroscopy. *Physics and Chemistry of Minerals* **1998,** *25* (5), 323-327.

[40] Huang, J. Y., HRTEM and EELS studies of defects structure and amorphous-like graphite induced by ball-milling. *Acta Materialia* **1999,** *47* (6), 1801-1808.

[41] Behr, M. J.; Mkhoyan, K. A.; Aydil, E. S., Catalyst rotation, twisting, and bending during multiwall carbon nanotube growth. **Submitted 2010**.

[42] Nellist, P. D.; Pennycook, S. J., The principles and interpretation of annular dark-field Z-contrast imaging. *Advances in Imaging and Electron Physics, Vol 113* **2000,** *113*, 147-203.

[43] Sun, L.; Rodriguez-Manzo, J. A.; Banhart, F., Elastic deformation of nanometer-sized metal crystals in graphitic shells. *Applied Physics Letters* **2006,** *89*, 263104.

[44] Leapman, R. D.; Fejes, P. L.; Silcox, J., Orientation Dependence of Core Edges From Anisotropic Materials Determined by Inelastic-Scattering of Fast Electrons. *Physical Review B* **1983,** *28* (5), 2361-2373.

[45] Jin, Y. M.; Xu, H. F.; Datye, A. K., Electron energy loss spectroscopy (EELS) of iron Fischer-Tropsch catalysts. *Microscopy and Microanalysis* **2006,** *12* (2), 124-134.

[46] Yao, Y. G.; Feng, C. Q.; Zhang, J.; Liu, Z. F., "Cloning" of single-walled carbon nanotubes via open-end growth mechanism. *Nano Letters* **2009,** *9* (4), 1673-1677.

[47] Smalley, R. E.; Li, Y. B.; Moore, V. C.; Price, B. K.; Colorado, R.; Schmidt, H. K.; Hauge, R. H.; Barron, A. R.; Tour, J. M., Single wall carbon nanotube amplification: En route to a type-specific growth mechanism. *Journal of the American Chemical Society* **2006,** *128* (49), 15824-15829.

7 Effect of Hydrogen on Catalyst Nanoparticles in Carbon Nanotube Growth

The structures of carbon nanotubes grown from catalytic nanoparticles via plasma-enhanced chemical vapor deposition in CH_4/H_2 mixtures show a strong dependence on the H_2-to-CH_4 ratio in the feed gas. A suite of characterization techniques, including optical emission, infrared, and Raman spectroscopies combined with convergent-beam and selected-area electron diffraction, and high-resolution (Scanning)TEM imaging were used to systematically investigate the interrelation amongst plasma gas phase composition, catalysts morphology, catalyst structure, and carbon nanotube structure. Hydrogen plays a critical role in determining the final carbon nanotube structure through its effect on the catalyst crystal structure and morphology. At low H_2-to-CH_4 ratios (~1), iron catalyst nanoparticles are converted to Fe_3C and well-graphitized nanotubes grow from elongated Fe_3C crystals. High (>5) H_2-to-CH_4 ratios in the feed gas result in high hydrogen concentrations in the plasma and strongly reducing conditions, which prevents conversion of Fe to Fe_3C. In the latter case, poorly-graphitized nanofibers grow from ductile BCC iron nanocrystals that are easily deformed into tapered nanocrystals that yield nanotubes with thick walls.

7.1 Introduction

Carbon nanotubes exhibit a combination of unique thermal, optical, and electronic properties that make them desirable for a wide range of applications from transparent conducting films to sensors and transistors [1]. Many of these properties depend on how the carbon atoms are arranged within the graphene wall(s) [2, 3]. Precise structural control of this arrangement remains the key challenge to realizing their technological potential [4]. Plasma-enhanced chemical vapor deposition (PECVD) from methane-hydrogen or acetylene-hydrogen gas mixtures using catalytic iron nanoparticles enables large-scale growth of dense carbon nanotubes (CNTs). Hydrogen is required to grow well-graphitized CNTs [5], however, the structure of the nanotubes can vary significantly depending on how much hydrogen is present during growth. A number of research groups varied the fraction of hydrogen in the precursor

gas mixture and reported changes in carbon nanotube size, structure, morphology, or areal nanotube density [5-12]. A general consensus is that hydrogen etches away any amorphous carbon that may deposit on the catalyst and block the nanotube growth [4]. However, this mechanism alone does not explain the strong dependence of nanotube structure on hydrogen concentration. Another issue that has not yet been addressed systematically is the effect of hydrogen on the shape, structure and composition of the catalyst particles. Indeed, CNTs and carbon nanofibers (CNFs) have been reported to grow by PECVD or CVD from a number of different catalyst morphologies [13], and catalyst phases, including pure iron and a variety of iron carbide phases, such as Fe_3C, Fe_5C_2, and Fe_7C_3 [14-18]. Nanotube structure appears to have some correlation to the shape and size of the catalyst [13, 19]. However, a thorough examination of catalyst crystals as a function of hydrogen concentration in the plasma has not yet been reported. In this study, convergent beam electron diffraction (CBED) and high-resolution transmission electron microscopy (HR-TEM) and related techniques were used to explain the changes in catalyst crystal morphology, size, composition, and structure as a function of hydrogen concentration in the feed gas and in the plasma.

7.2 Materials and Methods

Dense multiwall carbon nanotube (MWCNT) films were grown using a radio-frequency (RF at 13.56 MHz) inductively-coupled plasma and initially iron catalyst through PECVD. The iron catalyst was deposited on native-oxide coated silicon substrates as a 10 nm thick film using electron-beam evaporation. Substrates were placed on a resistively-heated substrate platen located 25 cm below the transformer-coupled plasma coil, in a down-stream type configuration [20]. Before nanotube growth, the iron catalyst film was exposed to a H_2:Ar (50 sccm:5 sccm) plasma (200 W RF power) at 700 ^oC for 15 minutes to break apart the film to form nanometer-size metal islands, and to reduce oxides present in the catalyst film. Growth of the nanotubes was conducted at 800 ^oC and 10 Torr using a plasma maintained with 200 W RF power in a CH_4:H_2:Ar gas mixture. In this study, the flow rate of hydrogen was varied from 0 to 100 sccm, while the CH_4:Ar flow rate ratio remained fixed at 5 sccm:68 sccm. H_2 Dihydrogen flow rates

used in this study were 0, 5, 25, 50, and 100 sccm, which correspond to H_2-to-CH_4 flow rate ratios of 0, 1, 5, 10, and 20, respectively.

Relative concentrations of H, CH, and C_2 species in the plasma were monitored using optical emission spectroscopy (OES) in conjunction with actinometry as described by Coburn and Chen [21]. Argon was chosen as the actinometer; its flow remained constant at 68 sccm for all experiments. All peak intensities in OES measurements were normalized relative to the Ar 750.4 nm emission line, to account for changes in the electron density and distribution of electron energies [21, 22]. Emission averaged over the entire plasma volume was coupled via a fiber-optic cable to an Acton Research Corporation SpectraPro-275 0.275 Meter Triple Grating Monochromator/Spectrograph equipped with a photomultiplier tube. Using a grating with 1200 grooves/mm combined with a 50 μm entrance slit width yielded 0.15 nm spectral resolution. All spectra were collected with a 0.1 nm scan step and 200 ms integration time. Emission intensities from species of interest were measured from peak heights.

Absorption by infrared active gas phase species was examined with and without plasma activation using Fourier Transform Infrared (FTIR) spectroscopy (Nicolet Magna-IR 550 FTIR spectrometer). Methane and acetylene could be detected using FTIR. Gas temperature and methane dissociation fraction in the plasma were calculated from measured infrared absorption spectra. The IR beam from the spectrometer was directed into the plasma reaction chamber through KBr windows. Total path length of the IR beam through the plasma was 54.5 cm. The transmitted beam was then detected with an external, cooled HgCdTe detector. Absorption spectra in the range of 650-4000 cm^{-1} with a spectral resolution of 0.5 cm^{-1} were averaged over 300 scans and recorded. The change in magnitude as well as the change in rotational-level population of the methane rotation-vibration absorption band, centered at 3017 cm^{-1}, was used to calculate the change in CH_4 density and gas rotational temperature, respectively. All spectra were collected relative to reference spectra with no gas flowing through the reaction chamber.

Average CNT structure was characterized using Raman spectroscopy. Raman spectra of the nanotube films were collected using a Witec alpha300R Raman spectrometer in the confocal backscattering geometry. An argon ion laser (514.5 nm wavelength) operating at 20 mW and

focused to ~1 μm spot provided excitation. Raman scattering was detected using a DV401 CCD peltier-cooled detector.

Characterization of individual CNTs and catalysts, including high-resolution imaging combined with CBED and selected area electron diffraction (SAED), was conducted using an FEI Tecnai F-30 microscope with a Schottky field-emission electron gun operated at 300 keV. Nanotubes were removed from the Si/SiO_2 substrates by sonication in ethanol for 30 seconds, and then transferred to copper TEM grids coated with a lacey carbon support film. Images and diffraction patterns were recorded using a Gatan CCD.

7.3 Results and Discussion

7.3.a Gas Phase Analysis

Optical emission provided the relative concentrations of optically active reactive species in the plasma as a function of the dihydrogen concentration in the feed gas. In all experiments, emission from atomic H (H_α at 656 nm), CH (431 nm), C_2 (516 nm), and Ar (750.4 nm) was detected; these are commonly observed emission lines from plasmas containing Ar, CH_4, and H_2 [23]. Using actinometry, changes to the relative ground-state concentration of each species present under different hydrogen flows were determined. As an example, the relative ground-state H and Ar concentrations, [H]/[Ar] can be related to their relative emission intensity ratio, I_{656}/I_{750}, through the relation $[H]/[Ar] = kI_{656}/I_{750}$, where k is the proportionality constant [21]. Ma et al. found very good agreement between relative specie concentrations in a microwave $CH_4/Ar/H_2$ plasma determined using actinometry and absolute densities measured with cavity ring-down spectroscopy [24]. Figure 7-1 shows the relative ground-state concentrations of the H, CH, and C_2, as a function of H_2-to-CH_4 flow ratio. Relative H concentration is lowest in the pure methane plasma. Hydrogen atoms can be produced only from CH_4 under these conditions. As H_2 gas is added to the plasma, relative H concentration increases linearly. Over the range of H_2-to-CH_4 ratios used in this study, the relative H atom concentration was found to vary by a factor of three. An opposite trend was observed for CH and C_2 species. Relative concentrations

of these species are at a maximum in the pure methane plasma. With addition of only 5 sccm of H_2 (equal to methane flow), their relative concentration in the plasma dropped significantly. At 25 sccm H_2, this ratio was approximately half that compared to the pure methane plasma. Further increase of H_2, to 10 times the amount of CH_4, resulted in a smaller decrease of both CH and C_2 concentrations.

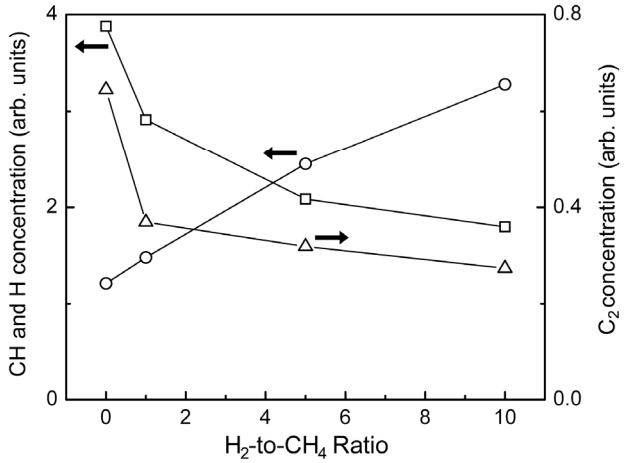

Figure 7-1. Optical emission intensities of H_α (656 nm, ○), CH (431 nm, □), and C_2 (516 nm, △) normalized with the Ar 750.4 nm emission intensity, and plotted as a function of H_2-to-CH_4 flow rate ratio.

Figure 7-2(a) shows a typical IR rotation-vibration absorption band of gas-phase methane in the reaction chamber, centered at 3017 cm^{-1}. The black curve was obtained with the plasma off, while the red curve was measured after turning on the plasma at 200 W RF power. The gas temperature and the fraction of methane dissociated by the plasma were calculated from IR spectra . The population of rotational levels follows a Boltzmann distribution, and was used to calculate the rotational temperature of the gas molecules as shown in Figure 7-2(b). Details of this calculation are presented in the Appendix. With the plasma off, the gas temperature was 300 K, while with the plasma on, the highest calculated rotational temperature was found to be 345 K. The rotational, translational, and vibrational temperatures are all approximately equal because of the high pressure (10 Torr) used in these experiments. With no significant change in gas temperature during plasma activation, the concentration of reactive species formed in the plasma through dissociation of methane or hydrogen could be determined from pressure

measurements, as presented in the Appendix. Additionally, fraction of methane dissociation could be calculated from IR absorption measurements. The magnitude of the red absorption band is less than that of the black [see Figure 7-2(a)] because a fraction of the methane molecules are dissociated in the plasma to form other species. This change in absorption is a direct measure of the fraction of methane dissociated in the plasma. Figure 7-3(a) shows the fraction of methane dissociated in the plasma as a function of the H_2-to-CH_4 flow rate ratio. This fraction ranges from 56% in the pure methane plasma, to only 21% when the H_2 flow rate is 50 sccm (10 times the CH_4 flow rate). The absolute concentration of methane molecules as well as the concentration of methane molecules that are dissociated to form other reactive species, (e.g., C_2, C_2H_2, CH_x, etc.) in the plasma are also plotted in Figure 7-3(a). Over the range investigated, it is found that increasing the amount of hydrogen in the gas mixture decreases the concentration of reactive species that are formed from the dissociation of methane by a factor of three.

In addition to methane absorption bands, also present in spectra from all experiments with plasma activation were absorption bands corresponding to acetylene, C_2H_2, located at 3300 cm^{-1} and 730 cm^{-1} [25]. The integrated intensity of the absorption band located at 730 cm^{-1} is plotted as a function of H_2-to-CH_4 flow rate ratio in Figure 7-3(b). Consistent with the other carbon-containing species formed in the plasma, i.e. CH and C_2, the concentration of C_2H_2 also decreases with increasing H_2 fraction. The decrease in acetylene concentration (~34%) over the range investigated is of similar magnitude to the observed change in fraction of methane dissociation (~35%).

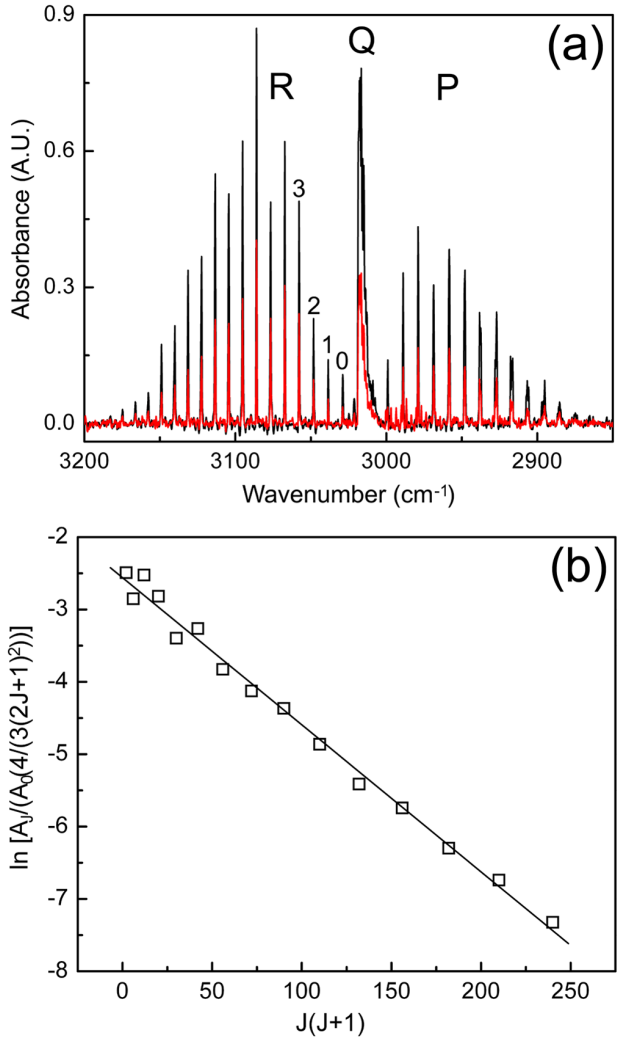

Figure 7-2. (a) Typical rotation-vibration IR absorption spectra of methane gas at 10 Torr with plasma on (red) and plasma off (black). The first few rotational peaks of the R branch are labeled with the appropriate angular momentum quantum number. (b) The intensities of rotational absorption peaks from the R branch are displayed on a Boltzmann plot. A linear fit yielded a slope inversely proportional to the gas temperature.

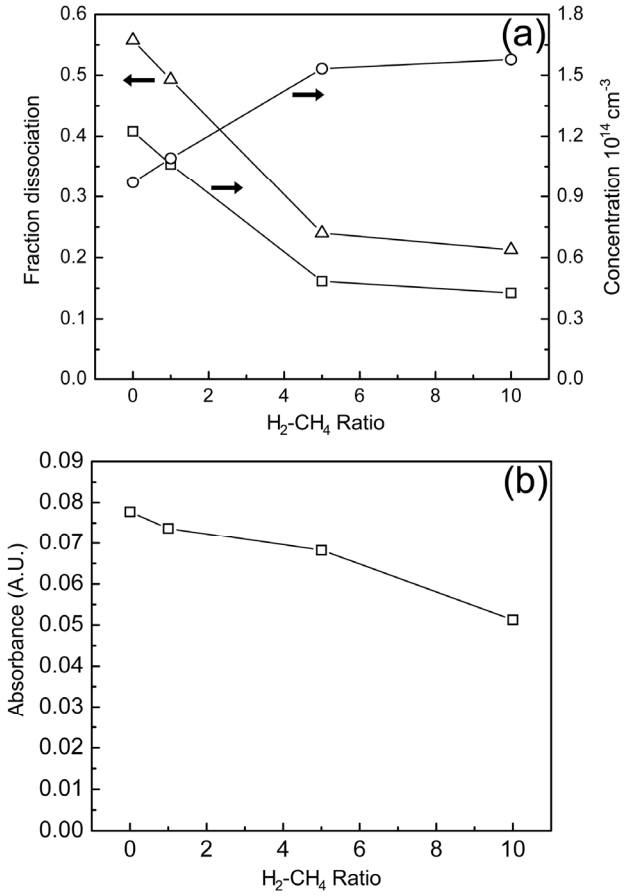

Figure 7-3. (a) Fractional dissociation of CH_4 in the plasma (△), concentration of CH_4 that is not dissociated (○), and concentration of CH_4 that was dissociated in the plasma (□) as a function of H_2-to-CH_4 flow rate ratio. (b) Integrated intensity of acetylene absorption peak at 730 cm^{-1} as a function of H_2-to-CH_4 flow rate ratio.

In summary, gas phase characterization indicates that when H_2-to-CH_4 ratio in the feed gas is increased from 0 to 10, concentration of H atoms in the plasma increases by approximately a factor of 3 while the concentration of C containing molecules and molecular fragments decreases by approximately a factor of two to three depending on the species. The gas temperature does not rise significantly. Thus, increasing the H_2-to-CH_4 ratio by an order of magnitude also increases the flux of H atoms to C-containing molecules impinging on the

substrate by approximately an order of magnitude. We use this information to help interpret the observed changes in the catalyst and CNT structure.

7.3.b CNT Structure

A broad range of carbon nanotube structures and sizes were observed with TEM, SEM, and Raman spectroscopy as the H_2-to-CH_4 ratio in the feed gas was varied. The left column of SEM images in Figure 7-4 shows the cross-sectional views of CNT films grown under different H_2-to-CH_4 ratios. SEM images show the relatively dense films of carbon nanotube structures that grow normal to the substrate at all but the very highest hydrogen dilution, H_2-to-CH_4 ratio of 20 (100 sccm H_2). CNTs were not produced at an H_2-to-CH_4 ratio of 20, and thus images from this experiment are not included in Figure 7-4. Next to each SEM image, in the second column, is a bright field (BF) HR-TEM image that shows the representative CNT structure produced in each experiment. SEM and TEM analysis revealed that as the fraction of hydrogen was changed, the average CNT length, as well as both the average diameter and diameter distribution of the CNTs changed. Nanotubes grew to lengths ranging from 3.3-7 microns, depending on the H_2-to-CH_4 ratio, after 30 minutes of plasma deposition. The shortest nanotubes were produced with no added hydrogen. Figure 7-5 shows the average length, and diameter, with standard deviations, of CNTs from each experiment, as measured from HRTEM images. Equal parts hydrogen and methane produced CNTs with the smallest average diameter, 29 nm, and narrowest diameter distribution. As the H_2-to-CH_4 ratio was increased above one, the average diameter and diameter distribution increased significantly.

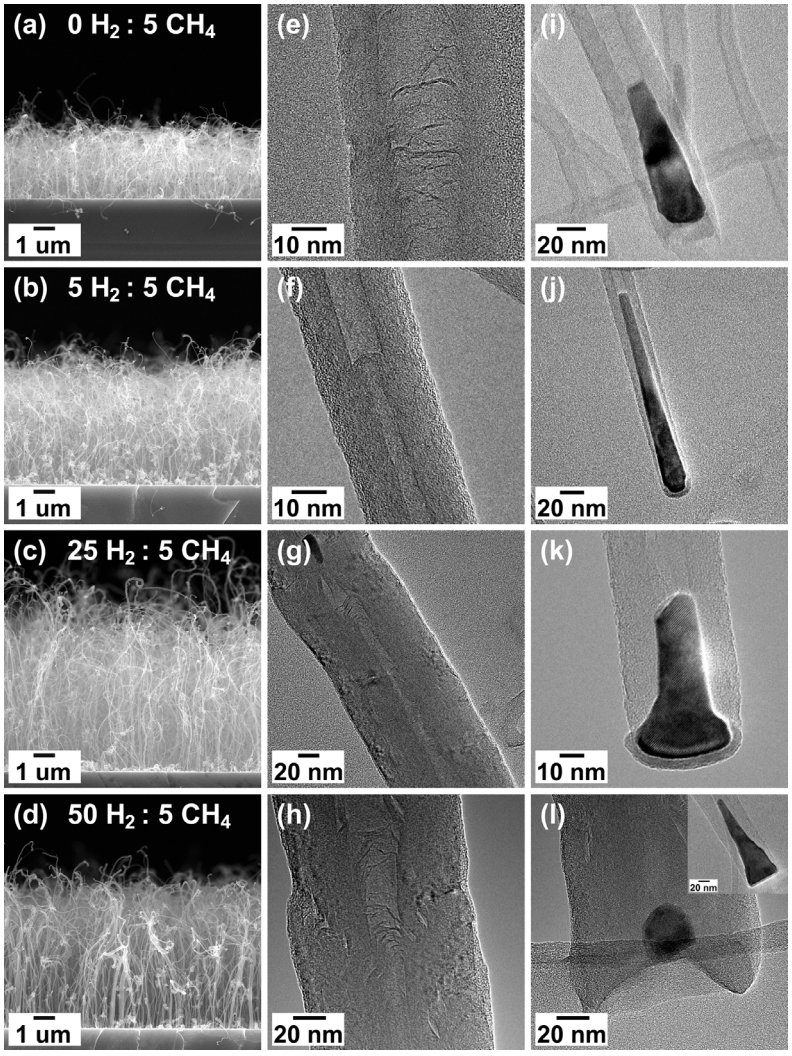

Figure 7-4. (a)-(d) in the first column show cross-section SEM images of MWCNT films grown by catalytic PECVD using a 10 nm iron catalyst layer. H_2-to-CH_4 flow rate ratio increases from top to bottom, and is indicated on each image. (e)-(h) in the second column show representative BF-TEM images of the most commonly-observed CNT structures for each experiment in the first column. (i)-(l) in the third column show representative BF-TEM images of the most abundant catalyst crystal morphology observed inside the bases of the MWCNTs shown in the corresponding (same row) first and second columns. The MWCNTS were deposited with feed gas that contained (a,e,i) 0 sccm H_2 and 50 sccm CH_4, (b,f,j) 5 sccm H_2 and 5 sccm CH_4, (c,g,k) 25 sccm H_2 and 5 sccm CH_4, (d,h,l) 50 sccm H_2 and 5 sccm CH_4.

A methane plasma, with no added H_2, produced CNTs with an average diameter of 42 nm (Figure 7-4 (a), (e) and (i)). Most tubes exhibited frequent cupping along their length, i.e.,

interior walls would connect to form cups perpendicular to the nanotube axis, as shown in Figure 7-4(e). Dangling graphene walls that neither formed full cups nor continuous walls were observed frequently on the interior of these tubes. Tube walls were found to extend beyond the catalyst crystal located at the base of the nanotube (Figure 7-4(i)), indicating that the catalyst was lifted a few nanometers off the substrate during growth.

Equal parts H_2 and CH_4 produced the most well-graphitized tubes (Figure 7-4 (b), (f) and (j)), which were also the thinnest nanotubes with a very narrow diameter distribution (29 ± 5 nm). While occasional cupping was observed, all walls, both interior and exterior, were continuous, intact, and approximately constant diameter the entire length of the nanotube in most tubes.

At five times the amount of H_2 relative to CH_4, a much wider variety of structures and sizes of tubes were produced (Figure 7-4 (c), (g) and (k)). The most abundant nanotubes were ~40 nm in diameter; however, a number of tubes with diameters close to ~100 nm were also present. Those with diameters ~40 nm were of similar quality as those grown with no added H_2 and resembled the tube shown in Figure 7-4(e). The large diameter tubes, however, were highly defective, and consisted of very thick walls, i.e., large number of walls (Figure 7-4(g)). The interior diameter was typically 1/9 the exterior diameter (compared to 1/3 for the smaller diameter tubes produced in all experiments), and contained numerous deformed cupped graphene layers, as well as sections of kinked walls.

Further increase in the H_2-to-CH_4 ratio, to 10, yielded many more large-diameter CNTs (Figure 7-4 (d), (h) and (l)). CNTs with diameters ~100 nm or larger were now the most abundant type. All tubes, including the smaller-diameter tubes were very defective, exhibiting kinks, cups, and deformed interior graphene layers (Figure 7-4(h)). Most graphene walls were not parallel to the tube axis, but rather at a variety of angles, up to ~45 degrees. When the H_2 flow was increased to 100 sccm, no significant nanotube growth was observed. TEM analysis revealed that some catalysts produced fat and deformed carbon nanofiber-like structures, without an open interior and many catalysts were merely encapsulated with graphene shells.

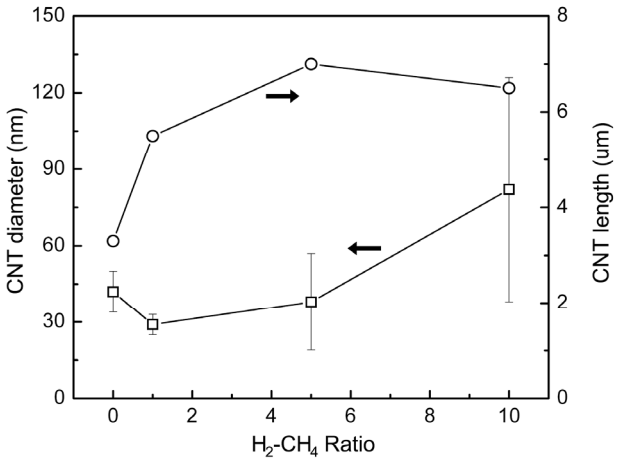

Figure 7-5. Average CNT diameter (□), and CNT length (○) as a function of H_2-to-CH_4 flow rate ratio. Error bars are the standard deviation for each sample and is a measure of the diameter distribution.

Raman spectroscopy captured a clear change in the average CNT structure as a function of H_2-to-CH_4 ratio in the feed gas mixture. The inset in Figure 7-6 shows a typical Raman spectrum obtained from a carbon nanotube film which shows two major peaks, a G peak at ~1580 cm^{-1}, and a D peak at ~1350 cm^{-1}. The ratio of peak intensities, I(D)/I(G), is often used as a measure of a carbon material's structure, and crystalline quality [26, 27]. The G peak corresponds to the in-plane stretching of sp^2 C-C bonds in rings or chains, while the D peak corresponds to breathing modes of sp^2 C-C bonds in rings [27]. The ratio I(D)/I(G) for CNTs grown in our experiments is plotted as a function of H_2-to-CH_4 ratio in Figure 7-6. A dramatic decrease in this ratio is observed as the fraction of H_2 in the feed gas is increased. This decrease in I(D) indicates increased disorder within the graphite (CNT wall) structure [27]. Specifically, this disorder may be manifested as a decrease in the average in-plane graphite cluster size [28], or as other structural disorder that break the graphite structure symmetry. This would suggest that increasing H_2 produces CNTs whose walls more resemble bulk graphite, with relatively long-range order and few structural defects. Certain defects that may be present in the CNT walls would not necessarily be detectable using only TEM characterization. Alternatively, the observed decrease in I(D)/I(G) may be a measure of the amount of amorphous carbons present. Since a relatively large film area, ~1 micron was probed in a Raman measurement, the averaged Raman signal contains information from all carbons present, which may include amorphous

carbons in addition to the graphite-like CNT structures. Thus, in this interpretation, increasing hydrogen concentration decreases the amount of amorphous carbon deposited.

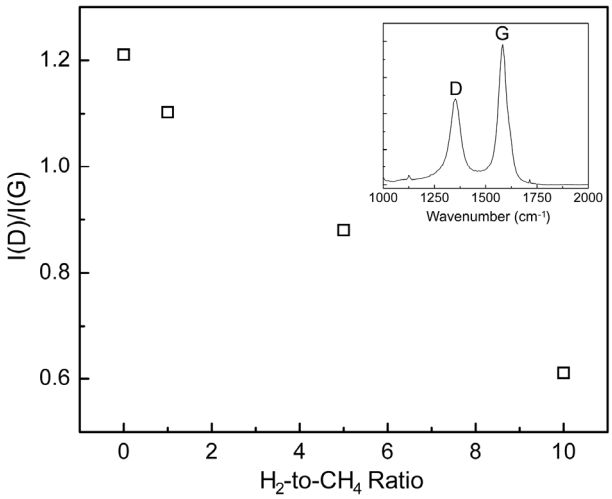

Figure 7-6. Raman spectra (inset) from a MWCNT film. The ratio of the D and G peak intensities, I(D)/I(G), as a function of H_2-to-CH_4 flow rate ratio.

7.3.c Catalyst Morphology and Crystalline Phase

Careful examination of the changes in the catalyst nanoparticle sizes and morphologies as a function of the H_2-to-CH_4 ratio suggests that one mechanism by which hydrogen affects CNT structure is through its effect on the catalyst nanoparticles. Indeed, it appears that the wide range of CNT sizes and structures observed in these experiments is a direct result of the range of sizes, morphologies, and crystal structures of the catalyst crystals from which these nanotubes grow. Figure 7-4 (right column) and Figure 7-7 show a collection of representative BF-TEM images of catalyst nanocrystals observed inside the base of MWCNTs. A clear change in both the size and shape of the catalyst crystals is evident as the amount of H_2 in the feed gas is increased.

The majority of CNTs grown from methane plasma, without H_2, grew from slightly elongated oval-shaped catalyst crystals, approximately 100 nm in length, which exhibited rough and deformed faces (Figure 7-4(i), Figure 7-7 (a) and (b)). The highly disordered interior structure of the CNTs that grew from these catalysts, as described previously, is likely due to the rough

and irregular catalyst edges. However, since the overall catalyst size is consistent, the resulting CNT diameter distribution is still narrow.

Addition of a small amount of H_2 (equal to methane flow) drastically improved the shape of the catalysts. Elongated tear-drop shaped catalysts with a constant smooth taper and lengths greater than 150-200 nm were commonly observed inside the base of the MWCNTs (Figure 7-4(j), Figure 7-7 (d) and (e)). The interfaces between the catalyst particles and the nanotube walls appeared very smooth, while the bases exhibited clear faceting. Production of well-graphitized CNTs with a very narrow diameter distribution was due to the similarity of all catalysts in this sample.

With 5 times more H_2 than CH_4, a considerable change in catalyst shape was observed. Figure 7-4(k) and Figure 7-7(g) show that the catalysts found inside the base of the most abundant CNTs, with diameters ~40-45 nm, were much shorter than those observed in experiments conducted with no or little H_2. These catalysts consisted of a 30-40 nm long cylindrical region of approximately constant diameter, followed by a region at the base which flares outwards to define the exterior diameter of the CNT. During growth, the cylindrical portion of the catalyst often became detached from the flared base region. This is evident by the high number of cylindrical catalysts observed ~5-10 nm up inside the base of the nanotube, as shown in the inset of Figure 7-7(g). Although not nearly as abundant, a second, much larger catalyst type was observed inside the base of nanotubes with diameters ~90-100 nm (Figure 7-7(h)). Consisting of a perfectly flat base, this cone-shaped catalyst exhibited numerous step-edges as it extended up into the CNT.

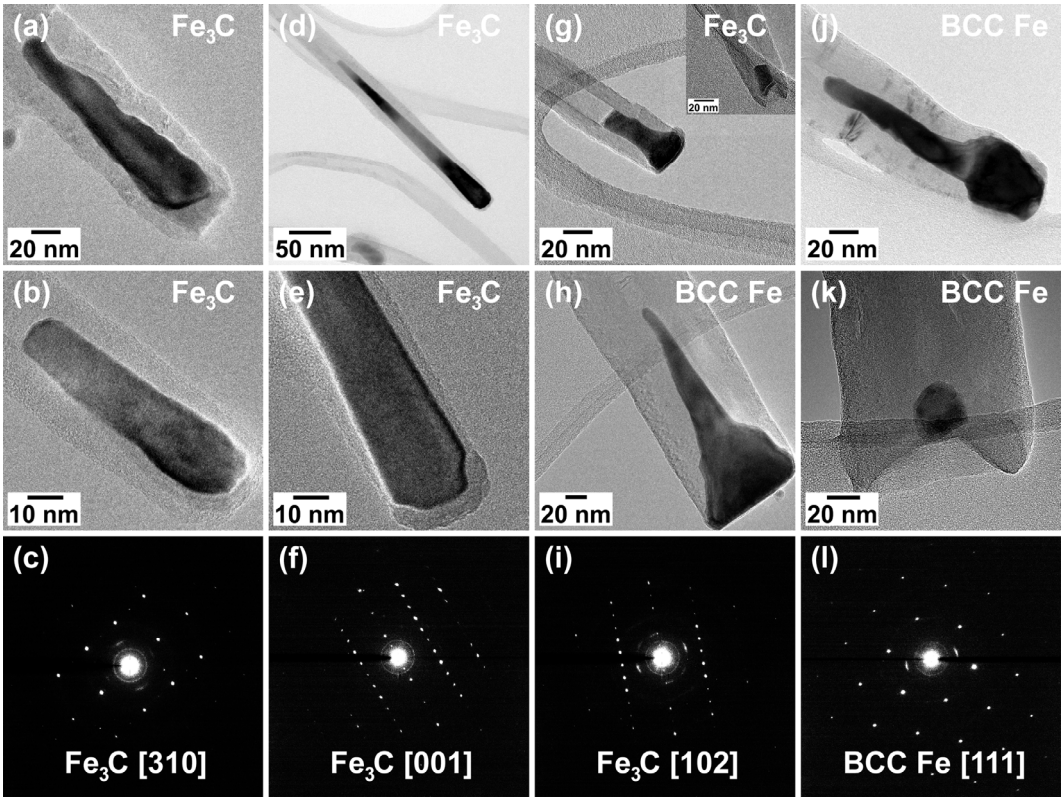

Figure 7-7. BF-TEM images of (top two rows), and SAED patterns (bottom row) from, the most abundant catalyst crystals observed inside the base of MWCNTs grown using H_2-to-CH_4 flow rate ratios of (sccm H_2 : sccm CH_4) (a)-(c) 0:5, (d)-(f) 5:5, (g)-(i) 25:5 sccm, and (j)-(l) 50:5 sccm.

A H_2 flow of 50 sccm, 10 times the methane flow rate, was the highest hydrogen fraction found to produce CNTs. The widest range of catalyst morphologies and sizes was also observed under these conditions. All catalysts examined in CNTs grown with a H_2-to-CH_4 ratio of 10 appeared highly deformed. In addition to the conical-shaped catalysts inside CNTs with diameters ~90-100 nm (Figure 7-4(l) inset), as observed in the previous experiment, multiple other morphologies were present. Tadpole-shaped catalysts were often observed inside nanotubes with diameters ~50-60 nm, as shown in Figure 7-7(j). Inside the base of the CNTs with diameters over 100 nm, catalysts appeared roughly spherical, yet much smaller (typically ~25 nm) than the nanotube diameter (Figure 7-4(l) and Figure 7-7(k)). Most of these larger nanotubes, however, were open at their base, suggesting that during removal by sonication from the substrate, tubes were separated from their catalysts.

In addition to effecting catalyst morphology, hydrogen controls the crystalline phase of the catalysts. Using CBED pattern analysis combined with crystal tilting, the crystalline phase of the most abundant catalyst crystals at the base of CNTs from each experiment was determined. From each sample, 12 to 22 crystals were individually tilted, using a double-tilt holder inside the TEM, to multiple connected zone axes (not shown). The symmetry of each zone axis combined with the angular relationships between pairs of zone axes uniquely define the crystal system [29]. Examples of single-crystal electron diffraction patterns obtained from the most abundant catalyst phase from each experiment are shown in Figure 7-7 (c), (f), (i), and (l). Although each catalyst is single crystalline, they exhibit combinations of small-angle (~1^o-3^o) rotations, twists, and bends along their axial length between adjacent locations, as reported elsewhere [30]. The most abundant catalysts inside the base of CNTs grown with 0, 5, and 25 sccm H_2 flows were found to be of the Fe_3C (cementite) crystal phase (orthorhombic space group Pnma no. 62, a = 0.5008 nm, b = 0.4465 nm, c = 0.6725 nm). However, the larger catalysts that produced tubes with diameters ~90-100 nm with 25 sccm H_2 were found to be body-centered cubic (BCC) iron (cubic space group I23 no. 197, a = 0.287 nm). Similarly, at 50 sccm, the catalysts producing the abundant large diameter tubes were also determined to be BCC iron.

7.3.d Discussion

The observations above suggest that the H_2-to-CH_4 ratio in the feed gas determines the relative fluxes of atomic H and C-containing-species impinging on the catalyst. We will refer to this ratio as the H-to-C ratio for simplicity even though C may be brought to the catalyst in a variety of molecular fragments. The ratio of H-to-C flux in turn determines the CNT structure through the catalysts morphology and phase. For example, the H-to-C flux determines the phase of the catalyst particle. When H concentration in the plasma is low compared to C containing species, Fe catalyst particles are quickly converted into Fe_3C as C containing species adsorb and react on the Fe surface. In contrast, it appears that under strongly reducing environments, i.e., when H atom concentration is increased, Fe_3C is unable to form, and hence the nanotubes grow from BCC iron catalyst nanocrystals. It appears that in presence of high H concentrations, CH_x fragments adsorbing on the surface could easily be converted back to volatile methane and

desorbed from the surface before they have a chance to convert the iron particle into carbide. Indeed, when H_2-to-CH_4 ratio was increased to five, a small number of BCC catalyst crystals were observed. At even higher H_2-to-CH_4 ratios and correspondingly high hydrogen concentrations, the majority of nanotubes grew from BCC iron catalyst nanocrystals. These findings may help explain why CNTs have been observed growing from a variety of iron-based catalysts. It is possible that differences in absolute atomic hydrogen concentration in different reactors or under different plasma operating conditions may help account for the variety of reported catalyst phases and morphologies found inside MWCNTs [14-18].

Elongated Fe_3C catalyst crystals that produce relatively thin, well-graphitized CNTs are formed when H_2-to-CH_4 ratio in the feed gas is approximately one. However, when the catalyst shape is tapered and the widths of the tip and the base are disparate, many walls form and emanate from the edges of the catalyst particles. It seems that this situation leads to thick CNT walls with very small ratio of the inner diameter to the outer diameter. Moreover, severely tapered catalyst shapes are most common when the catalyst is BCC iron. This difference is likely due to the differences in the mechanical properties of Fe_3C and BCC iron. BCC Fe plastically deforms and yields much easier than Fe_3C: Yield strengths of BCC Fe and Fe_3C are ~140 MPa and ~5 GPa, respectively. The catalyst experiences very large compressive stresses during growth, which would squeeze and taper the catalyst nanoparticle. Moreover, a positive feedback loop is set up during initial stages of growth wherein tapering the nanocrystal leads to formation of additional CNT walls which in turn increases the compressive stress and causes more taper which leads to more walls.

7.4 Conclusions

The relation among gas phase composition, catalyst structure and morphology, and CNT structure during PECVD of CNTs, was studied using a combination of material and gas-phase characterization techniques. Optical emission and IR absorption spectroscopy revealed that addition of H_2 to a CH_4/Ar plasma resulted in a decrease in the concentration of reactive carbon-containing species, specifically CH, C_2, and C_2H_2, but an increase in atomic hydrogen concentration. As the amount of hydrogen was increased, the average diameter, diameter

distribution, and CNT structure changed, because the size, shape, and phase of the catalyst crystals changed. At H_2-to-CH_4 ratios of 0, 1, and 5, CNTs grew from Fe_3C catalyst nanocrystals. Equal parts H_2 and CH_4 produced CNTs of the highest quality and uniformity. As H_2 was increased further, CNTs no longer grew from Fe_3C catalysts, but rather from BCC iron catalyst nanoparticles. Severe deformation of ductile iron nanocrystals leads to the formation of a tapered catalyst shape, which in turn produces CNTS with many walls and a very small inner diameter to outer diameter ratio.

7.5 References

[1] Baughman, R. H.; Zakhidov, A. A.; de Heer, W. A., Carbon nanotubes - the route toward applications. *Science* **2002,** *297* (5582), 787-792.

[2] *Carbon nanotubes advanced topics in the synthesis, structure, properties, and applications*. Berlin ; New York : Springer: Berlin ; New York, 2008.

[3] Dresselhaus, M. S.; Dresselhaus, G.; Charlier, J. C.; Hernandez, E., Electronic, thermal and mechanical properties of carbon nanotubes. *Philosophical Transactions of the Royal Society a-Mathematical Physical and Engineering Sciences* **2004,** *362* (1823), 2065-2098.

[4] Meyyappan, M., A review of plasma enhanced chemical vapour deposition of carbon nanotubes. *Journal of Physics D-Applied Physics* **2009,** *42*, 213001.

[5] Bell, M. S.; Teo, K. B. K.; Milne, W. I., Factors determining properties of multi-walled carbon nanotubes/fibres deposited by PECVD. *Journal of Physics D-Applied Physics* **2007,** *40* (8), 2285-2292.

[6] Caughman, J. B. O.; Baylor, L. R.; Guillorn, M. A.; Merkulov, V. I.; Lowndes, D. H.; Allard, L. F., Growth of vertically aligned carbon nanofibers by low-pressure inductively coupled plasma-enhanced chemical vapor deposition. *Applied Physics Letters* **2003,** *83* (6), 1207-1209.

[7] Lee, T. Y.; Han, J. H.; Choi, S. H.; Yoo, J. B.; Park, C. Y.; Jung, T.; Yu, S.; Yi, W. K.; Han, I. T.; Kim, J. M., Effects of source gases on the growth of carbon nanotubes. *Diamond and Related Materials* **2003,** *12* (3-7), 851-855.

[8] Nolan, P. E.; Lynch, D. C.; Cutler, A. H., Carbon deposition and hydrocarbon formation on group VIII metal catalysts. *Journal of Physical Chemistry B* **1998,** *102* (21), 4165-4175.

[9] Chhowalla, M.; Teo, K. B. K.; Ducati, C.; Rupesinghe, N. L.; Amaratunga, G. A. J.; Ferrari, A. C.; Roy, D.; Robertson, J.; Milne, W. I., Growth process conditions of vertically aligned carbon nanotubes using plasma enhanced chemical vapor deposition. *Journal of Applied Physics* **2001,** *90* (10), 5308-5317.

[10] Woo, Y. S.; Jeon, D. Y.; Han, I. T.; Lee, N. S.; Jung, J. E.; Kim, J. M., In situ diagnosis of chemical species for the growth of carbon nanotubes in microwave plasma-enhanced chemical vapor deposition. *Diamond and Related Materials* **2002,** *11* (1), 59-66.

[11] Lim, S. H.; Yoon, H. S.; Moon, J. H.; Park, K. C.; Jang, J., Optical emission spectroscopy study for optimization of carbon nanotubes growth by a triode plasma chemical vapor deposition. *Applied Physics Letters* **2006,** *88*, 033114.

[12] Delzeit, L.; McAninch, I.; Cruden, B. A.; Hash, D.; Chen, B.; Han, J.; Meyyappan, M., Growth of multiwall carbon nanotubes in an inductively coupled plasma reactor. *Journal of Applied Physics* **2002,** *91* (9), 6027-6033.

[13] Rodriguez, N. M.; Chambers, A.; Baker, R. T. K., Catalytic engineering of carbon nanostructures. *Langmuir* **1995,** *11* (10), 3862-3866.

[14] Kim, H.; Sigmund, W., Iron particles in carbon nanotubes. *Carbon* **2005,** *43* (8), 1743-1748.

[15] Yao, Y.; Falk, L. K. L.; Morjan, R. E.; Nerushev, O. A.; Campbell, E. E. B., Synthesis of carbon nanotube films by thermal CVD in the presence of supported catalyst particles. Part II: the nanotube film. *Journal of Materials Science-Materials in Electronics* **2004,** *15* (9), 583-594.

[16] Golberg, D.; Mitome, M.; Muller, C.; Tang, C.; Leonhardt, A.; Bando, Y., Atomic structures of iron-based single-crystalline nanowires crystallized inside multi-walled carbon nanotubes as revealed by analytical electron microscopy. *Acta Materialia* **2006,** *54* (9), 2567-2576.

[17] Yoshida, H.; Takeda, S.; Uchiyama, T.; Kohno, H.; Homma, Y., Atomic-scale in-situ observation of carbon nanotube growth from solid state iron carbide nanoparticles. *Nano Letters* **2008,** *8* (7), 2082-2086.

[18] Blank, V. D.; Alshevskiy, Y. L.; Zaitsev, A. I.; Kazennov, N. V.; Perezhogin, I. A.; Kulnitskiy, B. A., Structure and phase composition of a catalyst for carbon nanotiber formation. *Scripta Materialia* **2006,** *55* (11), 1035-1038.

[19] Tanaka, A.; Yoon, S. H.; Mochida, I., Preparation of highly crystalline nanofibers on Fe and Fe-Ni catalysts with a variety of graphene plane alignments. *Carbon* **2004,** *42* (3), 591-597.

[20] Agarwal, S.; Takano, A.; van de Sanden, M. C. M.; Maroudas, D.; Aydil, E. S., Abstraction of atomic hydrogen by atomic deuterium from an amorphous hydrogenated silicon surface. *Journal of Chemical Physics* **2002,** *117* (23), 10805-10816.

[21] Coburn, J. W.; Chen, M., Optical-Emission Spectroscopy of Reactive Plasmas - A Method for Correlating Emission Intensities to Reactive Particle Density. *Journal of Applied Physics* **1980,** *51* (6), 3134-3136.

[22] Gicquel, A.; Chenevier, M.; Hassouni, K.; Tserepi, A.; Dubus, M., Validation of actinometry for estimating relative hydrogen atom densities and electron energy evolution in plasma assisted diamond deposition reactors. *Journal of Applied Physics* **1998,** *83* (12), 7504-7521.

[23] Denysenko, I. B.; Xu, S.; Long, J. D.; Rutkevych, P. P.; Azarenkov, N. A.; Ostrikov, K., Inductively coupled Ar/CH4/H-2 plasmas for low-temperature deposition of ordered carbon nanostructures. *Journal of Applied Physics* **2004,** *95* (5), 2713-2724.

[24] Ma, J.; Ashfold, M. N. R.; Mankelevich, Y. A., Validating optical emission spectroscopy as a diagnostic of microwave activated $CH_4/Ar/H_2$ plasmas used for diamond chemical vapor deposition. *Journal of Applied Physics* **2009,** *105*, 043302.

[25] Deschenaux, C.; Affolter, A.; Magni, D.; Hollenstein, C.; Fayet, P., Investigations of CH_4, C_2H_2 and C_2H_4 dusty RF plasmas by means of FTIR absorption spectroscopy and mass spectrometry. *Journal of Physics D-Applied Physics* **1999,** *32* (15), 1876-1886.

[26] Nemanich, R. J.; Glass, J. T.; Lucovsky, G.; Shroder, R. E., Raman-scattering characterization of carbon bonding in diamond and diamondlike thin-films. *Journal of Vacuum Science & Technology a-Vacuum Surfaces and Films* **1988,** *6* (3), 1783-1787.

[27] Ferrari, A. C.; Robertson, J., Interpretation of Raman spectra of disordered and amorphous carbon. *Physical Review B* **2000,** *61* (20), 14095-14107.

[28] Tuinstra, F.; Koenig, J. L., Raman spectrum of graphite. *The Journal of Chemical Physics* **1970,** *53* (3), 1126-1130.

[29] Williams, D. B.; Carter, C. B., *Transmission electron microscopy : a textbook for materials science*. New York : Plenum Press: New York, 1996.

[30] Behr, M. J.; Gaulding, E. A.; Mkhoyan, K. A.; Aydil, E. S., Catalyst rotation, twisting, and bending during multiwall carbon nanotube growth. **Submitted 2010**.

8 Hydrogen Etching and Cutting of Multiwall Carbon Nanotubes

The interaction of H atoms with the curved concentric graphene walls of a multiwall carbon nanotube (MWCNT) and the stacked planar graphene sheets of graphite was investigated using a combination of high resolution transmission electron microscopy (HRTEM) in conjunction with electron energy-loss and Raman spectroscopies. Continuous cylindrical graphene walls of a nanotube are etched and amorphized by the H atoms. Etching is not uniform across the length of the CNT, but rather, small etch pits form at defective sites on the CNT walls along the entire nanotube length. Once an etch pit is formed, etching proceeds rapidly, and the remainder of the CNT is quickly etched away. The carbon K core-loss edge spectra collected from etch pits do not differ from spectra collected from pristine CNT walls, indicating that reactions occur exclusively at the exposed graphene edges. Similar observations were made when sheets of planar graphite were exposed to H atoms. Confocal Raman spectroscopic measurements revealed that H etching occurs preferentially at the graphite edges. Eventually, large holes appear in the graphite, as observed under HRTEM. Etched holes in planar graphite are similar to the etch pits that form when a graphene layer is rolled up to form the cylindrical walls of a CNT. Once a hole or etch pit is formed, the edges of the planar graphene sheets or cylindrical CNT walls become exposed, and H etching proceeds quickly from these edges.

8.1 Introduction

A fundamental understanding of the interactions of atomic and molecular hydrogen with nanostructured carbon materials such as carbon nanotubes (CNTs), graphite, and graphene, is important for several reasons. First, hydrogen is ubiquitous during the synthesis of these materials using methods such as plasma-enhanced chemical vapor deposition (PECVD) [1]. A fundamental understanding of the interactions of H with CNTs and graphene layers can lead to an improved understanding of the role of H during their synthesis. Second, CNTs and graphene have been suggested as potential hydrogen storage materials [2]. Finally, hydrogen has the

ability to change both the electronic properties and the atomic arrangements of carbon atoms in these nanostructured carbon materials. For example, it has been shown that addition of hydrogen to a hydrocarbon precursor gas is required to grow well-graphitized CNTs; changing the amount of hydrogen present during growth drastically affects the structure of the carbon nanotubes [3-11]. Specifically, we showed, recently, that the highest quality MWCNTs with the narrowest diameter distribution were produced when H_2 and CH_4 were added in equal proportions to the plasma. On the other hand, if the H_2-to-CH_4 ratio in the feed gas is too high, CNTs do not grow [3].

Exposure to an H_2 plasma can drastically change the electronic properties of CNTs. Zhang et al. found that exposure of SWCNTs to an RF hydrogen plasma for 3 minutes created various C-H_x species on the CNT side walls and resulted in a significant decrease in its electrical conductance [12]. Density functional theory calculations show that the band gap of a SWCNT can be changed dramatically through the hydrogenation of its graphene walls [13]. Similar electronic changes are observed when a single layer of graphite, also known as graphene, is hydrogenated. Upon hydrogenation, the normally highly-conductive semimetal graphene is transformed into an insulator [14]. Hydrogenation, and hence the changes in the electronic properties, have been found to be completely reversible by heating to ~450-600 ^{o}C [14-16].

The atomic structure of a CNT can also undergo severe physical distortions and even structural changes when H atoms interact with its cylindrical graphene wall(s). This is the case when the flux of H atoms is much larger than the modest H-atom fluxes present during CNT synthesis from CH_4/H_2 gas mixtures. For example, Muniz et al. studied the effects of hydrogen chemisorption using molecular dynamics simulations and found that upon hydrogenation, CNTs expand with increasing H coverage [17]. When the H dose and H-atom exposure temperature is increased, irreversible structural changes to the CNT structure can begin [18]. For example, Zhang et al. observed that when plasma power, or H-exposure time was increased, CNTs were cut and etched [12]. Rao et al. found that SWCNTs were easily etched by H_2 at 900 ^{o}C but remained unaffected at 800 ^{o}C [19].

In addition to etching, interactions with H atoms have also been predicted to induce structural rearrangements in the layered graphene nanotube and planar graphite structures. For example, a variety of crystalline carbon phases, such as diamond [20], and other hydrogenated crystalline carbon phases [21] have been predicted to form as a result of repeated interactions between H atoms and the concentric graphene walls of a MWCNT. Experiments by Sun et al. [22] and Yang et al. [23] suggest that indeed H-atom exposure can transform MWCNTs to diamonds. Unfortunately, these reports lack the atomic-scale chemical analysis needed to show unambiguously that the observed crystals are indeed composed of carbon.

In this study, we use atomic-scale chemical analysis, specifically electron energy-loss spectroscopy (EELS), coupled with high-resolution transmission electron microscopy (HRTEM), and confocal Raman spectroscopy to systematically investigate the evolution of MWCNTs and planar graphite when they are exposed to H atoms generated through electron impact dissociation in an H_2 plasma.

8.2 Materials and Methods

MWCNTs used in this study were grown using a radio-frequency (RF at 13.56 MHz) inductively-coupled plasma and iron catalyst through PECVD, as described in a previous publication [24]. CNTs grew to ~4 microns in length, diameters ranged from ~25-35 nm, and the number of concentric graphene walls was typically greater than 20. CNT films were sonicated briefly in ethanol to remove them from the silicon substrate, and then dispersed from solution on amorphous silicon nitride membrane window TEM grids, obtained from SPI Supplies, Inc. For comparison, we also purchased and used MWCNTs from Catalytic Materials LLC. These CNTs had outer diameters ranging from 9 to 24 nm, and were typically composed of 10 or more concentric graphene walls. The third material studied was graphite. For these studies, highly-oriented pyrolytic graphite (HOPG) disks, grade SPI-3, which exhibit a mosaic angle ~$3.5^o \pm 1.5^o$, and an average grain size of 30-40 nm were obtained from SPI Supplies Inc.

CNTs and HOPG disks were exposed to hydrogen atoms created by electron-impact dissociation of H_2 in an H_2:Ar (50:2.5 sccm) plasma maintained with 200 W RF power in the

same inductively-coupled plasma reactor used for CNT growth [25]. Hydrogen atom exposures were conducted over a temperature range of 25 ^{o}C to 725 ^{o}C, and over a pressure range of 0.15 – 1 Torr, in increments of 15 minutes. To prevent ion bombardment, the plasma source was located approximately 25 cm above the substrate platen, while a grounded stainless-steel mesh immediately above the substrate prevented electric fields from forming a plasma immediately above the substrate. As a result, the sample was not irradiated with ions or electrons during plasma exposure. During H_2 plasma exposure at 0.15 Torr, we determined the H-atom flux to the substrate to be 2.2×10^{17} $cm^{-2}s^{-1}$ using a method based on measuring the changes in the free-electron concentration in a polycrystalline ZnO thin film as a result of H incorporation, with Fourier-transform infrared spectroscopy. The details of this method are given in the Appendix.

The temperature of the resistively-heated substrate platen was monitored using a thermocouple, while substrate temperature was calibrated independently by measuring the temperature-dependent position of the direct band edge of silicon with a spectroscopic ellipsometer. During H exposure at 25 ^{o}C, the substrate heater was turned off; the thermocouple typically measured a temperature of 30 ^{o}C after 15 minutes of H-atom exposure.

CNTs and HOPG disks were examined for structural changes after each 15-minute increment of H-exposure with HRTEM and EELS using a Tecnai G2 F30 TWIN 300-keV field emission gun TEM, equipped with a bottom-mounted Gatan Ultrascan 4000 SP digital CCD camera, and Gatan 2002 GIF spectrometer. All samples were held under a heat lamp for approximately 1 hour before inserting them into the microscope. Unique markings on the TEM grids enabled us to return to and examine the same nanotube after each 15-minute H exposure. We typically kept track of numerous nanotubes but only show representative results here. In addition to HRTEM images, EELS spectra of the carbon K-edge, with onset at ~285 eV, were measured at multiple locations along the lengths of over 30 MWCNTs from each sample. During EELS acquisition, the electron beam was defocused, such that the beam diameter was slightly larger than the diameter of the CNT. The purpose of using a slightly spread beam was (i) to reduce the incident electron beam current density to prevent beam-induced damage to the CNT walls, and (ii) to sample the entire diameter of the nanotube, in order to average out changes in the C K-edge fine structure as a result of the inherent continuously-changing orientation of the CNT

graphene walls relative to the incident electron beam [26]. At each location, five EELS spectra were collected using a one-second integration time, which were then averaged to improve the signal-to-noise ratio. This brief exposure did not damage the CNT walls: the fine structure of the C K-edge remained constant. A camera length of 470 mm, and a 2 mm spectrometer entrance aperture yielded a collection semi-angle of 1.53 mrad and were kept constant throughout this entire study. An energy dispersion of 0.3 eV/channel was used. The energy resolution, measured as the full-width-at-half the maximum of the zero-loss peak was ~1.2 eV.

All EELS spectra were processed individually within Gatan Digital Micrograph and OriginLab software packages. The slowly-decreasing background present in all spectra, arising from multiple inelastic scattering events, was subtracted from each C K-edge by fitting the pre-edge background over a 60 eV wide window to an inverse power law function $I = AE^{-r}$, where the fitting parameter r ranged from 2-5 [27]. Relative changes to the π^* and σ^* peaks at ~285.5 eV and ~292.5 eV [28], respectively, were calculated by integrating the intensity under the peaks over a 1.5 eV wide window, centered around the maximum of each peak. No detectable amorphous carbon was found to build up as a result of the brief electron-beam exposures used in this study.

Average HOPG structure was further characterized using Raman spectroscopy. Raman spectra of the HOPG disks from face and edge locations were collected using a Witec alpha300R Raman spectrometer in the confocal backscattering geometry. An argon ion laser (514.5 nm wavelength) operating at 20 mW and focused to ~1 μm spot provided excitation. Raman scattering was detected using a DV401 CCD peltier-cooled detector.

8.3 Results and Discussion

8.3.a Observations with TEM

Examining individual MWCNTs with TEM after each 15-minute increment of H-atom exposure revealed that H atoms etch and amorphize the concentric graphene walls. Figure 8-1 shows a collection of bright-field (BF) TEM images of MWCNTs before H-exposure (Figure 8-1 (a)-

(c)), after 15 minutes H exposure (Figure 8-1 (d)-(f)), and after 30 minutes H exposure (Figure 8-1 (g)-(i)) at room temperature. The CNT shown in each panel is the same CNT across any row in Figure 8-1. The initial CNT structure, before exposure to the H atoms, is already quite defective. In fact, at numerous locations along the nanotube length, interior walls are connected to form cups perpendicular to the nanotube axis. Additionally, many graphene walls are oriented at an angle relative to the CNT axis and terminate at the tube exterior, which results in a rough CNT exterior with many exposed graphene edges. After 15 minutes of H-atom exposure, nanotube exteriors become significantly rougher. Careful examination reveals that at certain locations along the CNT length, small divots, or etch pits, ~2 nm deep are present and cut into the CNT walls. A few such locations are indicated in Figure 8-1(f) with arrows. Continued H-exposure for an additional 15 minutes significantly increases the size and number of these pits along the CNT walls. In some areas in the vicinity of etch pits, the initially-crystalline graphite-like CNT structure appears amorphous as a result of the H-atom exposure (Figure 8-1(i)). In this image, some regions of the CNT still exhibit lattice fringes that correspond to the ordered concentric graphene walls, while other regions do not, and appear completely disordered. Also evident in Figure 8-1 is the decrease in average diameter as a result of carbon removal from the exterior of the CNTs during exposure to H-atoms. Upon further H-atom exposure, for a cumulative time of 45 minutes, CNTs were completely etched from the silicon nitride TEM grid. The etching, or carbon removal rate, was found to increase substantially with increased H-exposure time.

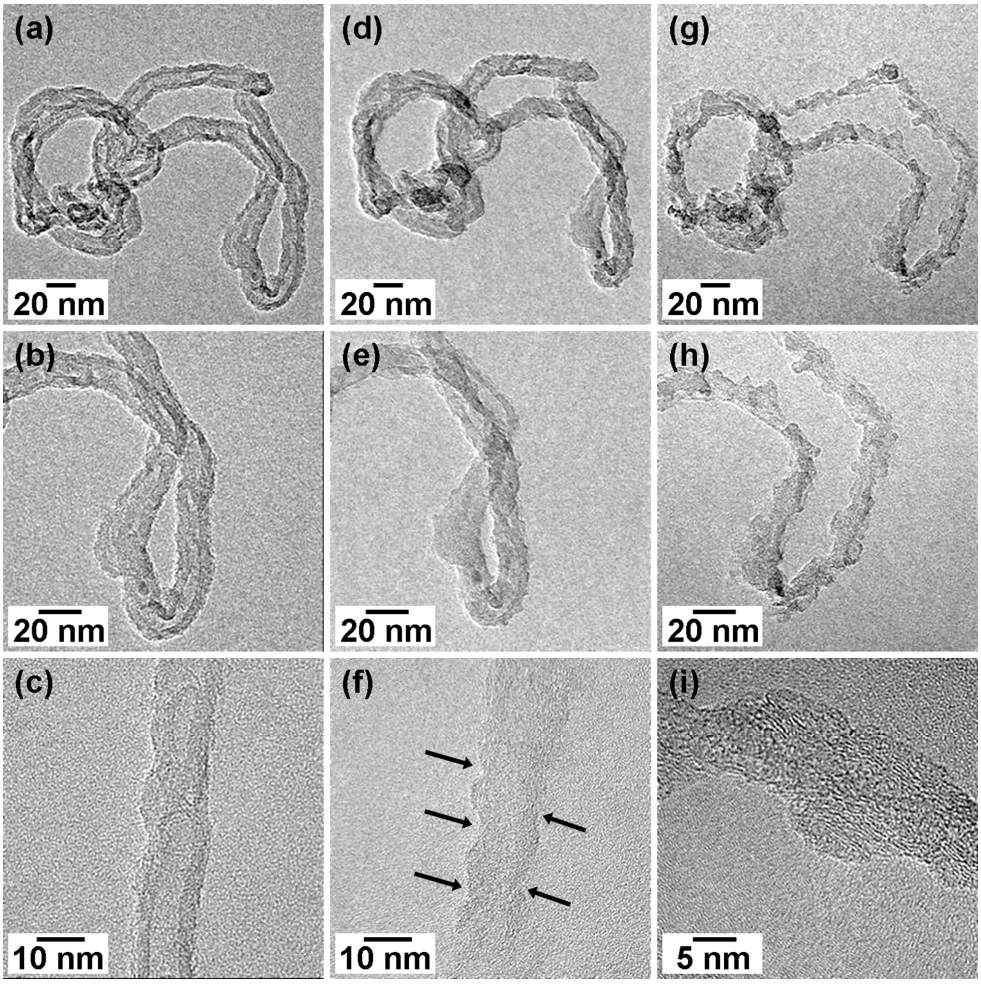

Figure 8-1. (a)-(c) in the first column show BF-TEM images of segments of a MWCNT before H-atom exposure. (d)-(f) show the same segments after 15 minutes of H-atom exposure at room temperature. Nanotube walls show increased roughness due to formation of etch pits as indicated in (f). (g)-(i) show the same segments after a total H-atom exposure of 30 minutes. Numerous deep etch pits are observed along the nanotube lengths. Some regions are also now amorphous. The CNT shown in each panel is the same CNT across any row.

Hydrogen atoms are also found to etch and change the structure of planar sheets of graphite. Experiments with planar graphite sheets further our understanding of the reactions occurring on CNTs. Figure 8-2 shows BF-TEM images of HOPG flakes that were exposed to H atoms for 6 hours at room temperature. Compared to the etching of MWCNTs over the course of 30 minutes (Figure 8-1), H reactions with HOPG occur much slower. The initially-continuous and highly-crystalline sheet of graphite appears disordered after 6 hours of H-atom exposure and

contains numerous holes as a result of the interactions with and etching by H atoms. Most changes were observed near the graphite edges. Some areas appear amorphized, while many sections of the graphite sheet exhibited squiggly lattice fringes either grouped together in small domains, or in pairs, indicating that the graphite structure has been significantly changed. The HOPG flakes before H-atom exposure, as shown in Figure 8-2(c), appear completely crystalline and do not exhibit holes. Thinking of the structure of a MWCNT as a rolled-up piece of graphite, holes in the graphite sheet are akin to the etch pits observed in the walls of MWCNTs. If a hole is present in the graphite sheet, then it forms a pit in the CNT walls when the sheet is rolled into a cylinder. These observations suggest that the atomic reactions of H with the ordered graphene networks of planar HOPG and MWCNTs are similar.

The anisotropic and nonuniform nature of graphene layer etching with H is especially evident when higher quality MWCNTs, i.e., nanotubes with continuous walls with no visual structural defects, are exposed to H atoms. Figure 8-3 (a) and (b) shows BF-TEM images of a one such well-graphitized MWCNT that was exposed to an H plasma for 10 minutes at 725 ^{o}C. After this relatively short H-atom exposure, numerous large etch pits had formed at multiple locations along the nanotube length; in some cases, hydrogen consumed approximately three-fourths of the nanotube diameter. Between etch pits, however, sections of pristine CNT graphene walls still exist; the walls in these regions appeared identical to the pre-exposed CNT. Often, these walls remained pristine until they terminated abruptly to form the edge of the etch pit. Once an etch pit forms, C is preferentially and rapidly removed from the edges of this pit. Consequently, continued H-exposure causes the etch pits to grow quickly both in width and depth. Figure 8-3 (c) and (d) shows a MWCNT from the same sample after only an additional 2 minutes (12 minutes total) of H exposure at 725 ^{o}C. During these additional 2 minutes, H atoms continued to preferentially react with and remove carbon from the exposed graphene edges of the existing etch pits, causing them to grow larger until the entire diameter of the CNT was cut in half. Figure 8-3(a) shows a CNT that has been cut into smaller segments by this etching process. Each segment usually contains a region that is still pristine. Occasionally, near the edges of the etch pits, or where the nanotube was cut in half, the CNT walls appear amorphous [see Figure 8-3(d)]. It is clear from these observations that H-etching occurs faster at the exposed graphene

edges within an etch pit while reactions with the continuous pristine graphene basal planes of nanotube walls between etch pits occur slowly.

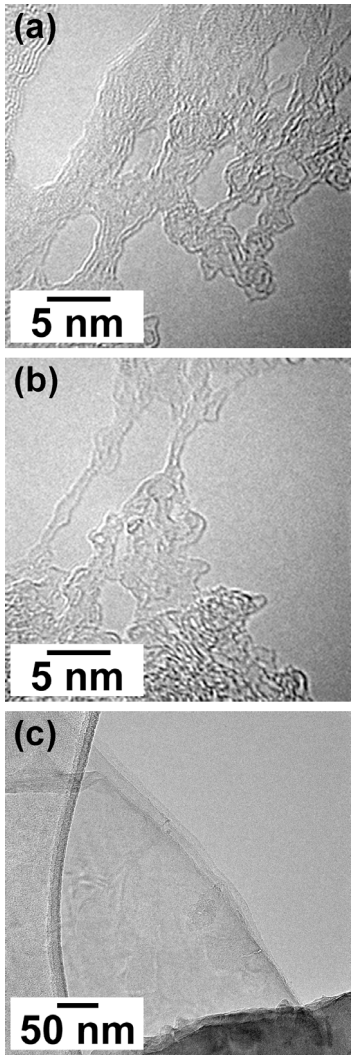

Figure 8-2. (a) and (b) High-resolution BF-TEM images of different locations along the edge of a HOPG flake after 60 minutes of H-atom exposure at room temperature. The initially highly-crystalline layered HOPG structure is now very disordered, as evident by the random and squiggly lattice fringes, and contains holes. (c) BF-TEM of a HOPG flake before H-atom exposure is highly crystalline, and does not contain holes.

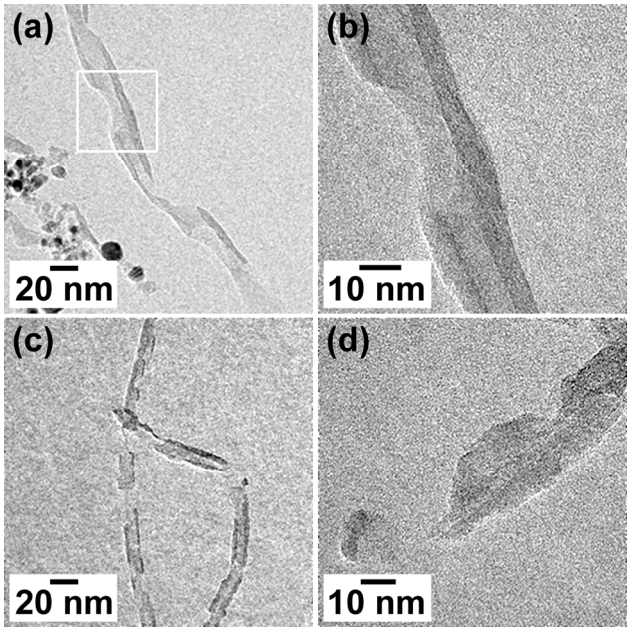

Figure 8-3. (a) BF-TEM image of a high-quality, well-graphitized MWCNT that has received 10 minutes of H-atom exposure at 725 ^{o}C. Numerous etch pits are present along the nanotube length; one etch pit is indicated with the white rectangle. (b) Magnified imaged of the etch pit enclosed by the white rectangle in (a). (c) A MWNCT from the same sample that received an additional 2 minutes of H-atom exposure. During this short additional exposure, H atoms reacted rapidly at the exposed graphene edges of etch pits to completely cut through the nanotube. (d) A magnified image of a location where the nanotube was cut shows that some of the carbon in this vicinity is amorphous.

8.3.b Raman spectroscopy

Raman spectroscopy was used to probe and compare the changes in the structure of a single piece of HOPG along its basal plane (face), and at its edges when exposed to H atoms from an H_2 plasma. First-order Raman spectra recorded, before H-exposure, from the face and edges of a HOPG disk are shown in Figure 8-4 (a) and (b), respectively. The Raman spectra show two major peaks, a G peak at ~1580 cm^{-1}, and a D peak at ~1350 cm^{-1} [29, 30]. The ratio, I(D)/I(G), is often used as a measure of the disorder in a graphitic carbon structure, or in the case of graphite, as a measure of its crystallite size, or interdefect distance [30, 31]. The G peak corresponds to in-plane stretching of sp^2 C-C bonds in rings or chains, while the D peak corresponds to breathing modes of sp^2 C-C bonds in rings only: the D peak is only present when the symmetry of the graphite is broken [29]. The ratio I(D)/I(G) was calculated from peak

heights and displayed on each plot of Figure 8-4. Peaks heights were used instead of the area under the peak, because it is known that the D peak width increases more than the G peak width with decreasing crystal size [32]. Before H-atom exposure, both spectra are dominated by the G peak at ~1580 cm^{-1} (Figure 8-4 (a) and (b)). The presence of the D peak on the face of the HOPG, though small, indicates that the structural order is not perfect even in this HOPG sample. Nevertheless, this gives a reference level for this ratio in a presumably highly ordered and symmetric graphitic structure like HOPG. Intensity ratios, I(D)/I(G), of 0.02 and 0.05 were determined from peak heights for the face and edge of the HOPG disk, respectively. Upon H-atom exposure of the HOPG disk for 1 hour at room temperature, significant changes to the spectra were observed (Figure 8-4 (c) and (d)). Specifically, a large increase in both the D and G peak widths, and the appearance of a new peak at ~1617 cm^{-1}, referred to as the D' peak [33-35], indicate increased disorder (i.e., defects) and the formation of new crystalline edges [36-38]. Most notable, however, is the dramatic increase in the D-band intensity at both the face and edge positions on the HOPG disk. The D-band intensity from the edge of the disk grew significantly and even surpassed the G-peak height. The I(D)/I(G) ratio at the HOPG edge after H-atom exposure has increased to 1.1, while at the face of the HOPG disk, it has only increased to 0.8. This larger ratio observed at the graphite edge indicates that a higher level of disorder is present here as compared to the graphite face, as a result of the 1 hour of H-atom exposure. This suggests that the exposed edges of graphite are more reactive, and thus H will react at these sites preferentially, causing structural transformations or etching to occur here first. This conclusion is corroborated with TEM images shown in Figure 8-2.

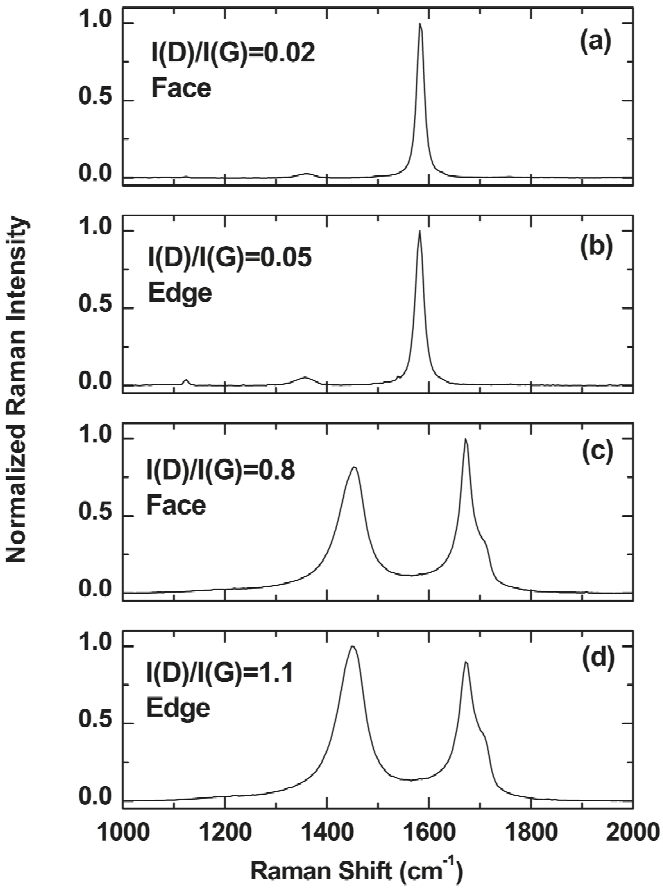

Figure 8-4. First-order Raman spectra of a HOPG flake face (a) and edge (b) before H-atom exposure. The intensity ratio I(D)/I(G) is was calculated and is displayed on each plot. Raman spectra obtained from the face (c) and edge (d) of the HOPG flake after 60 minutes of H-atom exposure at room temperature. The greater increase in the intensity ratio I(D)/I(G) at the HOPG edge indicates that H preferentially reacts here.

8.3.c Electron Energy-Loss Spectroscopy

To examine the reactions that cause etching and amorphization of the CNT walls, we examined the type of carbon bonding present as a function of H-atom exposure time using EELS. Specifically, we measured the C K core-loss edge at numerous etch pits and pristine regions along the lengths of over 30 MWCNTS after each increment of H-atom exposure at room temperature. For this experiment, EELS measurements were made after H exposures of 0.5, 2.5, 7.5, 17.5, and 30 minutes. A representative EEL spectrum obtained from a MWCNT is

shown in Figure 8-5(a). There are two primary peaks in the C K core-loss edge, the π* peak at 285.5 eV, and the σ* peak at 292.5 eV [28]. The intensity ratio of these two peaks depends on the orientation of the graphite-like CNT walls relative to the incident electron beam, and on the hybridization of carbon bonding present [27, 39-41]. All spectra were collected with the electron beam defocused, such that the diameter of the beam was larger than the CNT diameter. This practice averages the signal across many ring orientations so that any changes to the π*-to-(π*+σ*) ratio would be a direct measure of changes in carbon bonding hybridization. Initially, the pristine MWCNTs exhibit purely sp^2-hybridized carbon bonding. The average π*-to-(π*+σ*) intensity ratio of MWCNTs before H exposure as determined from measurements at various locations on over 30 nanotubes was 0.43. Any H-induced transformation of carbon bonding to sp^3-hybridized carbon either during the etching or amorphization processes would decrease this ratio from its initial value of 0.43, since a purely sp^3-bonded sample does not exhibit a π* peak [41, 42]. However, over the course of 30 minutes of H-atom exposure, no change to the relative intensities of the π* and σ* peaks was observed. The plot of Figure 8-5(b) shows that the π*-to-(π*+σ*) ratio as a function of H-exposure time remains unchanged, even though numerous etch pits had formed, and some regions appeared amorphous as a result of the exposure. A typical amorphous carbon material, which is composed of both sp^2- and sp^3-bonded carbon, produces an average π*-to-(π*+σ*) intensity ratio of ~0.35 [43]. A change of this magnitude would be easily discernible with EELS. However, the major contribution to the C K-edge signal comes from the graphene nanotube walls that surround each etch pit, because the incident electron beam is defocused. If the edges of an etch pit that appear amorphous are composed of only sp^3-bonded carbon, we calculate that this would contribute only ~4% to the total K-edge signal. Thus, the unchanged π*-to-(π*+σ*) ratio after H-atom exposure is primarily a measure of the structure of the continuous basal graphene walls of the carbon nanotube that surround each etch pit, and indicates that these carbon atoms remain purely sp^2-bonded. This further corroborates TEM and Raman observations that H atoms preferentially react and affect the structure of the CNT walls at exposed graphene edges.

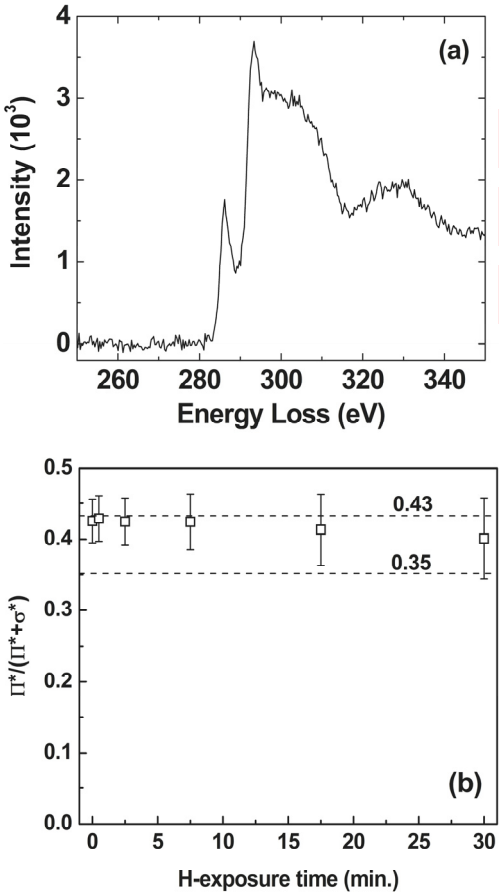

Figure 8-5. (a) A representative EELS spectrum of the carbon K-edge obtained from a MWCNT. The π* and σ* peaks are labeled. The incident electron beam was defocused such that the entire diameter of the nanotube was probed. (b) A plot of the π*-to-(π*+σ*) intensity ratio as measured by integrating over a 1.5 eV-wide window centered around each peak, as a function of H-plasma exposure time. This ratio remains constant over the 30 minutes of H-plasma exposure, which indicates that the amorphous carbon formed remains sp^2-hybridized.

8.3.d Discussion

The study and comparison of H interactions on planar graphite with H interactions on MWCNTs has offered insights into the observations made during etching of MWCNTs. Graphite is found to be most susceptible to incident H atoms at its exposed edges. Likewise, a carbon nanotube is most susceptible to H atoms at etch pits, where fresh graphene edges are exposed. The observed growth of etch pits and eventual cutting of the CNT diameter is a direct consequence of these sites' higher reactivity.

The initial formation of an etch pit may occur at a site along the outer CNT wall that contains a defect. Atomic-scale defects such as small changes in carbon ring size due to strain or dangling bonds on the outer wall of a MWCNT are not easy to detect even with TEM. However, appearance of hemispherical etch pits in distinct locations on the MWCNT walls and holes in planar graphene layers in HOPG point to existence of such defect sites that serve as the nucleation site for these pits and holes. Once hydrogen interacts with such defects to expose the edges of the stacked graphene layers, etching reactions proceed very quickly to widen the etch pit or the hole.

Curvature of the graphene CNT walls appears to play a significant role in the speed at which CNTs etch. We observe that thicker CNTs take longer H-atom exposure to etch than do thinner nanotubes, i.e., CNTs with higher curvature etch faster. This observation is consistent with studies by Zhang et al. who observed that small-diameter single-wall CNTs exhibit higher hydrogenation reactivity [44], and are etched and cut more easily by H atoms than are thicker diameter tubes [12]. Planar graphite has no curvature and we find that significantly longer H-atom exposures were needed to etch and transform the planar graphite samples, as compared to the very short H-atom exposures that etched and transformed MWCNTs.

8.4 Conclusions

The interaction of H atoms with the layered graphene structures in MWCNTs and HOPG was investigated using TEM, Raman spectroscopy, and EELS. Incident H atoms from the H_2 plasma preferentially react at the exposed graphene edges of HOPG flakes, resulting in etching, and structural transformations of the carbon atoms. Hydrogen atoms also react at defects present on the face of HOPG layers and etch holes through the HOPG flakes. This same anisotropic etching is also observed when MWCNTs are exposed to H-atoms generated in an H_2 plasma. It is observed that H reacts at various locations along the nanotube length to form etch pits into the nanotube walls; once formed, etch pits grow rapidly with further H exposure because of the large number of exposed graphene edges, until the entire tube diameter is consumed. Often, graphene walls in segments between etch pits remain pristine, while in other cases, graphene layers are amorphous as a result of the H exposure. Reactions with H atoms

occur much faster for MWCNTs than with HOPG, suggesting that curvature increases the reactivity.

8.5 References

[1] Meyyappan, M.; Delzeit, L.; Cassell, A.; Hash, D., Carbon nanotube growth by PECVD: a review. *Plasma Sources Science & Technology* **2003,** *12* (2), 205-216.

[2] Dillon, A. C.; Jones, K. M.; Bekkedahl, T. A.; Kiang, C. H.; Bethune, D. S.; Heben, M. J., Storage of hydrogen in single-walled carbon nanotubes. *Nature* **1997,** *386* (6623), 377-379.

[3] Behr, M. J.; Gaulding, E. A.; Mkhoyan, K. A.; Aydil, E. S., Effect of hydrogen on catalyst in carbon nanotube growth. **Submitted 2010**.

[4] Caughman, J. B. O.; Baylor, L. R.; Guillorn, M. A.; Merkulov, V. I.; Lowndes, D. H.; Allard, L. F., Growth of vertically aligned carbon nanofibers by low-pressure inductively coupled plasma-enhanced chemical vapor deposition. *Applied Physics Letters* **2003,** *83* (6), 1207-1209.

[5] Lee, T. Y.; Han, J. H.; Choi, S. H.; Yoo, J. B.; Park, C. Y.; Jung, T.; Yu, S.; Yi, W. K.; Han, I. T.; Kim, J. M., Effects of source gases on the growth of carbon nanotubes. *Diamond and Related Materials* **2003,** *12* (3-7), 851-855.

[6] Nolan, P. E.; Lynch, D. C.; Cutler, A. H., Carbon deposition and hydrocarbon formation on group VIII metal catalysts. *Journal of Physical Chemistry B* **1998,** *102* (21), 4165-4175.

[7] Bell, M. S.; Teo, K. B. K.; Milne, W. I., Factors determining properties of multi-walled carbon nanotubes/fibres deposited by PECVD. *Journal of Physics D-Applied Physics* **2007,** *40* (8), 2285-2292.

[8] Chhowalla, M.; Teo, K. B. K.; Ducati, C.; Rupesinghe, N. L.; Amaratunga, G. A. J.; Ferrari, A. C.; Roy, D.; Robertson, J.; Milne, W. I., Growth process conditions of vertically aligned carbon nanotubes using plasma enhanced chemical vapor deposition. *Journal of Applied Physics* **2001,** *90* (10), 5308-5317.

[9] Woo, Y. S.; Jeon, D. Y.; Han, I. T.; Lee, N. S.; Jung, J. E.; Kim, J. M., In situ diagnosis of chemical species for the growth of carbon nanotubes in microwave plasma-enhanced chemical vapor deposition. *Diamond and Related Materials* **2002,** *11* (1), 59-66.

[10] Lim, S. H.; Yoon, H. S.; Moon, J. H.; Park, K. C.; Jang, J., Optical emission spectroscopy study for optimization of carbon nanotubes growth by a triode plasma chemical vapor deposition. *Applied Physics Letters* **2006,** *88* (3).

[11] Delzeit, L.; McAninch, I.; Cruden, B. A.; Hash, D.; Chen, B.; Han, J.; Meyyappan, M., Growth of multiwall carbon nanotubes in an inductively coupled plasma reactor. *Journal of Applied Physics* **2002,** *91* (9), 6027-6033.

[12] Zhang, G. Y.; Qi, P. F.; Wang, X. R.; Lu, Y. R.; Mann, D.; Li, X. L.; Dai, H. J., Hydrogenation and hydrocarbonation and etching of single-walled carbon nanotubes. *Journal of the American Chemical Society* **2006,** *128* (18), 6026-6027.

[13] Barone, V.; Heyd, J.; Scuseria, G. E., Interaction of atomic hydrogen with single-walled carbon nanotubes: A density functional theory study. *Journal of Chemical Physics* **2004,** *120* (15), 7169-7173.

[14] Elias, D. C.; Nair, R. R.; Mohiuddin, T. M. G.; Morozov, S. V.; Blake, P.; Halsall, M. P.; Ferrari, A. C.; Boukhvalov, D. W.; Katsnelson, M. I.; Geim, A. K.; Novoselov, K. S., Control of graphene's properties by reversible hydrogenation: evidence for graphane. *Science* **2009,** *323* (5914), 610-613.

[15] Nikitin, A.; Ogasawara, H.; Mann, D.; Denecke, R.; Zhang, Z.; Dai, H.; Cho, K.; Nilsson, A., Hydrogenation of single-walled carbon nanotubes. *Physical Review Letters* **2005,** *95*, 225507.

[16] Zhang, H.; Meyer, F. W.; Meyer, H. M.; Lance, M. J., Surface modification and chemical sputtering of graphite induced by low-energy atomic and molecular deuterium ions. *Vacuum* **2008,** *82* (11), 1285-1290.

[17] Muniz, A. R.; Singh, T.; Maroudas, D., Effects of hydrogen chemisorption on the structure and deformation of single-walled carbon nanotubes. *Applied Physics Letters* **2009,** *94*, 103108.

[18] Lisowski, W.; Keim, E. G.; van den Berg, A. H. J.; Smithers, M. A., Structural and chemical evolution of single-wall carbon nanotubes under atomic and molecular deuterium interaction. *Carbon* **2005,** *43*, 1073-1083.

[19] Rao, F. B.; Li, T.; Wang, Y. L., Effect of hydrogen on the growth of single-walled carbon nanotubes by thermal chemical vapor deposition. *Physica E-Low-Dimensional Systems & Nanostructures* **2008,** *40* (4), 779-784.

[20] Muniz, A. R.; Singh, T.; Aydil, E. S.; Maroudas, D., Analysis of diamond nanocrystal formation from multiwalled carbon nanotubes. *Physical Review B* **2009,** *80* (14).

[21] Singh, T.; Behr, M. J.; Aydil, E. S.; Maroudas, D., First-principles theoretical analysis of pure and hydrogenated crystalline carbon phases and nanostructures. *Chemical Physics Letters* **2009,** *474* (1-3), 168-174.

[22] Sun, L. T.; Gong, J. L.; Zhu, Z. Y.; Zhu, D. Z.; He, S. X.; Wang, Z. X.; Chen, Y.; Hu, G., Nanocrystalline diamond from carbon nanotubes. *Applied Physics Letters* **2004,** *84* (15), 2901-2903.

[23] Yang, Q. Q.; Yang, S. L.; Xiao, C. J.; Hirose, A., Transformation of carbon nanotabes to diamond in microwave hydrogen plasma. *Materials Letters* **2007,** *61* (11-12), 2208-2211.

[24] Behr, M. J.; Mkhoyan, K. A.; Aydil, E. S., Catalyst rotation, twisting, and bending during multiwall carbon nanotube growth. **Submitted 2010**.

[25] Agarwal, S.; Takano, A.; van de Sanden, M. C. M.; Maroudas, D.; Aydil, E. S., Abstraction of atomic hydrogen by atomic deuterium from an amorphous hydrogenated silicon surface. *Journal of Chemical Physics* **2002,** *117* (23), 10805-10816.

[26] Leapman, R. D.; Silcox, J., Orientation dependence of core edges in electron-energy-loss spectra from anisotropic materials. *Physical Review Letters* **1979,** *42* (20), 1361-1364.

[27] Egerton, R. F., *Electron energy-loss spectroscopy in the electron microscope*. New York : Plenum Press: New York, 1996.

[28] Leapman, R. D.; Fejes, P. L.; Silcox, J., Orientation dependence of core edges from anisotropic materials determined by inelastic-scattering of fast electrons. *Physical Review B* **1983,** *28* (5), 2361-2373.

[29] Ferrari, A. C.; Robertson, J., Interpretation of Raman spectra of disordered and amorphous carbon. *Physical Review B* **2000,** *61* (20), 14095-14107.

[30] Tuinstra, F.; Koenig, J. L., Raman Spectrum of Graphite. *The Journal of Chemical Physics* **1970,** *53* (3), 1126-1130.

[31] Ferrari, A. C., Raman spectroscopy of graphene and graphite: Disorder, electron-phonon coupling, doping and nonadiabatic effects. *Solid State Communications* **2007,** *143* (1-2), 47-57.

[32] Cuesta, A.; Dhamelincourt, P.; Laureyns, J.; Martinez-Alonso, A.; Tascon, J. M. D., Comparative performance of X-ray diffraction and Raman microprobe techniques for the study of carbon materials. *Journal of Materials Chemistry* **1998,** *8* (12), 2875-2879.

[33] Nemanich, R. J.; Solin, S. A., 1^{ST}-order and 2^{ND}-order Raman-scattering from finite-size crystals of graphite. *Physical Review B* **1979,** *20* (2), 392-401.

[34] Thomsen, C.; Reich, S., Doable resonant Raman scattering in graphite. *Physical Review Letters* **2000,** *85* (24), 5214-5217.

[35] Saito, R.; Jorio, A.; Souza, A. G.; Dresselhaus, G.; Dresselhaus, M. S.; Pimenta, M. A., Probing phonon dispersion relations of graphite by double resonance Raman scattering. *Physical Review Letters* **2002,** *88*, 027401.

[36] Sadezky, A.; Muckenhuber, H.; Grothe, H.; Niessner, R.; Poschl, U., Raman micro spectroscopy of soot and related carbonaceous materials: Spectral analysis and structural information. *Carbon* **2005,** *43* (8), 1731-1742.

[37] Wang, Y.; Alsmeyer, D. C.; McCreery, R. L., Raman-Spectroscopy of Carbon Materials - Structural Basis of Observed Spectra. *Chemistry of Materials* **1990,** *2* (5), 557-563.

[38] Cancado, L. G.; Pimenta, M. A.; Neves, B. R. A.; Dantas, M. S. S.; Jorio, A., Influence of the atomic structure on the Raman spectra of graphite edges. *Physical Review Letters* **2004,** *93* (24), 4.

[39] Zhang, G. Y.; Mann, D.; Zhang, L.; Javey, A.; Li, Y. M.; Yenilmez, E.; Wang, Q.; McVittie, J. P.; Nishi, Y.; Gibbons, J.; Dai, H. J., Ultra-high-yield growth of vertical single-walled carbon nanotubes: Hidden roles of hydrogen and oxygen. *Proceedings of the National Academy of Sciences of the United States of America* **2005,** *102* (45), 16141-16145.

[40] Lifshitz, Y., Pitfalls in amorphous carbon studies. *Diamond and Related Materials* **2003,** *12* (2), 130-140.

[41] Saitoh, K.; Nagasaka, K.; Tanaka, N., Observation of the anisotropy of the inelastic scattering of fast electrons accompanied by the K-shell ionization of a carbon nanotube. *Journal of Electron Microscopy* **2006,** *55* (6), 281-288.

[42] Berger, S. D.; McKenzie, D. R.; Martin, P. J., EELS analysis of vacuum arc-deposited diamond-like films. *Philosophical Magazine Letters* **1988,** *57* (6), 285-290.

[43] Egerton, R. F.; Whelan, M. J., Electron energy loss spectra of diamond, graphite and amorphous carbon. *Journal of Electron Spectroscopy and Related Phenomena* **1974,** *3* (3), 232-236.

[44] Fallon, P. J.; Brown, L. M., Analysis of chemical-vapor-deposited diamond grain-boundaries using transmission electron-microscopy and parallel electron-energy-loss spectroscopy in a scanning-transmission electron-microscope. *Diamond and Related Materials* **1993,** *2* (5-7), 1004-1011.

9 On the transformation of carbon nanotubes to diamond

Carbon forms a variety of different allotropes including the familiar and well-established graphite, diamond, lonsdaleite, and fullerene structures, and has also been reported to exist in other cubic crystalline structures, referred to as i-carbon and n-diamond. Diamond, the hardest natural material known, usually requires extreme conditions to synthesize. Recently, it was reported that diamonds can be produced from multiwall carbon nanotubes that are exposed hydrogen atoms. However, despite convincing images, electron diffraction patterns, and Raman spectroscopy, no nanometer-scale chemical analysis has been presented. In light of this, we used nanometer-scale x-ray and energy-loss spectroscopies combined with high-resolution electron imaging and diffraction techniques to examine the possibility of H-induced structural transformations of multiwall carbon nanotubes to form other crystalline carbon phases, such as cubic diamond, lonsdaleite, i-carbon, and n-diamond.

9.1 Introduction

Carbon forms a variety of allotropes including cubic diamond, hexagonal diamond (lonsdaleite) [1, 2], graphite, and fullerenes [3, 4]. At ambient conditions, graphite is the most stable phase while cubic diamond is metastable. Cubic diamond can be formed under extreme conditions present deep within the earth [5, 6], by compressing graphite to high pressures [7, 8], or by activating graphitic carbon, by energetic ion and electron beams [9-12]. While surprising, it is also well known that thin diamond films can be grown through plasma enhanced chemical vapor deposition (PECVD) from methane and hydrogen in vacuum at high temperatures [13]. Lonsdaleite is only found in meteorites and is thought to have formed either through direct crystallization in space or by shock compression of graphitic carbon during the entry into the earth's atmosphere and subsequent impact [1, 2, 15].

Two additional cubic phases of carbon, referred to as n-diamond and i-carbon, have also been reported [7, 16]. These potential new phases have been encountered in carbon films deposited

from hydrocarbon and hydrogen containing electrical discharges and in carbonaceous materials that result upon shock compression of graphite. Their presence is typically argued based on electron diffraction evidence but, to our knowledge, no chemical analysis has been presented showing that the observed crystalline structures were composed purely of carbon [7, 16-18]. Peng et al. and Konyashin et al. are the only two studies that have provided high-resolution chemical analysis that showed carbon in crystals exhibiting lattice fringe spacings consistent with i-carbon and n-diamod phases [19, 20].

Sun et al. and Muniz et al. suggested that hydrogen can interact with and transform multiwall carbon nanotubes to a variety of crystalline carbon phases, such as diamond [25], lonsdaleite and other new hydrogenated crystalline carbon phases [26]. Indeed, it is well known that hydrogen atoms play a critical role in plasma deposition of group IV thin films such as nanocrystalline silicon, nanocrystalline germanium and diamond. In PECVD, diamond thin films nucleate and grow from hydrocarbon gases only when the feed gas contains significant amounts of H_2 or under conditions where atomic H is present in high concentrations [13, 21]. Another example is the transformation of hydrogenated amorphous silicon films to nanocrystalline silicon films upon exposure to H atoms from an H_2 plasma [22]. Crystallization of amorphous silicon has been shown to be mediated by the insertion into strained Si-Si bonds of H atoms as they diffuse through the film and by the concerted rearrangements of the bonds in the vicinity of the insertion reaction [23]. Recently, this mechanism was shown to produce crystalline silicon even at room temperature [24].

Thus, it may be reasonable to expect that H atoms interacting with concentric graphene walls of carbon nanotubes may transform them into other allotropes. Moreover, first-principles density-functional theory calculations coupled with molecular dynamics simulations showed possible mechanisms by which such transformations can occur and produce diamond and lonsdaleite from multiwall carbon nanotubes. Consistent with this expectation, Sun et al. reported that MWCNTs, when exposed to H atoms at 1073 K, are transformed to strings of diamonds [27]. In their report, they provided TEM images and selected area electron diffraction, but no nanometer-scale chemical analysis. Similarly, Yang et al. reported that exposure of MWCNTs to a hydrogen plasma transformed them to diamond [28]. However, their MWCNTs were

dispersed on a substrate that already contained nanometer size diamond crystals, and they also did not provide nanometer-scale chemical analysis.

Here we examine, carefully, whether cubic diamond, lonsdaleite, i-carbon, and n-diamond crystals can form from MWCNTs as a result of H-atom exposure. Specifically, we use high-resolution TEM imaging and diffraction combined with nanometer-scale EDX and EELS chemical analysis to examine nanocrystals that remain after hydrogen plasma exposure of multiwall carbon nanofibres (MWCNFs) and MWCNTs under a variety of conditions.

9.2 Experimental Methods

MWCNTs and multiwall carbon nanofibers (MWCNFs) were used as the starting materials for this study. MWCNFs were grown in our lab from an iron catalyst through plasma-enhanced chemical vapor deposition, in a similar fashion to a method reported earlier [29]. MWCNFs grew to ~4 microns in length, diameters ranged from ~40-60 nm, and the number of graphene walls was typically greater than 15. The name nanofiber is used to describe the stacked cup structure of the graphene sheets, as opposed to the long continuous cylindrical graphene walls of a nanotube. The MWCNTs used in this study were purchased from Catalytic Materials LLC. These CNTs were grown from an alloy catalyst containing cobalt. Nanotube outer diameters ranged from 9 to 24 nm, and the walls were usually composed of 10 or more concentric graphene layers. CNTs and CNFs were sonicated briefly in ethanol and then dispersed from solution on amorphous silicon nitride membrane window TEM grids, obtained from SPI Supplies, Inc.

MWCNFs and MWCNTs were exposed to hydrogen atoms created by electron-impact dissociation of dihydrogen in an H_2:Ar (50:2.5 sccm) plasma maintained with 200 W RF power. Hydrogen atom exposures were conducted over a temperature range of 300 K – 1073 K, and over a pressure range of 0.15 – 3.5 Torr, for durations ranging from 2-20 hours. The temperature of the resistively-heated substrate platen was monitored using a thermocouple, while substrate temperature was calibrated independently by measuring the temperature-dependent position of the direct band edge of silicon with a spectroscopic ellipsometer.

To prevent ion bombardment, the plasma source was located approximately 25 cm above the substrate platen, while a grounded stainless-steel mesh immediately above the substrate prevented electric fields from forming a plasma immediately above the substrate. As a result, the sample was not irradiated with ions or electrons during plasma exposure and received only H atoms and H_2 molecules. Control experiments conducted with H_2 alone did not produce the effects that were observed and described below. Thus we believe that the effects are only due to H atoms and hereafter refer to these plasma exposures as H-plasma exposure.

Nanocrystals that were present on the TEM grids after H-plasma exposure of CNFs and CNTs were examined with HRTEM, selected-area (SA) and convergent-beam (CB) electron diffraction, combined with energy-dispersive x-ray (EDX) and electron energy-loss (EEL) spectroscopies using a Tecnai G2 F30 TWIN 300-keV field emission gun TEM, equipped with a bottom-mounted Gatan Ultrascan 4000 SP digital CCD camera, and Gatan 2002 GIF.

9.3 Observations and Discussion

Examination of TEM grids initially covered with MWCNTs or MWCNFs after 15 hours of H-plasma exposure over a range of temperatures revealed that instead of fibers and tubes, TEM grids were covered with nanocrystals. Figure 9-1 shows BF-TEM images of MWCNFs that were exposed to an H_2 plasma for 15 hours at room temperature, and 3.5 torr. Long strings of crystallites, ~5 nm in size, are now present in locations where nanotubes once laid. The large cone-shaped crystals in both images are the Fe-based catalysts from which the nanofibers grew. The strings of crystals that follow behind each catalyst crystal look quite similar to the strings of crystals present in the TEM images of Sun et al [27].

In a similar experiment, MWCNTs were exposed to an H_2 plasma for 10 hours at room temperature. Figure 9-2 shows a BF-TEM image of an amorphous rod which contains numerous crystals, ~2-5 nm in size, embedded in it as indicated by the arrows. The figure inset is a HRTEM image of a representative crystal showing a 0.21 nm lattice fringe spacing. The majority of crystals examined from this sample all exhibited this 0.21 nm lattice fringe spacing.

In addition to the small crystals embedded in amorphous rod-like structures, chains of much larger crystals were also observed after H-plasma exposure. For example, Figure 9-3 shows a BF-TEM image of large agglomerates of crystallites, ~5-40 nm in diameter. This sample was initially covered with MWCNTs, and then exposed to an H_2 plasma for 10 hours at 725 K. Many of the crystals appear deformed, and rounded. Similar agglomerates of crystals were observed at all temperatures investigated, from 300 to 1073 K.

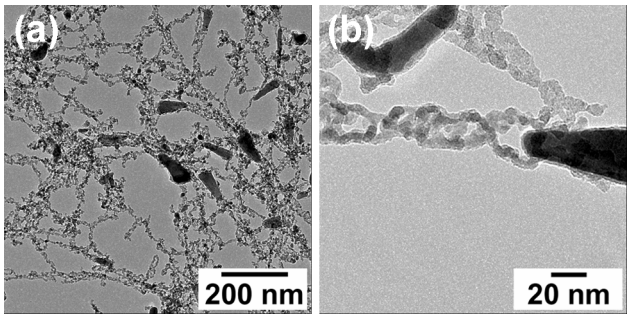

Figure 9-1. (a) BF-TEM image of strings of crystals present in locations were MWCNFs once laid. The nanofibers were exposed to an H-plasma at room temperature for 15 hours. The large cone-shaped crystals are the iron-based catalysts used to grow the nanofibers. (b) Magnified view of two nanocrystals strings.

Selected area electron diffraction (SAED) patterns from an ensemble of these crystals at numerous temperatures showed clear reflections consistent with those of cubic diamond, space group $Fd\bar{3}m$ with lattice parameter a = 0.357 nm at all temperatures between 300 K and 1073 K (Figure 9-4(a) and Table 9-1). Close inspection of individual nanocrystals with HRTEM showed lattice fringes separated by 0.206 nm (Figure 9-4(b)), the {111} interplanar spacing in cubic diamond. In addition to the diffraction rings that are consistent with cubic diamond, the (200) and (420) reflections, which are forbidden for the cubic diamond structure, were also present in the SAED patterns (Figure 9-4(a) and Table 9-1). These additional reflections combined with the allowed diamond reflections are consistent with a face-centered cubic (FCC) structure, space group $Fm\bar{3}m$ with a lattice parameter that is the same with that of cubic diamond, a = 0.357 nm. These forbidden reflections have been observed previously and were attributed to a new FCC carbon allotrope with a = 0.357 nm, named "n-diamond" because of its similarity to cubic diamond. This n-diamond phase has been produced using a range of

different processes [17, 18, 30], including shock compression of graphite, radio-frequency decomposition of hydrocarbons, and exposure of diamonds to hydrogen plasmas, but not from MWCNTs at room temperature. Many crystal structures have been proposed for n-diamond in order to account for the presence of these additional reflections [17, 31]; however, an unambiguous structure has not yet been determined.

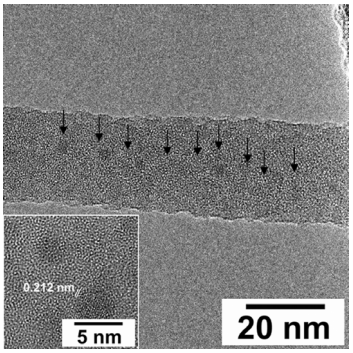

Figure 9-2. An amorphous nanorod observed after H-plasma exposure of a MWCNT at room temperature for 10 hours. Nanocrystals are observed embedded in the amorphous rod. The inset shows a high-resolution image of one representative nanocrystal with a lattice fringe spacing of 0.21 nm.

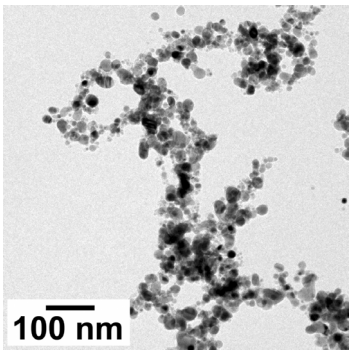

Figure 9-3. BF-TEM image of large agglomerates of crystallites, ~5-40 nm in diameter. This sample was initially covered with MWCNTs, and then exposed to an H plasma for 10 hours at 450 oC. Similar agglomerates of crystallites were observed in all samples exposed to H-plasmas over the temperature range from room temperature to 1073 K.

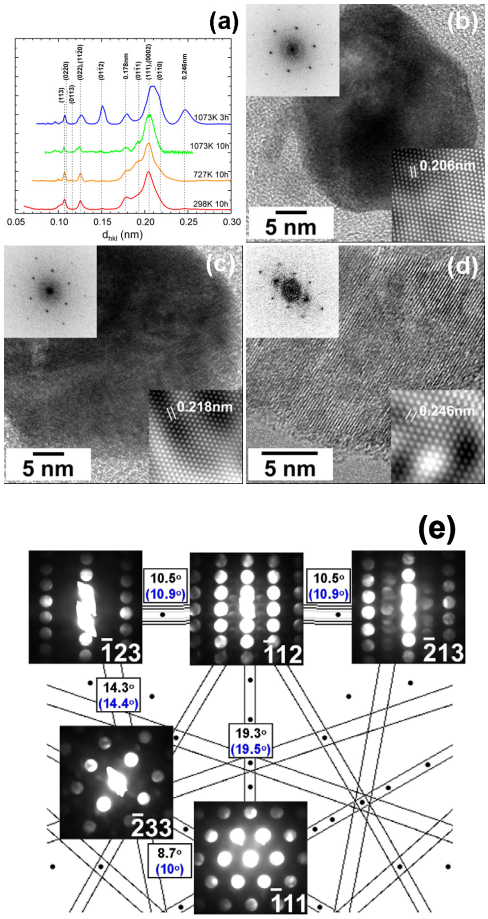

Figure 9-4. (a) SAED intensity versus interplanar spacing, d_{hkl}, for nanocrystals present after MWCNTs were exposed to an H plasma for 10 hours at 300 K, 727 K, and 1073 K and 3.5 hours of H exposure at 1073 K. Theoretical peak positions for cubic diamond and lonsdaleite are indicated by their 3- and 4-index Miller notation, respectively. Also indicated are the diffraction peaks at spacings of 0.178 nm and 0.246 nm that correspond to n-diamond and FCC carbon, respectively. (b)-(d) HRTEMs, inverse Fourier transforms (lower right insets), and power spectra (upper left insets) of nanocrystals present after exposure of MWCNTs to H for 10 hours at 300 K. (b) A nanocrystal showing lattice spacings consistent with diamond or n-diamond oriented along its [011] zone axis. (c) A nanocrystal showing lattice spacings consistent with lonsdaleite oriented along its [0001] zone axis. (d) An FCC nanocrystal with lattice parameter a = 0.426 nm oriented along its [011] zone axis. (E) CBED patterns obtained from a nanocrystal showing lattice fringe spacings of 0.246 nm and 0.213 nm. The patterns are superimposed on a simulated FCC Kikuchi map, which displays the symmetry and angular relationships (in boxes between CBED patterns) between pairs of zones. Individual CBED patterns show FCC symmetry with a = 0.426 nm.

The radially averaged SAED intensity from MWCNTs exposed to H at 1073 K for 10 hours shows that the reflection at 0.206 nm is broad and asymmetric (Figure 9-4(a)), indicating that there may be additional reflections on either side of this ring. Fitting the diffraction intensity with three peaks shows that these additional intensities are at 0.193 nm and 0.213 nm. Reflections at these same interplanar spacings appear clearly in diffraction patterns from MWCNTs treated at lower temperatures (Figure 9-4(a), *vide infra*); these indicate that, indeed, there are additional phases present in samples produced at 1073 K, but their diffractions are overshadowed by those that may correspond to cubic diamond and n-diamond.

While most reflections from samples exposed to H atoms at low temperatures (e.g., 300 K) match those of diamond and n-diamond, both SAED and HRTEM showed nanometer-size crystals whose observed symmetries and atomic planar spacings could not be accounted for by diamond, n-diamond. The observed planar spacings in the SAED pattern from an ensemble of carbon nanocrystals produced by H atom exposure of MWCNTs at several temperatures are listed in Table 9-1. For example, in samples exposed to H atoms at 300 K and 725 K, in addition to diffraction consistent with cubic diamond and n-diamond phases, strong reflections at 0.246 nm, 0.218 nm, 0.213 nm, 0.193 nm, and 0.150 nm are observed. While some of these reflections are close to each other and overlap, HRTEM of many individual nanocrystals from the same samples showed that they originate from two additional phases, one of which may be assigned to lonsdaleite. This and all assignments herein are based on lattice spacings and electron diffraction patterns (Figure 9-4(a)) recorded from crystals aligned along low-index zone axes. Convergent-beam electron diffraction (CBED) techniques were used to orient individual carbon nanocrystals along low-index zones before obtaining high-resolution images, as well as tilting individual crystals to multiple connected zones to establish their crystal class (Figure 9-4 (b)-(e)).

While presence of lonsdaleite can explain the reflections at 0.218 nm, 0.193 nm, and 0.150 nm, it does not account for the reflections at 0.246 nm and 0.213 nm. Furthermore, presence of these reflections in samples exposed to H for 3.5 hours at 1073 K without significant diffraction consistent with lonsdaleite, diffraction intensity at 0.193 nm shows that they are from different phases. Indeed, we find many single crystals with lattice spacing of 0.246 nm (Figure 9-4(d))

and diffraction patterns consistent with an FCC crystal structure observed along [011] (Figure 9-4(b)) and [001] (not shown) zone axes. Thus, the strong reflections at 0.246 nm, 0.213 nm, and 0.151 nm are consistent with the (111), (002), and (022) diffraction rings of an FCC carbon phase with lattice parameter a = 0.426 nm. To conclusively establish the FCC crystal symmetry, nanocrystals showing lattice fringe spacings of 0.246 nm and 0.213 nm were tilted in the electron microscope to at least 3 connected zone axes. Figure 9-4(e) shows one such nanocrystal that was tilted to align it with five different and connected zone axes. A focused electron probe was used to obtain CBED patterns at each zone axis from the single crystal. Observed pattern symmetry at each zone axis, as well as the measured angular relationships between pairs of zone axes match those expected for a crystal with FCC symmetry and lattice parameter a = 0.426 nm and establish the crystal class of this phase. The lattice parameter of the FCC phase is approximately the same as that reported for i-carbon, a previously observed but unidentified phase belonging to the cubic crystal system. However, electron diffraction from i-carbon and the FCC phase we observe do not follow the same selection rules.

Observed d_{hkl}				***Cubic diamond & n-diamond***		***Lonsdaleite***		***FCC***	
300 K 10 h	***727 K 10 h***	***1073 K 3.5 h***	***1073 K 10 h***	***hkl***	***d_{hkl}***	***hkl***	***d_{hkl}***	***hkl***	***d_{hkl}***
0.246		0.246						111	0.246
	0.218					100	0.218		
0.213		0.213						2	0.213
0.206	0.206	0.206	0.206	111	0.206	002	0.206		
0.191	0.193					101	0.193		
0.178	0.178	0.178	0.178	2	0.178				
0.151	0.15	0.151				102	0.15	22	0.151
0.128		0.128						113	0.128
0.126	0.126	0.126	0.126	22	0.126	110	0.126		
		0.123						222	0.123
						103	0.116		
						200	0.109		
0.107	0.107	0.107	0.107	113	0.108	112	0.107	4	0.107

Table 9-1. Comparison of observed d_{hkl} spacings through SAED with theoretical d_{hkl} spacings for cubic diamond, n-diamond, lonsdaleite, and the FCC phase.

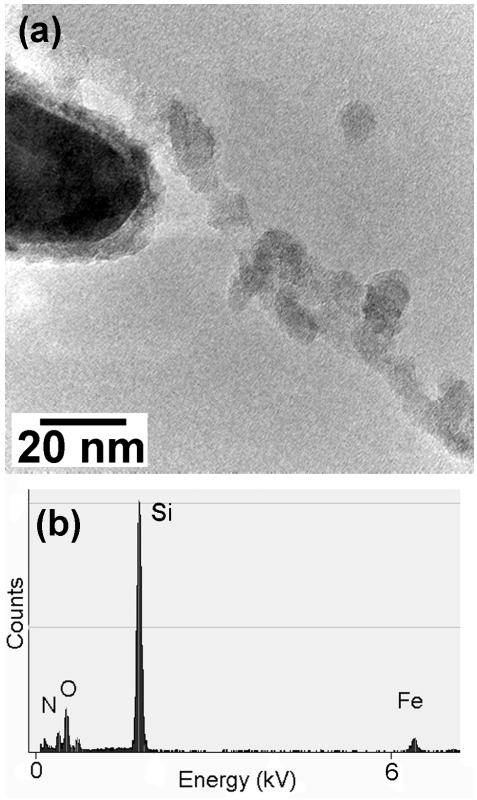

Figure 9-5. (a) BF-TEM image of a MWCNF that was exposed to an H-plasma for 15 hours at room temperature. This is the same sample as shown in Figure 9-1. (b) The string of nanocrystals were examined with EDX, and found to be composed of iron. No carbon is present. The silicon and nitrogen peaks are due to the amorphous Si_3N_4 TEM support film.

TEM images and electron diffraction provide convincing evidence that H atoms can transform the layered-graphene structure of MWCNTs and MWCNFs into other crystalline carbon phases, even at room temperature. Our diffraction is a perfect match to the multiple phases of carbon. However, nanometer-scale chemical analysis is vital to proving that these nanocrystals are indeed composed of carbon. Beginning with MWCNFs, we used a nanometer-sized converged electron beam to probe the chemical composition of the strings of crystals shown in Figure 9-1 with x-ray spectroscopy (EDX). Figure 9-5(a) shows a BF-TEM image of a string of nanocrystals that follow behind the large Fe-based cone-shaped catalyst crystal. EDX measurements (Figure 9-5(b)) of numerous individual nanocrystals in this string reveal that they are composed of iron, not carbon. In fact, no carbon was detected as shown in the representative EDX spectrum of Figure 9-5(b). It appears that small amounts of Fe have

diffused along the length of the carbon nanotube, which is quite unexpected at room temperature.

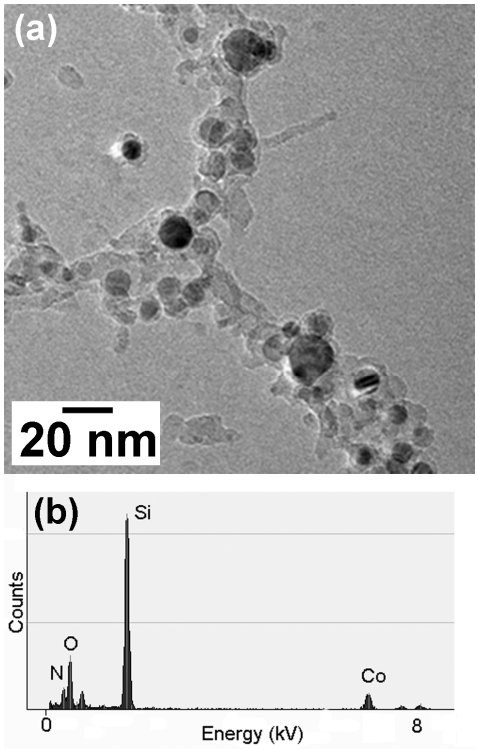

Figure 9-6. (a) Strings of nanocrystals present in locations where nanotubes once laid after H-plasma exposure under the same conditions used by Sun et al. (p = 1.1 Torr, 200 W, 1000 K). (b) Nanometer-scale EDX analysis of the nanocrystals reveals that they are in fact composed of cobalt, and cobalt and oxygen. No carbon is present. These crystals are hexagonal Co and FCC Co.

Similar measurements were made of MWCNTs that had undergone extensive H-plasma exposures. For example, the BF-TEM image of Figure 9-6(a) shows representative agglomerates of crystals that were present after 10 hours of H-plasma exposure of MWCNTs under 1.1 Torr hydrogen pressure at 1000 K. Diffraction from these crystals matches to cubic diamond and n-diamond, lonsdaleite, and i-carbon as discussed earlier. The H-plasma exposure conditions were chosen to be the exact same as those used by Sun et al. who claimed to have formed diamonds from MWCNTs [27]. Figure 9-6(b) shows a representative EDX spectrum obtained from an individual crystal. No carbon is present. Rather, we find that these crystals

are composed of cobalt, a metal that was used to catalyze the growth of the carbon nanotubes. Other crystals are composed of cobalt and oxygen. Measurements of large crystals (Figure 9-7(a)), for example in samples that were further annealed at high temperature after H-exposure show a greater fraction of crystals that contain cobalt and oxygen. The EDX and EELS spectra of crystals that contain cobalt and oxygen are shown in Figure 9-7 (b) and (c). The EELS spectrum in Figure 9-7(c) shows the presence of cobalt, and the clear absence of carbon at an energy loss of ~284 eV.

Conclusions drawn about the chemical composition or crystalline phase of nanocrystals merely on the basis of diffraction data and images is risky at best. A number of transition metals and their alloys have phases and crystal structures very close to those of carbon. In our case, cobalt and cobalt and oxygen form phases with crystal structures that are nearly indistinguishable from those of carbon. For example, the thermodynamically-stable phase of cobalt at temperatures below 725 K has a hexagonal crystal structure that is identical to that of lonsdaleite, space group P63/mmc no. 194, a = 0.251 nm, c = 0.407 nm [32]. At temperatures above 725 K, however, the thermodynamically stable phase of cobalt shifts to a face-centered cubic (FCC) crystal structure, space group $Fm\bar{3}m$ no. 225, a = 0.354 nm, similar to cubic diamond and n-diamond [33]. When crystal size is small, this phase has been found to be stable at temperatures much lower than 725 K however [34]. Finally cobalt forms an oxide, CoO, with the rock salt crystal structure, space group $Fm\bar{3}m$ no. 225, a = 0.427 nm [33]. This lattice parameter is very close to the reported lattice parameter of i-carbon, a = 0.426 nm [7]. Planar d_{hkl} spacings for each cobalt phase are shown in Table 9-2, alongside the d_{hkl} spacings for the carbon phases cubic diamond and n-diamond, lonsdaleite, and i-carbon. The symmetries and diffraction spacings of the cobalt phases are indistinguishable from those of the carbon phases, and thus it was critical that nanometer-scale chemical analysis of the observed nanocrystals was conducted.

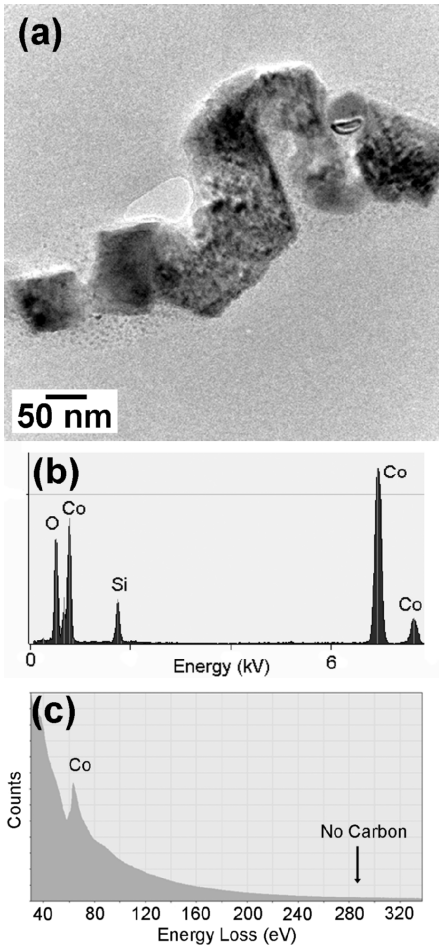

Figure 9-7. (a) A string of nanocrystals from an H-exposed MWCNT sample that was further annealed at high temperature. These crystals exhibited symmetries and d_{hkl} spacings consistent with FCC carbon a = 0.426 nm. Representative (b) EDX and (c) EELS spectra obtained from these crystals reveal that they are composed of cobalt and oxygen. Especially evident in the EELS spectrum is the absence of a carbon peak at ~284 eV. These crystals are CoO.

Cubic Diamond & n-diamond		FCC Cobalt		Lonsdaleite		Hexagonal Cobalt		FCC carbon		Cubic CoO	
hkl	d_{hkl}	***hkl***	d_{hkl}	***hkl***	d_{hkl}	***hkl***	d_{hkl}	***hkl***	d_{hkl}	***hkl***	d_{hkl}
111	0.206	111	0.205	100	0.218	100	0.217	111	0.246	111	0.246
002	0.178	002	0.177	002	0.206	002	0.204	002	0.213	002	0.213
022	0.126	022	0.125	101	0.193	101	0.192	022	0.151	022	0.151
113	0.108	113	0.107	102	0.15	102	0.148	113	0.128	113	0.129
				110	0.126	110	0.125	222	0.123	222	0.123
				103	0.116	103	0.115	004	0.107	004	0.107

Table 9-2. Comparsion of theoretical d_{hkl} spacings for cubic diamond, n-diamond, lonsdaleite, and the FCC phase with three cobalt phases: hexagonal cobalt, cubic cobalt, and cubic cobalt oxide.

That we did not observe H-induced transformation of MWCNTs to other crystalline carbon phases is consistent with our previous studies of H interaction with the layered graphene sheets of MWCNTs and planar graphite [35]. Specifically, we found that exposure of MWCNTs to H atoms created in a plasma resulted in the formation of etch pits and amorphous regions along the nanotube length at various locations. Further H exposure continued to etch away the carbon preferentially at sites of etch pits. At room temperature, most MWCNTs were easily etched by H-plasma exposure in 45 minutes, while at higher temperatures less time was required to completely etch the nanotubes. We conclude that in this study MWCNTs were etched away during the initial stages of the long (~10 hour) H-exposures, which left behind the cobalt-based catalyst crystals.

9.4 Conclusions

The possibility of H-induced transformations of MWCNTs and MWCNFs to other crystalline carbon structures was investigated using a combination of high-resolution electron imaging and diffraction techniques, combined with nanometer-scale EDX and EELS chemical analysis. After ~10 hour H-plasma exposures of MWCNTs at temperatures ranging from 300-1073 K, we observed the presence of nanocrystals with symmetries and planar d_{hkl} spacings consistent with those of cubic diamond, n-diamond, lonsdaleite, and i-carbon. However, EDX and EELS analysis revealed that these crystals were in fact cobalt-based, and did not contain carbon. The similarity of the cobalt and cobalt-oxide crystal structures to those of diamond, n-diamond,

lonsdaleite, and i-carbon illustrate the necessity to probe the chemical nature of nanocrystals, and not base conclusions solely on images and diffraction analysis.

9.5 References

[1] Frondel, C.; Marvin, U. B., Lonsdaleite, a hexagonal polymorph of diamond. *Nature* **1967,** *214* (5088), 587-589.

[2] Hanneman, R. E.; Strong, H. M.; Bundy, F. P., Hexagonal diamonds in meteorites: implications. *Science* **1967,** *155* (3765), 995-997.

[3] Kroto, H. W.; Heath, J. R.; O'Brien, S. C.; Curl, R. F.; Smalley, R. E., C60: Buckminsterfullerene. *Nature* **1985,** *318* (6042), 162-163.

[4] Iijima, S., Helical microtubules of graphitic carbon. *Nature* **1991,** *354* (6348), 56-58.

[5] Russell, S. S.; Pillinger, C. T.; Arden, J. W.; Lee, M. R.; Ott, U., A new type of meteoric diamond in the Enstatite Chondrite Abee. *Science* **1992,** *256* (5054), 206-209.

[6] Clarke, R. S.; Appleman, D. E.; Ross, D. R., An Antarctic iron meteorite contains preterrestrial impact-produced diamond and lonsdaleite. *Nature* **1981,** *291* (5814), 396-398.

[7] Hirai, H.; Kondo, K. I., Modified phases of diamond formed under shock compression and rapid quenching. *Science* **1991,** *253* (5021), 772-774.

[8] Erskine, D. J.; Nellis, W. J., Shock-induced martensitic phase transformation of oriented graphite to diamond. *Nature* **1991,** *349* (6307), 317-319.

[9] Banhart, F.; Ajayan, P. M., Carbon onions as nanoscopic pressure cells for diamond formation. *Nature* **1996,** *382* (6590), 433-435.

[10] Zaiser, M.; Banhart, F., Radiation-induced transformation of graphite to diamond. *Physical Review Letters* **1997,** *79* (19), 3680-3683.

[11] Krasheninnikov, A. V.; Banhart, F., Engineering of nanostructured carbon materials with electron or ion beams. *Nature Materials* **2007,** *6* (10), 723-733.

[12] Palnichenko, A. V.; Jonas, A. M.; Charlier, J. C.; Aronin, A. S.; Issi, J. P., Diamond formation by thermal activation of graphite. *Nature* **1999,** *402* (6758), 162-165.

[13] Angus, J. C.; Hayman, C. C., Low-pressure, metastable growth of diamond and diamondlike phases. *Science* **1988,** *241* (4868), 913-921.

[14] Fukunaga, K.; Matsuda, J.-i.; Nagao, K.; Miyamoto, M.; Ito, K., Noble-gas enrichment in vapour-growth diamonds and the origin of diamonds in ureilites. *Nature* **1987,** *328* (6126), 141-143.

[15] Bundy, F. P.; Kasper, J. S., Hexagonal diamond-a new form of carbon. *J. Chem. Phys.* **1967,** *46*, 3437.

[16] Vora, H.; Moravec, T. J., Structural investigation of thin-films of diamondlike carbon. *Journal of Applied Physics* **1981,** *52* (10), 6151-6157.

[17] Cowley, J. M.; Mani, R. C.; Sunkara, M. K.; O'Keeffe, M.; Bonneau, C., Structures of carbon nanocrystals. *Chemistry of Materials* **2004,** *16* (24), 4905-4911.

[18] Wen, B.; Zhao, J. J.; Li, T. J., Synthesis and crystal structure of n-diamond. *International Materials Reviews* **2007,** *52* (3), 131-151.

[19] Peng, J. L.; Bursill, L. A.; Jiang, B.; Orwa, J. O.; Prawer, S., Growth of c-diamond, n-diamond and i-carbon nanophases in carbon-ion-implanted fused quartz. *Philosophical Magazine B-Physics of Condensed Matter Statistical Mechanics Electronic Optical and Magnetic Properties* **2001,** *81* (12), 2071-2087.

[20] Konyashin, I.; Khvostov, V.; Babaev, V.; Guseva, M.; Mayer, J.; Sirenko, A., A new hard allotropic form of carbon: Dream or reality? *International Journal of Refractory Metals & Hard Materials* **2006,** *24* (1-2), 17-23.

[21] Lambrecht, W. R. L.; Lee, C. H.; Segall, B.; Angus, J. C.; Li, Z.; Sunkara, M., Diamond nucleation by hydrogenation of the edges of graphitic precursors. *Nature* **1993,** *364* (6438), 607-610.

[22] Layadi, N.; Cabarrocas, P. R. I.; Drevillon, B.; Solomon, I., Real-time spectroscopic ellipsometry study of the growth of amorphous and microcrystalline silicon thin-films prepared by alternating silicon deposition and hydrogen plasma treatment. *Physical Review B* **1995,** *52* (7), 5136-5143.

[23] Sriraman, S.; Agarwal, S.; Aydil, E. S.; Maroudas, D., Mechanism of hydrogen-induced crystallization of amorphous silicon. *Nature* **2002,** *418* (6893), 62-65.

[24] Mani, R. C.; Pavel, I.; Aydil, E. S., Deposition of nanocrystalline silicon films at room temperature. *Journal of Applied Physics* **2007,** *102*, 043305.

[25] Muniz, A. R.; Singh, T.; Aydil, E. S.; Maroudas, D., Analysis of diamond nanocrystal formation from multiwalled carbon nanotubes. *Physical Review B* **2009,** *80*, 144105.

[26] Singh, T.; Behr, M. J.; Aydil, E. S.; Maroudas, D., First-principles theoretical analysis of pure and hydrogenated crystalline carbon phases and nanostructures. *Chemical Physics Letters* **2009,** *474* (1-3), 168-174.

[27] Sun, L. T.; Gong, J. L.; Zhu, Z. Y.; Zhu, D. Z.; He, S. X.; Wang, Z. X.; Chen, Y.; Hu, G., Nanocrystalline diamond from carbon nanotubes. *Applied Physics Letters* **2004,** *84* (15), 2901-2903.

[28] Yang, Q. Q.; Yang, S. L.; Xiao, C. J.; Hirose, A., Transformation of carbon nanotabes to diamond in microwave hydrogen plasma. *Materials Letters* **2007,** *61* (11-12), 2208-2211.

[29] Behr, M. J.; Gaulding, E. A.; Mkhoyan, K. A.; Aydil, E. S., Effect of hydrogen on catalyst in carbon nanotube growth. **Submitted 2010**.

[30] Wen, B.; Zhao, J. J.; Li, T. J.; Dong, C.; Jin, J. Z., n-diamond from catalysed carbon nanotubes: synthesis and crystal structure. *Journal of Physics-Condensed Matter* **2005,** *17* (48), L513-L519.

[31] Bucknum, M. J.; Stamatin, I.; Castro, E. A., A chemically intuitive proposal for the structure of n-diamond. *Molecular Physics* **2005,** *103* (20), 2707-2715.

[32] Taylor, A.; Floyd, R. W., Precision measurements of lattice parameters of non-cubic crystals. *Acta Crystallographica* **1950,** *3*, 285-289.

[33] Wyckoff, R. W. G., *Crystal structures*. New York, Interscience Publishers: New York, 1963.

[34] Owen, E. A.; Jones, D. M., Effect of grain size on the crysatal structure of cobalt. *Proc. Phys. Soc. B* **1954,** *67*, 456-466.

[35] Behr, M. J.; Gaulding, E. A.; Mkhoyan, K. A.; Aydil, E. S., Hydrogen Etching and Cutting of Multiwall Carbon Nanotubes. **Submitted 2010**.

Bibliography

Abild-Pedersen, F.; Norskov, J. K.; Rostrup-Nielsen, J. R.; Sehested, J.; Helveg, S., Mechanisms for catalytic carbon nanofiber growth studied by ab initio density functional theory calculations. *Physical Review B* **2006,** *73*, 115419.

Agarwal, S.; Takano, A.; van de Sanden, M. C. M.; Maroudas, D.; Aydil, E. S., Abstraction of atomic hydrogen by atomic deuterium from an amorphous hydrogenated silicon surface. *J. Chem. Phys.* **2002,** *117*, 10805-10816.

Ajayan, P. M.; Schadler, L. S.; Giannaris, C.; Rubio, A., Single-walled carbon nanotube-polymer composites: Strength and weakness. *Advanced Materials* **2000,** *12* (10), 750-753.

Alfonsi, J. Small Crystal Models for the Electronic Properties of Carbon Nanotubes. University of Padova, Padova, 2008.

Angus, J. C.; Hayman, C. C., Low-Pressure, Metastable growth of diamond and diamondlike phases. *Science* **1988,** *241* (4868), 913-921.

Aydil, E. S.; Gottscho, R. A., Probing plasma/surface interactions. *Solid State Technology* **1997,** *40* (10), 181-190.

Bachtold, A.; Hadley, P.; Nakanishi, T.; Dekker, C., Logic circuits with carbon nanotube transistors. *Science* **2001,** *294* (5545), 1317-1320.

Banhart, F.; Ajayan, P. M., Carbon onions as nanoscopic pressure cells for diamond formation. *Nature* **1996,** *382* (6590), 433-435.

Barone, P. W.; Baik, S.; Heller, D. A.; Strano, M. S., Near-infrared optical sensors based on single-walled carbon nanotubes. *Nat. Mater.* **2005**, *4*, 86-U16.

Barone, V.; Heyd, J.; Scuseria, G. E., Interaction of atomic hydrogen with single-walled carbon nanotubes: A density functional theory study. *Journal of Chemical Physics* **2004,** *120* (15), 7169-7173.

Baughman, R. H.; Zakhidov, A. A.; de Heer, W. A., Carbon nanotubes – the route towards applications. *Science* **2002**, *297*, (5582), 787-792.

Begtrup, G. E.; Gannett, W.; Meyer, J. C.; Yuzvinsky, T. D.; Ertekin, E.; Grossman, J. C.; Zettl, A., Facets of nanotube synthesis: High-resolution transmission electron microscopy study and density functional theory calculations. *Physical Review B* **2009,** *79*, 205409.

Behr, M. J.; Gaulding, E. A.; Mkhoyan, K. A.; Aydil, E. S., Effect of hydrogen on catalyst in carbon nanotube growth. **2010**, in review.

Behr, M. J.; Mkhoyan, K. A.; Aydil, E. S., Catalyst rotation, twisting, and bending during multiwall carbon nanotube growth. **Submitted 2010**.

Behr, M. J.; Gaulding, E. A.; Mkhoyan, K. A.; Aydil, E. S., Hydrogen etching and cutting of multiwall carbon nanotubes. **Submitted 2010**.

Behr, M. J.; Mkhoyan, K. A.; Aydil, E. S., Orientation and morphological evolution of catalyst

nanoparticles during carbon nanotube growth. **submitted 2010**.

Bell, M. S.; Teo, K. B. K.; Milne, W. I., Factors determining properties of multi-walled carbon nanotubes/fibres deposited by PECVD. *Journal of Physics D-Applied Physics* **2007,** *40* (8), 2285-2292.

Berber, S.; Kwon, Y. K.; Tomanek, D., Unusually high thermal conductivity of carbon nanotubes. *Physical Review Letters* **2000,** *84* (20), 4613-4616.

Berger, S. D.; McKenzie, D. R.; Martin, P. J., EELS analysis of vacuum arc-deposited diamond-like Films. *Philosophical Magazine Letters* **1988,** *57* (6), 285-290.

Besteman, K.; Lee, J. O.; Wiertz, F. G. M.; Heering, H. A.; Dekker, C., Enzyme-coated carbon nanotubes as single-molecule biosensors. *Nano Letters* **2003,** *3* (6), 727-730.

Bethe, H., The theory of the passage of rapid neutron radiation through matter. *Annalen der Physik* **1930,** *5* (3), 325-400.

Biercuk, M. J.; Llaguno, M. C.; Radosavljevic, M.; Hyun, J. K.; Johnson, A. T.; Fischer, J. E., Carbon nanotube composites for thermal management. *Applied Physics Letters* **2002,** *80* (15), 2767-2769.

Blank, V. D.; Alshevskiy, Y. L.; Zaitsev, A. I.; Kazennov, N. V.; Perezhogin, I. A.; Kulnitskiy, B. A., Structure and phase composition of a catalyst for carbon nanotiber formation. *Scripta Materialia* **2006,** *55* (11), 1035-1038.

Blank, V. D.; Kulnitskiy, B. A.; Batov, D. V.; Bangert, U.; Gutierrez-Sosa, A.; Harvey, A. J., Electron microscopy and electron energy loss spectroscopy studies of carbon fiber formation at Fe catalysts. *Journal of Applied Physics* **2002,** *91* (3), 1657-1660.

Bower, C.; Zhu, W.; Jin, S. H.; Zhou, O., Plasma-induced alignment of carbon nanotubes. *Applied Physics Letters* **2000,** *77* (6), 830-832.

Bragg, W. L., The diffraction of short electromagnetic waves by a crystal. *Proceedings of the Cambridge Philosophical Society* **1913,** *17*, 43-57.

Browning, N. D.; Wallis, D. J.; Nellist, P. D.; Pennycook, S. J., EELS in the STEM: determination of materials properties on the atomic scale. *Micron* **1997,** *28* (5), 333-348.

Bucknum, M. J.; Stamatin, I.; Castro, E. A., A chemically intuitive proposal for the structure of n-diamond. *Molecular Physics* **2005,** *103* (20), 2707-2715.

Bundy, F. P.; Kasper, J. S., Hexagonal diamond-a new form of carbon. *J. Chem. Phys.* **1967,** *46*, 3437.

Busch, H., On the mode of action of the concentrating coil in the Braun tube. *Arch. Elektrotechnik* **1927,** *18*, 583-594.

Cancado, L. G.; Pimenta, M. A.; Neves, B. R. A.; Dantas, M. S. S.; Jorio, A., Influence of the atomic structure on the Raman spectra of graphite edges. *Physical Review Letters* **2004,** *93*, 2247401.

Cao, Q.; Hur, S. H.; Zhu, Z. T.; Sun, Y. G.; Wang, C. J.; Meitl, M. A.; Shim, M.; Rogers, J. A.,

Highly bendable, transparent thin-film transistors that use carbon-nanotube-based conductors and semiconductors with elastomeric dielectrics. *Advanced Materials* **2006,** *18* (3), 304-309.

Cao, Q.; Zhu, Z. T.; Lemaitre, M. G.; Xia, M. G.; Shim, M.; Rogers, J. A., Transparent flexible organic thin-film transistors that use printed single-walled carbon nanotube electrodes. *Applied Physics Letters* **2006,** *88* (11), 3.

Carbon nanotubes advanced topics in the synthesis, structure, properties, and applications. Berlin ; New York : Springer: Berlin ; New York, 2008.

Caughman, J. B. O.; Baylor, L. R.; Guillorn, M. A.; Merkulov, V. I.; Lowndes, D. H.; Allard, L. F., Growth of vertically aligned carbon nanofibers by low-pressure inductively coupled plasma-enhanced chemical vapor deposition. *Applied Physics Letters* **2003,** *83* (6), 1207-1209.

Chapman, B. N., *Glow discharge processes : sputtering and plasma etching*. New York : Wiley: New York, 1980.

Charlier, J. C.; Blase, X.; Roche, S., Electronic and transport properties of nanotubes. *Reviews of Modern Physics* **2007,** *79* (2), 677-732.

Charlier, J. C.; Eklund, P. C.; Zhu, J.; Ferrari, A. C., Electron and phonon properties of graphene: Their relationship with carbon nanotubes. In *Carbon Nanotubes*, Springer-Verlag Berlin: Berlin, 2008; Vol. 111, pp 673-709.

Chhowalla, M.; Teo, K. B. K.; Ducati, C.; Rupesinghe, N. L.; Amaratunga, G. A. J.; Ferrari, A. C.; Roy, D.; Robertson, J.; Milne, W. I., Growth process conditions of vertically aligned carbon nanotubes using plasma enhanced chemical vapor deposition. *Journal of Applied Physics* **2001,** *90* (10), 5308-5317.

Clarke, R. S.; Appleman, D. E.; Ross, D. R., An Antarctic iron meteorite contains preterrestrial impact-produced diamond and lonsdaleite. *Nature* **1981,** *291* (5814), 396-398.

Coburn, J. W.; Chen, M., Optical-emission spectroscopy of reactive plasmas - a method for correlating emission intensities to reactive particle density. *Journal of Applied Physics* **1980,** *51* (6), 3134-3136.

Coleman, J. N.; Khan, U.; Blau, W. J.; Gun'ko, Y. K., Small but strong: a review of the mechanical properties of carbon nanotube-polymer composites. *Carbon* **2006,** *44* (9), 1624-1652.

Colliex, C.; Manoubi, T.; Ortiz, C., Electron-energy-loss-spectroscopy near-edge fine-structures in the iron-oxygen system. *Physical Review B* **1991,** *44* (20), 11402-11411.

Collins, P. C.; Arnold, M. S.; Avouris, P., Engineering carbon nanotubes and nanotube circuits using electrical breakdown. *Science* **2001,** *292* (5517), 706-709.

Cowley, J. M.; Mani, R. C.; Sunkara, M. K.; O'Keeffe, M.; Bonneau, C., Structures of carbon nanocrystals. *Chemistry of Materials* **2004,** *16* (24), 4905-4911.

Crewe, A. V.; Isaacson, M.; Johnson, D., A simple scanning electron microscope. *Rev. Sci. Instrum.* **1969,** *40* (2), 241-246.

Crewe, A. V.; Wall, J.; Welter, L. M., A high-resolution scanning transmission electron

microscope. *Journal of Applied Physics* **1968,** *39* (13), 5861-5868.

Cuesta, A.; Dhamelincourt, P.; Laureyns, J.; Martinez-Alonso, A.; Tascon, J. M. D., Comparative performance of X-ray diffraction and Raman microprobe techniques for the study of carbon materials. *Journal of Materials Chemistry* **1998,** *8* (12), 2875-2879.

Cullity, B. D., *Elements of x-ray diffraction*. Upper Saddle River, NJ : Prentice Hall: Upper Saddle River, NJ, 2001.

de Broglie, L., Recherches sur la théorie des quanta. *Annales de Physique* **1925,** *3*.

Delzeit, L.; McAninch, I.; Cruden, B. A.; Hash, D.; Chen, B.; Han, J.; Meyyappan, M., Growth of multiwall carbon nanotubes in an inductively coupled plasma reactor. *Journal of Applied Physics* **2002,** *91* (9), 6027-6033.

Denysenko, I. B.; Xu, S.; Long, J. D.; Rutkevych, P. P.; Azarenkov, N. A.; Ostrikov, K., Inductively coupled $Ar/CH_4/H_2$ plasmas for low-temperature deposition of ordered carbon nanostructures. *Journal of Applied Physics* **2004,** *95* (5), 2713-2724.

Deschenaux, C.; Affolter, A.; Magni, D.; Hollenstein, C.; Fayet, P., Investigations of CH_4, C_2H_2 and C_2H_4 dusty RF plasmas by means of FTIR absorption spectroscopy and mass spectrometry. *Journal of Physics D-Applied Physics* **1999,** *32* (15), 1876-1886.

Dillon, A. C.; Jones, K. M.; Bekkedahl, T. A.; Kiang, C. H.; Bethune, D. S.; Heben, M. J., Storage of hydrogen in single-walled carbon nanotubes. *Nature* **1997,** *386* (6623), 377-379.

Ding, F.; Bolton, K.; Rosen, A., Iron-carbide cluster thermal dynamics for catalyzed carbon nanotube growth. *J. Vac. Sci. Technol. A* **2004**, 22, 1471-1476.

Ding, F.; Harutyunyan, A. R.; Yakobson, B. I., Dislocation theory of chirality-controlled nanotube growth. *P. Natl. Acad. Sci. USA* **2009**, *106*, 2506-2509.

Dresselhaus, M. S.; Dresselhaus, G.; Charlier, J. C.; Hernandez, E., Electronic, thermal and mechanical properties of carbon nanotubes. *Philosophical Transactions of the Royal Society a-Mathematical Physical and Engineering Sciences* **2004,** *362* (1823), 2065-2098.

Dreyfus, R. W.; Jasinski, J. M.; Walkup, R. E.; Selwyn, G. S., Optical diagnostics of low-pressure plasmas. *Pure and Applied Chemistry* **1985,** *57* (9), 1265-1276.

Egerton, R. F., *Electron energy-loss spectroscopy in the electron microscope*. New York : Plenum Press: New York, 1996.

Egerton, R. F.; Whelan, M. J., Electron energy loss spectra of diamond, graphite and amorphous carbon. *Journal of Electron Spectroscopy and Related Phenomena* **1974,** *3* (3), 232-236.

Elias, D. C.; Nair, R. R.; Mohiuddin, T. M. G.; Morozov, S. V.; Blake, P.; Halsall, M. P.; Ferrari, A. C.; Boukhvalov, D. W.; Katsnelson, M. I.; Geim, A. K.; Novoselov, K. S., Control of graphene's properties by reversible hydrogenation: evidence for graphane. *Science* **2009,** *323* (5914), 610-613.

Emmenegger, C.; Bonard, J. M.; Mauron, P.; Sudan, P.; Lepora, A.; Grobety, B.; Zuttel, A.; Schlapbach, L., Synthesis of carbon nanotubes over Fe catalyst on aluminium and suggested

growth mechanism. *Carbon* **2003,** *41* (3), 539-547.

Endo, M.; Strano, M. S.; Ajayan, P. M., Potential applications of carbon nanotubes. In *Carbon Nanotubes*, Springer-Verlag Berlin: Berlin, 2008; Vol. 111, pp 13-61.

Erskine, D. J.; Nellis, W. J., Shock-induced martensitic phase transformation of oriented graphite to diamond. *Nature* **1991,** *349* (6307), 317-319.

Fallon, P. J.; Brown, L. M., Analysis of chemical-vapor-deposited diamond grain-boundaries using transmission electron-microscopy and parallel electron-energy-loss spectroscopy in a scanning-transmission electron-microscope. *Diamond and Related Materials* **1993,** *2* (5-7), 1004-1011.

Fan, S. S.; Liu, L.; Liu, M., Monitoring the growth of carbon nanotubes by carbon isotope labelling. *Nanotechnology* **2003,** *14* (10), 1118-1123.

Ferrari, A. C., Raman spectroscopy of graphene and graphite: Disorder, electron-phonon coupling, doping and nonadiabatic effects. *Solid State Communications* **2007,** *143* (1-2), 47-57.

Ferrari, A. C.; Robertson, J., Interpretation of Raman spectra of disordered and amorphous carbon. *Physical Review B* **2000,** *61* (20), 14095-14107.

Frondel, C.; Marvin, U. B., Lonsdaleite, a Hexagonal Polymorph of Diamond. *Nature* **1967,** *214* (5088), 587-589.

Fuchs, E., X-Ray spectrometer attachment for Elmiskop I electron microscope. *Review of Scientific Instruments* **1966,** *37* (5), 623-626.

Fukunaga, K.; Matsuda, J.-i.; Nagao, K.; Miyamoto, M.; Ito, K., Noble-gas enrichment in vapour-growth diamonds and the origin of diamonds in ureilites. *Nature* **1987,** *328* (6126), 141-143.

Geim, A. K.; Novoselov, K. S., The rise of graphene. *Nat Mater* **2007,** *6* (3), 183-191.

Ghosh, S.; Bachilo, S. M.; Weisman, R. B., Advanced sorting of single-walled carbon nanotubes by nonlinear density-gradient ultracentrifugation. *Nat Nano* **2010,** *advance online publication*.

Gibson, R. F.; Ayorinde, E. O.; Wen, Y. F., Vibrations of carbon nanotubes and their composites: A review. *Composites Science and Technology* **2007,** *67* (1), 1-28.

Gicquel, A.; Chenevier, M.; Hassouni, K.; Tserepi, A.; Dubus, M., Validation of actinometry for estimating relative hydrogen atom densities and electron energy evolution in plasma assisted diamond deposition reactors. *Journal of Applied Physics* **1998,** *83* (12), 7504-7521.

Golberg, D.; Mitome, M.; Muller, C.; Tang, C.; Leonhardt, A.; Bando, Y., Atomic structures of iron-based single-crystalline nanowires crystallized inside multi-walled carbon nanotubes as revealed by analytical electron microscopy. *Acta Materialia* **2006,** *54* (9), 2567-2576.

Goldstein, J.; Newbury, D.; Joy, D.; Lyman, C.; Echlin, P.; Lifshin, E.; Sawyer, L.; Michael, J., *Scanning Electron Microscopy and X-ray Microanalysis*. Kluwer Academic/Plenum Publishers: New York, 2003.

Grabke, H. J., Metal dusting. *Materials and Corrosion-Werkstoffe Und Korrosion* **2003,** *54* (10), 736-746.

Granqvist, C. G., Transparent conductors as solar energy materials: A panoramic review. *Solar Energy Materials and Solar Cells* **2007,** *91* (17), 1529-1598.

Griffiths, D. J., *Introduction to electrodynamics*. Upper Saddle River, N.J. : Prentice Hall: Upper Saddle River, N.J., 1999.

Guldi, D. M.; Rahman, G. M. A.; Prato, M.; Jux, N.; Qin, S. H.; Ford, W., Single-wall carbon nanotubes as integrative building blocks for solar-energy conversion. *Angewandte Chemie-International Edition* **2005,** *44* (13), 2015-2018.

Han, S. M.; Aydil, E. S., Reasons for lower dielectric constant of fluorinated SiO_2 films. *Journal of Applied Physics* **1998,** *83* (4), 2172-2178.

Hanneman, R. E.; Strong, H. M.; Bundy, F. P., Hexagonal Diamonds in Meteorites: Implications. *Science* **1967,** *155* (3765), 995-997.

Harrick, N. J., *Internal reflection spectroscopy*. New York, Interscience Publishers: New York, 1967.

He, K.; Brown, A.; Brydson, R.; Edmonds, D. V., Analytical electron microscope study of the dissolution of the Fe_3C iron carbide phase (cementite) during a graphitisation anneal of carbon steel. *Journal of Materials Science* **2006,** *41* (16), 5235-5241.

Helveg, S.; Lopez-Cartes, C.; Sehested, J.; Hansen, P. L.; Clausen, B. S.; Rostrup-Nielsen, J. R.; Abild-Pedersen, F.; Norskov, J. K., Atomic-scale imaging of carbon nanofibre growth. *Nature* **2004,** *427* (6973), 426-429.

Heresanu, V.; Castro, C.; Cambedouzou, J.; Pinault, M.; Stephan, O.; Reynaud, C.; Mayne-L'Hermite, M.; Launois, P., Nature of the catalyst particles in CCVD synthesis of multiwalled carbon nanotubes revealed by the cooling step study. *Journal of Physical Chemistry C* **2008,** *112*, 7371-7378.

Herzberg, G., *Molecular spectra and molecular structure*. New York : Prentice-Hall: New York, 1939.

Hirai, H.; Kondo, K. I., Modified phases of diamond formed under shock compression and rapid quenching. *Science* **1991,** *253* (5021), 772-774.

Hofmann, S.; Blume, R.; Wirth, C. T.; Cantoro, M.; Sharma, R.; Ducati, C.; Havecker, M.; Zafeiratos, S.; Schnoerch, P.; Oestereich, A.; Teschner, D.; Albrecht, M.; Knop-Gericke, A.; Schlogl, R.; Robertson, J., State of transition metal catalysts during carbon nanotube growth. *Journal of Physical Chemistry C* **2009,** *113* (5), 1648-1656.

Hofmann, S.; Csanyi, G.; Ferrari, A. C.; Payne, M. C.; Robertson, J., Surface diffusion: The low activation energy path for nanotube growth. *Physical Review Letters* **2005,** *95*, 036101.

Hofmann, S.; Sharma, R.; Ducati, C.; Du, G.; Mattevi, C.; Cepek, C.; Cantoro, M.; Pisana, S.; Parvez, A.; Cervantes-Sodi, F.; Ferrari, A. C.; Dunin-Borkowski, R.; Lizzit, S.; Petaccia, L.; Goldoni, A.; Robertson, J., In situ observations of catalyst dynamics during surface-bound carbon nanotube nucleation. *Nano Letters* **2007,** *7* (3), 602-608.

Huang, J. Y., HRTEM and EELS studies of defects structure and amorphous-like graphite

induced by ball-milling. *Acta Materialia* **1999,** *47* (6), 1801-1808.

Ichida, M.; Mizuno, S.; Tani, K.; Saito, Y.; Nakamura, A., Exciton effects of optical transitions in single-wall carbon nanotubes. *Journal of the Physical Society of Japan* **1999,** *68* (10), 3131-3133.

Iijima, S., Helical microtubules of graphitic carbon. *Nature* **1991,** *354* (6348), 56-58.

Inokuti, M., Inelastic collisions of fast charged particles with atoms and molecules; the Bethe theory revisited. *Reviews of Modern Physics* **1971,** *43* (3), 297-347.

Introduction to microlithography. Washington, DC : American Chemical Society: Washington, DC, 1994.

Javey, A.; Guo, J.; Wang, Q.; Lundstrom, M.; Dai, H. J., Ballistic carbon nanotube field-effect transistors. *Nature* **2003,** *424* (6949), 654-657.

Jiang, D. E.; Carter, E. A., Carbon atom adsorption on and diffusion into Fe(110) and Fe(100) from first principles. *Physical Review B* **2005,** *71*, 045402.

Jin, Y. M.; Xu, H. F.; Datye, A. K., Electron energy loss spectroscopy (EELS) of iron Fischer-Tropsch catalysts. *Microscopy and Microanalysis* **2006,** *12* (2), 124-134.

Joseyacaman, M.; Mikiyoshida, M.; Rendon, L.; Santiesteban, J. G., Catalytic growth of carbon microtubules with fullerene structure. *Applied Physics Letters* **1993,** *62* (2), 202-204.

Journet, C.; Maser, W. K.; Bernier, P.; Loiseau, A.; delaChapelle, M. L.; Lefrant, S.; Deniard, P.; Lee, R.; Fischer, J. E., Large-scale production of single-walled carbon nanotubes by the electric-arc technique. *Nature* **1997,** *388* (6644), 756-758.

Kilic, C.; Zunger, A., n-type doping of oxides by hydrogen. *Applied Physics Letters* **2002,** *81* (1), 73-75.

Kim, H.; Sigmund, W., Iron particles in carbon nanotubes. *Carbon* **2005,** *43* (8), 1743-1748.

Kittel, C., *Introduction to solid state physics*. New York, Wiley: New York, 1966.

Kohl, H.; Reimer, L., *Transmission Electron Microscopy Physics of Image Formation*. New York, NY : Springer-Verlag New York: New York, NY, 2008.

Kong, J.; Franklin, N. R.; Zhou, C. W.; Chapline, M. G.; Peng, S.; Cho, K. J.; Dai, H. J., Nanotube molecular wires as chemical sensors. *Science* **2000,** *287* (5453), 622-625.

Konyashin, I.; Khvostov, V.; Babaev, V.; Guseva, M.; Mayer, J.; Sirenko, A., A new hard allotropic form of carbon: Dream or reality? *International Journal of Refractory Metals & Hard Materials* **2006,** *24* (1-2), 17-23.

Koratkar, N. A.; Suhr, J.; Joshi, A.; Kane, R. S.; Schadler, L. S.; Ajayan, P. M.; Bartolucci, S., Characterizing energy dissipation in single-walled carbon nanotube polycarbonate composites. *Applied Physics Letters* **2005,** *87*, 063102.

Kordas, K.; Toth, G.; Moilanen, P.; Kumpumaki, M.; Vahakangas, J.; Uusimaki, A.; Vajtai, R.; Ajayan, P. M., Chip cooling with integrated carbon nanotube microfin architectures. *Applied Physics Letters* **2007,** *90*, 123105.

Krasheninnikov, A. V.; Banhart, F., Engineering of nanostructured carbon materials with electron or ion beams. *Nature Materials* **2007,** *6* (10), 723-733.

Krishnan, A.; Dujardin, E.; Ebbesen, T. W.; Yianilos, P. N.; Treacy, M. M. J., Young's modulus of single-walled nanotubes. *Physical Review B* **1998,** *58* (20), 14013-14019.

Kroto, H. W.; Heath, J. R.; O'Brien, S. C.; Curl, R. F.; Smalley, R. E., C60: Buckminsterfullerene. *Nature* **1985,** *318* (6042), 162-163.

Lambert, J. B.; Shurvell, H. F., *Introduction to Vibrational Spectroscopy: Introduction to Organic Spectroscopy*. Prentice Hall: New Jersey, 1987.

Lambrecht, W. R. L.; Lee, C. H.; Segall, B.; Angus, J. C.; Li, Z.; Sunkara, M., Diamond nucleation by hydrogenation of the edges of graphitic precursors. *Nature* **1993,** *364* (6438), 607-610.

Landi, B. J.; Raffaelle, R. P.; Castro, S. L.; Bailey, S. G., Single-wall carbon nanotube-polymer solar cells. *Progress in Photovoltaics* **2005,** *13* (2), 165-172.

Layadi, N.; Cabarrocas, P. R. I.; Drevillon, B.; Solomon, I., Real-time spectroscopic ellipsometry study of the growth of amorphous and microcrystalline silicon thin-films prepared by alternating silicon deposition and hydrogen plasma treatment. *Physical Review B* **1995,** *52* (7), 5136-5143.

Leapman, R. D.; Fejes, P. L.; Silcox, J., Orientation dependence of core edges from anisotropic materials determined by inelastic-scattering of fast electrons. *Physical Review B* **1983,** *28* (5), 2361-2373.

Leapman, R. D.; Hunt, J. A., Comparison of detection limits for EELS and EDXS. *Microscopy Microanalysis Microstructures* **1991,** *2* (2-3), 231-244.

Leapman, R. D.; Silcox, J., Orientation dependence of core edges in electron-energy-loss spectra from anisotropic materials. *Physical Review Letters* **1979,** *42* (20), 1361-1364.

Lee, T. Y.; Han, J. H.; Choi, S. H.; Yoo, J. B.; Park, C. Y.; Jung, T.; Yu, S.; Yi, W. K.; Han, I. T.; Kim, J. M., Effects of source gases on the growth of carbon nanotubes. *Diamond and Related Materials* **2003,** *12* (3-7), 851-855.

Li, C. Y.; Chou, T. W., Axial and radial thermal expansions of single-walled carbon nanotubes. *Phys. Rev. B* **2005**, *71*, 235414.

Lifshitz, Y., Pitfalls in amorphous carbon studies. *Diamond and Related Materials* **2003,** *12* (2), 130-140.

Lim, S. H.; Yoon, H. S.; Moon, J. H.; Park, K. C.; Jang, J., Optical emission spectroscopy study for optimization of carbon nanotubes growth by a triode plasma chemical vapor deposition. *Applied Physics Letters* **2006,** *88*, 033114.

Lisowski, W.; Keim, E. G.; van den Berg, A. H. J.; Smithers, M. A., Structural and chemical evolution of single-wall carbon nanotubes under atomic and molecular deuterium interaction. *Carbon* **2005,** *43*, 1073-1083.

Loane, R. F.; Xu, P.; Silcox, J., Incoherent Imaging of Zone Axis Crystals with ADF STEM.

Ultramicroscopy **1992,** *40* (2), 121-138.

Loretto, M. H., *Electron beam analysis of materials*. London ; New York : Chapman & Hall: London ; New York, 1994.

Ma, J.; Ashfold, M. N. R.; Mankelevich, Y. A., Validating optical emission spectroscopy as a diagnostic of microwave activated $CH_4/Ar/H_2$ plasmas used for diamond chemical vapor deposition. *Journal of Applied Physics* **2009,** *105*, 043302.

Mani, R. C.; Pavel, I.; Aydil, E. S., Deposition of nanocrystalline silicon films at room temperature. *Journal of Applied Physics* **2007,** *102*, 043305

Marchand, M.; Journet, C.; Guillot, D.; Benoit, J. M.; Yakobson, B. I.; Purcell, S. T., Growing a carbon nanotube atom by atom: "And yet it does turn". *Nano Lett.* **2009**, *9*, 2961-2966.

Martel, R.; Schmidt, T.; Shea, H. R.; Hertel, T.; Avouris, P., Single- and multi-wall carbon nanotube field-effect transistors. *Applied Physics Letters* **1998,** *73* (17), 2447-2449.

Mattevi, C.; Hofmann, S.; Cantoro, M.; Ferrari, A. C.; Robertson, J.; Castellarin-Cudia, C.; Dolafi, S.; Goldoni, A.; Cepek, C., Surface-bound chemical vapour deposition of carbon nanotubes: In situ study of catalyst activation. *Physica E-Low-Dimensional Systems & Nanostructures* **2008,** *40* (7), 2238-2242.

McDowell, R. S., Rotational partition-functions for spherical-top molecules. *Journal of Quantitative Spectroscopy & Radiative Transfer* **1987,** *38* (5), 337-346.

McQuarrie, D. A., *Quantum chemistry*. Sausalito, Calif. : University Science Books: Sausalito, Calif., 2008.

McQuarrie, D. A.; Simon, J. D., *Physical Chemistry: A Molecular Approach*. University Science Books: Sausalito, 1997.

Melechko, A. V.; Merkulov, V. I.; McKnight, T. E.; Guillorn, M. A.; Klein, K. L.; Lowndes, D. H.; Simpson, M. L., Vertically aligned carbon nanofibers and related structures: Controlled synthesis and directed assembly. *Journal of Applied Physics* **2005,** *97*, 041301.

Merkoci, A.; Pumera, M.; Llopis, X.; Perez, B.; del Valle, M.; Alegret, S., New materials for electrochemical sensing VI: Carbon nanotubes. *Trac-Trends in Analytical Chemistry* **2005,** *24* (9), 826-838.

Meyyappan, M., A review of plasma enhanced chemical vapour deposition of carbon nanotubes. *J. Phys. D Appl. Phys.* **2009**, *42*, 213001.

Meyyappan, M.; Delzeit, L.; Cassell, A.; Hash, D., Carbon nanotube growth by PECVD: a review. *Plasma Sources Science & Technology* **2003,** *12* (2), 205-216.

Minami, T., New n-type transparent conducting oxides. *Mrs Bulletin* **2000,** *25* (8), 38-44.

Mkhoyan, K. A.; Silcox, J.; McGuire, M. A.; Disalvo, F. J., Radiolytic purification of CaO by electron beams. *Philosophical Magazine* **2006,** *86* (19), 2907-2917.

Moniruzzaman, M.; Winey, K. I., Polymer nanocomposites containing carbon nanotubes. *Macromolecules* **2006,** *39* (16), 5194-5205.

Muniz, A. R.; Singh, T.; Aydil, E. S.; Maroudas, D., Analysis of diamond nanocrystal formation from multiwalled carbon nanotubes. *Physical Review B* **2009,** *80*, 144105.

Muniz, A. R.; Singh, T.; Maroudas, D., Effects of hydrogen chemisorption on the structure and deformation of single-walled carbon nanotubes. *Applied Physics Letters* **2009,** *94*, 103108.

Nellist, P. D.; Pennycook, S. J., Incoherent imaging using dynamically scattered coherent electrons. *Ultramicroscopy* **1999,** *78* (1-4), 111-124.

Nellist, P. D.; Pennycook, S. J., The principles and interpretation of annular dark-field Z-contrast imaging. *Advances in Imaging and Electron Physics* **2000,** *113*, 147-203.

Nemanich, R. J.; Glass, J. T.; Lucovsky, G.; Shroder, R. E., Raman-scattering characterization of carbon bonding in diamond and diamondlike thin-films. *Journal of Vacuum Science & Technology a-Vacuum Surfaces and Films* **1988,** *6* (3), 1783-1787.

Nemanich, R. J.; Solin, S. A., 1^{ST}-order and 2^{ND}-order Raman-scattering from finite-size crystals of graphite. *Physical Review B* **1979,** *20* (2), 392-401.

Nikitin, A.; Ogasawara, H.; Mann, D.; Denecke, R.; Zhang, Z.; Dai, H.; Cho, K.; Nilsson, A., Hydrogenation of single-walled carbon nanotubes. *Physical Review Letters* **2005,** *95*, 225507.

Nolan, P. E.; Lynch, D. C.; Cutler, A. H., Carbon deposition and hydrocarbon formation on group VIII metal catalysts. *Journal of Physical Chemistry B* **1998,** *102* (21), 4165-4175.

Novoselov, K. S.; Geim, A. K.; Morozov, S. V.; Jiang, D.; Katsnelson, M. I.; Grigorieva, I. V.; Dubonos, S. V.; Firsov, A. A., Two-dimensional gas of massless Dirac fermions in graphene. *Nature* **2005,** *438* (7065), 197-200.

Owen, E. A.; Jones, D. M., Effect of grain size on the crystal structure of cobalt. *Proc. Phys. Soc. B* **1954,** *67*, 456-466.

Palnichenko, A. V.; Jonas, A. M.; Charlier, J. C.; Aronin, A. S.; Issi, J. P., Diamond formation by thermal activation of graphite. *Nature* **1999,** *402* (6758), 162-165.

Pankove, J. I., *Optical processes in semiconductors*. Englewood Cliffs, N.J., Prentice-Hall: Englewood Cliffs, N.J., 1971.

Payling, R., *Optical emission lines of the elements*. Chichester ; New York : Wiley: Chichester ; New York, 2000.

Peng, J. L.; Bursill, L. A.; Jiang, B.; Orwa, J. O.; Prawer, S., Growth of c-diamond, n-diamond and i-carbon nanophases in carbon-ion-implanted fused quartz. *Philosophical Magazine B-Physics of Condensed Matter Statistical Mechanics Electronic Optical and Magnetic Properties* **2001,** *81* (12), 2071-2087.

Pennycook, S. J.; Jesson, D. E., High-resolution z-contrast imaging of crystals. *Ultramicroscopy* **1991,** *37* (1-4), 14-38.

Raether, H., *Excitation of plasmons and interband transitions by electrons*. Berlin ; New York : Springer-Verlag: Berlin ; New York, 1980.

Rao, F. B.; Li, T.; Wang, Y. L., Effect of hydrogen on the growth of single-walled carbon

nanotubes by thermal chemical vapor deposition. *Physica E-Low-Dimensional Systems & Nanostructures* **2008,** *40* (4), 779-784.

Raty, J. Y.; Gygi, F.; Galli, G., Growth of carbon nanotubes on metal nanoparticles: A microscopic mechanism from ab initio molecular dynamics simulations. *Physical Review Letters* **2005,** *95*, 096103.

Ren, Z. F.; Huang, Z. P.; Xu, J. W.; Wang, J. H.; Bush, P.; Siegal, M. P.; Provencio, P. N., Synthesis of large arrays of well-aligned carbon nanotubes on glass. *Science* **1998,** *282* (5391), 1105-1107.

Rodriguez, N. M.; Chambers, A.; Baker, R. T. K., Catalytic engineering of carbon nanostructures. *Langmuir* **1995,** *11* (10), 3862-3866.

Rodriguez-Manzo, J. A.; Terrones, M.; Terrones, H.; Kroto, H. W.; Sun, L. T.; Banhart, F., In situ nucleation of carbon nanotubes by the injection of carbon atoms into metal particles. *Nature Nanotechnology* **2007,** *2* (5), 307-311.

Ruska, E.; Knoll, M., Das Elektronenmikroskop. *Z. Physik* **1932,** *36*.

Russell, S. S.; Pillinger, C. T.; Arden, J. W.; Lee, M. R.; Ott, U., A new type of meteoric diamond in the Enstatite Chondrite Abee. *Science* **1992,** *256* (5054), 206-209.

Sadezky, A.; Muckenhuber, H.; Grothe, H.; Niessner, R.; Poschl, U., Raman micro spectroscopy of soot and related carbonaceous materials: Spectral analysis and structural information. *Carbon* **2005,** *43* (8), 1731-1742.

Saito, R., *Physical properties of carbon nanotubes*. London : Imperial College Press: London, 1998.

Saito, R.; Jorio, A.; Souza, A. G.; Dresselhaus, G.; Dresselhaus, M. S.; Pimenta, M. A., Probing phonon dispersion relations of graphite by double resonance Raman scattering. *Physical Review Letters* **2002,** *88*, 027401.

Saitoh, K.; Nagasaka, K.; Tanaka, N., Observation of the anisotropy of the inelastic scattering of fast electrons accompanied by the K-shell ionization of a carbon nanotube. *Journal of Electron Microscopy* **2006,** *55* (6), 281-288.

Schaper, A. K.; Hou, H. Q.; Greiner, A.; Phillipp, F., The role of iron carbide in multiwalled carbon nanotube growth. *Journal of Catalysis* **2004,** *222* (1), 250-254.

Sharma, R.; Moore, E.; Rez, P.; Treacy, M. M. J., Site-Specific Fabrication of Fe Particles for Carbon Nanotube Growth. *Nano Letters* **2009,** *9* (2), 689-694.

Singh, T.; Behr, M. J.; Aydil, E. S.; Maroudas, D., First-principles theoretical analysis of pure and hydrogenated crystalline carbon phases and nanostructures. *Chemical Physics Letters* **2009,** *474* (1-3), 168-174.

Smalley, R. E.; Li, Y. B.; Moore, V. C.; Price, B. K.; Colorado, R.; Schmidt, H. K.; Hauge, R. H.; Barron, A. R.; Tour, J. M., Single wall carbon nanotube amplification: en route to a type-specific growth mechanism. *Journal of the American Chemical Society* **2006,** *128* (49), 15824-15829.

Smith, D. L., *Thin-film deposition : principles and practice*. New York : McGraw-Hill: New

York, 1995.

Sparrow, T. G.; Williams, B. G.; Rao, C. N. R.; Thomas, J. M., L_3/L_2 white-line intensity ratios in the electron energy-loss spectra of 3D transition-metal oxides. *Chemical Physics Letters* **1984,** *108* (6), 547-550.

Spataru, C. D.; Ismail-Beigi, S.; Benedict, L. X.; Louie, S. G., Quasiparticle energies, excitonic effects and optical absorption spectra of small-diameter single-walled carbon nanotubes. *Applied Physics a-Materials Science & Processing* **2004,** *78* (8), 1129-1136.

Sriraman, S.; Agarwal, S.; Aydil, E. S.; Maroudas, D., Mechanism of hydrogen-induced crystallization of amorphous silicon. *Nature* **2002,** *418* (6893), 62-65.

Sun, L. T.; Gong, J. L.; Zhu, Z. Y.; Zhu, D. Z.; He, S. X.; Wang, Z. X.; Chen, Y.; Hu, G., Nanocrystalline diamond from carbon nanotubes. *Applied Physics Letters* **2004,** *84* (15), 2901-2903.

Sun, L. T.; Krasheninnikov, A. V.; Ahlgren, T.; Nordlund, K.; Banhart, F., Plastic deformation of single nanometer-sized crystals. *Physical Review Letters* **2008,** *101*, 156101.

Sun, L.; Banhart, F.; Krasheninnikov, A. V.; Rodriguez-Manzo, J. A.; Terrones, M.; Ajayan, P. M., Carbon nanotubes as high-pressure cylinders and nanoextruders. *Science* **2006,** *312* (5777), 1199-1202.

Sun, L.; Rodriguez-Manzo, J. A.; Banhart, F., Elastic deformation of nanometer-sized metal crystals in graphitic shells. *Applied. Physics Letters* **2006,** *89*, 263104.

Tafto, J.; Krivanek, O. L., Site-specific valence determination by electron energy-loss spectroscopy. *Physical Review Letters* **1982,** *48* (8), 560-563.

Tanaka, A.; Yoon, S. H.; Mochida, I., Preparation of highly crystalline nanofibers on Fe and Fe-Ni catalysts with a variety of graphene plane alignments. *Carbon* **2004,** *42* (3), 591-597.

Tans, S. J.; Verschueren, A. R. M.; Dekker, C., Room-temperature transistor based on a single carbon nanotube. *Nature* **1998,** *393* (6680), 49-52.

Taylor, A.; Floyd, R. W., Precision measurements of lattice parameters of non-cubic crystals. *Acta Crystallographica* **1950,** *3*, 285-289.

Thess, A.; Lee, R.; Nikolaev, P.; Dai, H. J.; Petit, P.; Robert, J.; Xu, C. H.; Lee, Y. H.; Kim, S. G.; Rinzler, A. G.; Colbert, D. T.; Scuseria, G. E.; Tomanek, D.; Fischer, J. E.; Smalley, R. E., Crystalline ropes of metallic carbon nanotubes. *Science* **1996,** *273* (5274), 483-487.

Thomsen, C.; Reich, S., Doable resonant Raman scattering in graphite. *Physical Review Letters* **2000,** *85* (24), 5214-5217.

Tomota, Y.; Lukás, P.; Neov, D.; Harjo, S.; Abe, Y. R., In situ neutron diffraction during tensile deformation of a ferrite-cementite steel. *Acta Materialia* **2003**, *51* (3), 805-817.

Tompkins, H. G., *Spectroscopic ellipsometry and reflectometry : a user's guide*. New York : Wiley: New York, 1999.

Transmission electron energy loss spectrometry in materials science and the EELS atlas.

Weinheim [Germany] : Wiley-VCH: Weinheim [Germany], 2004.

Treacy, M. M. J.; Ebbesen, T. W.; Gibson, J. M., Exceptionally high Young's modulus observed for individual carbon nanotubes. *Nature* **1996,** *381* (6584), 678-680.

Trojanowicz, M., Analytical applications of carbon nanotubes: a review. *Trac-Trends in Analytical Chemistry* **2006,** *25* (5), 480-489.

Tuinstra, F.; Koenig, J. L., Raman spectrum of graphite. *The Journal of Chemical Physics* **1970,** *53* (3), 1126-1130.

van Aken, P. A.; Liebscher, B., Quantification of ferrous/ferric ratios in minerals: new evaluation schemes of Fe L-23 electron energy-loss near-edge spectra. *Physics and Chemistry of Minerals* **2002,** *29* (3), 188-200.

van Aken, P. A.; Liebscher, B.; Styrsa, V. J., Quantitative determination of iron oxidation states in minerals using Fe L-2,L-3-edge electron energy-loss near-edge structure spectroscopy. *Physics and Chemistry of Minerals* **1998,** *25* (5), 323-327.

Van de Walle, C. G., Hydrogen as a cause of doping in zinc oxide. *Physical Review Letters* **2000,** *85* (5), 1012-1015.

von Ardenne, M., Das Elektronen-Rastermikrosop. *Z. Physik A-Hadron Nucl.* **1938,** *109*, 553-572.

Vora, H.; Moravec, T. J., Structural investigation of thin-films of diamondlike carbon. *Journal of Applied Physics* **1981,** *52* (10), 6151-6157.

Wang, X. S.; Li, Q. Q.; Xie, J.; Jin, Z.; Wang, J. Y.; Li, Y.; Jiang, K. L.; Fan, S. S., Fabrication of Ultralong and Electrically Uniform Single-Walled Carbon Nanotubes on Clean Substrates. *Nano Letters* **2009,** *9* (9), 3137-3141.

Wang, Y.; Alsmeyer, D. C.; McCreery, R. L., Raman-spectroscopy of carbon materials - structural basis of observed spectra. *Chemistry of Materials* **1990,** *2* (5), 557-563.

Wen, B.; Zhao, J. J.; Li, T. J., Synthesis and crystal structure of n-diamond. *International Materials Reviews* **2007,** *52* (3), 131-151.

Wen, B.; Zhao, J. J.; Li, T. J.; Dong, C.; Jin, J. Z., n-diamond from catalysed carbon nanotubes: synthesis and crystal structure. *Journal of Physics-Condensed Matter* **2005,** *17* (48), L513-L519.

Wen, C. Y.; Huang, C. C.; Cheng, H. Z.; Lu, H. Y., Orientation relations between carbon nanotubes grown by chemical vapour deposition and residual iron-containing catalysts. *Journal of Materials Science* **2008**, *43* (1), 123-131.

What is a Carbon Nanotube? www.seas.upenn.edu/mse/research/nanotubes.html.

White, C. T.; Mintmire, J. W., Density of states reflects diameter in nanotubes. *Nature* **1998,** *394* (6688), 29-30.

White, C. T.; Todorov, T. N., Quantum electronics - Nanotubes go ballistic. *Nature* **2001,** *411* (6838), 649-651.

Williams, D. B.; Carter, C. B., *Transmission electron microscopy : a textbook for materials*

science. New York : Plenum Press: New York, 1996.

Wirth, C. T.; Zhang, C.; Zhong, G. F.; Hofmann, S.; Robertson, J., Diffusion- and reaction-limited growth of carbon nanotube forests. *Acs Nano* **2009,** *3* (11), 3560-3566.

Wolden, C. A.; Barnes, T. M.; Baxter, J. B.; Aydil, E. S., Infrared detection of hydrogen-generated free carriers in polycrystalline ZnO thin films. *Journal of Applied Physics* **2005,** *97*, 043522.

Woo, Y. S.; Jeon, D. Y.; Han, I. T.; Lee, N. S.; Jung, J. E.; Kim, J. M., In situ diagnosis of chemical species for the growth of carbon nanotubes in microwave plasma-enhanced chemical vapor deposition. *Diamond and Related Materials* **2002,** *11* (1), 59-66.

Wood, I. G.; Vocadlo, L.; Knight, K. S.; Dobson, D. P.; Marshall, W. G.; Price, G. D.; Brodholt, J., Thermal expansion and crystal structure of cementite, Fe_3C, between 4 and 600 K determined by time-of-flight neutron powder diffraction. *Journal of Applied Crystallography* **2004**, *37*(1), 82-90.

Wu, Z. C.; Chen, Z. H.; Du, X.; Logan, J. M.; Sippel, J.; Nikolou, M.; Kamaras, K.; Reynolds, J. R.; Tanner, D. B.; Hebard, A. F.; Rinzler, A. G., Transparent, conductive carbon nanotube films. *Science* **2004,** *305* (5688), 1273-1276.

Wyckoff, R. W. G., *Crystal structures*. New York, Interscience Publishers: New York, 1963.

Xu, C. H.; Fu, C. L.; Pedraza, D. F., Simulations of point-defect properties in graphite by a tight-binding-force model. *Physical Review B* **1993,** *48* (18), 13273-13279.

Yang, Q. Q.; Yang, S. L.; Xiao, C. J.; Hirose, A., Transformation of carbon nanotubes to diamond in microwave hydrogen plasma. *Materials Letters* **2007,** *61* (11-12), 2208-2211.

Yao, Y. G.; Feng, C. Q.; Zhang, J.; Liu, Z. F., "Cloning" of Single-Walled Carbon Nanotubes via Open-End Growth Mechanism. *Nano Letters* **2009,** *9* (4), 1673-1677.

Yao, Y.; Falk, L. K. L.; Morjan, R. E.; Nerushev, O. A.; Campbell, E. E. B., Synthesis of carbon nanotube films by thermal CVD in the presence of supported catalyst particles. Part I: The silicon substrate/nanotube film interface. *Journal of Materials Science-Materials in Electronics* **2004,** *15* (8), 533-543.

Yao, Y.; Falk, L. K. L.; Morjan, R. E.; Nerushev, O. A.; Campbell, E. E. B., Synthesis of carbon nanotube films by thermal CVD in the presence of supported catalyst particles. Part II: the nanotube film. *Journal of Materials Science-Materials in Electronics* **2004,** *15* (9), 583-594.

Yoshida, H.; Takeda, S.; Uchiyama, T.; Kohno, H.; Homma, Y., Atomic-scale in-situ observation of carbon nanotube growth from solid state iron carbide nanoparticles. *Nano Letters* **2008,** *8* (7), 2082-2086.

Yoshida, H.; Uchiyamai, T.; Takeda, S., Environmental transmission electron microscopy observations of swinging and rotational growth of carbon nanotubes. *Japanese Journal of Applied Physics Part 2-Letters & Express Letters* **2007,** *46* (36-40), L917-L919.

Young, T., Experimental demonstration of the general law of the interference of light. *Philosophical Transactions of the Royal Society of London* **1804,** *94*.

Yu, M. F.; Lourie, O.; Dyer, M. J.; Moloni, K.; Kelly, T. F.; Ruoff, R. S., Strength and breaking mechanism of multiwalled carbon nanotubes under tensile load. *Science* **2000,** *287* (5453), 637-640.

Yu, Z. H.; Hahn, M. A.; Maccagnano-Zacher, S. E.; Calcines, J.; Krauss, T. D.; Alldredge, E. S.; Silcox, J., Small-angle rotation in individual colloidal CdSe quantum rods. *Acs Nano* **2008,** *2* (6), 1179-1188.

Zaiser, M.; Banhart, F., Radiation-induced transformation of graphite to diamond. *Physical Review Letters* **1997,** *79* (19), 3680-3683.

Zhang, G. Y.; Mann, D.; Zhang, L.; Javey, A.; Li, Y. M.; Yenilmez, E.; Wang, Q.; McVittie, J. P.; Nishi, Y.; Gibbons, J.; Dai, H. J., Ultra-high-yield growth of vertical single-walled carbon nanotubes: Hidden roles of hydrogen and oxygen. *Proceedings of the National Academy of Sciences of the United States of America* **2005,** *102* (45), 16141-16145.

Zhang, G. Y.; Qi, P. F.; Wang, X. R.; Lu, Y. R.; Mann, D.; Li, X. L.; Dai, H. J., Hydrogenation and hydrocarbonation and etching of single-walled carbon nanotubes. *Journal of the American Chemical Society* **2006,** *128* (18), 6026-6027.

Zhang, H.; Meyer, F. W.; Meyer, H. M.; Lance, M. J., Surface modification and chemical sputtering of graphite induced by low-energy atomic and molecular deuterium ions. *Vacuum* **2008,** *82* (11), 1285-1290.

Zhang, J. Q.; Ostrovski, O., Cementite formation in CH_4-H_2-Ar gas mixture and cementite stability. *Isij International* **2001,** *41* (4), 333-339.

A Appendix: Plasma Diagnostics

A.1 Gas Temperature Measurements

Fourier transform infrared spectroscopy was used to measure the gas temperature in the plasma during carbon nanotube growth assuming that the translational, vibrational, rotational degrees of freedom are all equilibrated. This is an excellent assumption under the relatively high pressure of 10 torr used for nanotube growth. Thus the gas temperature can be measured by extracting the rotational temperature from a rotational-vibrational absorption band of methane.

Rotational-vibrational absorption band of methane at 3017 cm^{-1} shown in Figure 7-2(a) consists of three branches, labeled P, Q, and R. The series of peaks that make up the P and R branches are due to transitions between rotational energy levels, each corresponding to a different value of angular momentum [1]. The angular quantum numbers associated with the first few peaks of the R branch are indicated in Figure 7-2(a). The intensity of each rotational line is proportional to the fraction of molecules that were initially in that particular rotational energy level [2]. At equilibrium, Boltzmann statistics describe the relative populations of rotational levels, and the intensity distribution among rotational levels in the R branch can be used to determine the rotational temperature. The number of molecules in the J^{th} energy level, N_J, relative to the number in the ground state, N_0, for CH_4 is given by

$$\frac{A_J}{A_o} = \frac{N_J}{N_o} = \frac{4}{3(2J+1)^2} \exp\left(-\frac{BJ(J+1)}{kT}\right)$$

where J is the angular momentum quantum number, A_J and A_0 are the absorption intensities of the Jth and ground state energy level peaks, respectively, B is the rotational constant of the molecule, k is the Boltzmann constant, and T is the absolute temperature [2, 3]. A plot of $J(J+1)$ vs. $\ln [A_J/(A_0(4/(3(2J+1)^2))]$ yielded a straight line with slope equal to B/kT, as shown in Figure 7-2(b). The rotational constant of methane was calculated from absorption measurements with no plasma activation with known gas temperature of 300 K to be 6.33 cm^{-1}.

This value was then used in calculating the gas temperature while plasma was turned on. Gas temperatures calculated with this method ranged from 300 to 345 K.

A.2 CH_4 Dissociation Measurements

The fraction of methane molecules dissociated in the plasma to form other reactive species was calculated by measuring the change in the magnitude of methane absorption upon igniting the plasma. Figure 7-2(a) shows the two overlaid absorbance spectra obtained with plasma off (black) and on (red). Absorbance, or optical density of the methane gas, A, is related logarithmically to the fraction, I, of incident light, I_o, that passes through the gas in the chamber by $A = -log(I/I_o)$. The absorbance, A is also related to the concentration of absorbing species, N (cm^{-3}), their absorption cross-section, σ (cm^2), and the path length that the light travels through the absorbing medium by $A = \sigma\, n\, l$. Since the density of methane gas in the reaction chamber is known (partial pressure of CH_4 is calculated from gas flows and total pressure), an absorbance measurement without plasma activation yielded both the integrated and average methane absorption cross-sections across the band centered at 3017 cm^{-1}. Specifically, an integrated absorption cross-section across the band, $\int_{\tilde{\nu}_1}^{\tilde{\nu}_2} \sigma(\tilde{\nu}) d\tilde{\nu}$, was calculated to be 6.18×10^{17} cm by integrating the measured absorbance across the entire absorption band, from 3001.2-3178.8 cm^{-1}. While the average absorption cross-section across the band, $\int_{\tilde{\nu}_1}^{\tilde{\nu}_2} \sigma(\tilde{\nu}) d\tilde{\nu} \Big/ \int_{\tilde{\nu}_1}^{\tilde{\nu}_2} d\tilde{\nu}$, was calculated to be 3.48×10^{19} cm^2.

A.3 References

[1] Herzberg, G., *Molecular spectra and molecular structure*. New York : Prentice-Hall: New York, 1939.

[2] McQuarrie, D. A., *Quantum chemistry*. Sausalito, Calif. : University Science Books: Sausalito, Calif., 2008.

[3] McDowell, R. S., Rotational partition-functions for spherical-top molecules. *Journal of Quantitative Spectroscopy & Radiative Transfer* **1987,** *38* (5), 337-346.

B Appendix: Measurement of H-atom Flux

We developed a method for measuring the H-atom flux at the plane of the substrate surface during H_2 plasma exposure. Our method is based on infrared measurements of the change in free-electron absorption in a polycrystalline ZnO film when this film exposed to H atoms. Hydrogen acts as an electron donor in ZnO [1, 2], and thus the concentration of hydrogen-generated free carriers can be extracted from their absorption in the infrared, as demonstrated by Wolden et al. [3] The change in the concentration of free carriers can in turn be related to the flux of H atoms impinging on a ZnO film placed on the substrate platen.

A 110 nm thick polycrystalline ZnO thin film was grown from solution on a trapezoidal-shaped GaAs attenuated-total-reflection (ATR) crystal. The beveled edges of the crystal were first masked so that the film was deposited only on the top face. Next, the crystal was placed top-face down in a 0.01 M solution of zinc nitrate and methenamine in ethanol. At 80 ^{o}C, a 110 nm thick film was grown in 1 hour.

The ZnO-coated GaAs ATR crystal was placed on the substrate platen located approximately 25 cm below the RF plasma coil. An IR beam from a Nicolet Magna-IR 550 FTIR spectrometer was directed into the plasma reaction chamber through KBr windows and focused onto the 45^{o} beveled edge of the GaAs ATR crystal, in which it underwent 31 internal reflections from the top and bottom crystal surfaces, sampling the ZnO film 15 times. After exiting the opposite 45^{o} beveled edge of the ATR crystal, the transmitted beam was detected with an external, cooled HgCdTe detector. Absorption spectra in the range from 650-5000 cm^{-1} with a spectral resolution of 2 cm^{-1} were averaged over 300 scans and recorded after each 20-second exposure to a 200 W H_2/Ar plasma up to 120 seconds total exposure. The H_2 and Ar flow rates were 50 and 2.5 sccm, respectively, and the chamber pressure was 0.15 Torr. All spectra were collected relative to the ZnO-coated ATR crystal before H exposure so that any measured changes in absorbance were solely due to the incident H atoms from the plasma.

Figure B-1(a) shows the FTIR spectra of the 110 nm thick polycrystalline ZnO on GaAs ATR crystal obtained after every 20 seconds up to 120 seconds of total H-atom exposure. The

observed broad-band absorption closely follows a wavelength dependence of λ^2, as predicted by the Drude model for free-electron absorption in a polycrystalline semiconductor [4]. The increase in broad-band absorption with longer H-atom exposure is due to the increase in the number of H atoms that become incorporated into the film. This change in carrier concentration was extracted from the frequency dependence of the free-electron absorption and the complex part of the dielectric function using the Drude model and an optical model for the multiple reflections that occur in ATR geometry [5]. In ATR geometry, the extinction coefficient, $k(\tilde{\nu})$, is related to the infrared absorbance, $A(\tilde{\nu})$, by

$$k(\tilde{\nu}) = \frac{A(\tilde{\nu})}{4\pi\tilde{\nu}N_R d_e(\tilde{\nu})},$$

where $\tilde{\nu}$, N_R, and d_e are the wavenumber, the number of internal reflections in the internal crystal, and the effective thickness of the ZnO film, respectively. The effective thickness is used here instead of the ZnO film thickness, because the IR beam, when reflected from the GaAs-ZnO interface, decays exponentially into the ZnO film [6]. The effective thickness was calculated using the three-layer optical model of the GaAs-ZnO-vacuum stack as presented by Han et al. [5] The imaginary component of the dielectric constant, $\varepsilon_2(\tilde{\nu})$, is related to the extinction coefficient by $\varepsilon_2(\tilde{\nu}) = 2nk(\tilde{\nu})$, where n is the refractive index of ZnO. Next, the Drude model relates $\varepsilon_2(\tilde{\nu})$ to the film conductivity, σ, and carrier relaxation time, τ, through

$$\varepsilon_2(\tilde{\nu}) = \frac{\sigma}{\varepsilon_0\omega\left(\omega^2\tau^2 + 1\right)},$$

where ω is the frequency in radians/s $(\omega = 2\pi c\tilde{\nu})$ and ε_0 is the permittivity of vacuum. Both σ and τ were determined from a nonlinear least-squares fit of the experimental data to the Drude model. The increase in carrier concentration, N_e, could then be calculated from σ and τ by

$$N_e = \frac{\sigma m^*}{e^2\tau},$$

where e is the electron charge and $m^* = 0.32$ is the effective mass of electrons in ZnO [7]. Figure B-1(b) shows the calculated carrier concentration as a function of H-atom exposure time. Assuming that all H atoms that reach the ZnO surface incorporate into the film and donate one electron, then the flux, F_H, of H atoms to the surface can be calculated from the slope of the plot in Figure B-1(b) by

$$F_H = \delta \frac{d}{dt} N_e ,$$

where $\delta = 110$ nm is the ZnO film thickness. This method yielded an H-atom flux of 2.2×10^{17} $cm^{-2}s^{-1}$ for an H_2:Ar (50:2.5 sccm) 200 W RF plasma at 0.15 Torr.

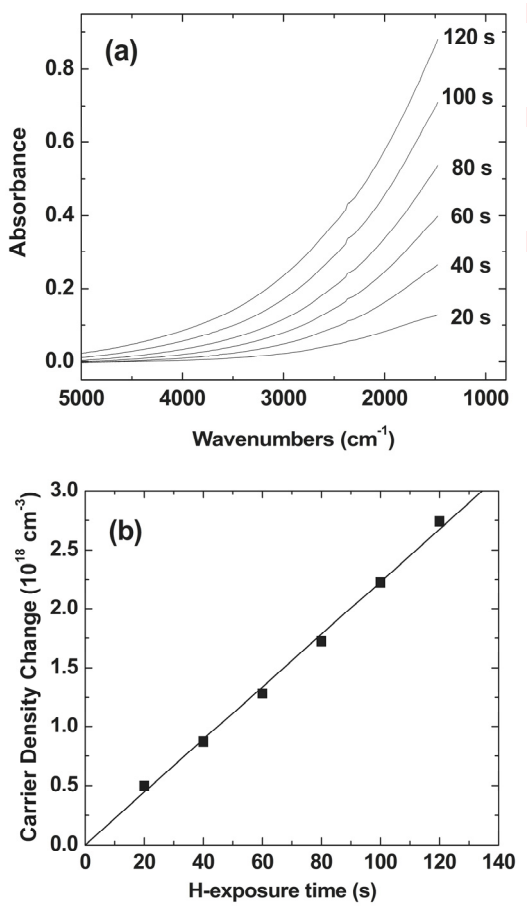

Figure B-1. (a) Infrared absorption spectra, obtained in attenuated-total-reflection mode, of a 110 nm thick polycrystalline ZnO film after 20-second H-atom exposures at room temperature. The broad-band free-electron absorption increases as H atoms from the plasma are incorporated into the film. (b) A plot of the increase in carrier density as calculated from the absorption spectra as a function of the H-atom exposure time. The slope of this plot multiplied by the ZnO film thickness yields the H flux to the film surface, 2.2×10^{17} $cm^{-2}s^{-1}$.

B.1 References

[1] Van de Walle, C. G., Hydrogen as a cause of doping in zinc oxide. *Physical Review Letters* **2000,** *85* (5), 1012-1015.

[2] Kilic, C.; Zunger, A., n-type doping of oxides by hydrogen. *Applied Physics Letters* **2002,** *81* (1), 73-75.

[3] Wolden, C. A.; Barnes, T. M.; Baxter, J. B.; Aydil, E. S., Infrared detection of hydrogen-generated free carriers in polycrystalline ZnO thin films. *Journal of Applied Physics* **2005,** *97*, 043522.

[4] Pankove, J. I., *Optical processes in semiconductors*. Englewood Cliffs, N.J., Prentice-Hall: Englewood Cliffs, N.J., 1971.

[5] Han, S. M.; Aydil, E. S., Reasons for lower dielectric constant of fluorinated SiO_2 films. *Journal of Applied Physics* **1998,** *83* (4), 2172-2178.

[6] Harrick, N. J., *Internal reflection spectroscopy*. New York, Interscience Publishers: New York, 1967.

[7] Minami, T., New n-type transparent conducting oxides. *Mrs Bulletin* **2000,** *25* (8), 38-44.